EXPERIMENTAL STUDY ON THE SUBCOOLED BOILING FLOW VIA OPTICAL MEASUREMENT TECHNIQUES

A Dissertation

by

JUN SOO YOO

Submitted to the Office of Graduate and Professional Studies of
Texas A&M University
in partial fulfillment of the requirements for the degree of

DOCTOR OF PHILOSOPHY

Chair of Committee,	Yassin A. Hassan
Committee Members,	Kalyan Annamalai
	Hamn-Ching Chen
	Wiliam H. Marlow
Head of Department,	Yassin A. Hassan

May 2015

Major Subject: Nuclear Engineering

ABSTRACT

A series of experimental work to investigate the subcooled boiling flow in a vertical square upward flow channel is described. As experimental methods, high-speed photography and infrared (IR) thermometry were employed simultaneously. The research scope explored includes (i) measurement issues of fundamental bubble parameters through visualization, (ii) experimental methodology to achieve both enhanced two-phase flow visualization and accurate wall temperature measurement, and (iii) measurement of diverse aspects of bubble dynamics as well as wall heat transfer by applying the verified experimental approach.

Before producing the actual data, substantial effort was first made to identify the critical measurement issues of fundamental bubble parameters in a forced convective boiling system. Those issues have never been explicitly addressed in previous studies despite the possibly critical impacts on the experimental results. Thus, a series of systematic experimental investigations was performed to uncover those issues and to verify the errors created by not addressing them, based on which more suitable ways of observing and characterizing such parameters through experiments were discussed.

Then, an experimental strategy to achieve high-fidelity optical measurements using both high-speed photography and IR thermometry was established. To attain the goal, the important issues such as test section design, IR thermal imaging issues, visualization strategy, wall temperature tracking method, and experimental validations were extensively addressed. Also, the feasibility of current experimental approach was demonstrated through the subcooled flow boiling experiment.

Finally, by employing the experimental strategy established, an experimental investigation of the subcooled boiling flow was conducted. The experiment was performed in a vertical square upward flow channel using refrigerant Novec^{TM} 7000, in which a single nucleation site was purposely activated for a fundamental study of subcooled flow boiling process. The various aspects of bubble behavior under different subcooled flow boiling conditions were examined using both micro- and macroscopic views of high-speed cameras while measuring the wall temperature/heat flux with IR thermometry. Additionally, based on the measurements of various bubble parameters as well as wall heat transfer, relevant relations among those parameters and the underlying mechanisms were intensively discussed.

DEDICATION

This dissertation is dedicated to my parents and beloved sister Jimin.

ACKNOWLEDGEMENTS

I acknowledge Dr. Yassin A. Hassan, my advisor and the chair of my committee for his support during the course of my research and study at Texas A&M University. Also, I would like to thank my committee members, Dr. Kalyan Annamalai, Dr. Hamn-Ching Chen, and Dr. William Marlow for taking their time to work with me until fulfilling all the requirements of the doctoral program.

Special thanks are given to my parents and sister Jimin for their incredible understanding, patience, and encouragement. Without their help and sacrifice, it would have been impossible for me to complete this work. I am grateful to them for everything.

TABLE OF CONTENTS

Page

ABSTRACT ii

DEDICATION iv

ACKNOWLEDGEMENTS v

TABLE OF CONTENTS vi

LIST OF FIGURES ix

LIST OF TABLES xiv

CHAPTER I INTRODUCTION 1

CHAPTER II IDENTIFICATION OF CRITICAL ISSUES ON THE MEASUREMENT OF FUNDAMENTAL BUBBLE PARAMETERS THROUGH VISUALIZATION 3

- A. Introduction 3
- B. Comparative analysis of experimental studies in the literature 9
- C. Experimental setup and measurement strategy 15
  - 1. Hydraulic loop and instruments 15
  - 2. Test section and heater design 16
  - 3. Visualization strategy 19
  - 4. Test conditions and measurement strategy 20
- D. Issue identification for the proper investigation of bubble parameters 21
  - 1. Measurement view issues 21
  - 2. Issue related to the recording speed of visualization 30
  - 3. Issue of sample size 34
  - 4. Judging the bubble departure moment 41
- E. Image analysis method 43
  - 1. Overview of image analysis procedure 43
  - 2. Image processing algorithm 45
  - 3. Error analysis of automated image analysis method 48
- F. Summary and conclusions 50

CHAPTER III ACCURATE WALL TEMPERATURE MEASUREMENT USING INFRARED THERMOMETRY WITH ENHANCED TWO-PHASE FLOW VISUALIZATION 53

- A. Introduction 53
- B. Experimental strategy and measurement issues 60
  - 1. Material selection and test section design 60
  - 2. Measurement strategy 63
  - 3. Wall temperature measurement issues 64
- C. Analysis method for wall temperature tracking 66
- D. Optical property measurement 69
  - 1. Experimental procedure and measured optical properties 69
  - 2. Validation of measured properties of semi-transparent media 75
- E. Experimental validation with the proposed heater wall design 77
  - 1. Validation of ITO film’s optical properties and the steady-state test 78
  - 2. Transient test 82
  - 3. Heat flux measurement 87
- F. Application in a subcooled flow boiling experiment 90
- G. Uncertainty quantification 94
- H. Conclusions 96

CHAPTER IV EXPERIMENTAL OBSERVATION ON BUBBLE DYNAMICS AND WALL HEAT TRANSFER ARISING FROM A SINGLE NUCLEATION SITE – PART 1: EXPERIMENTAL STRATEGY AND MICROSCOPIC OBSERVATION OF BUBBLE BEHAVIORS 97

- A. Introduction 97
- B. Experimental facility 102
  - 1. Flow boiling loop and instruments 102
  - 2. Experimental strategy and procedures 105
  - 3. Data collection, image analysis, and repeatability test 109
  - 4. Measurement uncertainty (for HSV 1) 114
  - 5. Test conditions 116
- C. Result and discussion 119
  - 1. Visual observation of nucleating behaviors 119
  - 2. Bubble growth behavior 122
  - 3. Axial bubble velocity 127
  - 4. Bubble release frequency 132
  - 5. Local bubble number variation and evaporative heat flux 140
- D. Summary and conclusions 147

CHAPTER V EXPERIMENTAL OBSERVATION ON BUBBLE DYNAMICS AND WALL HEAT TRANSFER ARISING FROM A SINGLE NUCLEATION SITE AT SUBCOOLED FLOW BOILING CONDITIONS – PART 2:

MACROSCOPIC OBSERVATION OF BUBBLE BEHAVIORS AND WALL HEAT TRANSFER 151

A. Introduction 151
B. Main interests of present study 157
C. Repeatability test 160
D. Measurement uncertainty (for HSV 3 and IR thermometry) 162
E. Experimental results and discussion 163
  1. Bubble growth behavior 163
  2. Axial bubble velocity 170
  3. Local bubble number variation 177
  4. Local bubble size distribution 183
  5. Time-averaged local wall heat transfer coefficient 190
F. Summary and conclusions 196

CHAPTER VI SUMMARY AND CONCLUSIONS 200

REFERENCES 203

APPENDIX A. 216

A.1. Derivation of apparent reflectivity and apparent transmissivity 216
A.2. Radiation balance equation and coefficients required for validation tests in Section D.2 in Chapter III 218
A.3. Heater wall temperature tracking through the multilayer 221

LIST OF FIGURES

Page

Figure II-1. Schematic of test section and ITO-coated glass heater.................................17

Figure II-2. Visual observation of vapor bubbles for subcooled flow boiling experiment (not to scale)...18

Figure II-3. Estimation of 3D volume equivalent diameter (Deq, 3D)............................23

Figure II-4. 2D-based bubble departure diameters from different measurement views; blue lines on the right border of side view images indicate the heater surface..24

Figure II-5. Departure bubbles' aspect ratio and the difference of 2D-based bubble departure diameters (Deq, 2D-side, and Deq, 2D-top) contrasted with the 3D volume equivalent diameters 27

Figure II-6. Bubble departure phenomena at the nucleation site (Type 1: direct lift-off from the heater wall, Type 2: departure through sliding).............................27

Figure II-7. Images of bubble nucleation from the different measurement views...........28

Figure II-8. Average bubble departure frequency analysis using the visual images of different measurement views...30

Figure II-9. Average bubble departure frequency measured with different recording speeds..31

Figure II-10. Time intervals between the nucleation events during the measurement period for case 1...34

Figure II-11. Average bubble departure frequency depending on the number of observations 36

Figure II-12. Average bubble departure diameter depending on the number of observations 36

Figure II-13. Individual bubble departure frequencies during the measurement period and the PDFs..40

Figure II-14. Individual bubble departure diameters during the measurement period and the PDFs..41

Figure II-15. Automatic image analysis algorithm for the fundamental bubble parameter analysis 45

Figure II-16. Image processing algorithm applied in the present image analysis method 48

Figure II-17. Error analysis for the average bubble departure frequency 50

Figure III-1. Overview of present study considering the general process for introducing the new experimental approach 60

Figure III-2. Heater wall design (top) and measurement strategy (bottom) in the subcooled flow boiling experiment (view from the top of channel) 63

Figure III-3. Temperature distortions captured by the IR camera due to the Narcissus effect 65

Figure III-4. Optical property measurement of the materials composing the heater wall 70

Figure III-5. Temperature tracking results through a single layer of a semi-transparent medium 76

Figure III-6. Temperature tracking results through the double layer of semi-transparent media 77

Figure III-7. Experimental setup to validate the ITO film's optical properties 79

Figure III-8. Validation of temperature-tracking algorithm under steady-state conditions 82

Figure III-9. Experimental setup for transient test with cold air injection 83

Figure III-10. Validation test under transient condition 84

Figure III-11. Axial centerline temperature profile variation after the cold air injection (L0=3 cm) 86

Figure III-12. Variation of axial wall temperature profiles based on coupling the 1D and 2D heat conduction equations 87

Figure III-13. Heat balance relation at the wall to obtain the local heat input to the fluid qin 89

Figure III-14. Validation of heat flux measurement using the present algorithm 89

Figure III-15. Visual measurement of vapor bubbles and 2D wall temperature map (before calibration) in the vertical upward test section................................91

Figure III-16. Axial distribution of wall temperature at the centerline...........................93

Figure III-17. Horizontal wall temperature profiles at different axial locations (non-filled symbols: axial locations upstream of the nucleation site; filled symbols: axial locations downstream of the nucleation site) 94

Figure IV-1. High-speed visualization of vapor bubbles and heater surface temperature measurement in the subcooled flow boiling experiment........104

Figure IV-2. Representative bubble images taken from the three high-speed cameras.106

Figure IV-3. Multi-layer design of heater wall and the heater surface temperature measurement using IR thermometry...108

Figure IV-4. Repeatability test on the bubble size based on the measurement of HSV 1 (left) and HSV 3(right) 111

Figure IV-5. Repeatability test on the axial bubble velocity based on the measurement of HSV 1 114

Figure IV-6. Main interests of present study with the schematic of image analysis procedure for HSV 1..118

Figure IV-7. Boiling behaviors at the single nucleation site affected by the varying inlet subcooling (top), liquid mass flux (middle), and wall heat flux (bottom) 121

Figure IV-8. Effects of inlet subcooling (ΔTsub,in) on bubble growth behavior along the flow path 125

Figure IV-9. Effects of liquid mass flux (G) on bubble growth behavior along the flow path 126

Figure IV-10. Effects of wall heat flux (qw) on bubble growth behavior along the flow path 127

Figure IV-11. Effects of inlet subcooling (ΔTsub,in) on axial bubble velocity............129

Figure IV-12. Effects of liquid mass flux (G) on axial bubble velocity 131

Figure IV-13. Effects of wall heat flux (qw) on axial bubble velocity..........................131

Figure IV-14. Effects of inlet subcooling (ΔTsub,in) on bubble release frequency 134

Figure IV-15. Dependence of bubble release frequency on liquid mass flux (G) at ΔTsub,in=4.6 °C 135

Figure IV-16. Dependence of bubble release frequency on liquid mass flux (G) at ΔTsub,in=13.5 °C 136

Figure IV-17. Dependence of bubble release frequency on the Ja number 140

Figure IV-18. Bubble number reduction through the region L/L0=0.41~0.44 depending on liquid mass flux (G, left) and wall heat flux (qw, right) 144

Figure IV-19. Bubble number reduction through the region L/L0=0.41~0.44 depending on inlet subcooling (ΔTsub,in)..144

Figure IV-20. Relative portion of local evaporative heat flux (qe/qw) depending on liquid mass flux (G, left) and wall heat flux (qw, right)............................146

Figure IV-21. Relative portion of local evaporative heat flux (qe/qw) depending on inlet subcooling (ΔTsub,in)...147

Figure V-1. Measured parameters of interest and the image analysis procedures.........159

Figure V-2. Repeatability tests on the parameters measured in present study..............161

Figure V-3. Effects of inlet subcooling (ΔTsub,in) on bubble growth along the flow path..167

Figure V-4. Effects of liquid mass flux (G) on bubble growth along the flow path 169

Figure V-5. Effects of wall heat flux (qw) on bubble growth along the flow path........170

Figure V-6. Effects of inlet subcooling (ΔTsub,in) on axial bubble velocity 173

Figure V-7. Effects of liquid mass flux (G) on the axial bubble velocity.....................175

Figure V-8. Effects of wall heat flux (qw) on axial bubble velocity.............................177

Figure V-9. Effects of inlet subcooling (ΔTsub,in) on local bubble number variation along the flow path 180

Figure V-10. Effects of liquid mass flux (G) on local bubble number variation along the flow path 182

Figure V-11. Effects of wall heat flux (qw) on local bubble number variation along the flow path 183

Figure V-12. Effects of inlet subcooling (ΔTsub,in) on probability density function (PDF) for bubble size and its development in the upward flow direction .. 187

Figure V-13. Effects of liquid mass flux (G) on probability density function (PDF) for bubble size and its development in the upward flow direction 188

Figure V-14. Effects of wall heat flux (qw) on probability density function (PDF) for bubble size and its development in the upward flow direction 189

Figure V-15. Effects of inlet subcooling (ΔTsub,in) on time-averaged wall heat transfer coefficient 193

Figure V-16. Effects of liquid mass flux (G) on time-averaged wall heat transfer coefficient 195

Figure V-17. Effects of wall heat flux (qw) on time-averaged wall heat transfer coefficient 196

Figure A-1. Energy reflection and transmission throughout the semi-transparent medium 217

Figure A-2. Experimental setup for validation test with a single layer of medium 218

Figure A-3. Radiation balance equation and coefficients used for the single-layer validation test 219

Figure A-4. Validation test with double layers of medium 220

Figure A-5. Radiation balance equation and coefficients used for the double-layer validation test 220

Figure A-6. Schematic of wall temperature tracking algorithm 223

Figure A-7. Derivation of coefficients used in Eq. (III-1) 224

LIST OF TABLES

Page

Table II-1. Visual measurement of vapor bubble dynamics in forced convective boiling experiments..10

Table II-2. Observation of bubble departure frequency under different experimental conditions...33

Table III-1. Measured optical properties of the materials composing the heater wall.....74

Table III- 2. Major sources of uncertainty for the wall temperature tracking.................95

Table IV-1. Summary of test conditions and local parameters measured......................117

CHAPTER I

INTRODUCTION

Boiling heat transfer has drawn great attention over the last half century because of its decent feature, the highly efficient heat transfer mode that can be integrated to the engineered systems, and it has become one of the most researched topics within the heat transfer community. However, the underlying physics of the enhanced heat transfer mode associated with boiling is yet to be fully understood, and the lack of information about the basic principles and the involved sub-processes still prevents the mechanistic prediction of the boiling phenomenon with reasonable accuracy. Mostly, the difficulties of the experimental study of boiling originate from the inherently random and chaotic nature of the phenomenon. In other words, the measured parameters from any boiling experiment are always given in terms of a distribution rather than a single deterministic value. In addition, the occurrence of boiling is often quite sensitive to small changes in heater surface conditions, and the onset of boiling due to such an unexpected perturbation can lead to significant changes in the overall heat transfer characteristics of the system while increasing the phenomenological complexity. This implies that in order to achieve the truly reliable experimental data that can provide the correct physical information regarding boiling heat transfer careful attention is required.

In this study, a series of experimental works has been performed to investigate the subcooled boiling phenomenon in a square, vertical, upward flow channel. The experimental methods employed were the advanced optical measurement techniques high-speed photography and infrared (IR) thermometry, with which we observed both the bubble dynamics and the wall heat transfer simultaneously in a single experimental facility. The measurement methods used in this work provide an advantage over the traditional point measurements in the sense that the bubble dynamics as well as the wall heat transfer features can be observed as 2-dimensional (2-D) field with relevant scales without disturbing the flow inside. During this work, however, several key experimental issues were found that must be correctly addressed in order to avoid misleading experimental results obtained by the application of present experimental methods. In particular, a review of the literature revealed that many experimental works are still being made without properly addressing those issues despite their critical impact on the experimental results. In this context, before producing the actual data, we made substantial effort to identify the critical measurement issues and to establish a proper measurement system that can provide the reliable experimental data during the subcooled flow boiling experiment using the selected experimental methods. Then, the experimental data under various subcooled flow boiling conditions were collected and analyzed based on the present measurement system and the results were discussed.

This dissertation describes an extensive series of experimental work, including the identification of boiling parameter measurement issues (Chapter II), experimental methodology establishment (Chapter III), and measurement of various two-phase flow and wall heat transfer parameters in a subcooled flow boiling experiment based on the experimental approach verified in this study (Chapter IV and Chapter V).

CHAPTER II

IDENTIFICATION OF CRITICAL ISSUES ON THE MEASUREMENT OF FUNDAMENTAL BUBBLE PARAMETERS THROUGH VISUALIZATION[*]

A. Introduction

Much attention has been paid to the efficient heat transfer mode of forced convective boiling due to its promising future for engineering applications, such as the cooling systems of nuclear reactors, electronic and propulsion devices. However, the physical mechanism involved in boiling is yet to be fully understood because its inherent nature is quite complicated, while the advances in experimental and analytical techniques to investigate the specifics of it are relatively limited. Nevertheless, in recent decades, many efforts to combine the rapidly advancing experimental achievements and mathematical tools to analyze the complex flow behaviors have led to substantial progress in understanding the two-phase flow system. As an effort to analyze or predict the detailed two-phase flow behaviors, the two-fluid (time-averaged) model—which handles the transient behaviors of two different phases separately—has been widely used. However, since the actual behaviors of each phase are not independent of each other, the interaction terms, called the interfacial transfer terms, play an important role under this two-fluid model framework because those terms control the local mass,

---

[*] Reprinted with permission from "A proper observation and characterization of wall nucleation phenomena in a forced convective boiling system" by J. Yoo, Carlos E. Estrada-Perez, Yassin A. Hassan, 2014, *International Journal of Heat and Mass Transfer*, **76**, 568-584, Copyright 2014 by Elsevier Ltd.

momentum, and energy transfer between phases. As a result, the performance of two-fluid model depends heavily on the validity of the interfacial transfer terms which need to be well defined based on experimental information. In particular, for subcooled and saturated boiling flow, bubble nucleation at the heated wall (i.e., wall nucleation) is one such important piece of information needed from experiments because it is the main mechanism of enhancing the local heat transfer through the increase of interfacial area, the large evaporative heat transfer, and interactions between the liquid and vapor phase [1, 2]. The bubble nucleation parameters usually considered in mechanistic models are (i) bubble departure and lift-off diameter, (ii) bubble departure frequency, and (iii) active nucleation site density. Thus, detailed experimental data about these fundamental bubble parameters are crucial to accurately predict the wall nucleation phenomena, and many experimental works have been performed in this context.

Klausner et al. [3] measured the bubble departure diameter in a horizontal forced convective boiling facility using saturated R-113. They found that asymmetric bubble growth and surface tension force are important to hold the bubble at the nucleation site before departure. In particular, the bubble departure and lift-off were conceptually distinguished in their work: Bubble departure was defined as the moment when the bubble leaves the nucleation site, while bubble lift-off indicated the moment when bubble is detached from the heated wall. In their experiments, vapor bubbles typically left the nucleation sites by sliding a finite distance along the heater rather than directly lifting off the wall. Subsequently, Zeng et al. [4] obtained additional data sets for the bubble lift-off diameter using the same facility. Zeng et al. suggested a prediction model for bubble departure and bubble lift-off diameter in which the bubble inclination angle is estimated as part of the dynamic solution instead of being used as an empirical constant. Also, they argue that the prediction model can be applied to the vertical boiling flow with proper modifications. Nucleation site density was measured in the same experimental facility, revealing the strong dependence of nucleation site density on the vapor velocity, heat flux, system pressure, and cavity size [5]. Using FC-87, Thorncroft et al. [6] studied the bubble growth and detachment process for the vertical upflow and downflow boiling. The data were collected under slightly subcooled boiling conditions (ΔT_{sub}=1-5K), and significant differences in bubble behaviors were observed between the upflow and downflow tests. Prodanovic et al. [7] investigated the bubble size, bubble life time, bubble growth time, and bubble condensation time for the subcooled boiling flow of water in a vertical upward annulus channel. Based on the measured data, Proanovic et al. suggested semi-empirical correlations to predict variations in bubble size and life time. Situ et al. [8] measured the bubble lift-off diameter in a vertical upward annulus channel. They obtained the bubble lift-off diameter for 91 test conditions at atmospheric pressure. Based on the data collected, a non-dimensional prediction model for the bubble lift-off diameter was proposed; the proposed model fit their experimental data with a relative error of ±35.2%. Later, Situ et al. [9] measured the bubble departure frequency in the same facility. They compared the existing models and correlations to the existing experimental data in the literature as well as to their own data. Then, an empirical correlation that correlates the dimensionless bubble departure frequency and the non-dimensional nucleate boiling heat flux was derived; the average prediction error was revealed as ±113%. Using a test section geometry similar to Situ et al. [8] and Situ et al. [9], Euh et al. [10] measured the bubble departure frequency under various subcooled boiling conditions of water. They argued that mass flux, heat flux, subcooling, and pressure are the major parameters affecting the bubble departure frequency. Euh et al.'s experimental data were compared with the existing models, and they proposed a new prediction model by modifying Situ et al.'s model [9]. Chu et al. [11] observed the bubble lift-off diameter as well as the bubble nucleation frequency in a vertical annulus test section through which water flowed upward under various subcooled boiling conditions. They investigated the bubble lift-off diameter as well as bubble nucleation frequency depending on heat flux, mass flux, and subcooling degree. Note that in Chu et al.'s work, the mean values of bubble parameters measured were estimated by averaging the measured values over the several nucleation sites under each experimental condition. This was to avoid biased result of bubble characteristics induced by the specific microstructure of individual nucleation sites. Recently, Brooks et al. [12] measured bubble departure frequency, departure diameter, and several bulk flow parameters, e.g., void fraction and interfacial area concentration, for the subcooled boiling conditions of water in a vertical annulus channel. The bubble parameters measured were compared with the existing models, and the modeling of wall nucleation source terms in the interfacial area transport equation [2] was discussed based on the result.

In addition to the experimental and modeling work described above, many efforts have been made by various researchers to better understand and predict the wall nucleation phenomena under various forced convective boiling conditions, and those efforts are still ongoing. However, considerable variation and inconsistency still exist among the experimental investigations, even under similar test conditions. These differences often hinder progress toward better insight into the underlying physics of wall nucleation phenomena. This is mainly due to the inherently chaotic nature of the boiling mechanism, indicating that the experimental results are quite sensitive to many variables such as heater wall surface condition and flow boundary condition. In addition, substantial errors and measurement uncertainties may occur due to limitations of the imaging techniques used to observe the nucleating bubbles. Specifically, optical distortions, limited resolution, and difficulty in the analysis of images crowded with bubbles at high heat flux conditions are important issues to be considered for the accurate measurement of fundamental bubble parameters. Also, the specific strategy of bubble imaging by experimentalist and the obtained quality of bubble image can affect the measurement results. Moreover, due to the normally strong stochastic features of boiling process [3, 4, 13-15], a limited number of experimental observations may not represent the boiling characteristics and the parametric effect properly. For instance, when considering the significant differences in the number of experimental observations used by different researchers (Table II-1), the question of whether or not the sample number used was truly representative of the measured parameter under the given experimental conditions arises. Undoubtedly, if the statistical average at each test condition is not reliable, the uncertainty will increase [16] and the resulting experimental information can be even misleading.

To the best of our knowledge, no efforts have been made to treat these issues explicitly, and experimental investigations are still being performed without addressing or quantifying the effects of those issues. However, as will be shown in the following sections, failure to consider those fundamental issues may significantly mislead experimental investigations and subsequently compromise the quality of the physical models which are derived based on experimental results. In this context, we first discuss the possible issues of bubble imaging (or visual experiment) for the measurement of fundamental bubble parameters based on the comparative analysis of experimental studies in the literature (Section B). Then, in an effort to experimentally verify the individual issues, we performed subcooled flow boiling experiment (Section C) in which various aspects of measurement issues on the bubble departure diameter and bubble departure and/or nucleation frequency were investigated (Section D). Lastly, we suggest an image analysis method to more efficiently and accurately extract the quantitative information from the experimental images of boiling bubbles. The validity of this method of analysis is demonstrated in Section E.

B. Comparative analysis of experimental studies in the literature

Ten different visual experimental studies were reviewed and compared based on items which are expected to have an impact on the experimental results; these are listed in Table II-1. All the studies reviewed intended to measure the fundamental bubble parameters through visualization of bubbles under forced convective boiling conditions but using different measurement strategies. They provided measured data that can be used to suggest or validate prediction models related to wall nucleation. Since experimental studies performed in the same facility or by the same authors usually shared the same measurement strategies, they are grouped together; thus, such studies were put into the same column in Table II-1. In this section, we discuss the differences among those experimental studies as well as possibly critical issues never addressed explicitly before. This will help us to clarify the current status of experimental works and additional efforts that need to be made to improve the quality of experimental investigations for fundamental bubble parameters associated with wall nucleation.

Table II-1. Visual measurement of vapor bubble dynamics in forced convective boiling experiments

	Euh et al. [10]; Ozar [17]	**Chu et al. [11]**	**Situ et al. [8, 9]**	**Basu et al. [18]; Basu [19]**	**Prodanovic et al. [7]; Fraser et al. [20]**
Channel geometry	Annulus	Annulus	Annulus	Square (flat heater/3×3 rod bundle)	Annulus
Working fluid	Water	Water	Water	Water	Water
Flow direction	Vertical (upflow)	Vertical (upflow)	Vertical (upflow)	Vertical (upflow)	Vertical (upflow)
Resolutions (spatial, temporal)	64 μm/pix, 5 kHz	12 μm/pix, 5–10 kHz	16 μm/pix, 5 kHz	50 μm/pix, 1.2 kHz	[c], 6–8 kHz
Measured parameters	Bubble departure frequency	Lift-off diameter, nucleation frequency	Lift-off diameter [8], bubble departure frequency [9]	Bubble release frequency, bubble waiting/growth time, bubble departure size, nucleation site density, etc.	Bubble growth/condensation rate, bubble life time, bubble detachment diameter
Measurement view[a]	Top view	Side view	Side view	Top view (nucleation site density) Side view (bubble size, frequency)	Side view
Average bubble departure frequency (definition)	$\sum_{i} / \sum_{i} \tau_{i}$	$\sum_{i} / \sum_{i} \tau_{i}$	$\sum_{i} / \sum_{i} \tau_{i}$	[c]	[c]
Characteristic length of the bubble size	[c]	Effective diameter based on 2D projected area	[c]	[c]	Feret diameter
Bubble departure moment (How it was determined)	[c]	Bubble lift-off moment from the wall was determined manually.	Bubbles within a certain sizes were selected without judgment of departure moment [9].	[c]	Manually determined
Number of observations used to calculate statistical average	150–200[b]	About 100–120 observations were used for average lift-off diameter.	Typically 50 observations were used for average lift-off diameter [8]. But it was not specified for bubble departure frequency [9].	A minimum of 3 observations were used for average bubble departure frequency and bubble departure diameter.	About 100 observations were used to estimate the average lift-off diameter.
Statistical analysis	A typical distribution of nucleation time interval was provided.	[c]	[c]	[c]	Statistical distribution of detachment diameter was shown at a certain single test condition [20].

[a] The measurement view was inferred based on the typical bubble images shown in the publication(s).
[b] From Figure 8 in the paper, it is inferred that 150–200 observations were typically used to calculate the average bubble departure frequency.
[c] Not described explicitly

Table II-1 continued.

	Brooks et al. [12]	**Okawa et al. [21]**	**Thorncroft et al. [6]**	**Klausner et al. [3]**	**Maurus et al. [22, 23]**
Channel Geometry	Annulus	Cylindrical Tube	Square	Square	Square
Working Fluid	Water	Water	FC-87	R-113	Water
Flow direction	Vertical (upflow)	Vertical (upflow)	Vertical (upflow/downflow)	Horizontal	Horizontal
Resolutions (spatial, temporal)	4.7 μm/pix, 10 kHz	50 μm/pix, 4 kHz	20 μm/pix, 2 kHz	25.4 μm/pix, -	Top: >8 μm, 7.5 Hz Side: >40 μm, 9 kHz
Measured parameters	Bubble departure diameter, bubble departure frequency, void fraction, interfacial area concentration	Void fraction, nucleate site density, bubble release frequency, bubble life time, bubble size (lift-off diameter)	Bubble growth rate, bubble departure/lift-off diameter, bubble waiting time	Bubble departure diameter	Bubble density, bubble spacing, void fraction, bubble size/lifetime/waiting time/lift-off probability
Measurement view[a]	[d]	Bottom view[e]	Side view (25–30° angle above the heater)	Side view	Top and side view
Average bubble departure frequency (definition)	$\sum_{i} \ / \sum_{i} \tau_i$	$f_b = N/(\pi D \Delta z n_s \Delta t)$[f]	[c]	[c]	[c]
Characteristic length of the bubble size	[c]	Sphere-equivalent bubble diameter was estimated from the projected bubble area.	Chord length through the bubble centroid parallel to the heater surface	Longest chord length parallel to the heating surface which bisects the bubble surface	[c]
Bubble departure moment (How to determine?)	[c]	Maximum diameters within the bubble lifetime were assumed to be equal to the lift-off diameter.	Manually determined (Immediately after the first sign of displacement from the nucleation site)	Manually determined	[c]
Number of observations for statistical average	Over 100 departing bubbles were considered for bubble departure frequency and departure diameter.	[c]	4–124 observations were used for the average bubble departure/lift-off diameter.	About 200 observations were used to estimate the average bubble departure diameter.	[c]
Statistical analysis	[c]	[c]	PDFs for departure/lift-off diameter were provided.	PDFs for bubble departure diameter were provided.	Results were given as distribution functions.

[a] The measurement view was inferred based on the typical bubble images shown in the publication(s).

[b] From Figure 8 in the paper, it is inferred that 150–200 observations were typically used to calculate the average bubble departure frequency.

[c] Not described explicitly

[d] The measuring view of the authors' observation was not clarified, but the measurements seemed to be performed at the same facility as Euh et al. [10] and Ozar [17] in which top view was used for the visual measurement of bubble departure frequency.

[e] Visualization was performed from the bottom side of bubble through the transparent heater.

[f] f_b: mean bubble release frequency, D: tube diameter, n_s: nucleation site density, Δz: height of cylindrical control volume, Δt: time interval.

Among the studies shown in Table II-1, the spatial resolutions ranged from 4.7 μm to 64 μm and the temporal resolutions, i.e., the recording speed of high speed camera, varied from 1.2 kHz to 10 kHz. That is, a difference of ten times or more existed among the spatial and/or temporal resolutions across the ten studies reviewed. Since measurement accuracy depends directly on the resolution of the cameras used in the experiment, obviously those differences affect the measurements of bubble size, bubble growth rates, and other parameters related to wall nucleation such as nucleation frequency and waiting time. As expected, such differences in resolution can be quantified simply as measurement uncertainties [24, 25].

Secondly, the different researchers observed the wall nucleation motions using different measurement views. The measurement views employed (Tables II-1) were inferred based on the typical bubble images shown in each study. Measurements of bubble departure/lift-off diameter and bubble departure and/or nucleation frequency were performed mostly from the side of bubble (side view) because the departure process can be observed in detail from this view. However, some researchers applied different measurement views to observe the boiling motions: Euh et al. [10] investigated the bubble departure frequency from the top of bubbles (see figure on p. 18, top view), while Okawa et al. [21] measured the various bubble parameters from the bottom of bubbles through a transparent heater. Therefore, it is important to see how significantly the measurement perspectives can affect the experimental observations for bubble departure (or nucleation) frequency and bubble size measurements.

Researchers evaluated the bubble's size, e.g., diameter at bubble departure and lift-off moment, in several different ways. In other words, the characteristic length to represent the bubble size at departure or lift-off moment was estimated differently by different researchers. Chu et al. [11] and Okawa et al. [21] used the equivalent bubble diameter based on the 2D projected bubble area obtained from the side and bottom views, respectively. Klausner et al. [3] and Thorncroft et al. [6] used the chord length bisecting the bubble parallel to the heater surface to define the bubble departure and/or lift-off diameter (see Table II-1). Prodanovic et al. [7] used a Feret diameter indicating the distance between the opposing parallel tangents on the bubble surface to characterize the bubble size. However, the characteristic length representing the bubble size should be evaluated by considering the physical meaning or specific use in the prediction models so that the empirical insight is reflected correctly. For instance, if the bubble departure diameter is used to estimate the total evaporative heat transfer before departure as in the existing prediction models [1], it should be defined to characterize the actual volume of bubble faithfully at the departure moment. The suitability of characteristic length for bubble departure and lift-off diameters should be discussed in this context and this is treated in detail in Section D.

In order to measure the bubble departure diameter, it is also important to capture the instant when the bubble leaves the nucleation site (i.e., bubble departure moment) properly. However, determining the departure moment is difficult if the bubble first moves away from the nucleation site by sliding without lifting off the wall because the bubble moves fast in a continuous manner. For this reason, previous studies usually determined the departure moment manually without any specific criteria, or it was not considered at all [9]. This issue will be discussed in more detail in Section D, and an image analysis method to treat this issue is introduced in Section E.

The number of experimental observations (i.e., sample size) for statistical averages of measured bubble parameters varied substantially among the previous experimental works shown in Table II-1. From 3–200 experimental observations were used to obtain the average of measured bubble parameters at given experimental conditions, and these averages were used to develop and validate the physical models. Currently we have no proof that the number of observations was sufficient to characterize the wall nucleation behaviors. As discussed in the introduction, we must pay careful attention to this issue because the small sample sizes may cause statistically significant deviations from truly representative values due to strong fluctuations in behaviors associated with boiling. Additionally, it is noted that only a few authors [3, 6, 22] presented any stochastic features of the fundamental bubble parameters other than statistical averages.

The discussion above implies that several issues in previous measurements of fundamental bubble parameters still remained unidentified, and the effects of said issues need to be understood better; otherwise, the experimental information could be significantly misleading. In this context, we performed subcooled flow boiling experiments in which various aspects of bubble departure diameter and bubble departure frequency measurements are investigated. In the following section, the experimental facility as well as the specific measurement strategy to achieve the goal is described.

C. Experimental setup and measurement strategy

1. Hydraulic loop and instruments

The test loop was designed to perform the subcooled flow boiling experiment at atmospheric pressure. The refrigerant 3M™ Novec™ 7000 was used as the working fluid due to its low latent heat as well as the low saturation point which requires less energy for boiling. The liquid flow was driven by a constant speed centrifugal pump, and the liquid flow rate through the test loop was adjusted using the control valves installed downstream of the pump and upstream of the test section. The fluid flowed vertically upward across the square test section which had a 10 mm width (D) and a total height of 305 mm. The test section was preceded by an entry length (L) of ~610 mm long (i.e., L/D≈61) made of acrylic so that the liquid flow would be hydro-dynamically fully developed before entering the test section (Figure II-1). The fluid temperature entering the test section was controlled using a small plate heat exchanger connected to a thermostat. Prior to the experiment, a degassing procedure was performed on the loop. The test loop was heated, and a vigorous forced convective boil was maintained for approximately two hours to ensure that the dissolved gases in the liquid were eliminated from the test loop.

The liquid flow rate was measured using a Micro Motion® ELITE® CMF025 Coriolis mass flow meter. For the fluid temperature measurement at the inlet and outlet of the test section, the HYP0 mini-hypodermic probe (T-type) with a needle diameter of 0.2 mm by OMEGA Engineering Inc. was used. The heater power was estimated by measuring the current and voltage of the power supply (XHR 600V, AMETEK®) connected to the heater. The inlet and outlet pressures of the test section were measured using the OMEGA® PX309 series pressure transducers. The heater surface temperature distribution was evaluated using a FLIR SC8000 HD infrared camera. The measurement uncertainties were as follows: flow rate ±0.05% of reading, fluid temperature ±0.5^{o}C, heater power ±1.1% (full scale), pressure ±0.25% (full scale), differential pressure ±0.25/±0.5% (full scale), and wall temperature ±2% of reading.

Measurements of flow rate, fluid temperature, heater power, and pressure were recorded using a data acquisition system by National Instrument Inc. Due to the highly turbulent features of the test conditions during the study, 24,000 samples were obtained per channel with a sampling frequency of 100 Hz over a 4-minute measurement period. The samples were subsequently averaged to represent the test conditions for each measurement.

2. Test section and heater design

To observe the boiling motions, a test section of 10×10 mm^2 enclosed by transparent acrylic walls except for the heater wall side was designed. The heater wall consisted of a 0.5 mm thickness soda-lime glass substrate on which an electro-conductive Indium-Tin-Oxide (ITO) film was deposited. Due to the conductive property of ITO, the heat flux on the ITO film (i.e., heater surface) could be controlled using a DC power supply connected to the copper electrode as shown in Figure II-1. This heater was used to boil the liquid on the interior surface of the square channel on one side with a heated area of 9×265 mm^2. In Figure II-1 (right), it is seen that the heated area of ITO film was designed to be slightly narrower than the original channel width (10 mm), which was done to avoid boiling at the channel corner due to trapped liquid in small gaps between the heater wall and acrylic walls. To make this heater design, the ITO film was etched (Figure II-1, right) using highly-concentrated hydrogen chloride (HCL) liquid after the ITO was coated on top of the glass substrate.

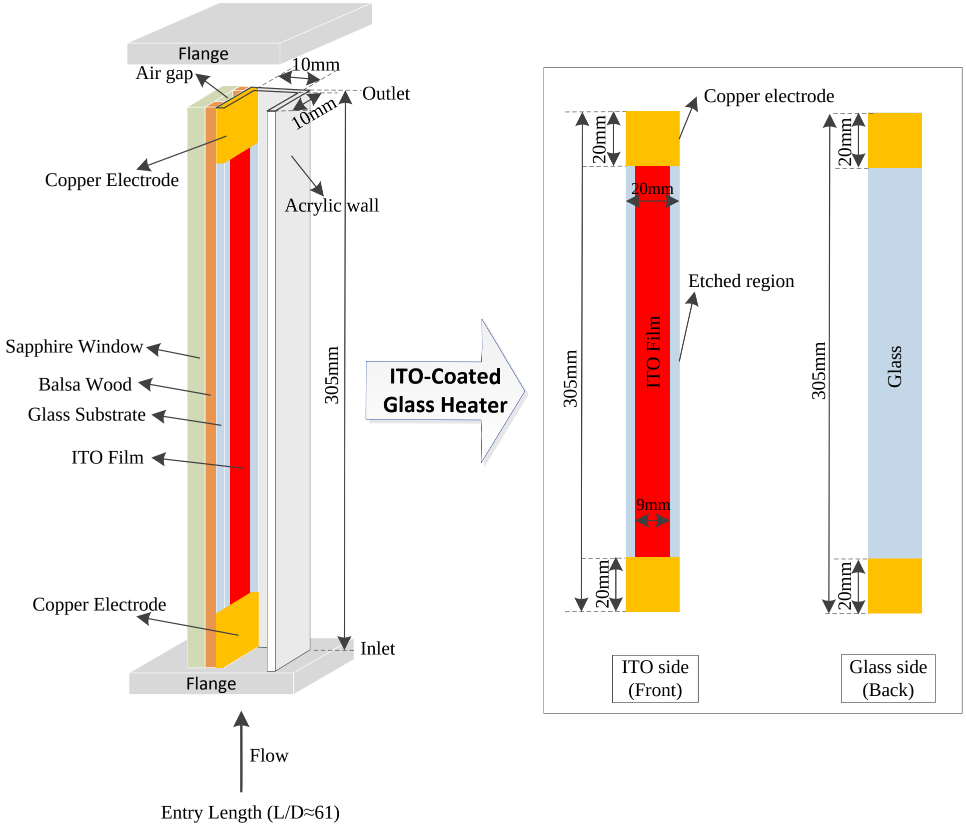

Figure II-1. Schematic of test section and ITO-coated glass heater

As part of the insulation system on the heater wall side, a sapphire window was placed next to the ITO-coated glass substrate as shown in Figure II-2. This design was devised to reduce the heat loss to the environment because the air trapped between the glass substrate and the sapphire window can work as insulation. With this test section design, illumination light to visualize the boiling motions inside the channel became available from all directions because all the composing materials used, i.e., the ITO, soda-lime glass, sapphire, and acrylic are highly transparent in visible light. This helped improve the quality of bubble images obtained from the high speed cameras. At the same time, since both the sapphire window and soda-lime glass substrate are translucent to mid-wave infrared (IR) radiation (i.e., 3–5 μm), the heater surface temperature – the ITO film – can be measured using the mid-wave IR camera through the materials after applying a proper calibration.

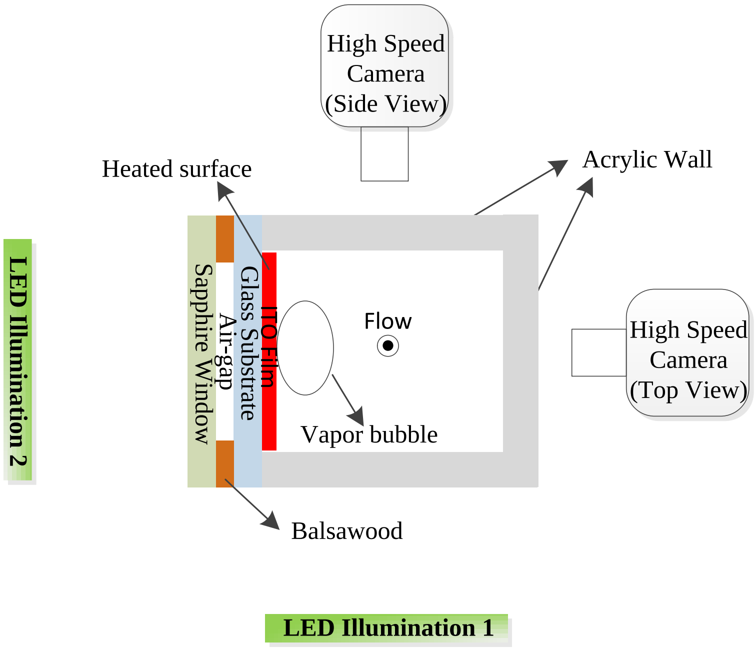

Figure II-2. Visual observation of vapor bubbles for subcooled flow boiling experiment (not to scale)

3. Visualization strategy

Figure II-2 shows the arrangement of high speed cameras around the test section which is viewed from the top of channel. In this study, the visual observation of vapor bubble was performed using two high speed cameras (Photron FASTCAM SA5 and Phantom® Miro® M310) which were located to capture the same boiling motion from two different measurement views (i.e., top and side views in Figure II-2). The two cameras were triggered at the same time via a BNC cable and subsequently recorded the boiling motion at the same speeds, which enables the synchronization of both cameras' image sequences.

Two LED lamps were used for illumination, as shown in Figure II-2. We typically recorded images of 448×520 pixels from the side view and 448×320 pixels from the top view. After the experiment, a known-sized wire mesh was inserted, and the images were taken at the measurement section for calibration purposes. Then, the bubble sizes in the recorded images were calibrated based on the wire mesh images. The spatial resolution of the side view measurements and the top view measurements were estimated as 5.56 μm and 4.90 μm, respectively. For the temporal resolutions, typically a recording speed of 20 kHz was used to observe the boiling motions, but a wide range of recording speeds (1–20 kHz) were tested as well to discuss the related measurement issues which will be treated in detail in Section D.

4. Test conditions and measurement strategy

Using the experimental setup and visualization strategy mentioned above, the subcooled flow boiling experiment was performed at a heat flux of 10.6 to 24.3 kW/m^2; a liquid mass flux of 216 to 424 kg/m^{2}s; and a liquid subcooling of 14°C at the test section inlet. Under these test conditions, behaviors of fundamental bubble parameters regarding wall nucleation, i.e., bubble departure diameter and bubble departure frequency, were investigated at a single nucleation site created on the heater wall. In particular, we analyzed the experimental results obtained from (i) two different measurement views, (ii) different recording speeds of cameras, and (iii) different numbers of experimental observations with the aim of experimentally evaluating the measurement issues. Specifically, the synchronized image sequences of bubbles at the nucleation site obtained from the side and top views were captured to assess issues associated with measurement views. To investigate the influence of camera recording speed capturing the boiling motion on the experimental result, bubble departure frequency was measured at different recording speeds (1–20 kHz) under same test condition and compared. Considering that the number of experimental observations used to estimate the statistical average varied greatly among the previous studies, the effect of sample size on the experimental results were studied as well. Although the test conditions in this study were limited in terms of flow rates, heat fluxes, subcooling degree, pressure, and so on, we can say that the measurement issues discussed here are common to general flow boiling experiments investigating the wall nucleation phenomena through visualization. In the following section, the measurement issues regarding bubble departure diameter and bubble departure frequency uncovered through the present study are discussed in detail.

D. Issue identification for the proper investigation of bubble parameters

1. Measurement view issues

a. Bubble size measurement

In previous studies, bubble sizes such as bubble departure and lift-off diameters were estimated using 2D bubble images obtained either from a side view or top view measurement (Table II-1). In this section, the issue of bubble size measurement caused by different measurement perspectives is discussed based on the synchronous observations of boiling from the top and side views as discussed in Section C.3 and C.4. For bubble departure and lift-off diameter measurements, previous researchers have mostly observed the boiling motion from the side view (see Figure II-2) because the departure and lift-off processes can be detected better from this view. However, it is often more convenient to capture the numerous nucleation sites or bubbles from other views, and so some researchers attempted to measure the bubble sizes based on images obtained from the top or bottom of the bubbles [21, 23].

Also, note that different researchers used different definitions of characteristic length to define the bubble departure and lift-off diameters (see Table II-1). As discussed in Section 2, the measured bubble departure and lift-off diameters should be adequate to obtain the actual bubble volume at the departure and lift-off moment based on the values. This implies that, in principle, 3D bubble information is required because the vapor bubbles often deform under forced convective boiling conditions. The appropriateness of characteristic lengths representing the bubble departure and lift-off diameters used in the literature should be discussed by testing how well the actual bubble volume can be represented based on the definitions of such parameters. In this study, we estimated the 3D bubble volume by considering the actual bubble shapes inferred by the observations of synchronized bubble images from the top and side views. As illustrated in Figure II-3, the departure bubble shapes from the side view measurement were observed to be close to elliptical; whereas, the corresponding bubbles images observed from the top view were almost always well fitted to circular. Thus, the actual 3D bubble shape can be reasonably approximated as a prolate or oblate spheroid from which the actual bubble volume can be estimated. As a result, the volume equivalent diameter was obtained based on the actual volume of the bubble (see Figure II-3), which is considered to be the most suitable characteristic length for bubble departure and lift-off diameters. We used these volume equivalent diameters as reference criteria to discuss the suitability of departure and lift-off diameters estimated using the 2D bubble images obtained from a side view or top view measurement.

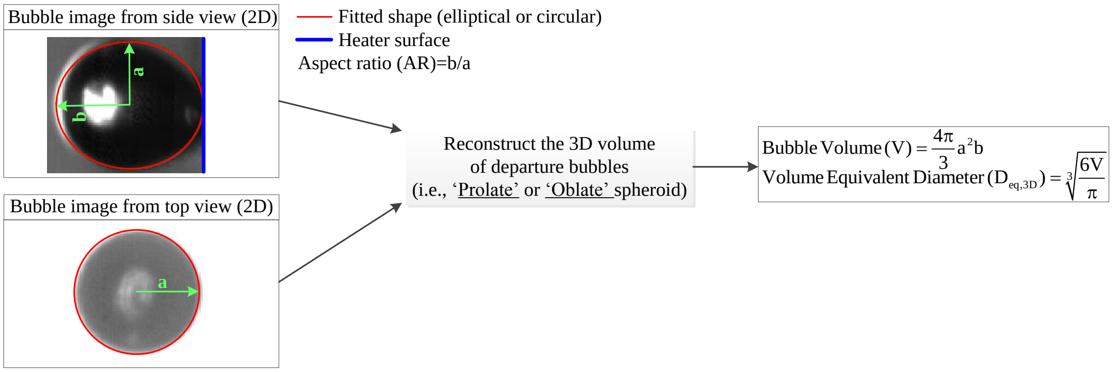

Figure II-3. Estimation of 3D volume equivalent diameter ($D_{eq,\,3D}$)

In Figure II-4, nine different sizes of departure bubbles obtained under subcooled flow boiling conditions are shown. The wide range of bubble sizes and shapes found in the present experiments are compared to investigate the departure bubble behaviors using different measurement views; the bubble images shown are the representative ones selected at different test conditions. The bubble images for the side and top views were captured at the same temporal moment, when the bubbles departed from the nucleation site. Bubbles leaving the nucleation site (i.e., departure bubbles) are marked with dotted red lines in Figure II-4. It is found that the departure bubble shapes observed from the top view look almost circular for all cases; similar observations were reported by others [26, 27]. In contrast, departure bubble shapes from the side view appear more deformed. As expected, this led to different estimates of bubble departure diameter depending on which measurement view was used. In particular, we discuss the case when the bubble departure diameters are estimated by equivalent diameters based on the 2D projected bubble area (i.e., 2D-based equivalent diameter). The specific values of the 2D-based equivalent diameter for the side view ($D_{eq,\,2D\text{-}side}$) and that for the top view ($D_{eq,\,2D\text{-}top}$) for all cases are shown in Figure II-4. Then, we can see that for small bubbles (cases 1–5), the 2D-based equivalent diameters for the side view $D_{eq,\ 2D\text{-}side}$ overestimated those for the top view $D_{eq,\ 2D\text{-}top}$, while the opposite was found for large bubbles (cases 8 and 9). Obviously, this trend is related to the specific shape deformation observed in each case.

	Case 1	Case 2	Case 3	Case 4	Case 5	Case 6	Case 7	Case 8	Case 9
Side View	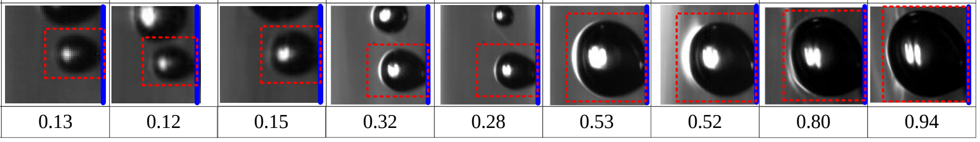								
$D_{eq,\ 2D\text{-}side}$ [mm]	0.13	0.12	0.15	0.32	0.28	0.53	0.52	0.80	0.94
Top View	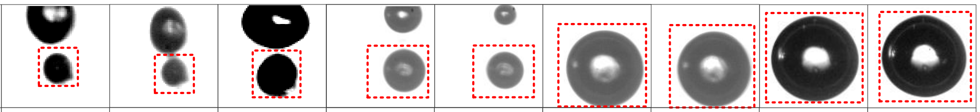								
$D_{eq,\ 2D\text{-}top}$ [mm]	0.10	0.09	0.14	0.28	0.26	0.53	0.52	0.83	0.96

Figure II-4. 2D-based bubble departure diameters from different measurement views; blue lines on the right border of side view images indicate the heater surface

In Figure II-5, the aspect ratios (AR) of departure bubbles for side view measurement shown in Figure II-4 were compared (left axis: the black solid line with the square symbol). This shows that smaller bubbles tend to elongate against the heater wall (AR>1, prolate spheroid); whereas, larger bubbles are likely to be flatter (AR<1, oblate spheroid) before they departed from the nucleation site. Thus, the 2D-based equivalent diameters from the top view were underestimated compared to the side view measurement for small bubbles, while 2D-based equivalent diameters for larger bubbles based on the top view were overestimated as compared to the estimate made based on the side view measurement. The bubbles' shape deformation was also found to be related to bubble departure behaviors. Two different types of bubble departure behaviors were observed during this study (Figure II-6). Specifically, the bubbles departed from the nucleation site as they detached from the heater surface (Type 1) or moved away from the site through sliding (Type 2). Also, we observed that the degree of deformation was higher when bubbles detached directly from the heater surface (Type 1 in Figure II-6) as opposed to when bubbles departed from the nucleation site through sliding (Type 2 in Figure II-6). In addition, smaller bubbles were more likely to deform ($AR>1$) and subsequently detach from the heater wall (Type 1), and this trend became more noticeable as the liquid flow rate increased or the wall superheated level decreased. Similar findings were reported by Okawa et al. [28], who argued that the inertial force of liquid flowing towards the bubble base caused the detachment of small bubbles from the wall.

In Figure II-5 we can see the relative differences of the 2D-based equivalent diameters against the 3D volume equivalent diameters (i.e., $D_{eq,\ 2D\text{-}side}$ vs. $D_{eq,\ 3D}$ and $D_{eq,\ 2D\text{-}top}$ vs. $D_{eq,\ 3D}$) (right axis: the blue and red dashed lines with circle and triangle symbols, respectively). It can be seen that $D_{eq,\ 2D\text{-}top}$ significantly underestimates the $D_{eq,\ 3D}$, especially for small bubbles; whereas, the difference between $D_{eq,\ 2D\text{-}side}$ and $D_{eq,\ 3D}$ stays within 5% regardless of the bubble size or shape. This different result between the two measurement views occurs because the bubbles' shape deformation can be relatively well captured from the side view, while such shape changes were rarely observed from the top view. This implies that the 2D-based equivalent diameter obtained from direct measurements of the top or bottom view can hinder the measurement accuracy due to the bubble shape deformation which look more noticeable for the small bubbles having a prolate spheroid shape (AR>1). On the other hand, the error for the top view measurement was reduced for the large bubbles which had an oblate spheroid shape (AR<1) because they were usually less deformed compared to the small bubbles. However, even in case of side view measurement, if the departure diameters are estimated as chord length across the bubble parallel to the heater surface as attempted in several previous studies [3, 6], the same issue with the top view measurement will happen. Therefore, careful attention is required both for the measurement view and characteristic length for bubble departure diameter to control for this issue. The present observations as well as the observed bubble images shown in previous [26-28] indicates that the volume equivalent diameter can be approximated well from the side view measurement because the shape deformation from the top view has been observed as relatively negligible.

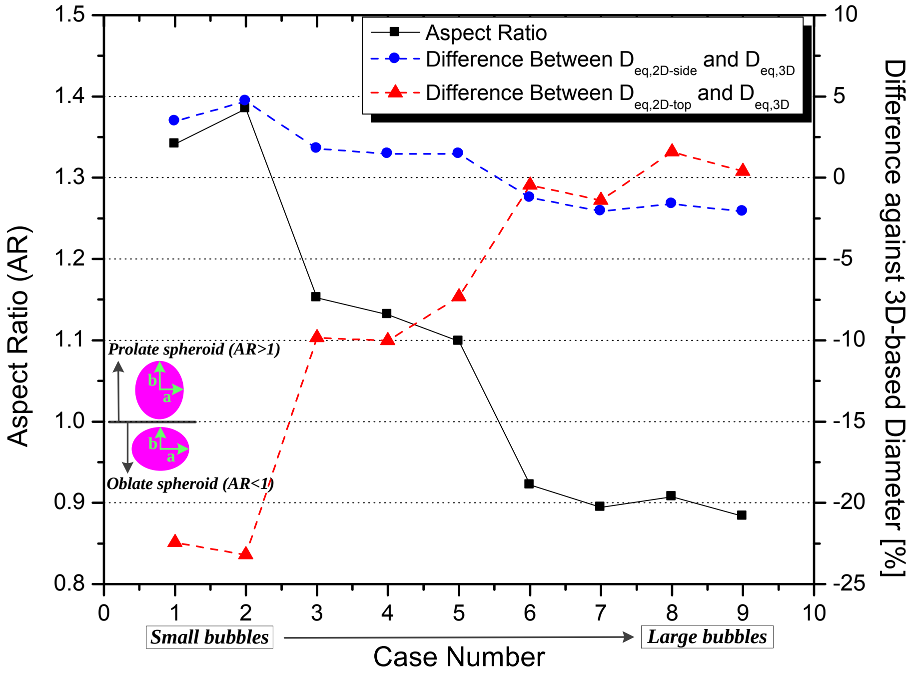

Figure II-5. Departure bubbles' aspect ratio and the difference of 2D-based bubble departure diameters ($D_{eq,\ 2D\text{-}side}$, and $D_{eq,\ 2D\text{-}top}$) contrasted with the 3D volume equivalent diameters

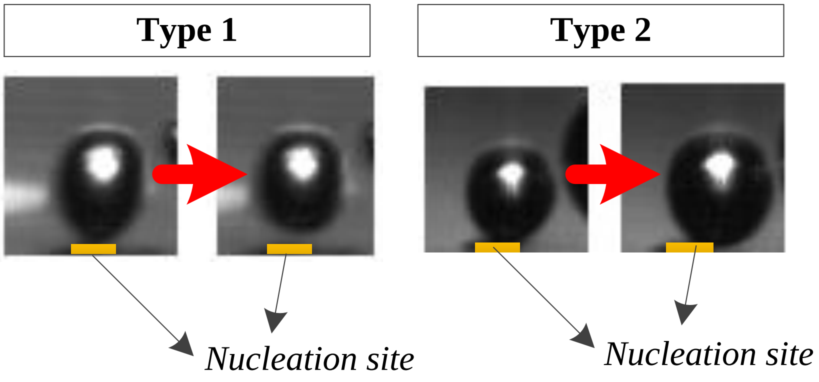

Figure II-6. Bubble departure phenomena at the nucleation site (Type 1: direct lift-off from the heater wall, Type 2: departure through sliding)

b. Bubble departure frequency measurement

In the visual experimental studies shown in Table II-1, the bubble departure frequency was also measured either from the side or the top view. However, the different measurement views may induce significant discrepancies in the estimation of bubble departure frequency as well. To quantify those discrepancies, synchronized bubble image sequences at the same nucleation site were obtained from the two measurement views. Figure II-7 compares the results from the both views. Clearly, detailed nucleating motions are often hard to capture from the top view because large bubbles blocked newly formed, smaller bubbles beneath them. The zoomed-in images in Figure II-7 show this issue in more detail. We defined the average bubble departure frequency as

$$\overline{f_{dep}} = \frac{\sum_{i}}{\sum_{i} \tau_{i}} \qquad \text{(II-1)}$$

where $\overline{f_{dep}}$ is the average bubble departure frequency, i is the i^{th} nucleation event, and τ is the time period between two nucleation events.

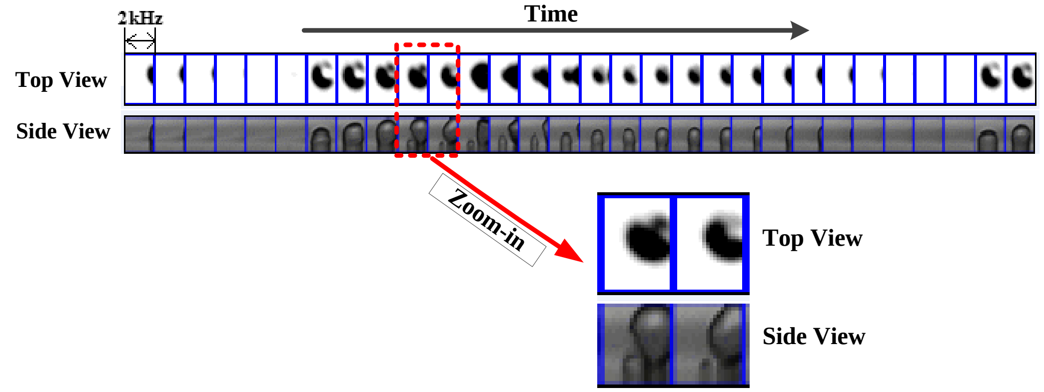

Figure II-7. Images of bubble nucleation from the different measurement views

Due to the issue illustrated in Figure II-7, we see in Figure II-8 that the average bubble departure frequency estimated using the top view measurement significantly underestimated determinations made using the side view measurements by almost half. Interestingly, both average frequencies obtained from the two measurement views seem to converge on certain values as the number of experimental observations increases. However, direct comparison of the synchronized bubble image sequences obtained from the two measurement views confirmed that the top view measurements have obvious limitations for this frequency measurement. Also, such errors caused by improper measurement view cannot be compensated even with sufficiently large number of samples. Considering the relative strength of the flowing liquid’s inertia, surface tension, and bubble growth inertia force, those issues are expected to become more noticeable for experimental conditions in which low bubble sliding velocities and high bubble nucleation frequencies are observed. For instance, large departing bubbles will reside a longer period of time within the measurement area, blocking the view of multiple nucleation instances from the top.

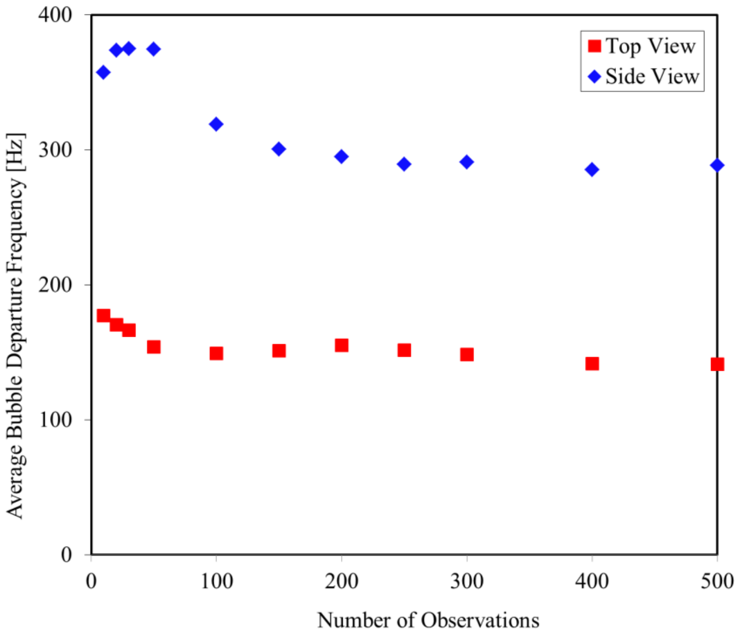

Figure II-8. Average bubble departure frequency analysis using the visual images of different measurement views

2. Issue related to the recording speed of visualization

The recording speed of visualization is another critical issue for the proper observation of bubble nucleation phenomena in a forced convective boiling experiment. In order to quantify the influence of this issue, a sensitivity analysis was performed. A single experimental condition was selected from which the effect of recording speed on the bubble departure frequency measurement was investigated based on the side view measurement. Specifically, the nucleating bubble motion under the same test condition was examined with different recording speeds ranging from 1 kHz to 20 kHz; the lower speed images were obtained from the 20 kHz image set. Then, using Eq. (II-1), the average bubble departure frequency was estimated from the image sequences at the different recording speeds. The results are shown in Figure II-9; clearly the average bubble departure frequency was underestimated for the cases with a recording speed below 5 kHz. For the recording speed of 1 kHz, only about 65% of bubble nucleation events were captured compared to the number recorded at speeds ≥5 kHz during the same measurement period. Apparently, this is because fast-occurring bubble nucleation motions which happened within a very short time period were not captured at low recording speeds. Note that all of the average departure frequencies shown in Figure II-9 seem to converge on specific values as the experimental observations increase. However, the values obtained from recording speeds of 1 kHz and 2 kHz are obviously incorrect.

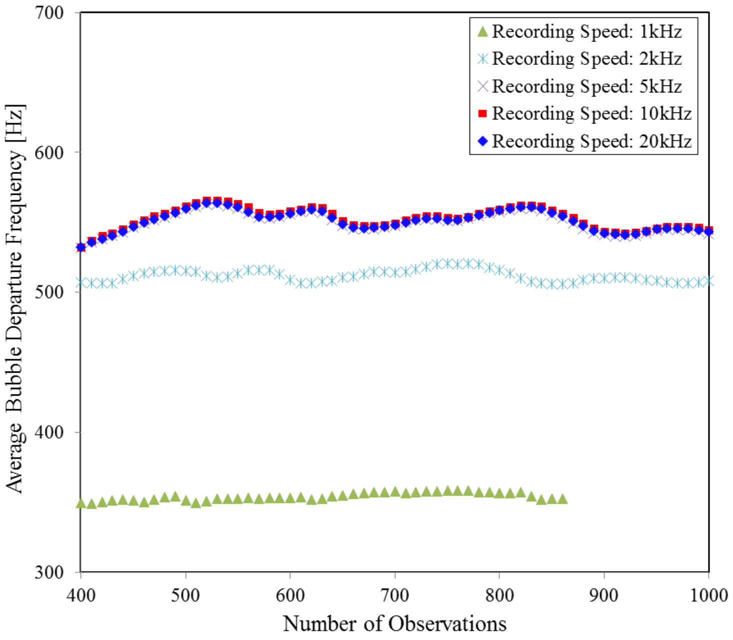

Figure II-9. Average bubble departure frequency measured with different recording speeds

Necessarily, the required recording speed for the proper observation of bubble departure frequency depends on the specific experimental conditions. We should note that, if the temporal resolution employed is insufficient, even the average behavior of nucleation process can be considerably misleading. To further assess this issue, the measured bubble departure frequencies for four different experimental conditions are shown in Table II-2. In the table, f_{AVG} indicates the average bubble departure frequency while f_{MAX} and f_{MIN} respectively denote the maximum and minimum bubble departure frequency observed during the 20 kHz measurement for each test condition. The specific way the individual departure frequencies such as f_{MAX} and f_{MIN} were obtained is described in Section D.3. For all of the different experimental conditions, we see that f_{MAX} and f_{MIN} are quite far from the statistical average f_{AVG}. In particular, for case 4 test condition, f_{MAX} was estimated to be more than five times bigger than f_{AVG}, while the measured f_{MIN} was more than three times smaller than f_{AVG}. This large distribution of departure frequency may be attributed to the intermittent behavior of bubble nucleation, which implies that very fast and very slow bubble nucleation occurred during the measurement period. However, those behaviors of fluctuation seemed quite random, and so the trends are difficult to predict. Thus, the only conclusion derived here is that the recording speed must be high enough to minimize issues caused by such strong behavior of fluctuations in bubble nucleation.

Table II-2. Observation of bubble departure frequency under different experimental conditions

Experimental Information				Measured Value		
Case No.	Liquid Flow (kg/m^2s)	Heat Flux (kW/m^2)	Inlet Subcooling (°C)	f_{AVG} (Hz)	f_{MAX} (Hz)	f_{MIN} (Hz)
1	216.3	10.6	14.0	533.7	1250.0	235.3
2	216.3	13.9	14.0	227.7	487.8	129.0
3	424.1	19.1	14.0	711.6	1176.5	266.7
4	424.1	24.3	14.0	635.0	3333.3	180.2

In Figure II-10, time intervals between consecutive nucleating bubbles observed under case1 test condition (defined in Table II-2) are shown for the entire measurement period (~2.5 s). To obtain these data, measurements were made at a recording speed of 20 kHz, which was assumed to be fast enough to detect the nucleation events under this test condition. Then, the recorded bubble images were analyzed using the image analysis method described in Section E. The nucleation time intervals shown in Figure II-10 gave us insight into the minimum recording speed required to capture the bubble nucleation accurately under this test condition. The minimum required recording speed is twice the observed maximum nucleation frequency or twice the inverse of the minimum time interval (2.5 kHz) presented in Figure II-10 so that every individual bubble nucleation event can be detected properly through the consecutive image sequences.

The recording speed of visualization is also an issue for the measurement of bubble departure diameter because the recording speed affects the observation of bubble departure moment at the nucleation site. This will be discussed in Section D.4.

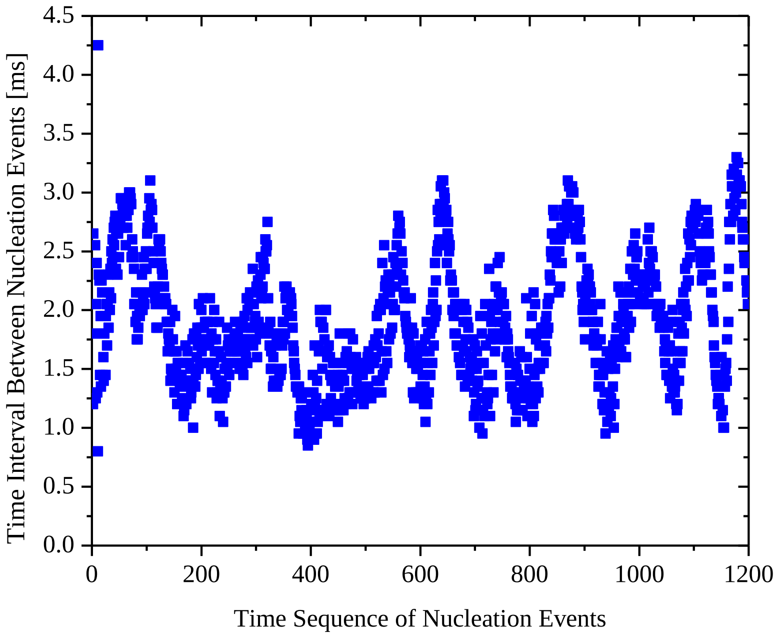

Figure II-10. Time intervals between the nucleation events during the measurement period for case 1

3. Issue of sample size

For the mechanistic modeling of wall nucleation based on experimental information, the obtained statistical values need to accurately represent the boiling characteristics at each experimental condition. Due to the inherently chaotic behaviors found in flow boiling, no doubt the boiling-related parameters require a large number of observations for reliable statistics. A review of the literature shows that for the bubble departure and lift-off diameters or bubble departure frequency measurements, a maximum of 200 experimental observations were used to estimate the statistical averages (see Table II-1); from those results, several mechanistic models were suggested and validated. However, none of those studies provided sufficient evidence that such sample sizes and the resulting averages were adequate under the given experimental conditions.

In this context, we studied the effect of the number of experimental observations, the sample size, on the statistical average and other stochastic features of the measured bubble parameters. Figures II-11 and II-12 show the variation of average bubble departure frequency and average bubble departure diameter depending on the number of experimental observations under two subcooled flow boiling conditions selected for discussion (i.e., Experimental Condition 1 and 2 in Figure II-11 and II-12). All the measurements and analyses were performed based on the same nucleation site. For each test condition, the measurements were made twice to compare the average values between the two separate sets of measurements under identical test conditions. Almost 50,000 consecutive images were taken at the recording speed 20 kHz for each set of measurements, meaning a total of nearly 100,000 images were obtained for each test condition. On the left in Figure II-11, we see that the variation of the average departure frequency seemed quite significant for the separate sets of measurements until the number of observations reached about 300, at which point the average bubble departure frequencies obtained from the two separate measurements under experimental condition 1 converge on very similar values. This implies that significant measurement uncertainty is expected if the sample size, the number of experimental observations, is less than 300 under experimental condition 1.

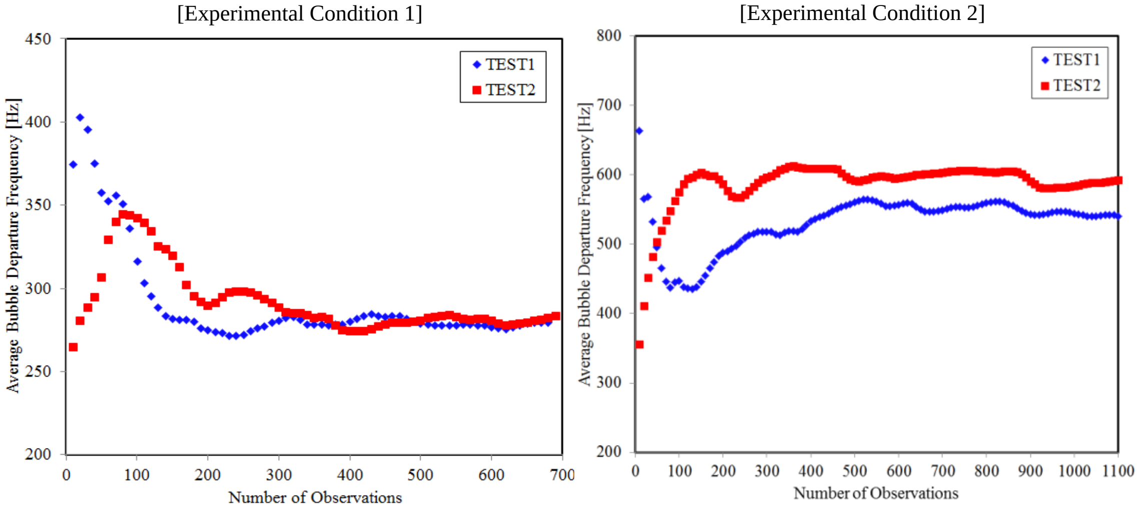

Figure II-11. Average bubble departure frequency depending on the number of observations

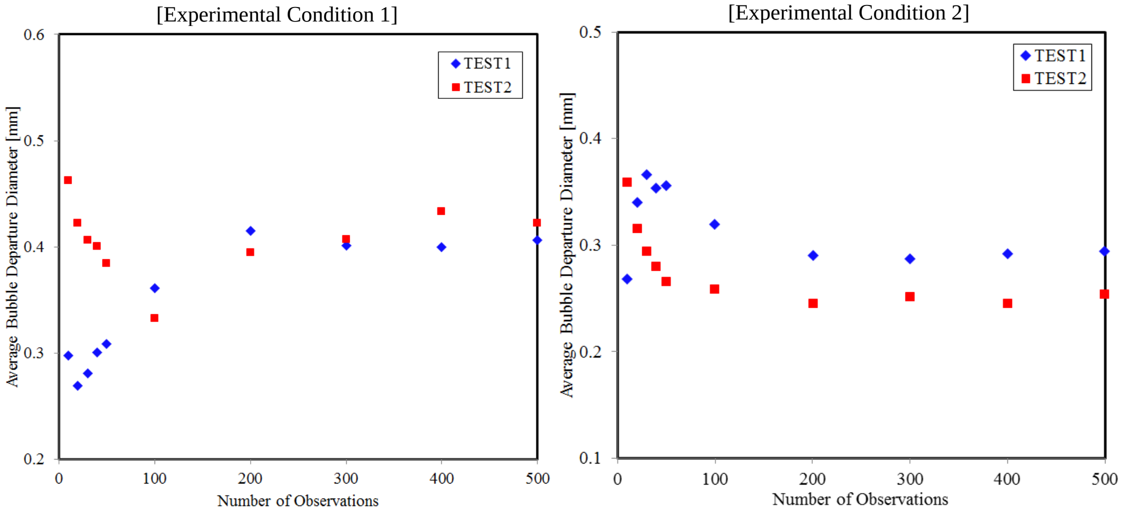

Figure II-12. Average bubble departure diameter depending on the number of observations

On the other hand, under experimental condition 2, the average bubble departure frequencies shown on the right in Figure II-11 seem to require more than 500 observations before the averages of the two separate measurements converge. However, the converging average bubble departure frequencies for the two separate measurements show more discrepancies under experimental condition 2 as compared to the results of experimental condition 1. From this observation we inferred that there was a stronger variation in bubble departure frequencies measured under experimental condition 2. Actually, the detailed information of bubble departure frequency and the probability density function (PDF) shown in Figure II-13 show that the bubble departure frequency under experimental condition 2 has a wider range of distribution (i.e., 200–1600 Hz) than that of experimental condition 1. The individual bubble departure frequencies during the measurement period shown in Figure II-13 were obtained by the following equation:

$$f_{dep,i} = \frac{1}{(\tau_{g,i} + \tau_{w,i})} \tag{II-2}$$

where $f_{dep,i}$ is the bubble departure frequency, $\tau_{g,i}$ is the bubble growth time after the ith nucleation event, and $\tau_{w,i}$ is the bubble waiting time after the ith nucleation event.

Regarding the fluctuating behavior of bubble departure frequency, the flow boundary conditions such as the liquid flow rate, liquid temperature, and wall heat flux can also affect the specific motions of bubble nucleation. Thus, we estimated the random errors of the liquid flow rate, inlet liquid temperature, and wall heat flux for the two separate measurement sets at each experimental condition; the random errors of the flow boundary condition were estimated based on the root mean squares of the measured data given by the data acquisition system. Then, the difference of the random errors between the two separate measurement sets was calculated as less than 0.02% for both experimental conditions. Also, the working fluid used is electrically non-conductive as well as non-corrosive, and the time period between the two measurement sets was not long enough to induce any significant changes of the heater surface condition. This implies that the difference of average bubble departure frequencies between the two measurement sets under experimental condition 2 shown in Figure II-11 originated from the inherently strong random features of wall nucleation rather than caused by the random errors of the flow boundary conditions and/or the different heater surface conditions.

Similar issues exist in the case of the average bubble departure diameter. Note that, in Figures II-12 and II-14 the total number of observations for the bubble departure diameter analyses was less than those presented for the bubble departure frequency analyses. The reduced number of samples was due to the conditional sampling used to ensure the high quality images of departing bubbles (Section E). Also, the smaller sample size may be the reason why the stochastic features (e.g., PDF) between the two sets of measurements shown in Figure II-14 seem to have more discrepancies than those shown in Figure II-13. Additionally, in Figure II-14 it is interesting to say that a wider distribution range of measured bubble departure diameters is found under experimental condition 1 than under experimental condition 2, the opposite of what was found for the bubble departure frequency.

Based on this discussion, we can say that even 200 experimental observations, the maximum number found in the literature, may not guarantee reliable statistics (e.g., averages, PDFs). This implies that a reliability study on the obtained statistical value for each measured parameter needs to be performed more carefully. In particular, for the statistical average, we recommend increasing the number of experimental observations until a converging value under given experimental conditions is reached as we showed in this study. Otherwise, the acquired experimental information such as parametric effect may misdirect researchers' conclusions and consequently distort and corrupt the validity of the models developed based on them. Additionally, stochastic features other than averages, such as the PDFs of measured parameters, need to be investigated since the experimental information obtained from the average is usually insufficient to characterize the wall nucleation feature [3, 4, 13, 22].

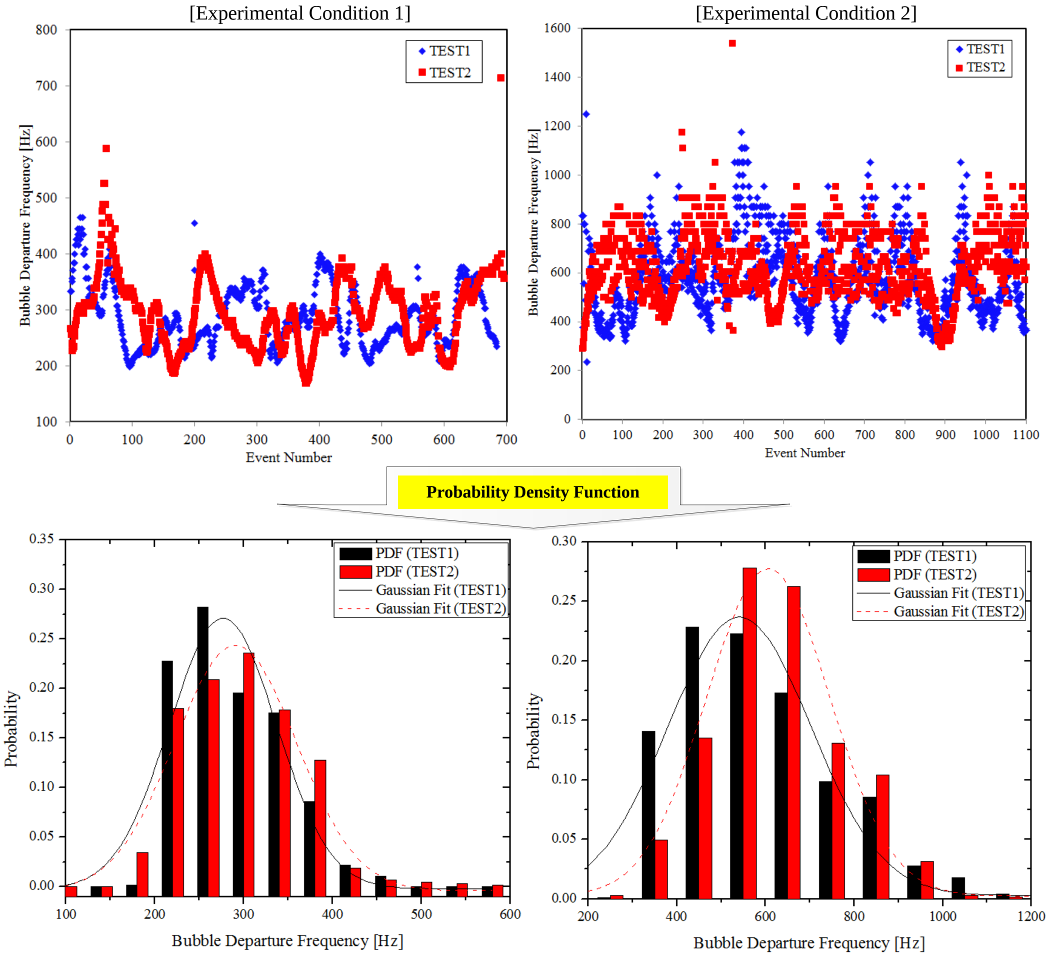

Figure II-13. Individual bubble departure frequencies during the measurement period and the PDFs

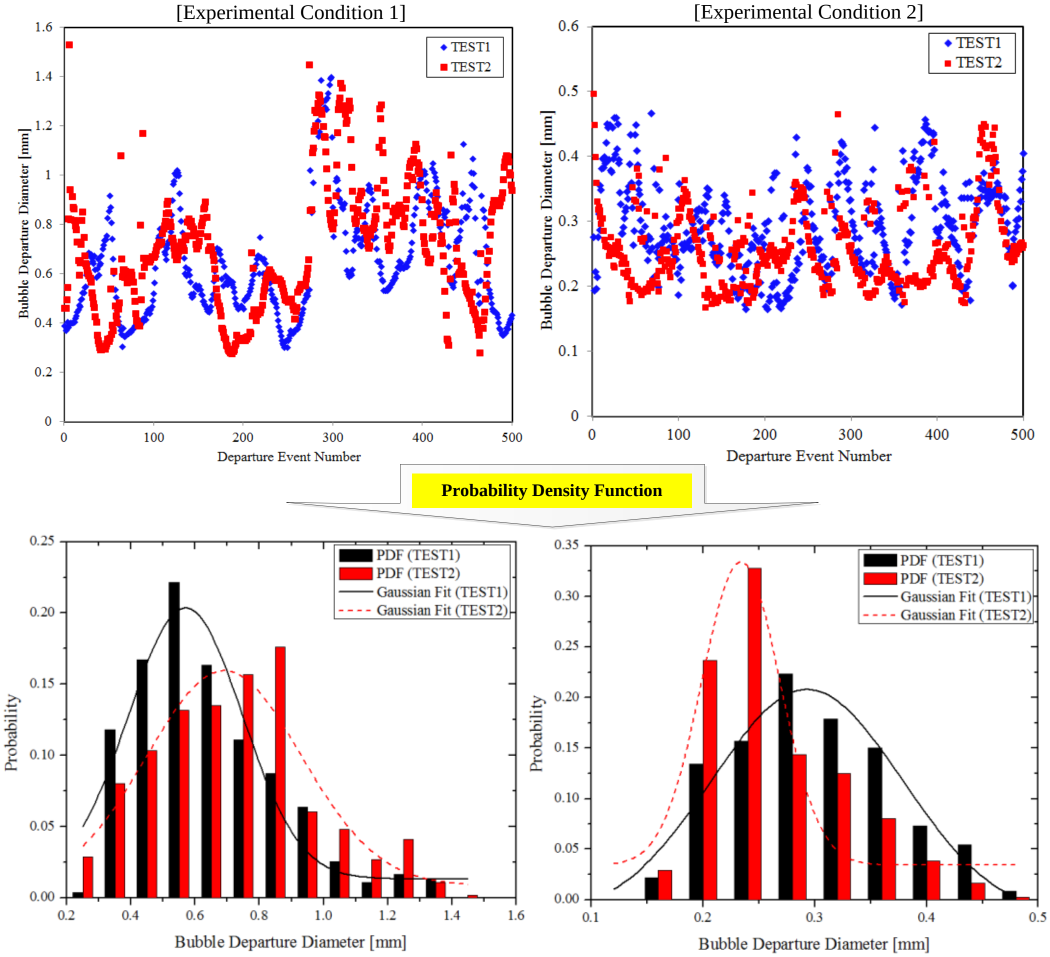

Figure II-14. Individual bubble departure diameters during the measurement period and the PDFs

4. Judging the bubble departure moment

In the previous subcooled and saturated flow boiling experiments, there have been reported difficulties to evaluate the bubble departure diameter correctly due to problems of defining and identifying the bubble departure moment. Okawa et al. [28] mentioned that the bubble departure was hard to detect in their experiment due to the short period of bubbles' residence time at the nucleation sites. In Situ et al. [9], for the same reason only bubbles of certain sizes were selected to estimate the bubble departure diameter in their analyses. The difficulty originates mainly from the fact that the temporal and/or spatial resolutions of the measurements were not high enough to detect the quick process of bubble departure, and these deficiencies can affect the resulting measurement of bubble departure diameter. For instance, during the sensitivity analysis of different recording speeds shown in Figure II-9, we saw that the bubble departure process was hard to capture correctly at slower recording speeds. This implies that the measurement resolution must be high enough to detect the bubble departure process precisely in order to obtain accurate measurement of bubble departure diameter.

Also, it is still unclear how to determine the bubble departure moment in a consistent manner especially when the bubbles leave the nucleation site without detaching from the wall (i.e., type 2 in Figure II-6). As discussed by Chu et al. [11], such bubble departure moments are hard to identify because the bubble moves fast away from the nucleation site in a continuous manner. For the consistency of data analysis, it is helpful to define the bubble departure moment with specific criteria without relying on the observers' interpretation. Furthermore, by having such specific identification criteria for bubble departure, automatic data analysis becomes possible; otherwise, human analyses of visual images will take much time and effort due to the large amount of required experimental observations for reliable statistics (Section D.3). Thus, we propose departure moment identification criteria working consistently under the framework of an automatic image analysis algorithm devised in this study. The specific criteria and the image analysis algorithm are described in the following section.

E. Image analysis method

Above, we showed that a sufficient number of experimental observations is required to properly characterize the representative features of wall nucleation under subcooled flow boiling conditions. To estimate fundamental bubble parameters such as bubble departure diameter and bubble departure frequency in an efficient and accurate way by considering all the measurement issues discussed, we developed an automatic image analysis method.

1. Overview of image analysis procedure

Figure II-15 briefly shows the procedures of the image analysis method. First, the original images are converted to binary images (step 1). Then, two rectangular regions are placed above the nucleation site, 'region 1' and 'region 2' in Figure II-15, to detect bubble nucleation (signal 1) and the bubble growing process (signal 2) based on the intensity of signal variations within those regions. Both signals are required to distinguish signal variations induced by the actual bubbles' growing process from variations induced by background noises appearing during the image processing procedures in step 1. Then, based on the signal variations, bubble nucleation (or departure) frequency, bubble growth time, etc. can be determined as shown in Figure II-15 (step 2).

Once a bubble begins to grow after nucleation, the growth time in the image analysis method is defined as the period from the nucleation moment captured by signal 1 until signal 2 peaks. After that peak, the magnitude of signal 2 decreases as the bubble moves away from the nucleation site. Bubble departure is considered to occur at this moment, i.e., when signal 2 begins to decrease after the peak. In this way, the bubble departure moments can be determined consistently during the entire measurement period. Subsequently, all images of bubble departure moments are collected for bubble departure diameter analysis (step 3). After that, if needed, any poor quality images can be filtered so that the resulting statistics are more reliable (step 4). Alternatively, to ensure a sufficient sample size for more reliable statistics on bubble departure diameter, instead of filtering, separate image processing can be conducted on the images containing departing bubbles. The processed bubble images of low quality can easily be filtered out using shape-defining parameters such as bubble circularity, which are available in image analysis software like ImageJ [29]. Then, using the image analysis software, the 2D projected bubble area or the characteristic lengths needed are obtained for the departing bubbles found in the selected images (step 5).

In this study, all the procedures described above, (1) image processing, (2) intensity signal analysis, (3) selective collection of bubble departure images, (4) image filtering, and (5) statistical analysis of the bubble departure diameter as well as of the bubble departure frequency, were performed using the in-house computerized analysis program and macro functions of ImageJ [29]. By doing so, the time needed to analyze the numerous visual images was reduced significantly while obtaining additional detailed information such as the statistical distribution of the measured bubble parameters under subcooled flow boiling conditions.

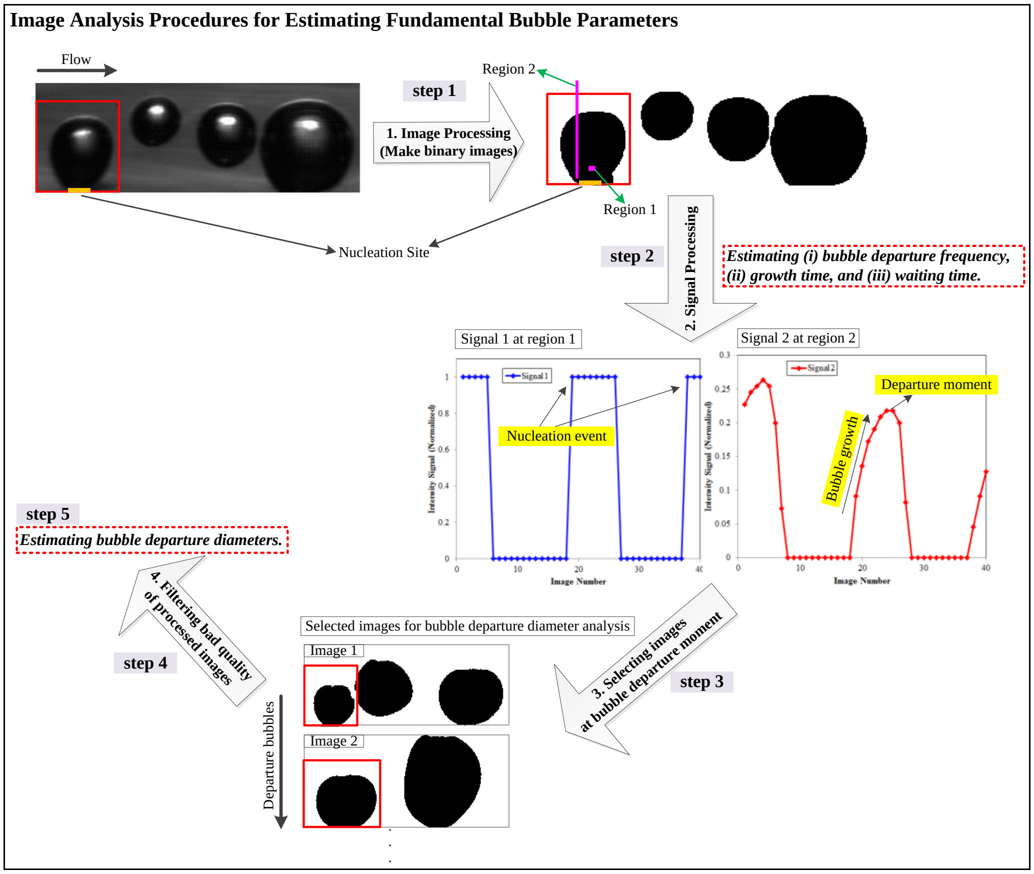

Figure II-15. Automatic image analysis algorithm for the fundamental bubble parameter analysis

2. Image processing algorithm

One of the most important parts of the image analysis method described in Section E.1 is to convert original gray scale images containing bubbles into binary images through the image processing in step 1 so that the boiling motions can be detected reliably through the automatic image analysis using the intensity signal variation. However, under subcooled or saturated flow boiling conditions, achieving high quality binary images with a single image processing algorithm is a challenge. The difficulty originates from the fact that, even within a short measurement time period, the refractive index of the flowing liquid around the bubble fluctuates significantly due to variations in liquid density close to the heater surface. Consequently, the images obtained often have uneven and time-varying background around the bubbles which makes extracting only the bubble information from the original images problematic using the simple method of image processing. To overcome this difficulty, the authors tried to find an efficient image processing algorithm to achieve better quality of processed binary images. Of course, the specific image processing algorithm for enhancing the discrimination of liquid background from the bubbles themselves depends on the quality of the original images, the test conditions, the person who performs the analysis, the image analysis software, and more. However, by investigating the common features of visual images taken under the subcooled flow boiling conditions of the present study, the image processing algorithm shown in Figure II-16 was developed.

Using the original images taken under the subcooled flow boiling condition (step A), inverted gray scale images are obtained for all the images (step B). Then, using the image calculation tool of image analysis software such as ImageJ or MATLAB®, the original images are subtracted from the inverted images (step C). Since the gray scale differences between the original and inverted images are usually considerably less for the liquid background than those for the bubbles themselves, the background noises around the bubble can be reduced significantly through this subtraction. After subtraction, the images can be further improved using various functions available from the image analysis tool (step D). For instance, the brightness, contrast, and color balance of the images can be adjusted. Special functions to remove smooth continuous background, based on the concept of the ‘rolling ball’ algorithm [30], and various image filters can be also used at this stage to enhance the discrimination of bubbles from the background. Next, the images are converted to binary images (step E), and any transparent holes inside the bubbles are filled in, which is required to estimate the projected bubble area in the image analysis method shown in Figure II-15. If the holes cannot be filled due to the open boundaries of bubble images, the ‘dilate’ and ‘erode’ function implemented in the image analysis software can be used to reconstruct the original bubble images. For instance, bubble image can be dilated until the bubble shape is enclosed. Then, after filling the hole inside the bubble, the bubble image can be eroded again to recover the original bubble size. However, careful attention should be paid to this procedure because the bubble shape can be substantially distorted if the ‘dilate’ and ‘erode’ functions are abused. Therefore, we applied this algorithm restrictively. Instead, the binary bubble images which are still open after the image processing procedure are filtered out through the image filtering process as discussed in Section E.1. Before filling in the bubbles, the imaginary heater wall can be also introduced in the images in case the original walls were removed during the image processing procedures.

Image Processing Procedure | **Processed Images**

Step A: Take snapshots of the original consecutive images with high speed camera

Step B: Invert gray scale of the original images

Step C: Subtract the original images in step A from the inverted images obtained in step B.

Step D: (i) Adjust brightness/contrast/color balance, and (ii) apply proper filters to the images in step C to reduce the background noises.

Step E: Transform the images in step D to binary images

Step F: Add or subtract the binary images of heater wall and fill the holes in the bubbles to estimate the projected bubble area.

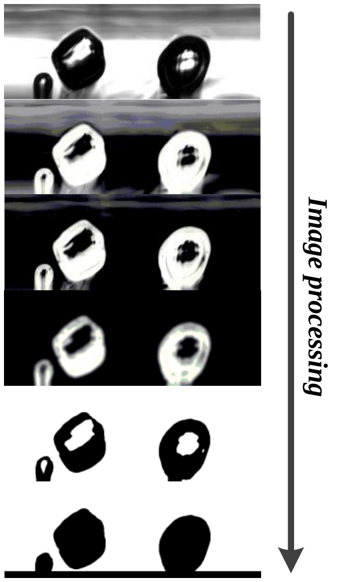

Figure II-16. Image processing algorithm applied in the present image analysis method

3. Error analysis of automated image analysis method

To verify the performance of the aforementioned image analysis algorithm with respect to the bubble departure frequency, the results obtained from the automatic image analysis algorithm were compared with those from the manual analysis. The manual analysis was performed by counting the nucleation events at the specific nucleation site based on the original images of the recorded films. This error analysis was conducted for the two subcooled flow boiling conditions, and an outside observer who had no knowledge of the results from the automated analysis carried out the manual analysis for both test conditions. For each test condition, almost 50,000 consecutive images were analyzed. More than 1300 and 2000 observations of nucleation events in each test condition were available. In Figure II-17, the average bubble departure frequencies obtained from the manual analysis and those from the automatic image analysis are compared according to the number of observations. The discrepancy between manual and automated analysis was found to be less than 0.4% in both test conditions.

One of the major sources of measurement uncertainty in the present image analysis algorithm is the effect of the specific image processing algorithm on the bubble size measurement. As discussed in Section E.2, the specific image processing algorithm used to discriminate the liquid background from the bubble itself is dependent on various factors. In order to quantify the measurement uncertainty introduced by the specific image processing algorithm, 10 different sizes of departing bubbles were randomly selected under different subcooled flow boiling conditions. Then, each size of bubble was evaluated repeatedly by applying different image processing algorithms. From the differences in the measured bubble sizes depending on the image processing algorithm, the standard deviations were obtained for each size of bubble, from which the maximum value was selected to estimate the measurement uncertainty induced by image processing. Those values are ±15.1 μm for the side view and ±15.9 μm for top view measurements at a 95% confidence level. Combining these values with the measurement uncertainty due to the spatial resolution of the images [25], measurement uncertainty of bubble size was finally determined to be ±16.1 μm for the side view and ±16.6 μm for the top view measurements.

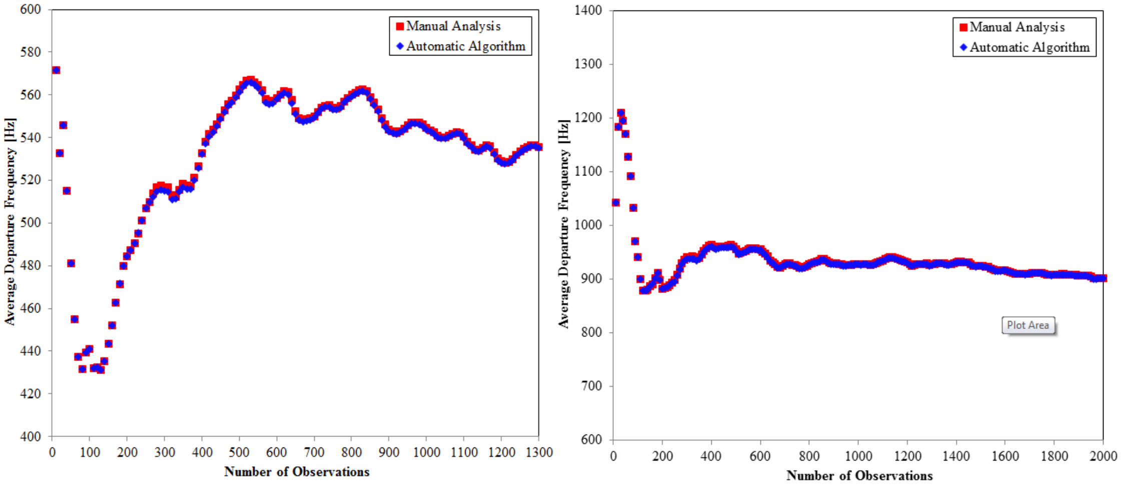

Figure II-17. Error analysis for the average bubble departure frequency

F. Summary and conclusions

The comparative analysis of previous studies revealed that there are still several unidentified issues in the visual measurement of fundamental bubble parameters that have never been treated explicitly despite their possibly critical impact on experimental results. In this study, through the intensive analysis of present experimental observations under subcooled flow boiling conditions, it was verified that the visual measurement of bubble departure diameter and bubble departure frequency can be significantly affected by (i) measurement views, (ii) recording speed of images, and (iii) number of experimental observations (sample size).

The findings regarding the measurement view show that the side view can provide more accurate information in many cases but not always. Specifically, it was found that measurements from the top view may considerably distort the bubble departure frequency measurement because small nucleating bubbles can be easily missed from this view due to the overlapping bubble images. Also, the measurement accuracy of bubble departure diameter was shown to be significantly deteriorated for small bubbles when the bubble size was estimated from the top view; whereas, better accuracy was shown from the side view measurement. However, even from the side view measurement, the same issue of bubble size measurement from the top view may happen unless the characteristic length for bubble departure diameter is properly defined. Therefore, both the measurement view and characteristic length should be carefully considered to achieve the reliable measurement of bubble departure and lift-off diameter.

For the recording speed of visualization, insufficient camera speeds substantially damage the measurement accuracy on bubble departure frequency measurement. As can be expected, fast-occurring bubble nucleation phenomena were infrequently captured with low recording speeds, which resulted in underestimation of average bubble departure frequency. Due to strong fluctuating behaviors of bubble nucleation, the recording speed of the camera should be carefully determined because the time interval between the nucleating bubbles has quite a wide range even within a short measurement time period.

This study also clearly demonstrates that the number of experimental observations can significantly affect the experimental insight based on the measured parameters. Particularly, we observed that even the maximum number of observations (≈200) used in previous literature does not appear to ensure reliable statistics (e.g., averages, PDFs) under the test conditions used in this study. Thus, this issue still requires much attention to gain better insight based on the measured fundamental bubble parameters and their statistics. In particular, for reliable statistical averages, we strongly recommend using at least the number of experimental observations ensuring convergence of the average value at a given experimental condition as illustrated in Section D. The image analysis algorithm developed by the authors helps analyze a large number of images efficiently with reliable accuracy.

In fact, universal criteria or specific rules and numbers to simply treat all the issues discussed are hard to give, because the boiling phenomenon is inherently chaotic and the experimental results depend strongly on multiple factors. Nevertheless, we believe that the efforts of experimentalists to correctly address the issues will significantly improve the quality of experimental investigations, which in turn will ensure better insight into the underlying physics of boiling process based on experiments. In this context, the experimental findings and discussions in this study will provide valuable guidance toward proper observation and characterization of the wall nucleation phenomena in a subcooled flow boiling system or, more generally, in a forced convective boiling system.

CHAPTER III

ACCURATE WALL TEMPERATURE MEASUREMENT USING INFRARED THERMOMETRY WITH ENHANCED TWO-PHASE FLOW VISUALIZATION[*]

A. Introduction

The heat transfer augmentation caused by boiling has been of great concern to researchers due to its potential to improve the cooling systems of many engineering applications. Often, the performance of engineering devices such as electronics and nuclear reactors has been limited by the amount of power that can be dissipated while using them because the operating temperature must be kept within specified limits to maintain the reliability. However, the traditional cooling systems employing the single-phase forced convection have limitations in addressing this issue, implying that alternative approach like boiling heat transfer needs to be introduced to make a breakthrough.

In order to realize the enhanced heat transfer of boiling in engineering applications, the physical mechanism should be understood well so that we can predict its performance with reasonable accuracy. In view of this, numerous experimental efforts have been made to obtain better insight into the boiling mechanism with various experimental techniques. Among such efforts, optical methods such as flow visualization

---

[*] Reprinted with permission from “An accurate wall temperature measurement using infrared thermometry with enhanced two-phase flow visualization in a convective boiling system” by J. Yoo, Carlos E. Estrada-Perez, Yassin A. Hassan, 2015, *International Journal of Thermal Sciences*, **90**, 248-266, Copyright 2015 by Elsevier Ltd.

and infrared (IR) thermometry are considered effective because they can provide direct observation of the thermal-hydraulic features related to boiling. Consequently, high-speed photography [3, 9, 11] and a laser-based flow visualization technique [31] have been utilized to study the hydrodynamics of liquid/vapor phases in a boiling system. For a wall heat transfer study, the thermal patterns under boiling conditions can be also visualized, for which liquid crystal thermography [32-34] and infrared (IR) thermometry [35-39] have been employed.

The above-mentioned optical techniques have an advantage over traditional methods relying on local probe sensors because the hydrodynamic and thermal features of interest can be captured non-intrusively with high spatial and temporal resolution. As a result, even the micro-physics of the two-phase flow such as wall boiling and local mass/momentum/energy transfer can be characterized without any disturbance of instrument. Also, using a measurement of macro-scale, the transitional changes between different flow regimes, e.g., single-phase/two-phase flow regions, bubbly/slug/annular flow regimes, can be captured over a large area.

In recent years, rapidly growing computing power and advances in high-speed imaging technology have led to aspirations among researchers to combine high-speed IR thermometry with the high-speed visualization techniques. So far, such attempts have been made primarily in pool boiling experiments [40-42] with a few flow boiling experiments in mini-/micro-channels [43]. All of these experiments were designed to observe the bubble dynamics and the wall temperature field simultaneously. This is obviously an appealing experimental approach because it can provide direct insight into the relation between hydrodynamic bubble motions and wall heat transfer. However, such efforts are rare in general convective boiling experiments, especially for technical applications involving a large heated area.

To achieve reliable data measurement from both high-speed flow visualization and IR thermometry, several sources of measurement error, especially optical issues, must be addressed correctly. Otherwise, the reliability of the parameters measured will decline substantially, despite the apparently sophisticated visual images obtained from such methods. Therefore, to implement both techniques in a single experimental facility, several issues must be taken into particular consideration. First, the materials composing the test section should be determined by considering their optical properties; and the experimental design should consider the feasibility both for flow visualization and IR thermometry. Also, since both techniques provide optical images from which quantifiable data can be acquired, optical distortions should be prevented. Additionally, to accurately estimate the target object’s temperature from the thermal images taken by IR camera, proper calibration considering the optical property is required.

In this chapter, we discuss the experimental strategy assuring both enhanced flow visualization and accurate wall temperature measurement using high-speed photography and IR thermometry. Our particular interest is focused on the improved observation of two-phase flow hydrodynamics as well as the wall temperature distribution in a convective boiling system which involves a large heated area. For this approach, the heater wall design is especially important because it directly affects the quality of IR temperature measurement and the flow visualization. In literatures, about three different types of heater wall configurations have been utilized for the boiling study employing IR thermometry. Some of those are described here with brief descriptions of the wall temperature measurement strategies, after which the relevance of each approach for the present application is discussed.

(i) A heating channel coated with IR-opaque material

A heating channel lined with IR-opaque material of high emissivity has been primarily used in flow boiling experiments in mini- and micro-channels. Hapke et al. [35] examined the wall heat transfer characteristics under flow boiling conditions in a mini-channel. They painted the outer wall of the test section with black lacquer (emissivity≈0.94) to ensure high sensitivity of the IR temperature measurement. Then, the outer-wall temperature distribution was measured by IR camera, from which the inner wall temperature touching the fluid was evaluated by assuming quasi-steady conditions of the wall. The similar approach was also taken by Boye et al. [44] who performed a flow boiling experiment with water in a circular mini-channel. On the other hand, Barber et al. [43] attempted the high-speed photography along with IR thermometry in a rectangular micro-channel made of borosilicate glass. In order to visualize the boiling motions inside the channel while measuring the outer wall temperature using IR camera, they employed the transparent metallic deposit on the outer wall of the glass channel. Then, the local heat transfer characteristics at different flow boiling regimes were studied.

(ii) A thin metal foil heater

Recently, to observe the wall heat transfer characteristics during boiling, a thin metal foil on the order of micrometers thickness has been used as a heater by itself. This approach has been adopted to perform fundamental boiling studies with high spatial and temporal resolution at the local nucleation site. Golobic et al. [40] performed an experiment under subcooled and saturated pool boiling conditions with water at atmospheric pressure. To create the boiling, they used a platinum heating foil of 6 μm thickness with a 2–3 μm thick layer of black paint on the back side. Then, a high-speed IR camera measured the two-dimensional wall temperature field during the growth of bubbles. Schweizer and Stephan [45] studied the nucleate boiling of FC-72 under variable gravitational conditions. The measurements were performed at a single artificial cavity created on a thin heating foil made of stainless steel 25 μm thick. Similarly to Golobic et al. [40], Schweizer and Stephan [45] applied a coat of black paint to the back side of the heating foil for the IR thermometry. Kunkelmann et al. [42] investigated the effect of three-phase contact line motion on the local evaporative heat transfer within a micro-region. For the heater in this experiment, a stainless steel foil 20 μm thick was used, and the wall temperature was measured using IR camera while bubbles' motions were recorded by high-speed video camera.

(iii) A heating film deposited on an IR-transparent substrate

The heater wall temperature can be also measured using IR camera through an IR-transparent substrate onto which an IR-opaque heating film is deposited. Theofanous et al. [36] used an IR camera to visualize the dynamic thermal patterns on the heated wall in a pool boiling experiment. As a heating element, titanium films of 140–1000 nm thickness were deposited on 130 μm thick borosilicate glass. Then, the IR camera captured the thermal footprint created by the boiling motion through the glass substrate. In Gerardi et al. [41], a transparent and electrically conductive indium-tin-oxide (ITO) film was used as a heating element for their saturated pool boiling study. The IR-opaque ITO film was attached to a 0.4 mm thick sapphire substrate through which the bubble nucleation and the transient wall temperature were observed. Recently, in Fischer et al. [46], an enhanced emissivity of chromium-based layer was applied on a 2 mm thick IR-transparent calcium fluoride (CaF_2) substrate, and a pure chromium heating layer was laid on top of that. Then, an IR camera detected the wall temperature through the CaF_2 substrate during the boiling process. In Kim et al. [47], a silicon wafer was employed as a substrate of the heater wall, and a polyimide tape coated with a thin black paint was attached to the substrate to improve the signal detected by IR camera for their wall heat transfer study.

(iv) Discussion on the previous experimental design approaches

The relevance of each approach described above for the present application can be discussed based on the specific measurement targets of the present study. The first approach (i) is inapplicable because the flow visualization is restricted by the opaque film on the outer wall of the test channel. Even in the case that the channel wall and the heating element are configured for enabling visualization as in Barber et al. [43], the IR camera cannot directly measure the surface temperature of the inner wall touching the fluid due to the IR-opaque film on the outer wall. Thus, the time-varying inner wall temperature due to the boiling is hard to capture with this approach unless the channel wall is extremely thin. The second approach (ii), which employs a thin metal foil as a heater, is better for capturing the transient wall temperature induced by boiling using the IR camera. However, achieving a large heated area is difficult because of the structurally weak nature of the thin foil. Also, the low heat capacity of thin foil can alter the boiling process compared to the thicker heaters. Therefore, in the present study we based the heater wall design on the third approach (iii). However, we avoided using the well-known IR transparent materials such as CaF_2, sapphire, and zinc selenide as a substrate because they are usually very expensive and/or problematic to treat as a large piece. Instead, soda-lime glass was used, for which the additional effort for calibration is necessary to accurately measure the wall temperature.

A series of extensive efforts required to achieve the high-fidelity measurement employing both the IR thermometry and the high-speed photography are described in this chapter. As shown in Figure III-1, the present efforts were made by considering the general process that must be pursued for phasing in the new experimental techniques or approaches properly. We treated all the details, including the test section design, IR measurement issues, visualization strategy, wall temperature tracking method, and experimental validations. Then, the subcooled flow boiling experiment was performed using the verified approach, during which we could clearly see the detailed relation between the bubble motions and the wall heat transfer as the bubbles develop throughout the flow channel.

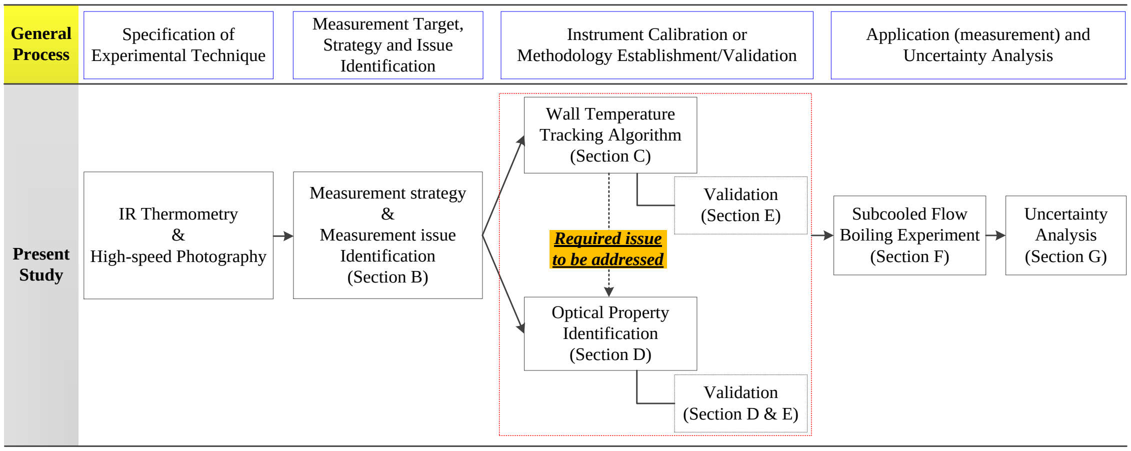

Figure III-1. Overview of present study considering the general process for introducing the new experimental approach

B. Experimental strategy and measurement issues

1. Material selection and test section design

For the simultaneous application of high-speed photography and IR thermometry, the test section walls should be transparent in visible light; whereas, the heater surface (i.e., wall) touching the fluid should be opaque to IR radiation so that the wall temperature can be measured by IR camera. If a thin heating film is deposited on the substrate, the substrate should be at least semi-transparent to the IR spectral range of interest so that the varying temperature on the film can be directly captured through the substrate using IR camera. A high-speed IR camera (SC8000, FLIR Systems, Inc.) working for a mid-wave IR (i.e., 3–5 μm) range was utilized in this study.

The mechanical strength of substrate is also an important factor to consider because we want to investigate the flow boiling features over a relatively large heated area. Also, the thermal properties of substrate are important because they can affect the temperature profile within the substrate which subsequently affects the determination of the local heat transfer parameters [46, 47]. For instance, high thermal conductivity would readily smear out any temperature gradients within the substrate, resulting in a lower magnitude of temperature difference across the substrate used to estimate the local heat transfer coefficient or local heat flux.

Accordingly, the test section for the flow boiling experiment was designed as shown in Figure III-2. The channel geometry is square (10×10 mm^2), and the fluid flows upward through a vertical test section with a total height of 305 mm and a heated length (L_0) of 265 mm on one side. The test section is enclosed by transparent acrylic walls except for the heater wall side. On the heater wall side, ITO film is attached to a soda-lime glass substrate. The ITO film is exposed to the test fluid, 3M™ Novec™ 7000, within the channel and is heated by an electrical current.

As shown in Figure III-2 (top), the heater wall has multi-layer configuration which is to improve the insulating features of test section. In particular, a sapphire window is installed next to the glass substrate so that the trapped air between the glass substrate and sapphire window can prevent the heat loss to the environment. Note that all the materials composing the test section, including the ITO film, are transparent to visible light. Thus, the illuminating light for flow visualization is available from every direction around the test section (Figure III-2, bottom), which ensures enhanced bubble imaging with high-speed video cameras. Meanwhile, since ITO film is opaque to mid-wave IR radiation while the soda-lime glass substrate and sapphire window are semi-transparent to such IR range, the ITO temperature can be measured through the multilayer walls. The soda-lime glass was utilized as substrate for the ITO film due to its availability and cost effectiveness compared to well-known IR-transparent materials as well as its thermal, optical, and mechanical properties. Specifically, soda-lime glass has low thermal conductivity (≈0.94 W/m-K), is semi-transparent to mid-wave IR radiation, and is mechanically strong enough to be treated at a large size. However, soda-lime glass has not been widely used in IR thermometry, and the specific composition may change depending on the manufacturer. Therefore, in order to achieve the accurate wall temperature measurement, the properties of such materials, especially the optical properties, should be verified first (Section D). Also, the thickness of glass substrate should be proper to capture the reasonable amount of IR radiation originating from the ITO. Here, we used 0.5 mm thick soda-lime glass (Bayview Optics, Inc.).

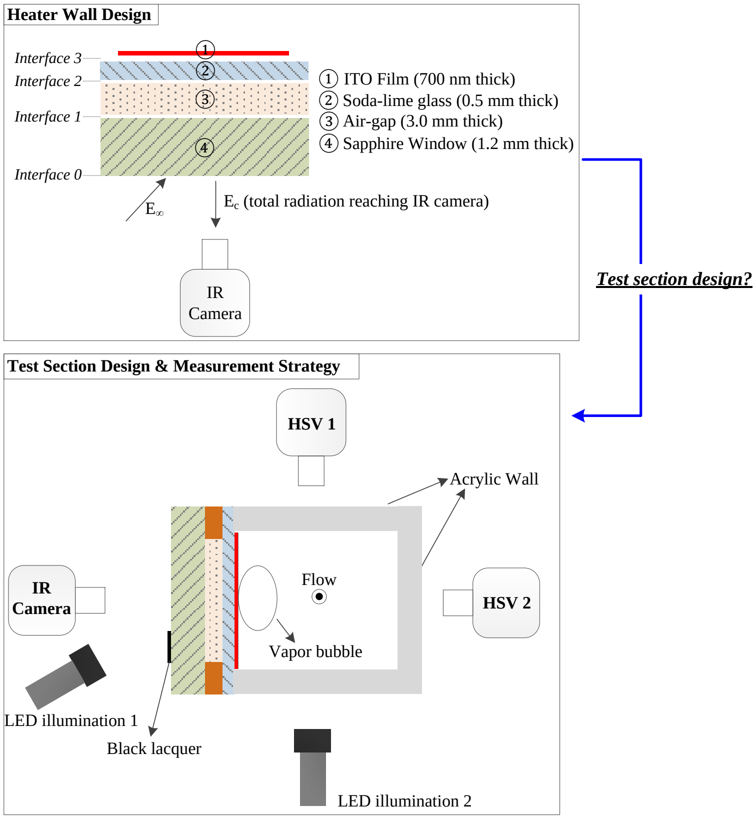

Figure III-2. Heater wall design (top) and measurement strategy (bottom) in the subcooled flow boiling experiment (view from the top of channel)

2. Measurement strategy

In Figure III-2 (bottom), the cameras arrangement applied to the present subcooled flow boiling experiment is shown. Two high-speed video cameras were used to observe vapor bubble motions while the temperature of the wall (i.e., ITO film) is measured by an IR camera located on the heater wall side. To improve the image quality taken from both high-speed video cameras, LED illumination was used from two sides. Also, the two high-speed video cameras (HSV 1 and HSV 2) are synchronized so that the bubbles' behavior can be observed from different views. On the outer surface of the sapphire window, black lacquer was painted on one edge to provide the boundary condition for the wall temperature tracking (see Section C). This experimental setup allows capturing the detailed boiling motions along with the corresponding wall temperature field.

3. Wall temperature measurement issues

The ITO has been often employed in previous boiling studies aiming to visualize the boiling motions along with the wall temperature measurement using IR thermometry due to its unique optical feature [28, 41, 48]. However, we should note that substantial errors might be caused in IR-based temperature measurement unless special attention is paid due to the ITO's high reflectivity of IR radiation.

Figure III-3 shows the axial wall temperature profile (total length L_0=265 mm) measured by IR camera for the unheated (left) and heated (right) single-phase upward flow. The axial temperature profile is expected to be flat in the unheated case and linear in the heated case, but the obvious temperature distortions are found in Figure III-3. This is because the IR radiation from the heated body of IR camera was reflected onto the surface of the ITO film, and the reflected radiation returned back to the IR camera, which led to the distortion in the temperature measurement of the wall (ITO film). This phenomenon is called the Narcissus effect [49, 50]. The camera lens and/or the instruments around the test section can create similar reflective effects unless the temperature measurement is performed with special care. To prevent such reflection, we used a black rubber plate to cover the front of the IR camera except for the lens. In addition, the IR camera was positioned at a small angle to the heater surface instead of being perpendicular, which was to avoid the reflection caused by the optical lens.

Due to the low emissivity of ITO (ε≈0.16, see Section D and E), surrounding conditions such as ambient temperature may also have substantial impacts on the IR-based temperature measurement in the present application. Therefore, the related uncertainty should be carefully addressed (Sections E and G). Furthermore, due to the multi-layer design of heater wall (Figure III-2), the IR camera cannot directly capture the correct wall temperature because the total energy measured by the IR camera (E_c) consists of the energy emitted by the several layers composing the heater wall. Thus, this multi-layer wall effect should be taken into consideration, which is discussed in the following section.

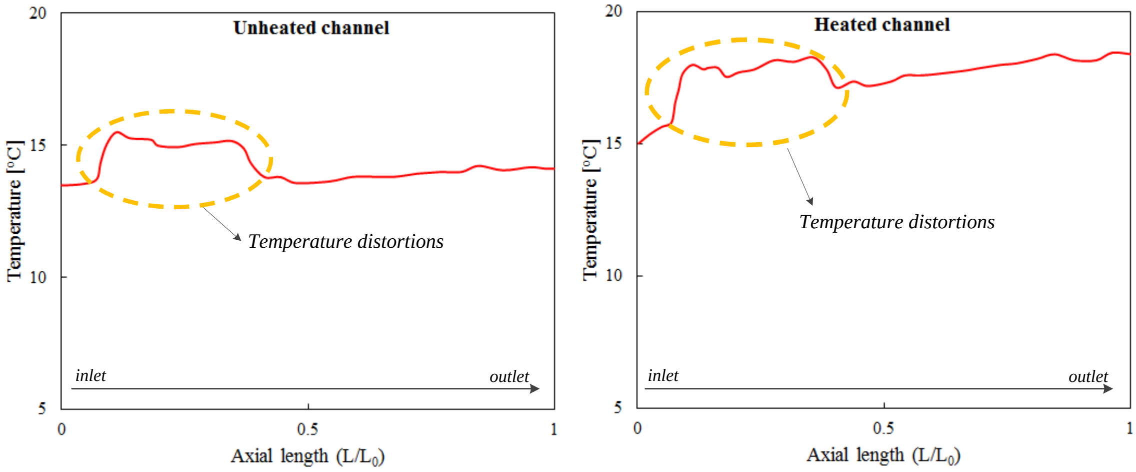

Figure III-3. Temperature distortions captured by the IR camera due to the Narcissus effect

C. Analysis method for wall temperature tracking

In Figure III-2, we can easily find that the IR radiation originating from the ITO film would decrease significantly as it goes through the glass substrate and sapphire window before reaching the IR camera. This implies that the amount of IR radiation emitted by the ITO film must be estimated correctly for accurate wall temperature measurement. Here, the total radiation reaching the IR camera consists of energy emitted by several layers, i.e., ITO film, soda-lime glass, and sapphire, leading to the following radiation balance equation:

$$E_c = \rho_{\infty-c}E_\infty + \varepsilon_{sap-c}E_{sap} + \varepsilon_{g-c}E_g + \tau_{ITO-c}E_{ITO} \qquad \text{(III-1)}$$

where E_c is the total radiation measured by the IR camera; E_∞ is the background radiation introduced by the surroundings ($E_\infty = \sigma F_{3-5\mu m}(T)T_\infty^4$); E_{sap}, E_g, and E_{ITO} are the emission from the sapphire, soda-lime glass, and ITO film, respectively; σ is the Stefan-Boltzmann constant (W/m^2-K^4); and T_∞ is the ambient temperature. $F_{3\text{-}5\mu m}$ represents the fraction of radiation energy within the wavelength interval 3–5 μm, which can be obtained from tables or by numerically integrating Planck’s distribution [51]. Note that the radiation emitted by air is neglected in Eq. (III-1), because the transmissivity of air can be assumed as unity (i.e., τ_∞=1) at short distances between the IR camera and the target object, implying that the emission/reflection due to air can be neglected.

The coefficients of each term used in Eq. (III-1) were determined based on the approach employed by Kim et al. [47]. Following their approach, the infinite number of transmissions, absorptions, and reflections of radiation across the media composing the heater wall is considered to obtain the analytical expressions of those coefficients. The derivations are described in detail in Appendix A.3. The final forms of each coefficient are given as follows:

$$\rho_{\infty-c} = \rho_{sap-\infty} + \frac{(1-\rho_{sap-\infty})^2 \tau_{sap}^2 \rho_{app,sap-\infty,1}}{1-\rho_{sap-\infty}\rho_{app,sap-\infty,1}\tau_{sap}^2} \qquad \text{(III-2)}$$

$$\varepsilon_{sap-c} = \frac{(1-\rho_{sap-\infty})(1+\rho_{app,sap-\infty,1}\tau_{sap})}{1-\rho_{sap-\infty}\rho_{app,sap-\infty,1}\tau_{sap}^2} \qquad \text{(III-3)}$$

$$\varepsilon_{g-c} = [\frac{(1-\rho_{g-\infty})(1+\rho_{ITO-g}\tau_g)}{1-\rho_{g-\infty}\rho_{ITO-g}\tau_g^2}][\frac{1-\rho_{sap-\infty}}{1-\rho_{sap-\infty}\rho_{app,g-\infty,2}}][\frac{(1-\rho_{sap-\infty})\tau_{sap}}{1-\rho_{sap-\infty}\rho_{app,sap-\infty,1}\tau_{sap}^2}] \qquad \text{(III-4)}$$

$$\tau_{ITO-c} = [\frac{\tau_g}{1-\rho_{g-\infty}\rho_{ITO-g}\tau_g^2}][\frac{1-\rho_{g-\infty}}{1-\rho_{sap-\infty}\rho_{app,g-\infty,2}}][\frac{(1-\rho_{sap-\infty})^2\tau_{sap}}{1-\rho_{sap-\infty}\rho_{app,sap-\infty,1}\tau_{sap}^2}] \qquad \text{(III-5)}$$

where $\rho_{sap-\infty}$ and $\rho_{g-\infty}$ are the reflectivity at the sapphire-air interface and glass-air interface, respectively; $\rho_{app,sap-\infty,1}$ is the apparent reflectivity at interface1 between the sapphire and the air gap; $\rho_{app,g-\infty,2}$ is the apparent reflectivity at interface 2 between the glass and the air gap; ρ_{ITO-g} is the reflectivity at interface 3 between the ITO film and the glass; and τ_g and τ_{sap} are the transmissivity of glass and sapphire, respectively. Note that, for the semi-transparent medium to IR radiation (e.g., glass, sapphire), the concepts of apparent reflectivity ($\rho_{app,m-\infty}$) and apparent transmissivity ($\tau_{app,m-\infty}$) are used in addition to the normal reflectivity ($\rho_{m-\infty}$) and normal transmissivity (τ_m), which is to consider the infinite number of reflections/transmissions throughout the medium (see Appendix A.1). Due to the high absorptivity/emissivity of IR radiation of soda-lime glass, the temperature profile across the medium can substantially affect the amount of radiation reaching the IR camera. Thus, we employed the 1D heat conduction equation to obtain the temperature profile across the multi-layer, which is coupled with Eq. (III-1) as in Kim et al. [47]. The overall algorithm is described as follows.

Given the assumed initial temperature profile across the multi-layer, ambient temperature (T_∞), and total radiation captured by the IR camera (E_c), the wall temperature (T_{ITO}) is obtained first using Eq. (III-1). The wall temperature obtained is then used as one of the boundary conditions for the subsequent transient heat conduction simulation. The other boundary condition is given by the temperature measured by the IR camera on the outer surface of the sapphire window where the black lacquer is, as shown in Figure III-2. Then, by solving the heat conduction equation with these boundary conditions, the temperature profile across the multi-layer wall is updated. Subsequently, the wall temperature T_{ito} at the new time step can be obtained using Eq. (III-1) in the same way mentioned before. Repeating this process allows the tracking of time-dependent wall temperature variation. It is noted that as the initial temperature profile across the multi-layer is arbitrarily assumed, the true temperature of the wall can be obtained after the influence of initial condition is dampened out. Kim et al. [47] proved that this two-way coupled algorithm works in the multi-layer design of wall composed of silicon substrate, polyimide tape, and black paint. However, such method has not been attempted and/or validated yet for the materials adopted in our study for which the optical properties must be identified.

D. Optical property measurement

1. Experimental procedure and measured optical properties

The optical properties, i.e., reflectivity, transmissivity, and emissivity of the materials were measured using an experimental setup shown in Figure III-4 with a blackbody source (Infrared Systems Development Corp., emissivity $\varepsilon_{B.B}$=0.96±0.02). In this study, we were particularly concerned with how the properties of the selected materials, in particular the ITO and soda-lime glass, behave within the temperature and spectral ranges of interest, which were 20–85 ºC and 3–5 μm. In general, optical properties depend on temperature and wavelength; and such dependency may affect the performance of the present wall temperature tracking discussed in Section C. Therefore, to measure the optical properties of the target objects and to evaluate the temperature dependency of such properties, an air-temperature-control system was installed as shown in Figure III-4. Using this system, the temperature of target object was controlled by injection of cold or hot air; and the temperature measurement using IR camera was conducted at different temperatures of target object without any disturbance during the measurement because the transmissivity of air is always almost unity.

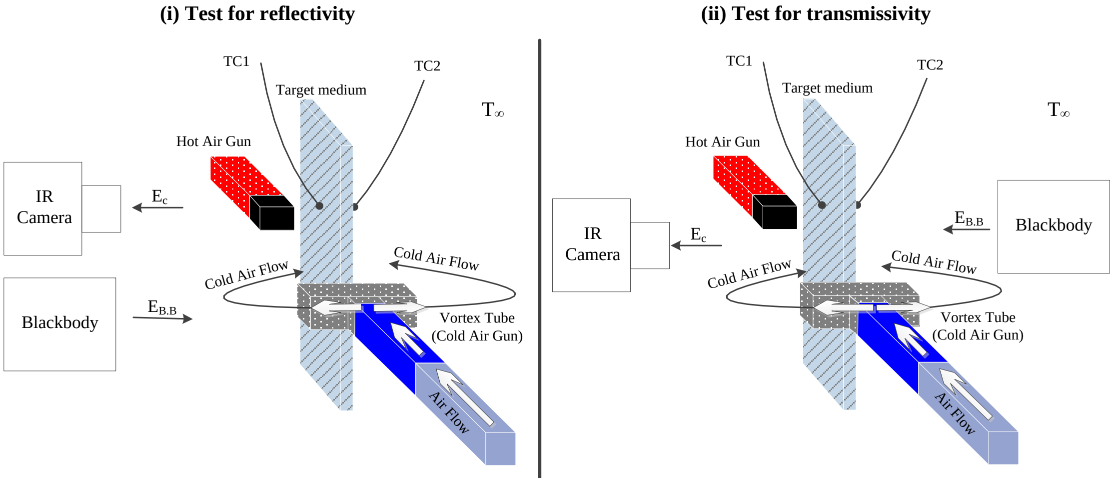
(i) Test for reflectivity

(ii) Test for transmissivity

Figure III-4. Optical property measurement of the materials composing the heater wall

The specific procedures for optical property measurement are as follows. (1) A blackbody source temperature is fixed at a certain level (60 ºC). (2) The thermocouple tips (K-type) are placed at symmetrical locations on each side of the medium within the area in which the temperature, or more accurately the radiation, is measured by the IR camera (see Figure III-4). (3) Hot or cold air is injected toward the target medium until the surface temperature of both sides of the medium reaches a steady state as measured by the thermocouples. The injection of hot or cold air must be carefully controlled to achieve surface temperatures as similar as possible on both sides of the medium because this allows the simple assumption of a uniform temperature profile across the medium. (4) At each temperature of the target medium, the total radiation (E_c) is measured using the IR camera with and without a blackbody source. Then, using the difference between the total radiation with and without a blackbody source, the reflectivity and transmissivity can be obtained. Note that the total radiation reaching the IR camera is determined by the (i) emission, (ii) reflection, and (iii) transmission of radiation throughout the medium:

$$E_c = E_{emission} + E_{reflection} + E_{transmission} \qquad \text{(III-6)}$$

where $E_{emission}$ is the radiation emitted by the medium ($=\varepsilon_{app,m-\infty}F_{3\text{-}5\mu m}(T)\sigma T_m^4$); $E_{reflection}$ is the radiation reflected by the medium; and $E_{transmission}$ is the radiation transmitted through the medium.

In the experimental setup shown in Figure III-4 (left side), $E_{reflection}$ is determined by the blackbody source temperature ($=\rho_{app,m-\infty}F_{3\text{-}5\mu m}(T)\sigma\varepsilon_{B.B}T_{B.B}^4$) or the ambient temperature ($=\rho_{app,m-\infty}F_{3\text{-}5\mu m}(T)\sigma T_\infty^4$), depending on whether a blackbody source is used or not. In contrast, neither $E_{emission}$ nor $E_{transmission}$ depends on the existence of a blackbody source as long as T_m and T_∞ are fixed. Therefore, using the difference of total radiation captured by the IR camera (E_c) between the measurement with and without a blackbody source, the $\rho_{app,m-\infty}$ at a certain T_m can be obtained based on the following equation:

$$\begin{aligned}
&(E_c)_{\text{with B.B}} - (E_c)_{\text{without B.B}} \\
&= (E_{emission} + E_{reflection} + E_{transmission})_{\text{with B.B}} \\
&\qquad\qquad - (E_{emission} + E_{reflection} + E_{transmission})_{\text{without B.B}} \\
&= (E_{reflection})_{\text{with B.B}} - (E_{reflection})_{\text{without B.B}} \\
&= \rho_{app,m-\infty}F_{3-5\mu m}(T)\sigma\varepsilon_{B.B}T_{B.B}^4 - \rho_{app,m-\infty}F_{3-5\mu m}(T)\sigma T_\infty^4
\end{aligned} \qquad \text{(III-7).}$$

In the case of a reflectivity measurement for the ITO film using Eq. (III-7), the normal reflectivity (ρ_{ITO}) is used instead of apparent reflectivity because the ITO film is assumed to be completely opaque to IR radiation, implying that transmission and reflection within the film do not exist. In other words, the radiation phenomenon is treated as a surface phenomenon instead of a volumetric phenomenon for opaque materials like ITO.

The $\tau_{app,m-\infty}$ was measured based on the experimental setup shown in Figure III-4 (right side). Here, the $E_{transmission}$ depends on the blackbody source temperature ($=\tau_{app,m-\infty}F_{3\text{-}5\mu m}(T)\sigma\varepsilon_{B.B}T_{B.B}{}^4$) or the ambient temperature ($=\tau_{app,m-\infty}F_{3\text{-}5\mu m}(T)\sigma T_\infty{}^4$), depending on whether a blackbody source is used or not. Meanwhile, since neither $E_{emission}$ nor $E_{reflection}$ is affected by the use of a blackbody source while T_m and T_∞ are kept same, $\tau_{app,m-\infty}$ can be obtained based on the following equation:

$$\begin{aligned}
&(E_c)_{\text{with B.B}} - (E_c)_{\text{without B.B}} \\
&= (E_{emission} + E_{reflection} + E_{transmission})_{\text{with B.B}} \\
&\qquad\qquad - (E_{emission} + E_{reflection} + E_{transmission})_{\text{without B.B}} \\
&= (E_{transmission})_{\text{with B.B}} - (E_{transmission})_{\text{without B.B}} \\
&= \tau_{app,m-\infty}F_{3-5\mu m}(T)\sigma\varepsilon_{B.B}T_{B.B}^4 - \tau_{app,m-\infty}F_{3-5\mu m}(T)\sigma T_\infty^4
\end{aligned} \qquad \text{(III-8).}$$

In addition to optical property measurements for different temperatures of the target medium, we also measured transmissivity of the soda-lime glass while varying the blackbody source temperature over the range 40–80ºC.

Table III-1 shows the measured properties of the materials, i.e., the ITO film, soda-lime glass and sapphire. The major sources of uncertainty during the measurements were (i) temperature fluctuations of the target medium during the air cooling/heating process, (ii) the local temperature gradient within the measurement area, and (iii) the emissivity of the blackbody source. The effects of (i) and (ii) increased when the temperatures of the target medium were over 60ºC. Nevertheless, the measured properties did not show noticeable changes under the various test conditions applied during this study. The uncertainty of the measured optical properties shown in Table III-1 was obtained by taking the twice of standard deviation of the repeated measurements at various test conditions to ensure a 95% confidence level.

Once $\rho_{app,m-\infty}$ and $\tau_{app,m-\infty}$ are determined for each target object, $\rho_{m-\infty}$ and τ_m can be obtained using the following relationships:

$$\rho_{app,m-\infty} = \rho_{m-\infty} + \frac{(1-\rho_{m-\infty})^2 \rho_{m-\infty} \tau_m^2}{1-\rho_{m-\infty}^2 \tau_m^2} \tag{III-9}$$

$$\tau_{app,m-\infty} = \frac{(1-\rho_{m-\infty})^2 \tau_m}{1-\rho_{m-\infty}^2 \tau_m^2} \tag{III-10}$$

Because Eqs. (III-9) and (III-10) are non-linear systems of equations dependent on each other, the solutions can be found through an iterative process based on the measured properties (i.e., $\rho_{app,m-\infty}$, $\tau_{app,m-\infty}$) until the unknowns (i.e., $\rho_{m-\infty}$, τ_m) are found. Equations (III-9) and (III-10) are derived in Appendix A.1; the derivation can also be found in Kim et al. [47]. After obtaining $\rho_{m-\infty}$ and τ_m, the absorption coefficient (a) can be estimated based on the relationship $\tau=\exp(-aL)$ derived from Beer's law. In addition, the refractive index, or the reflectivity at the interfaces (e.g., ρ_{ITO-g}, see Appendix A.3.), can be estimated using the Fresnel equation, which is widely used to represent radiation behavior across an interface between two media. Assuming that the incoming radiation is perpendicular to the flat surface of target medium, the Fresnel equation is given by

$$\rho_{A-B} = \left(\frac{n_A - n_B}{n_A + n_B}\right)^2 \tag{III-11}$$

where ρ_{A-B} is the reflectivity at the interface between the media A and B, and n is the refractive index. When the medium comes in contact with air (∞), $\rho_{A-\infty}$ can be obtained if

n_A is known while n_A can be obtained if $\rho_{A-\infty}$ is known by assuming n_∞=1. In this way, all the properties required to solve the Eq. (III-1) can be defined.

The refractive index of the soda-lime glass and the sapphire used in this study were estimated based on the measured properties (Table III-1) and using Eqs. (III-9) through (III-11). Then, for validation purposes, the refractive index values obtained were compared with those found in the literature. The refractive index of sapphire (n_{sap}) is known to be about 1.6~1.7 at λ=3-5 μm while the estimated value based on the present measurements was $n_{sap}\approx 1.63$. In the case of the soda-lime glass, finding the refractive index (n_g) within the spectral range of interest was difficult; but n_g is known to be about 1.5 at λ=1-2 μm while the refractive index estimated based on the measured properties in Table III-1 was $n_g\approx 1.41$. These results indicate that the measured values are reasonable. To confirm the validity of these measured properties for the temperature tracking, further validation was performed and is discussed in Section D.2.

Table III-1. Measured optical properties of the materials composing the heater wall

	Nominal Value	Uncertainty
Apparent transmissivity of glass ($\tau_{app,g-\infty}$)	0.42	0.018
Apparent reflectivity of glass ($\rho_{app,g-\infty}$)	0.04	0.004
Reflectivity of ITO (ρ_{ITO})	0.82	0.019
Apparent reflectivity of sapphire ($\rho_{app,sap-\infty}$)	0.11	0.002
Apparent transmissivity of sapphire ($\tau_{app,sap-\infty}$)	0.84	0.018

2. Validation of measured properties of semi-transparent media

To validate the measured properties of soda-lime glass and sapphire, several tests were performed. Specifically, the IR camera, blackbody source, and the semi-transparent medium employed in this study were arranged similarly to the experimental setup for the transmissivity measurement (Figure III-4, right side). Then, the blackbody source temperature was observed through the semi-transparent medium using the IR camera. The radiation balance equation and the derivation of coefficients required for these tests are given in Appendix A.2. T_∞ was measured by a T-type thermocouple, and the semi-transparent medium was assumed to stay in thermal equilibrium with the surroundings, meaning that temperature variation within the medium is ignored.

Firstly, the measurements were performed with a single layer of soda-lime glass and with a single layer of sapphire window placed between the IR camera and the blackbody source (i.e., single-layer test). The radiation emitted by the blackbody source was measured through the single layer of each medium, and calibration was performed using the measured optical properties (Table III-1) as well as the corresponding radiation balance equation (see Appendix A.2). The results are shown in Figure III-5, which shows that after applying the calibration, the measured (or tracked) blackbody source temperature agrees well with that measured by the thermocouple, within 0.7 ºC for the soda-lime glass and 0.4ºC for the sapphire. The assumptions of thermal equilibrium and a uniform temperature profile across the medium are considered the major sources of uncertainty during this test. For the soda-lime glass, the assumptions seem to have more impact on the temperature tracking results than for the sapphire due to the high emissivity of the soda-lime glass. Figure III-5 also shows the difference between the direct temperature measurements using the IR camera without calibration and the ones when calibrated. Note that the simple adjustment of the emissivity value in the IR camera software (ExaminIR, FLIR Systems Inc.) is not enough to make this temperature measurement accurate, because the volumetric effect of the radiation phenomenon within the semi-transparent medium cannot be accounted for in that way.

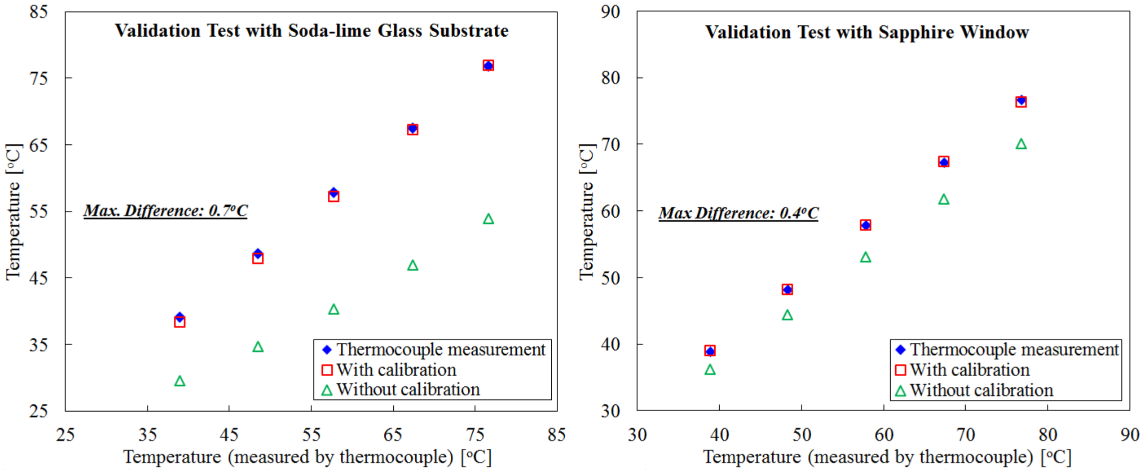

Figure III-5. Temperature tracking results through a single layer of a semi-transparent medium

After a test using a single medium, the sapphire window and soda-lime glass were placed together between the IR camera and the blackbody source so that the blackbody source temperature could be measured through both media (i.e., double-layer test). The radiation balance equation and the derivation of coefficients for this test are given in Appendix A.2. Figure III-6 shows the temperature tracking results for the double-layer test; the maximum deviation compared to the direct measurements using thermocouple was found to be 0.6 ºC. The main sources of uncertainty during this test are considered to be the same as those for the single-layer test. From the results shown in Figures III-5 and III-6, we concluded that the measured optical properties of the soda-lime glass and the sapphire window shown in Table III-1 are valid enough for accurate temperature tracking through these media using IR thermometry.

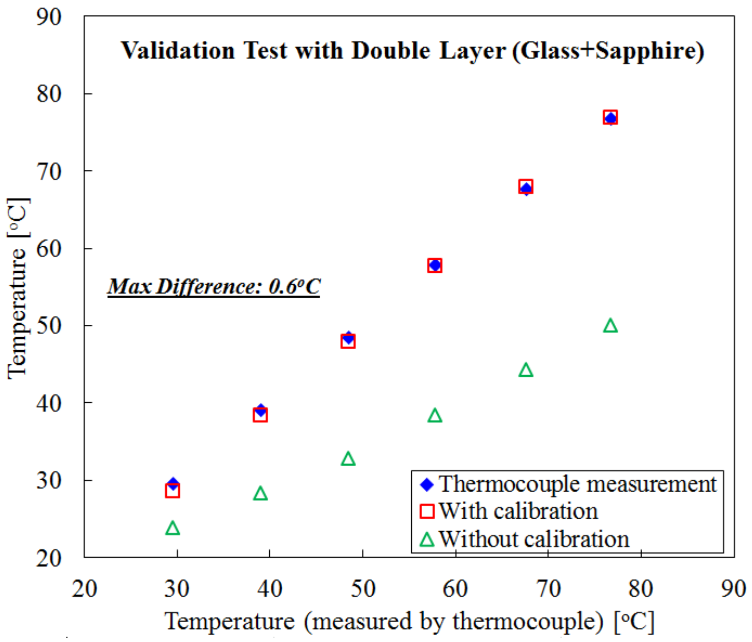

Figure III-6. Temperature tracking results through the double layer of semi-transparent media

E. Experimental validation with the proposed heater wall design

The multi-layer design of heater wall shown in Figure III-2 contains a thin ITO film attached to the soda-lime glass substrate. Thus, the optical properties of the ITO should be verified as well. Also, the overall performance of the wall temperature tracking algorithm should be demonstrated before it is applied to the actual application, e.g., subcooled flow boiling experiment, which are described in this section.

1. Validation of ITO film's optical properties and the steady-state test

Due to the opaqueness of ITO to IR radiation (i.e., $\tau_{ITO}=0$), the emissivity of ITO (ε_{ITO}) can be determined based on the measured reflectivity shown in Table III-1 along with the following relation:

$$\alpha_{ITO} + \rho_{ITO} = \varepsilon_{ITO} + \rho_{ITO} = 1 \tag{III-12}$$

where α is the absorptivity, ρ is the reflectivity, ε is the emissivity, and $\alpha=\varepsilon$ is assumed according to Kirchhoff's law.

When treating low emissivity and IR-opaque material such as ITO, the optical properties must be determined with special care, otherwise small errors in the measured properties may cause substantial errors in the final result of temperature tracking. Therefore, to confirm the validity of ITO's measured property, we performed the validation test for which the similar experimental setup shown in Kim et al. [47] was utilized which is presented in Figure III-7. During this test, the same heater wall design shown in Figure III-2 was used, and the ITO temperature was observed from both sides simultaneously using gold-coated mirrors which are highly reflective of IR radiation ($\rho_{gold}\approx 0.95$). That is, the ITO temperature was directly measured from the ITO side while the temperature was also measured through the semi-transparent media. Due to the thinness of the ITO film, the ITO temperatures measured from both sides are expected to be same if the optical properties of the materials used and the governing equation are correct. Since the measured properties of soda-lime glass and sapphire window were verified in Section D, we only focus on the properties of the ITO. To obtain the boundary condition at the outer surface of the sapphire window, which is required for ITO temperature tracking through the semi-transparent media, a material with high emissivity such as black lacquer or graphite paint (Ted Pella, Inc.) was applied as shown in Figure III-7. The measured emissivities of the black lacquer and the graphite paint were 0.976 and 0.75, respectively.

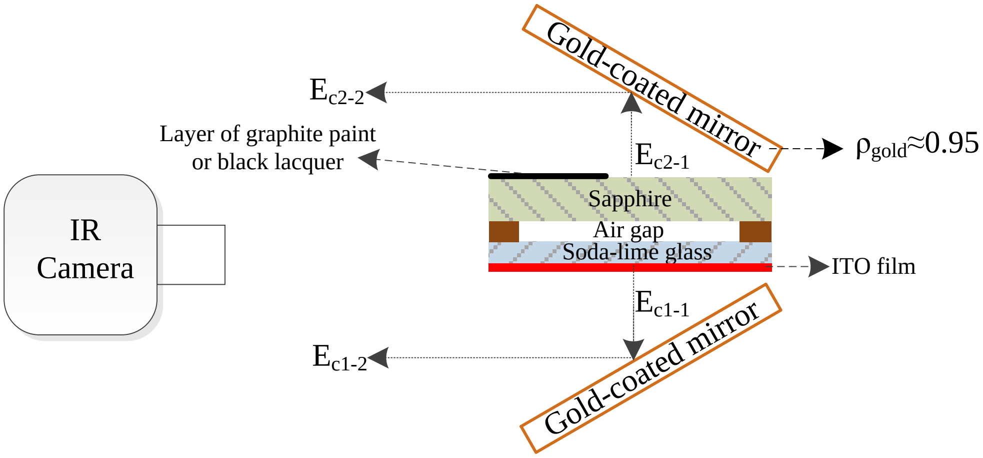

Figure III-7. Experimental setup to validate the ITO film's optical properties

The radiation balance equations used to measure the ITO temperature from the ITO side or through the semi-transparent media using the experimental setup shown in Figure III-7 can be written as follows:

(i) from the ITO side:

$$E_{c1-1} = \rho_{ITO} E_{\infty} + (1 - \rho_{ITO}) E_{ITO} \tag{III-13}$$

$$E_{c1-2} = \rho_{gold} E_{c1-1} + (1 - \rho_{gold}) E_{gold} \qquad \text{(III-14)}$$

(ii) through the semi-transparent media:

$$E_{c2-1} = \rho^{*}_{\infty-gold} E_{\infty} + \varepsilon^{*}_{sap-gold} E_{sap} + \varepsilon^{*}_{g-gold} E_{g} + \tau^{*}_{ITO-gold} E_{ITO} \qquad \text{(III-15)}$$

$$E_{c2-2} = \rho_{gold} E_{c2-1} + (1 - \rho_{gold}) E_{gold} \qquad \text{(III-16)}$$

where E_{c1-1} and E_{c2-1} represent the total radiation reaching the gold-coated mirrors from the ITO side and through the semi-transparent media, respectively; E_{c1-2} and E_{c2-2} are the total radiation measured by the IR camera from each side after being reflected by the gold-coated mirrors (see Figure III-7). ρ_{gold} is the reflectivity of the gold-coated mirror, and E_{gold} is the energy emitted by the gold-coated mirror ($=\sigma F_{3\text{-}5\mu m}(T) T_{gold}^4$). The coefficients used in Eq. (III-15) are derived in the same way as those in Eq. (III-1), described in Appendix A.3.

The validation process of the ITO properties is as follows: First, the ITO temperature was observed from both sides for various temperatures of ITO film within a range of 30–85 °C, which was controlled using electrical Joule heating. The measurements at different ITO temperatures were performed under steady-state conditions. By comparing the tracked temperatures from the two sides, the ITO properties (i.e., ρ_{ITO}, $\varepsilon_{ITO}=1-\rho_{ITO}$) shown in Table III-1 were slightly adjusted so that we could find the optimum properties to ensure the best performance of the present temperature-tracking. As a result, the optimum ρ_{ITO} was determined as 0.84, which was a little larger than the nominal value obtained from the optical property measurement

(0.82) discussed in Section D (see Table III-1). Accordingly, the ε_{ITO} was adjusted based on the relation $\varepsilon_{ITO} = 1-\rho_{ITO}$. Then, applying these ITO properties, the ITO temperature measurements under steady-state conditions were performed again, and the temperatures obtained from the two sides were compared, the results of which are shown in Figure III-8 (left side). The maximum difference was found to be 1.1 °C, which occurred when the ITO temperature was near 30 °C, the lowest temperature measured in this test. Note that, due to the low emissivity of ITO, the direct temperature measurement from the ITO side may have substantial uncertainty, especially at low ITO temperatures. For instance, small fluctuations in the ambient temperature may considerably affect the temperature tracking results from the ITO side because the surrounding conditions play a dominant role at lower ITO temperatures [see Eq. (III-13)]. Thus, to reduce measurement uncertainty caused by the ITO properties, a thin graphite paint of higher emissivity (ε=0.75) was applied to the ITO side. After that, the temperature measurement was performed again as described above. Due to the thinness of the layer of graphite paint, it was expected that the surface temperature of the graphite paint would be almost same as that of the ITO. In Figure III-8 (right side), the temperatures measured from both sides are compared. We can see that the largest difference still occurred at the lowest ITO temperature, near 30 °C, but the maximum discrepancy was reduced to 0.6 °C. These experimental findings indicate that the ITO properties determined here (i.e., ρ_{ITO}=0.84, ε_{ITO}=0.16) are sufficiently accurate to be used for the wall temperature tracking in the present study.

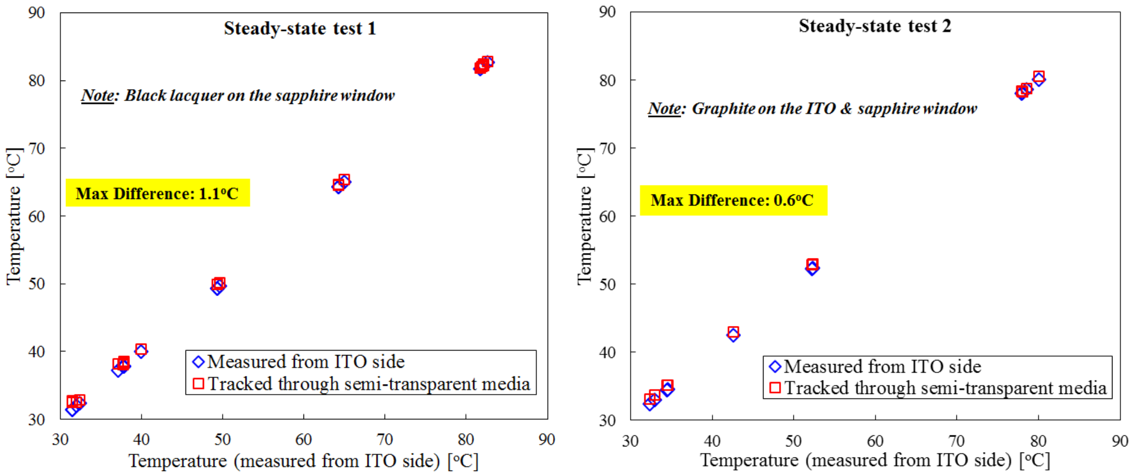

Figure III-8. Validation of temperature-tracking algorithm under steady-state conditions

2. Transient test

The performance of wall temperature tracking algorithm were also tested under transient conditions of the wall (i.e., ITO film) temperature. For the test, virtually the same experimental setup as that used for the steady-state test (Section E.1) was used, but an air cooling device was added to induce abrupt temperature change on the heater surface as shown in Figure III-9. The time-dependent variation of the heater surface temperature was investigated using the IR camera (recording speed: 30 Hz) directly from the ITO side as well as through the semi-transparent media, and the temperatures measured from both sides were compared. As discussed in Section E.1, since the surface temperature directly measured from the ITO side may have considerable uncertainty due to the effect of the ambient temperature, the ITO surface was covered with a thin layer of high-emissive material during the test.

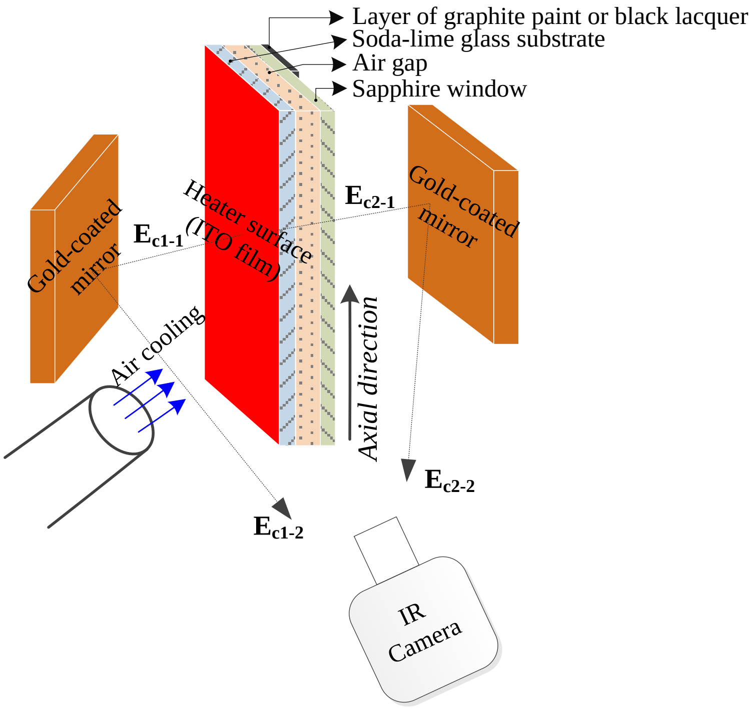

Figure III-9. Experimental setup for transient test with cold air injection

The variation of the ITO temperature measured from the two sides was first compared at the local position. Initially, the ITO film was electrically heated, and the surface temperature was kept constant (i.e., steady state) at a certain temperature. Then, cold air was abruptly injected to induce temperature drop on the ITO film. Figure III-10 shows the time-dependent variation of the ITO temperature measured from both sides. For the four different tests, which were performed separately, the wall temperatures obtained from the two sides agreed well, implying that temperature tracking through the semi-transparent media was successfully performed. The maximum difference between the direct ITO surface temperature measurement and the temperature measured through the semi-transparent media was 0.5 °C for the all test cases.

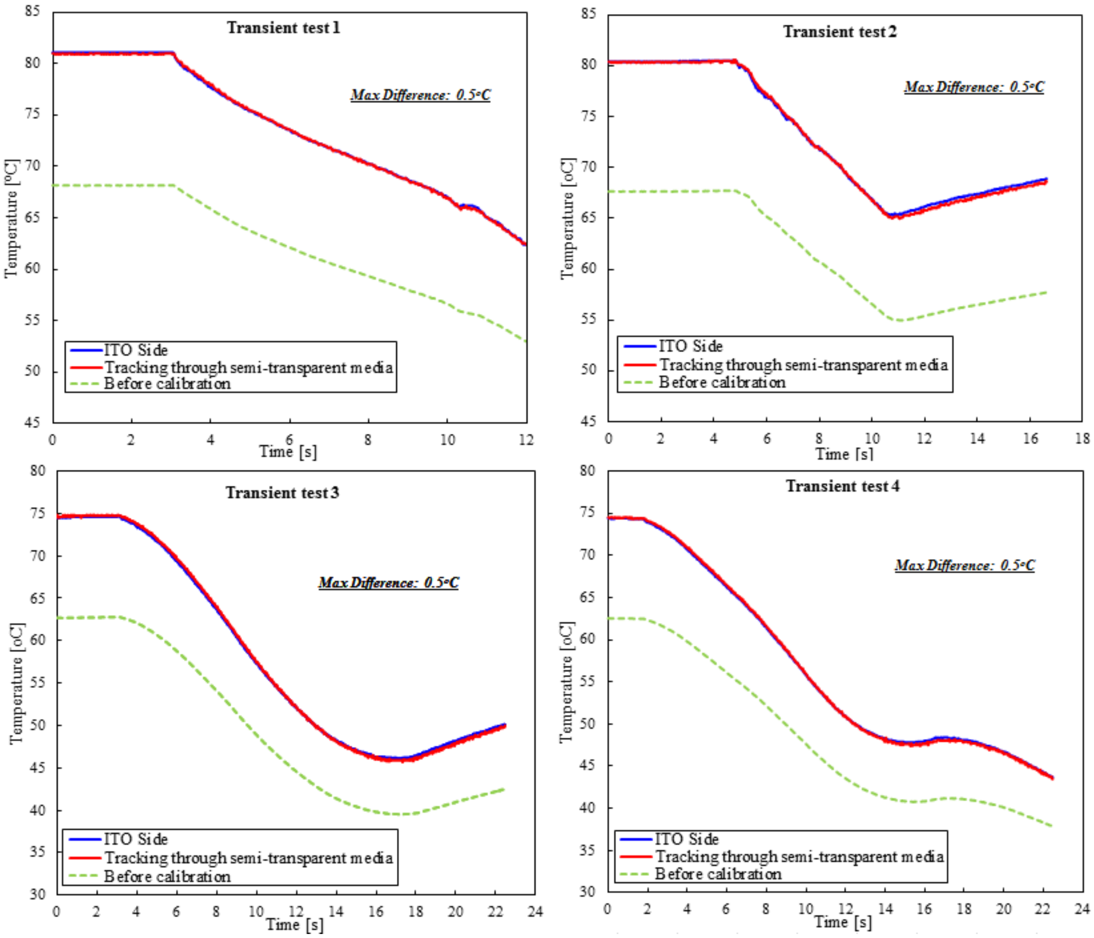

Figure III-10. Validation test under transient condition

Note that the above-mentioned wall temperature tracking was performed by coupling the 1D heat conduction equation with the Eq. (III-1). If the thickness of the glass substrate is thin and the temperature gradient through the glass thickness is much larger than in the other directions, 1D heat conduction can be assumed safely. However, if a significant temperature gradient occurs in other directions due to reasons such as the local boiling phenomenon, the multi-dimensional (multi-D) effect may increase, which can subsequently affect the performance of the present temperature tracking. Therefore, to better understand the multi-D heat conduction effect throughout the media in the present heater wall design, an additional test was performed. Specifically, starting from a steady-state ITO temperature condition, cold air was injected at the bottom of the ITO film to induce a significant temperature gradient on the wall in the axial direction. Then, the time-dependent variation of the spatial temperature profile was obtained by the IR camera from the two sides (i.e., directly from the ITO side and through the semi-transparent media). In Figure III-11, the axial centerline temperature profiles on the ITO film (total axial length L_0=3 cm) measured from the two sides are compared at several time instances after the injection of cold air. Then, we can see the tracked temperature through the semi-transparent media still agreed well with the temperature directly measured from the ITO side. This means that the multi-D effect of heat conduction was insignificant despite the large temperature gradient in the axial direction and hardly affected the performance of the present wall temperature tracking during this test.

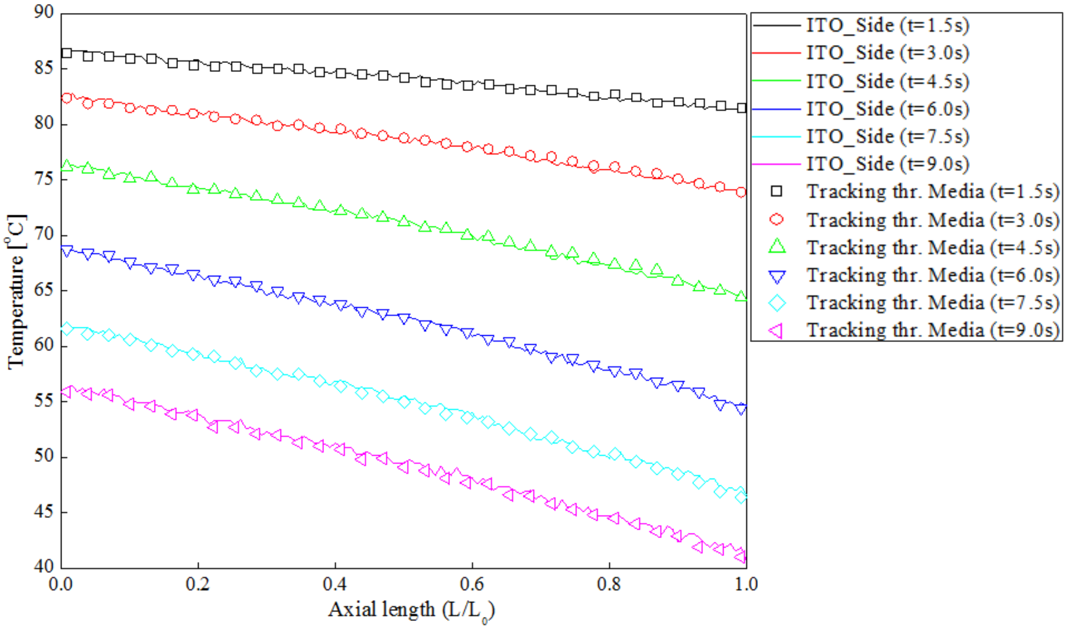

Figure III-11. Axial centerline temperature profile variation after the cold air injection (L_0=3 cm)

To further confirm the effect of multi-D heat conduction, we compared the axial temperature profiles obtained from the 1D and 2D heat conduction coupling algorithms. In Figure III-12, the axial temperature profile at different time instances (i.e., t=1.52 s and t=9.12 s) after the air injection (t=0) is shown. For the 2D heat conduction coupling algorithm, heat conduction along the axial direction was additionally considered. On the top and bottom boundaries (i.e., at L=0 and L_0), the 1D heat conduction algorithm was used to provide the boundary conditions required for the 2D heat conduction simulation. Figure III-12 shows that the wall temperature profiles obtained from the 1D and 2D heat conduction coupling algorithm are almost same, meaning that the multi-D effect of heat conduction did not play a critical role in the wall temperature tracking during this test.

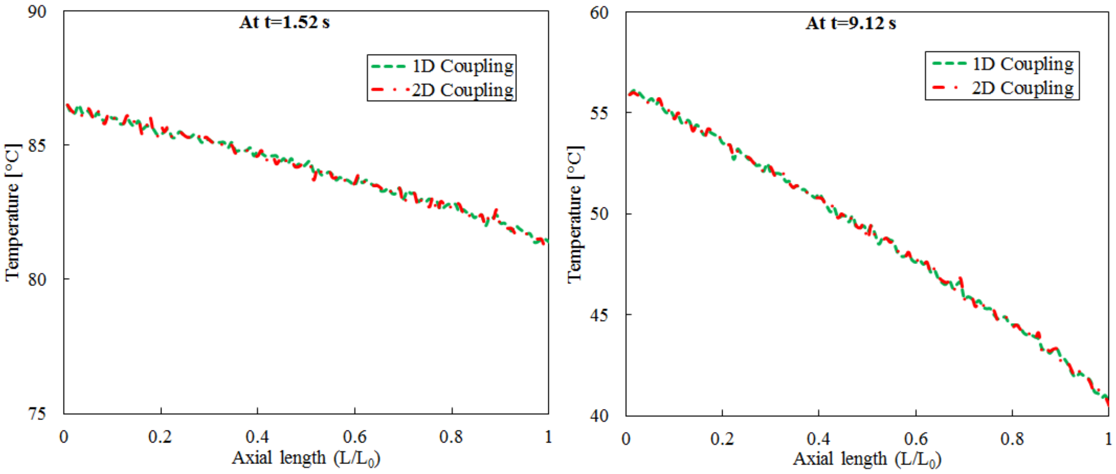

Figure III-12. Variation of axial wall temperature profiles based on coupling the 1D and 2D heat conduction equations

3. Heat flux measurement

Subsequent to all the validations for accurate wall temperature tracking described above, we conducted additional tests to confirm the performance of present algorithm for the heat flux measurement as well. Since the present algorithm provides the temperature profile across the multi-layer media as well as the heater surface temperature (see Figure A-6), the amount of heat entering the fluid during the single-phase convection and/or boiling process can also be obtained using this algorithm by considering the heat balance at the wall. In Figure III-13, the heat balance relation at the wall (i.e., heater surface) is presented which can be derived by neglecting the temperature gradient across the small thickness of ITO film. This relation implies that the amount of heat entering the fluid (q_{in}) can be determined by estimating the heat conduction through the glass thickness (q_{cond}), the heat retained within the ITO film during the transient process, and the total power provided by the power supply (q_{gen}). Obviously, the best way to confirm the validity of such estimation is to compare the results with the separate measurements of q_{in}. In this sense, we performed the heat loss test using the square test section described in Section B which was installed in the vertical upward flow boiling test loop (the specific loop configuration is described in Section F). This test was carried out while there was no fluid inside the loop and by keeping track of the heat input needed to maintain a given wall temperature at steady state which was monitored by IR camera. Then, the steady state temperatures achieved at various heat inputs were recorded after which the relation between the heat input and the average wall temperature over the heated area was obtained. Assuming that the heat removal due to the natural convection of air was negligible during this test, such relation can be used to estimate the average heat loss through the multi-layer heater wall for the actual flow boiling experiment. Therefore, using this relation, we could obtain the average heat flux entering the fluid (q_{in}) at various flow boiling conditions within the heat flux range 9~37 kW/m^2 given by power supply (i.e., Measurement 1 in Figure III-14). Then, the results are compared with the time-averaged heat fluxes calculated by the present algorithm in which the time-dependent heat storage within the thin ITO film was ignored. This is shown in Figure III-14 which indicates that the maximum difference between the two separate measurements for the q_{in} was found to be 1.9 %. This implies that the present algorithm keeps the validity for the heat flux measurement as well.

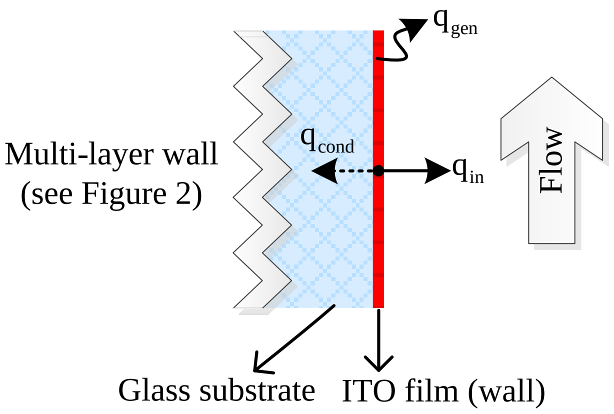

Heat balance relation: $$q_{in} = q_{gen} - q_{cond} - (\rho c_p)_w \delta_w \frac{\partial T_w}{\partial t}$$

Figure III-13. Heat balance relation at the wall to obtain the local heat input to the fluid q_{in}

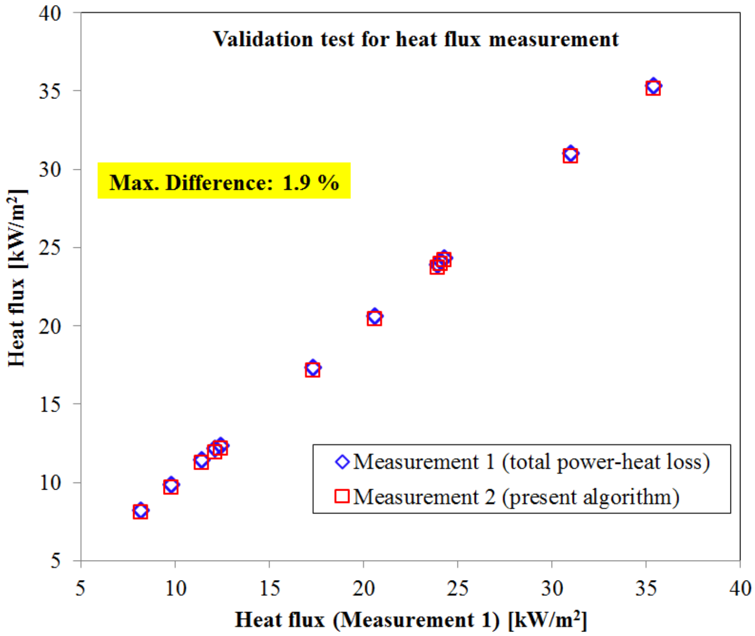

Figure III-14. Validation of heat flux measurement using the present algorithm

F. Application in a subcooled flow boiling experiment

Based on the experimental strategy and validations described above, a subcooled flow experiment was performed. The test loop was configured for a working fluid to be pumped upward through the test section of square geometry (see Figure III-2) at atmospheric pressure. The temperature of the working fluid to the test section was controlled through a small plate heat exchanger, and the flow rate was adjusted using a control valve placed downstream of a constant speed centrifugal pump. The refrigerant 3M™ Novec™ 7000 was used as a working fluid of which boiling point is 34 °C at atmospheric pressure. Also, an entry length (L) of $L/D \approx 61$ was used before the test section inlet so that a hydro-dynamically fully developed flow could be achieved in the measurement section. For this test, only a single nucleation site was created in order to allow a clear view of how such a boiling phenomenon fundamentally affects the heat transfer characteristics on the wall in relation to the vapor bubble motions. In addition, the IR camera was intended to capture the entire heated area to observe the wall heat transfer over the single-phase and two-phase flow regions, as shown in Figure III-15. The spatial and temporal resolutions of the thermal images from IR camera were 274 μm and 300 Hz, respectively.

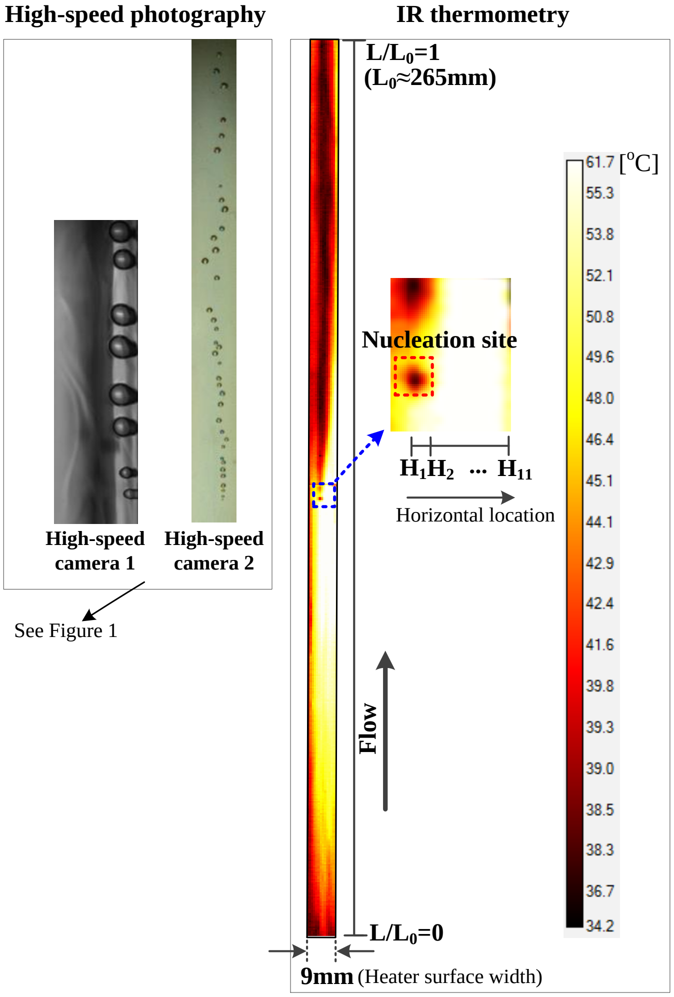

Figure III-15. Visual measurement of vapor bubbles and 2D wall temperature map (before calibration) in the vertical upward test section

Representative images captured by high-speed video camera and the 2D wall temperature map from IR thermometry are shown in Figure III-15, which were obtained at a test condition of inlet liquid temperature=20 °C, heat flux=13.9 kW/m^2, and liquid mass flux=216.3 kg/m^{2}s. In Figure III-16, the time-averaged centerline wall temperature in the axial direction is shown. We can see that the cooling performance at the heater surface changed drastically due to the appearance of the nucleation site located at $L/L_0 \approx$

0.5. As expected, the wall temperature profile increased almost linearly through the single-phase flow region, but the wall temperature dropped abruptly after the nucleation site because the nucleating and sliding bubbles enhanced the heat removal through evaporation. In particular, at the initial stage of bubble growth, the bubbles grew very fast, inducing a sharp wall temperature drop near the nucleation site. Another important mechanism for this cooling performance is thought to be the agitated liquid flow motion induced by the boiling bubbles. However, once the bubble grew up to a certain size at which the heat transfer between the liquid and vapor phases became more balanced ($L/L_0 \geq 0.6$), the wall temperature gradient in axial direction significantly reduced. Figure III-17 shows the horizontal temperature profile of the wall (from H_1 to H_{11}) at different axial locations (from $L/L_0=0.1$ to $L/L_0=1$). The nucleation site appeared near the left edge of the heater surface (H_1) just below the middle of the test section in the axial direction ($L/L_0 \approx 0.5$, see Figure III-13). In Figure III-17, the horizontal temperature profiles at the axial locations upstream and downstream of the nucleation site is drawn with the 'non-filled' and 'filled' symbols, respectively. The abrupt temperature drop on the wall where the nucleation site appeared (i.e., H_1 at $L/L_0=0.5$) is clear and the nucleation caused the large temperature gradient in the horizontal direction at that axial location. Interestingly, this temperature gradient in the horizontal direction diminished rapidly downstream of the nucleation site (i.e., $L/L_0 \geq 0.6$). This can be explained by the observation of vapor bubble motions obtained from the high-speed video cameras. In particular, viewed from the top of the vapor bubbles (i.e., from high-speed camera 2 in Figure III-15),we could clearly see that the horizontal waving motions of the bubbles were enhanced as the bubbles slid upward; whereas, such waving motions were not found near the nucleation site. Consequently, the heat removal due to the sliding bubbles occurred over a wider region at upper locations due to the bubbles' wider trajectory. For this reason, the wall temperature profile became flatter downstream of the nucleation site in Figure III-17.

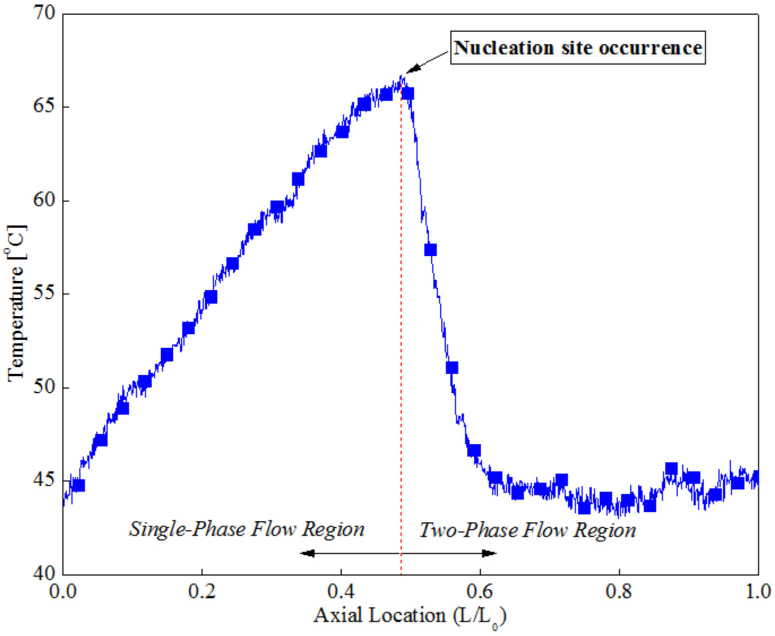

Figure III-16. Axial distribution of wall temperature at the centerline

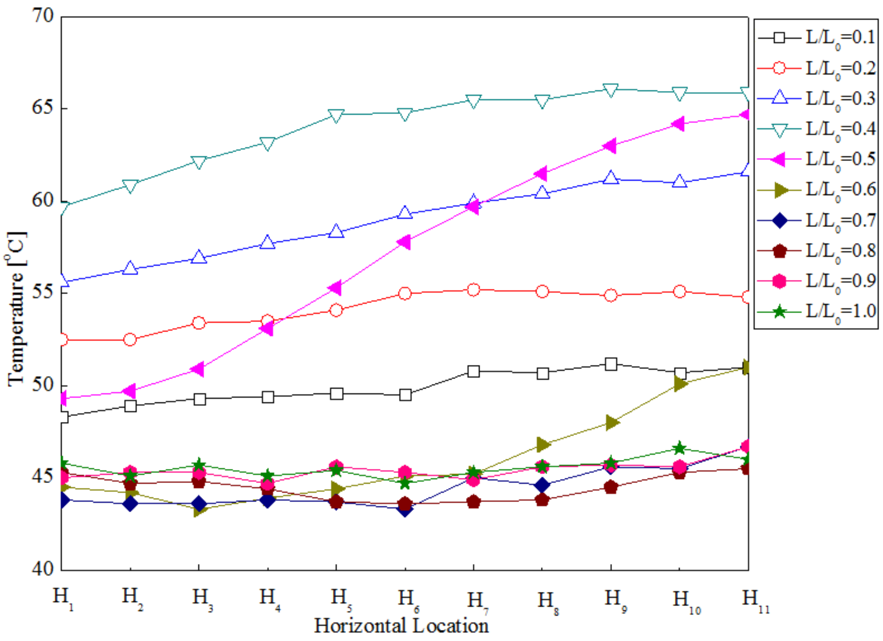

Figure III-17. Horizontal wall temperature profiles at different axial locations (non-filled symbols: axial locations upstream of the nucleation site; filled symbols: axial locations downstream of the nucleation site)

G. Uncertainty quantification

The uncertainty of the present temperature tracking depends on the uncertainties associated with the uncertainty of individual parameters used for the tracking, e.g., optical properties, thermal properties, and ambient temperature. The major sources of uncertainty considered are listed in Table III-2. These parameters were determined by investigating each parameter’s sensitivity in the present temperature tracking method. That is, only parameters of primary significance were selected. The ITO film’s optical properties were not considered here because they were obtained in a deterministic way through the validation process (see Section E.1). We found that the amount of uncertainty due to the ambient temperature (≈0.34 °C) hardly affected the temperature tracking result when the wall temperature tracking is performed using the proposed heater wall design. Thus, the ambient effect is not included in Table III-2. However, it is noted that this should not be the case for the direct temperature measurement of ITO surface due to the low emissivity of ITO. For the uncertainty of air's thermal conductivity, possible variations in the air temperature between 20–80 °C were considered.

Table III- 2. Major sources of uncertainty for the wall temperature tracking

Parameter	Nominal Value	Uncertainty
Apparent transmissivity of glass ($\tau_{app,g-\infty}$) Apparent reflectivity of glass ($\rho_{app,g-\infty}$) Apparent transmissivity of sapphire ($\tau_{app,sap-\infty}$) Apparent reflectivity of sapphire ($\rho_{app,sap-\infty}$)	See Table III-1.	
Thermal conductivity of glass (W/m-K)	0.94	0.01
Thermal conductivity of air (W/m-K)	0.026	0.004

After determining the uncertainty parameters, their uncertainty values, and the sensitivity in the present temperature tracking method, the overall uncertainty was calculated by combining the individual parameters' uncertainties using the following equation [25]:

$$U_T = \sqrt{\sum_{i=1}^{M} \left(\frac{\partial T}{\partial V_i} U_{V_i}\right)^2} \qquad \text{(III-17)}$$

where U_T is the uncertainty of the present temperature measurement, V_i is the i^th^ uncertainty parameter considered, M is the total number of uncertainty parameters considered, and $\partial T/\partial V_i$ and U_{V_i} are the sensitivity coefficient and uncertainty for V_i, respectively. The uncertainty associated with the heater surface temperature measurement using the present heater wall design was then estimated as 0.7 °C. Using the similar way, the uncertainty of heat flux measurement was estimated as 0.6 kW/m^2.

H. Conclusions

An experimental strategy to achieve both enhanced flow visualization and accurate wall temperature/heat flux measurement in a convective boiling system has been described. High-speed photography and IR thermometry were employed as experimental techniques, and the feasibility of applying both techniques to a forced convective boiling experiment which involves a large heated area was successfully demonstrated with extensive validations.

We expect that the present approach will help to achieve more useful insight into the boiling heat transfer mechanism, e.g., the effects of vapor bubbles on the heat transfer as they develop throughout the heated flow channel. In particular, the enhanced reliability of measurements using optical techniques would help to uncover the detailed relation between the bubble dynamics and the wall heat transfer. Also, it is expected that the flow visualization techniques such as particle image velocimetry (PIV) can be applied in the current experimental facility, which will allow the additional information about the liquid phase.

CHAPTER IV

EXPERIMENTAL OBSERVATION ON BUBBLE DYNAMICS AND WALL HEAT TRANSFER ARISING FROM A SINGLE NUCLEATION SITE – PART 1: EXPERIMENTAL STRATEGY AND MICROSCOPIC OBSERVATION OF BUBBLE BEHAVIORS

A. Introduction

Forced convective boiling has been extensively studied both theoretically and experimentally over the past decades because of its practical importance in safety, reliability, and performance of many engineering applications such as nuclear reactors and electronic devices. Consequently, many empirical correlations and/or mechanistic models have been proposed; these have been widely utilized in CFD simulations of two-phase flow boiling systems [52-56]. However, the ability to predict the complex thermal-hydraulic processes in boiling systems using CFD with such constitutive models/correlations still remains unsatisfactory. One of the key issues here is that the level of confidence of CFD analysis employing multi-fluid approach strongly relies on the validity of constituent closure models. Therefore, to overcome the current situation, the limitations of existing closure models should be clearly understood and improved based on the correct physical understanding of the complex processes associated with boiling. To this end, reliable experimental data that can be used for model validation and development are of critical importance. However, producing such high-quality data from any boiling experiment is not a simple task, and this difficulty is one of the major reasons why we can often find substantial scattering and/or inconsistency of the measured fundamental bubble parameters such as departure/lift-off bubble size and bubble frequency in the literature [7-9, 11]. The major issues and/or difficulties affecting measurement accuracy in boiling experiments can be described as follows:

(1) The difficulty of measuring and characterizing boiling process at a given condition originates from the chaotic nature of the phenomenon. That is, the experimental results of boiling parameters such as bubble size and frequency can be considerably affected even by small changes of the test boundary conditions. Also, boiling can often be initiated unexpectedly due to the small perturbations such as the random deposition of small impurities on the heater surface; and such incipience of boiling often significantly affects the overall heat transfer characteristics of the system while increasing its phenomenological complexity.

(2) Another issue results from the inherently stochastic (or random) nature of the measured boiling parameters. For instance, the vapor bubble size and frequency measurements under given boiling conditions are always presented as a distribution rather than a single deterministic value. This implies that such distributions are important for the description of boiling phenomena and should be well-characterized through experimental evidence in addition to the statistical average of the measured parameters. Also, the stochastic nature of boiling parameters usually requires the analysis of a large number of samples in order to correctly represent the boiling characteristics for a given test condition.

(3) As revealed in Chapter II or [57], due to the local, fast, and random nature of the wall nucleation process, the measurement view of bubbles and/or camera resolution can cause significant mis-measurement and lead to inaccurate experimental results of boiling parameters.

(4) Finally, gaining complete insight into the boiling heat transfer mechanism based on the limited number of parameters measured in a single experiment is always challenging because the boiling process generally accompanies a variety of thermal-hydraulic sub-processes which are strongly coupled to one another.

To the best of our knowledge, despite the extensive experimental works reported in literature, especially for forced convective boiling [3, 11, 58-61], few works are free of those issues mentioned above. This is often due to the limits of available experimental techniques and/or the significance of addressing such issues for experimental observation has yet to be well recognized within the community. Of course, our understanding of the boiling mechanism has progressed substantially due to such previous experimental efforts; and a number of empirical correlations [62, 63] and mechanistic models [3, 4, 55] have been developed and validated based on them. However, in order to fill the gap that is still debatable regarding the convective boiling heat transfer mechanism and its modeling, a more precise experimental approach is required. In particular, the effort to overcome the shortcomings existing in earlier experimental works related to the measurement issues described in the list above can be a good start to reach the goal more efficiently.

In this context, we devised a subcooled flow boiling experiment in a square, vertical, upward flow channel. The main objective is to improve the fundamental insight into the subcooled flow boiling process through the intensive and extensive observation of thermal-hydraulic parameters with a multi-scale observation approach. For this, high-speed photography and infrared (IR) thermometry were simultaneously employed based on the experimental method established in Chapter III or [64]. Using this method, we could capture both bubble behaviors and wall heat transfer features with high fidelity in a single flow boiling facility. In particular, we made a special effort to better investigate the characteristic features of the thermal-hydraulic process occurring in the subcooled flow boiling channel by addressing the anticipated issues of boiling measurement as follows:

First, to avoid the phenomenological complexity caused by the random presence of nucleation sites, the heater was designed to keep a single active nucleation site within the entire heated area during the present experiments.

Second, to improve the reliability of experimental results, a large number of images were taken and analyzed for each test condition; and the discussion of the experimental results was made after properly characterizing the measured parameters over the whole measurement period of each experimental case rather than discussing them after taking a few samples at a selected moment. The number of images (or amount of data) used to characterize the bubble behaviors was usually much larger than those used in the statistical analysis of bubble characteristics reported in literature [3, 6, 65].

Third, to investigate the various aspects of bubble behaviors within the test channel, the bubble behaviors were recorded using the three high-speed cameras of different resolutions (i.e., multi-scale observation) simultaneously.

Fourth, to gain deeper insight into the complex flow boiling phenomena, various parameters such as bubble size, axial bubble velocity, bubble release frequency, bubble size distribution, and local heat transfer coefficients were investigated together, and the relevant relations among them were studied.

Lastly, the measurement parameters of interest were observed within the relatively large area of the flow path rather than at the local position, enabling investigation of the axial development of such parameters.

This chapter is the first in a series of describing our work with the present subcooled flow boiling experiment. In this chapter, we focus on discussing the specific experimental strategy, measurement procedures, and the reliability of current measurement for the boiling parameters of interest. In addition, we address the various aspects of bubble behaviors near the nucleation site which were investigated in both qualitative and quantitative manners based on the high-resolution measurements of the bubbles using high-speed camera. In particular, the parametric effects of inlet subcooling, liquid mass flux, and wall heat flux on the bubble behaviors originating from the single nucleation site were discussed along with the underlying mechanisms of such behaviors.

B. Experimental facility

1. Flow boiling loop and instruments

The flow boiling loop was designed to perform the subcooled flow boiling experiment in a vertical square test section at atmospheric pressure. The refrigerant 3M^{TM} Novec^{TM} 7000 was employed as the working fluid (boiling point: 34 °C at 1 atm). The main components of the flow boiling loop included a centrifugal pump, control valves, a heat exchanger, a transparent vertical test section, and a degassing tank. The working fluid was circulated through the loop by the centrifugal pump which delivers a constant volumetric flow; the flow rate was manually controlled during the experiments by means of a control valve installed downstream of the pump and upstream of the vertical test section. The heat exchanger was used to control the temperature of the fluid entering the test section. Subsequent to the vertical test section, the degassing tank was installed at the highest position of the loop in order to keep the system at atmospheric pressure and to separate the vapors. Also, to ensure a hydro-dynamically fully developed flow within the test section, current loop was designed such that the fluid passes through the vertical channel with a length of $l/D_h \approx 61$ before the fluid enters the test section (l is the channel length preceding the test section and D_h is the hydraulic diameter of the channel).

The test section was vertically aligned and its flow area had a square geometry of 10×10 mm^2. The walls of the test section were made of transparent acrylic on three sides with the transparent heater wall serving as the fourth side. The heater wall consisted of multiple layers with a thin layer of conductive indium-tin-oxide (ITO) film as the heating element on the inner surface touching the fluid. This design of test section allowed us to observe the bubble motions simultaneously from different directions as shown by the camera positions in Figure IV-1. More details of the multi-layer heater wall design as well as the experimental strategy are discussed in Section B.2. The total height of test section was 305 mm, and the heated length L_0 was 224 mm (see Figure IV-1). The remaining part of the heater surface was painted with conductive silver paint (Ted Pella, Inc.) on both ends. These ends of heater wall were subsequently connected to the DC power supply (XHR 600V, AMETEK®) to provide the Joule heating through the ITO film during the experiments. Also, in order to prevent unexpected boiling caused by the trapped fluid at the joint of the walls, the heater surface width was designed to be narrower (i.e., 7.5 mm) than the square channel width of 10 mm.

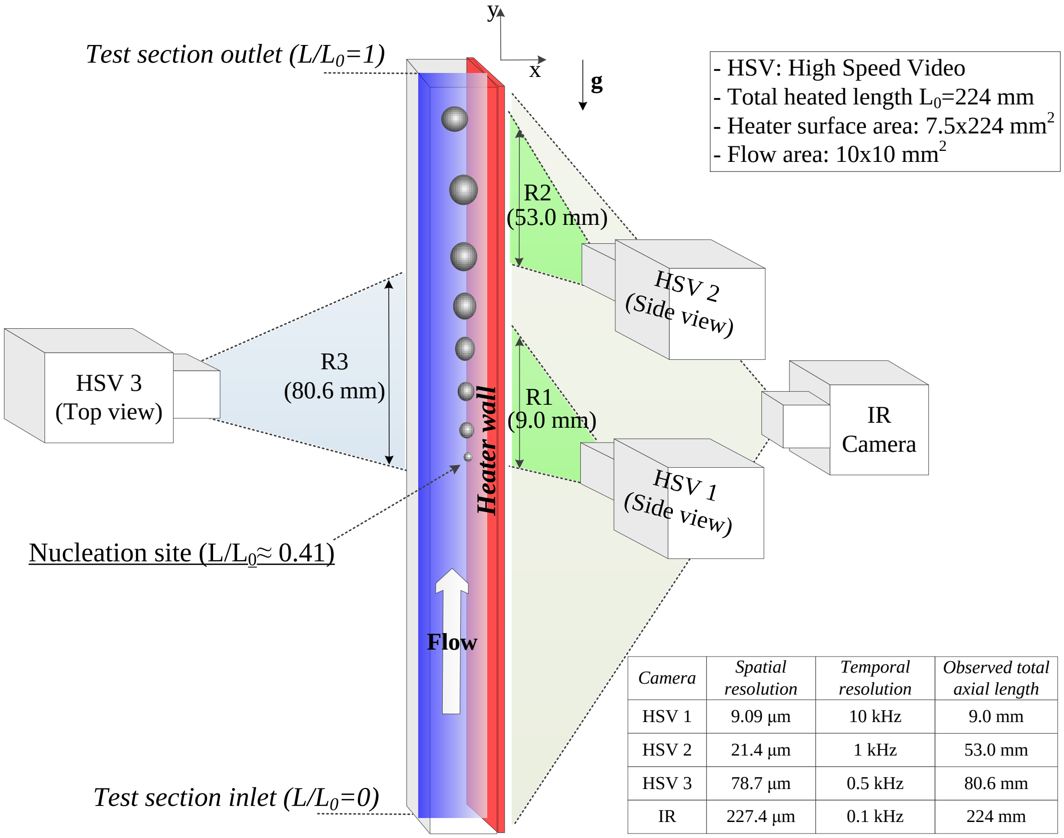

Camera	*Spatial resolution*	*Temporal resolution*	*Observed total axial length*
HSV 1	9.09 µm	10 kHz	9.0 mm
HSV 2	21.4 µm	1 kHz	53.0 mm
HSV 3	78.7 µm	0.5 kHz	80.6 mm
IR	227.4 µm	0.1 kHz	224 mm

Figure IV-1. High-speed visualization of vapor bubbles and heater surface temperature measurement in the subcooled flow boiling experiment

Prior to experiments, the loop was degassed by heating the fluid to the saturation temperature (=34 °C) and continuously circulating through the loop for several hours. During the experiments, the liquid flow rate was measured using a Coriolis flow meter (Micro Motion® Elite®). The fluid temperatures at the inlet and outlet of the test section were measured with T-type thermocouples (OMEGA® HYP-0 mini-hypodermic probe). Also, the ambient temperature around the test section was measured using a K-type thermocouple (OMEGA HSTC series). The measurement of the ambient temperature was subsequently used to estimate the actual heater surface temperature using IR thermometry (see Chapter III or [64]). These data obtained by each instrument were recorded (24,000 samples in 4 minutes for each test case) by the data acquisition system (National Instrument Inc.), and the average values were taken to represent the test boundary conditions in this study (Section B.5).

2. Experimental strategy and procedures

An experimental approach for both enhanced two-phase flow visualization and accurate wall temperature measurement described in Chapter III or [64] was employed and extended for the present study. Specifically, as shown in Figure IV-1, three high-speed cameras were arranged around the transparent test section for the micro- and macroscopic observation of bubble motions. High-speed video camera (HSV) 1 was to capture the boiling motions near the nucleation site from the side of bubbles (side view) at an angle of 25~30° above the heater with a resolution of 10 kHz, 9.09 μm. The bubble motions downstream (i.e., far from the nucleation site) were observed using HSV 2 from the same direction with HSV 1 (i.e., side view). HSV 3 was employed to observe the bubble motions from the top of bubbles (i.e., top view, with the heater wall defined as the bottom), which provided a different perspective than the other two cameras over a larger area. All of the three high-speed cameras and the IR camera were set up to be triggered at the same time via a BNC cable. The resolution of each camera and the total axial length observed are described in Figure IV-1. In Figure IV-2, representative bubble images taken from the three HSVs using the present approach are shown. In Figures IV-1 and IV-2, L denotes the relative axial position within L_0 (i.e., $0 \leq L \leq L_0$); the definition

L/L_0 is consistently used for all analyses presented in Chapters IV and V to represent the axial location of the bubbles.

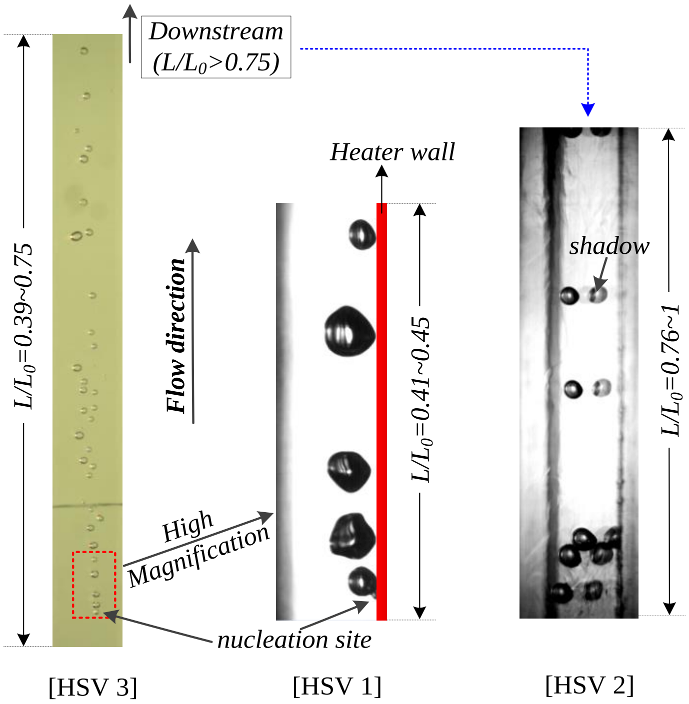

Figure IV-2. Representative bubble images taken from the three high-speed cameras

In Figure IV-1 we can see that an IR camera was also employed in the present experiment, which was to measure the heater surface temperature while capturing the bubble motions. Specifically, the IR camera detected the temperature over the entire heated area (7.5×224 mm^2) so that the varying characteristics of wall heat transfer between the single-phase and the boiling-affected regions can be clearly observed. Figure IV-3 illustrates the multi-layer heater wall design as well as the heater surface temperature measurement using IR thermometry in the present study. The detailed algorithm for measuring the accurate ITO film temperature through the multi-layer wall and the required experimental validations are described in Chapter II or [57]. In the present study an additional layer of the polyimide tape was attached to the ITO film as shown in Figure IV-3; the specific purpose of using this tape is described below in this section. Since the ITO is opaque to the IR spectral range of our interest (i.e., 3–5 μm), any IR signal originating from the inner surface of the polyimide film touching the fluid should not to reach the IR camera. In addition, despite the thinness of the polyimide tape (25 μm thick), the temperature difference between the ITO film and the inner surface of polyimide tape touching the fluid cannot be simply disregarded, especially in the high heat flux condition because the thermal conductivity of the elements composing the tape is low (i.e., polyimide film: 0.12 W/m-K; silicone adhesive: 0.2 W/m-K). Accordingly, we estimated the inner surface temperature of the polyimide film using the solution of steady-state heat conduction equation (1D) based on the time-averaged ITO surface temperature and local heat flux obtained by the algorithm described in Chapter III or [64]. Then, this inner surface temperature (i.e., heater surface temperature) was used to determine the local heat transfer coefficient and the Jacob number (Ja) presented in this study.

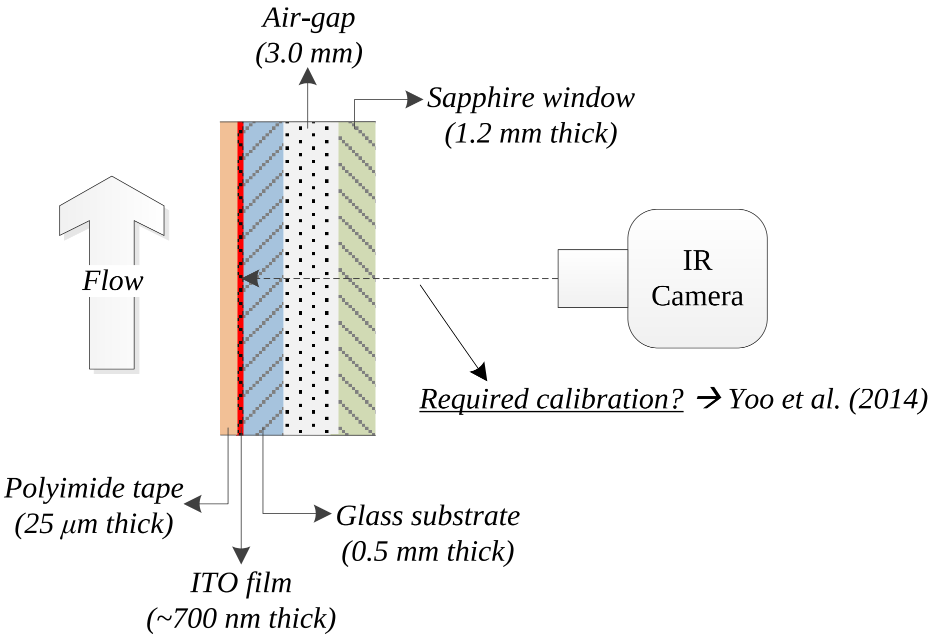

Figure IV-3. Multi-layer design of heater wall and the heater surface temperature measurement using IR thermometry

It is important to mention that we controlled the number of nucleation sites (1) and its location during this study by creating a preferential single nucleation site at the specified axial location, i.e., $L/L_0 \approx 0.41$. For this purpose, a thin polyimide tape with a silicone adhesive (CAPLINQ Crop.) with a total thickness of 26 μm (polyimide film: 13 μm, silicone adhesive: 13 μm) was attached on the ITO-coated glass surface (see Figure IV-2), and a small cavity was created on top of the polyimide film using a sharp needle. The surface of the polyimide film attached was generally smooth except for the cavity region; the surface roughness was estimated to be about 3 nm as measured by Atomic Force Microscopy. After the degassing process, to activate the nucleation on the single artificial cavity, sufficient power was initially supplied to the heater surface under low liquid flow condition until boiling initiated at numerous sites including the intended one.

Due to the complete degassing of the fluid as well as the smooth heater surface condition, such inception of vigorous boiling normally required very high heater power. After activating numerous nucleation sites over the entire heater surface area, the heater power was decreased again until only the single nucleation site located on the artificial cavity remained activated. Then, while maintaining the single nucleation site, test conditions such as liquid mass flux and wall heat flux were adjusted until reaching the targeted test condition. This process was facilitated due to the preferential nucleation on the single artificial cavity compared to the other regions within the heated area. Thus, we always kept the single nucleation site in this manner at the same location, and the boiling behaviors originating from the same cavity were investigated under the various subcooled flow boiling conditions.

3. Data collection, image analysis, and repeatability test

Due to the strong stochastic nature of boiling, a sufficient number of experimental data is required to correctly characterize the complex features of subcooled boiling flow for a given test condition. That is, the amount of experimental data must be large enough to ensure reliable statistics of the measured parameters. In the present work, HSV 1 and HSV 3 took 36,000 and 40,000 consecutive images, respectively for each test case. The recording speed applied was 10 kHz for HSV 1 and 0.5 kHz for HSV 3. Thus, the measurement period for HSV 1 and HSV 3 was 3.6 s and 80 s, respectively. For analyzing the bubbles' behavior (e.g., bubble size, center of mass location), all the images acquired were first converted to binary images via image processing, and the processed images were analyzed automatically using the macro function of ImageJ [29]. The efficient image processing algorithm to address the numerous images of nucleating bubbles for the side view measurement such as HSV 1 is described in Chapter II or [57]. From HSV 2, about 12,000 consecutive images were taken at a recording speed of 1 kHz, which were primarily used to qualitatively describe the bubble motions downstream of the test section.

For the heater surface temperature and local heat flux measurement, a total of 2,000 2-D thermal images (1000×34 pixels) covering the entire heated area were recorded for each test case at a frame rate of 100 Hz using an IR camera. Then, the raw thermal data were processed by applying the calibration algorithm and using the steady-state heat conduction equation to obtain the accurate heater surface temperature and local heat flux values. However, only 1,700 out of 2,000 processed thermal data were used to estimate the thermal parameters because the calibration algorithm used in this study requires the initial decay time until it tracks the true value (see Chapter III or [64]).

In order to evaluate the reliability of statistical average obtained from the measured parameters based on the image (or data) acquisition method mentioned above, a repeatability test was conducted for one of the subcooled flow boiling test conditions employed in this study. The results are shown in Figure IV-4 which presents the axial variation of average bubble size observed by HSV 1 (left side) and HSV 3 (right side). The repeatability tests 1 and 2 were performed at different times under the identical test condition. Also, due to the difference in spatial/temporal resolutions applied by each camera, we can see that the level of detail that can be observed for the bubble growth behavior within the region $0.41<L/L_0<0.45$ is quite different between the two shown on the left and right side of Figure IV-4. At present, however, we focus more on the repeatability issue associated with the two different image acquisition methods of HSV 1 and HSV 3.

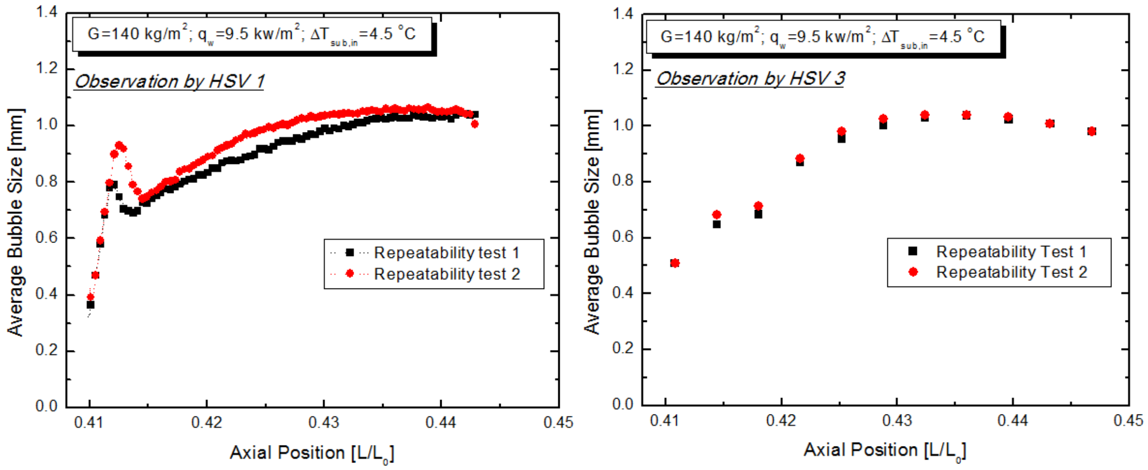

Figure IV-4. Repeatability test on the bubble size based on the measurement of HSV 1 (left) and HSV 3(right)

On the left side of Figure IV-4, the overall bubble growth behavior observed by HSV 1 looks largely repeatable between the two repeatability tests. However, it can be seen that the bubble size shows noticeable differences locally, up to ~0.2 mm at the axial location $0.41<L/L_0<0.415$, and it was found that such differences occurred at the local region where the fluctuating behaviors of bubble size were enhanced due to the coalescence and bouncing motions of bubbles near the nucleation site (more details about this will be discussed in Section C). The differences observed between the two repeatability tests shown on the left side of Figure IV-4 could be due to one or more of the following issues: First, the sample size used for the statistical average might be insufficient. Second, the measurement period of 3.6 sec for HSV 1 might not be long enough to characterize the bubble size variation resulting from the stochastic nature of boiling. Third, the characteristics of heater surface or artificial cavity might have changed during the time between the two repeatability tests. Fourth, the uncertainty of the test boundary conditions, e.g., liquid flow rate and wall heat flux may have affected the boiling process.

Of those four issues listed, we regard the first and second one as the dominant reasons for the discrepancy shown on the left side of Figure IV-4; and this argument can be supported by the improved repeatability results obtained from HSV 3 shown on the right side of Figure IV-4. As discussed, HSV 3 measured the bubble motions along the test section with a lower recording speed (0.5 kHz) compared to that of HSV 1 (10 kHz). Meanwhile, the measurement by HSV 3 was performed for 80 sec while the measurement period of HSV 1 was only 3.6 sec. Although the total number of images taken from HSV 1 and HSV 3 were comparable, such different recording specifics can make significant difference in the quality of resulting statistics. This is because the bubbles were generated and moved much less within the relatively short measurement time of HSV 1. As a result, the number of bubbles (or samples) captured during the measurement period was quite limited for HSV 1 compared to that for HSV 3. Necessarily, this limited sample size increased the uncertainty of the statistical average obtained based on the measurement of HSV 1, which is related to the stochastic nature of flow boiling phenomena. Mathematically, the Eq. (IV-1) can explain why the average bubble size based on the measurement of HSV 3 showed better repeatability (or less uncertainty) than those of HSV 1 as shown in Figure IV-4

$$\Delta u(\bar{x}) = \frac{\sigma_x}{\sqrt{N}} \tag{IV-1}$$

where x denotes a random variable, $\bar{x}$ is the statistical average, $\Delta u(\bar{x})$ is the standard uncertainty of $\bar{x}$, σ_x is the standard deviation, and N is the number of samples.

Obviously, the uncertainty defined in Eq. (IV-1) will increase as the statistical variation increases or the available number of samples decreases. Thus, it is important to take this into account as a part of experimental uncertainty, especially when the sample size is relatively limited like in the measurement of HSV 1. The details about the estimated uncertainty values will be described in Section B.4. Here, we only say that the uncertainty of bubble size measurement obtained by HSV 1 is judged to be reasonable.

In Figure IV-5, the repeatability test results of the axial bubble velocity measured by HSV 1 are presented. The measured axial bubble velocities show good agreement between the repeatability tests 1 and 2 within the local region of interest $0.41<L/L_0<0.45$. Also, it is interesting to mention that the repeatability of measured axial bubble velocity is observed to be better than that of measured bubble size shown on the left side of Figure IV-4. This implies that the local fluctuation of bubble size which causes a difference in average bubble size barely affected the average axial bubble velocity. Further discussion on the repeatability of measured parameters obtained by HSV 3 and IR thermometry will be given in Chapter V.

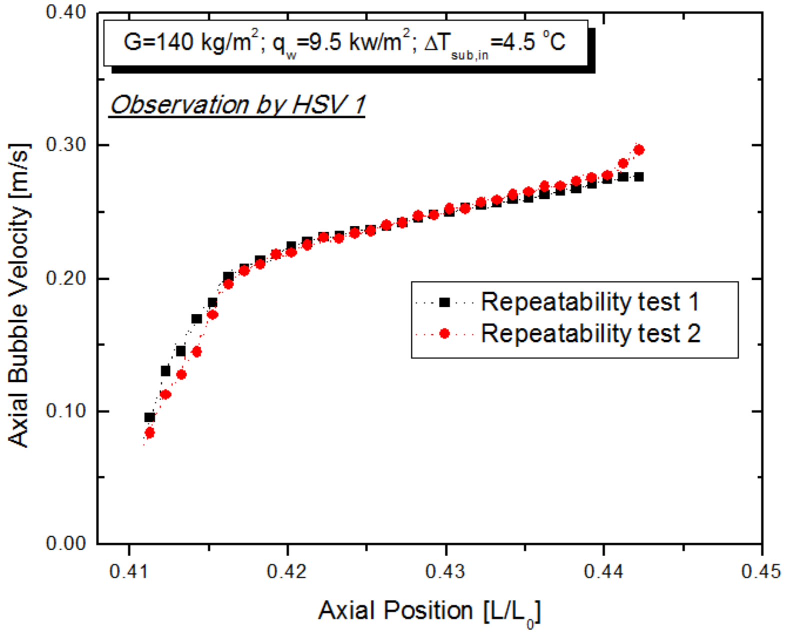

Figure IV-5. Repeatability test on the axial bubble velocity based on the measurement of HSV 1

To conclude, the repeatability test results along with the discussion mentioned above imply that the bubbles' characteristic behavior can be well represented by the statistical average obtained based on the data collection strategy applied to HSV 1 in the present subcooled flow boiling experiment. The details on the uncertainty analysis of the parameters measured by HSV 1 are described in the following section.

4. Measurement uncertainty (for HSV 1)

Several sources of measurement uncertainty can exist in bubble size measurement using HSV 1 due to (i) spatial resolution, (ii) sample size, (iii) image processing, etc. Among them, due to the high resolution and the enhanced bubble image quality achieved by HSV 1 (see Figure IV-6 and IV-7), the major source of uncertainty is expected to be the limited sample size caused by the limited measurement time of HSV 1 (3.6 sec) as discussed in Section B.3. This uncertainty can be estimated by Eq. (IV-1). However, we should note that such uncertainty varies depending on the given experimental conditions and on the location where the bubbles are captured within the test channel even under the same experimental conditions. Instead of addressing each of them separately, we estimated this uncertainty in a conservative manner by evaluating the uncertainties at the regions where the statistical variation significantly increased for each experimental condition. In general, within the measurement view of HSV 1 (i.e., $0.41<L/L_0<0.45$, see Figure IV-3), the fluctuations of bubble size were observed to become significantly enhanced at the regions where the bubbles detached from the heater surface and reattached again (i.e., bouncing motion) near the nucleation site. Or, if such bouncing motions of bubbles were insignificant given the experimental conditions, the statistical variation of bubble size tended to become slightly larger as the bubble grew while sliding downstream. Thus, we analyzed the bubble size distribution at such local regions over the entire experimental set and estimated the uncertainties using Eq. (IV-1); and the maximum value was finally selected as the uncertainty introduced by the stochastic nature of boiling during this study. The uncertainty obtained in this way is ±14.9 μm. Combining this with the uncertainty introduced by the spatial resolution of HSV 1 [25], the uncertainty for the bubble size measurement by HSV 1 is finally determined as ±17.5 μm.

Similarly, for the uncertainty quantification of axial bubble velocity measured by HSV 1, we analyzed the axial bubble velocity distribution at the axial locations near the nucleation site ($L/L_0 \approx 0.41$) and a region further downstream ($L/L_0 \approx 0.44$) for the entire set of experiments during this study (see Section B.5). Then, using Eq. (IV-1), we estimated the related uncertainties, from which the maximum value, 3.2×10^{-3} m/s, was selected as the uncertainty for the axial bubble velocity measurement in the present study. The uncertainty due to the erroneous detection of bubble displacement and/or time interval between the image pairs was neglected. Besides, the uncertainties of liquid flow rate, fluid temperature, and heater power given by the DC power supply were obtained as ±0.05% of reading, ±0.5 °C, and ±1.1% (full scale), respectively.

The uncertainty for the measured parameters obtained by HSV 3 as well as the IR camera will be discussed in Chapter V, which addresses the bubbles' behaviors over the larger area of flow path observed by HSV 3 and corresponding wall heat transfer measured by IR thermometry.

5. Test conditions

The present experiment was performed at atmospheric pressure for the ranges of liquid mass flux (G), wall heat flux (q_w), and inlet subcooling ($\Delta T_{sub,in}$) of about 140~700 kg/m^{2}s, 8~35 kW/m^2, and 4.5~13.6 °C, respectively. The specific test conditions as well as some local parameters addressed in this study are summarized in Table IV-1. As discussed in Section B.2, only a single nucleation site was intended to be activated over the entire heated area (7.5×225 mm^2) for the all test conditions; and the various aspects of bubble behaviors and their effects on the wall heat transfer were studied based on the circumstance of such single nucleation site convective boiling. The test conditions shown in Table IV-1 were chosen to systematically observe the effect of the individual control parameters, i.e., (i) inlet subcooling, (ii) liquid mass flux, and (iii) wall heat flux on the various thermal-hydraulic phenomena within the test channel.

Table IV-1. Summary of test conditions and local parameters measured

Exp. No.	G (kg/m^2s)	q_w (kW/m^2)	$\Delta T_{sub,in}$ (K)	Ja(1)	$f_{b,0}$(2) [Hz]	D_{max}(3) (mm)
1	140	9.7	13.5	34.1	159	0.73
2	140	11.6	13.6	42.8	163	0.78
3	140	8.1	13.5	24.1	152	0.67
4	280	11.9	13.5	19.8	133	0.55
5	420	12.2	13.5	6.3	239	0.27
6	420	20.4	13.5	30.6	148	0.48
7	420	23.7	13.5	39.5	282	0.51
8	420	17.1	13.5	20.6	139	0.39
9	560	24.0	13.6	24.2	207	0.37
10	700	24.2	13.5	14.6	331	0.25
11	700	30.9	13.5	27.1	343	0.32
12	700	35.1	13.5	34.9	523	0.36
13	700	26.4	13.6	18.4	295	0.28
14	140	9.5	4.50	49.1	135	1.02
15	420	20.1	4.50	45.8	380	0.76
16	700	30.5	4.50	42.6	769	0.43

(1) *Jacob number at the elevation of nucleation site (estimated based on the average heater surface temperature measured at* $L/L_0 \approx 0.41$*)*

(2) *Bubble release frequency (discussed in Section C.4)*

(3) *Maximum size of bubble measured within the region* $0.41 \leq L/L_0 \leq 0.44$

As previously mentioned, this chapter is the first part between the two chapters (i.e., Chapter IV and V) to investigate the bubble behaviors with micro- and macroscopic observation views of HSVs and the wall heat transfer characteristics along the test channel of subcooled boiling flow. In this chapter, the detailed bubble behaviors near the nucleation site observed by the high-resolution camera HSV 1 (see Figure IV-1) are discussed. Figure IV-6 summarizes the specific research interests addressed in this chapter along with the image analysis procedure applied to the visual measurement of bubbles by HSV 1. As shown in Figure IV-6, we discuss (i) the nucleating behavior at the nucleation site, (ii) bubble growth behavior in the direction of upward flow, (iii) axial bubble velocity, (iv) bubble release frequency, (v) bubble number variation, and (vi) local evaporative heat flux. The following discussions in section C are based on the parametric study of inlet subcooling, liquid mass flux, and wall heat flux for the given set of experiments detailed in Table IV-1.

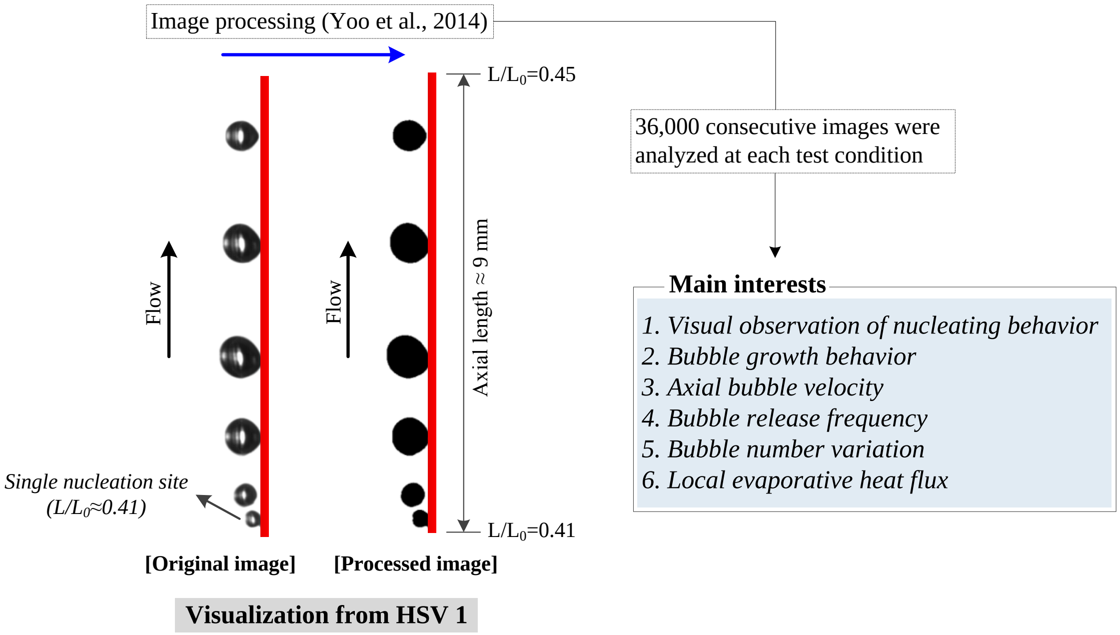

Figure IV-6. Main interests of present study with the schematic of image analysis procedure for HSV 1

C. Result and discussion

1. Visual observation of nucleating behaviors

This section provides the qualitative description of boiling behaviors at the single nucleation site based on the observation of vapor bubbles by HSV 1 under various subcooled flow boiling conditions. During this study, it was found that the boiling at the single nucleation site mostly belonged to a non-isolated bubble regime, meaning that the boiling bubbles interfered with each other before departing from the nucleation site due to the fast-occurring boiling process. Thus, the bubbles could grow fast at the nucleation site due to both the evaporation and coalescence. After this initial growth, the bubbles were typically observed to experience the following process: (i) bouncing and subsequently detaching from the wall (heater surface), (ii) condensing into a smaller sized bubble, (iii) reattaching to the heater surface, and (iv) sliding in the upward flow direction while growing. Thereafter, the bubbles were largely found to slide along the heater surface until they passed the outlet of the test section, which was observed by HSV 2 installed downstream in the test channel as shown in Figure IV-1. Note that we distinguish the concept of bubble lift-off [3] which does not consider the bubble reattachment from that of the bouncing motions of bubbles near the nucleation site observed during this study. Within the present set of experiments, bubble lift-off was observed only in two test cases Exp. No. 14 and 16.

In Figure IV-7, the vapor bubble motions at the nucleation site which were taken under the various subcooled flow boiling conditions are compared. The images presented are the representative ones which clearly show the differences in boiling behaviors influenced by the changes in inlet subcooling (Figure IV-7, top), liquid mass flux (Figure IV-7, middle), and wall heat flux (Figure IV-7, bottom). On the top left of the Figure IV-7, we can see that the bubble size increased significantly as the inlet subcooling decreased from 13.5 to 4.5 °C. On the other hand, at the higher liquid mass flux and wall heat flux conditions shown on the top right of Figure IV-7, the effect of varying the inlet subcooling on bubble size was observed to be less significant. However, the bouncing motions of bubbles became more noticeable when decreasing the inlet subcooling, and bubbles were generated and released from the nucleation site more frequently under lower inlet subcooling conditions. Additionally, by observing the bubbles' trajectory through the test channel from the top view using HSV 3 (see Figure IV-2), we found that the horizontal waving motion of bubbles was enhanced by decreasing the inlet subcooling; a similar observation was made when increasing the liquid mass flux. The middle section of Figure IV-7 shows the effects of liquid mass flux on the boiling bubbles' behavior near the nucleation site. Clearly, the bubbles' growth became significantly restricted as the liquid mass flux increased at constant inlet subcooling and wall heat flux conditions. Also, the bouncing motions of bubbles near the nucleation site became more noticeable as the liquid mass flux decreased. In the bottom of Figure IV-7, the boiling behaviors at the nucleation site affected by the changes in wall heat flux are presented. As expected, the bubbles grew faster at the nucleation site when the wall heat flux increased at constant liquid mass flux and inlet subcooling conditions. Also, we can see that the bouncing motions of bubbles became more noticeable as the wall heat flux increased. It is noted that the above-mentioned observations commonly imply that the bouncing motions of bubbles near the nucleation site increased at the test conditions causing an increase in heater surface temperature (i.e., increasing wall heat flux or decreasing liquid mass flux/inlet subcooling).

In the following sections, the various features of bubble behaviors observed by HSV 1 is discussed based on the quantitative analysis of numerous images obtained via image processing (see Figure IV-6), ensuring reliable statistics (i.e., statistical average).

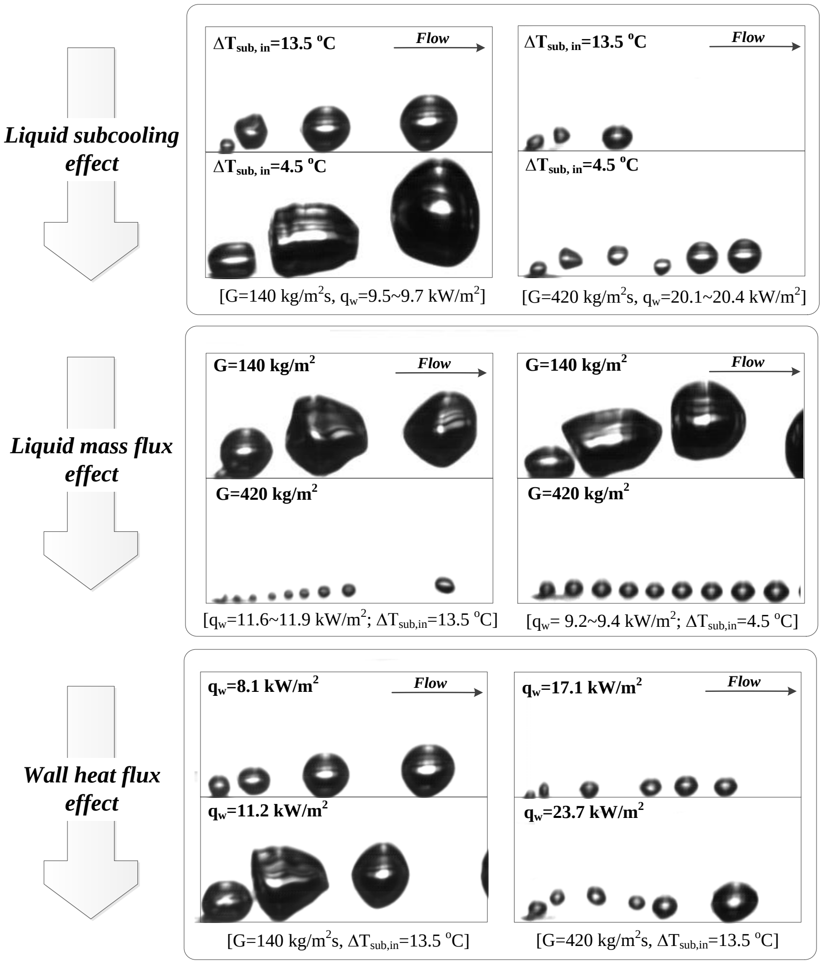

Figure IV-7. Boiling behaviors at the single nucleation site affected by the varying inlet subcooling (top), liquid mass flux (middle), and wall heat flux (bottom)

2. Bubble growth behavior

Bubble growth behavior under various subcooled flow boiling conditions is studied. Specifically, in this section, the effects of varying the test boundary conditions inlet subcooling, wall heat flux, and liquid mass flux on the characteristic bubbles' growth behavior along the flow direction are discussed. To this end, the axial flow path viewed from HSV 1 (Figures IV-2 and IV-6) was partitioned into 400 sectors, and the bubbles captured within each sector at each time frame were used to calculate the average bubble size in each sector. Typically, more than 300–500 bubbles were collected during the measurement period (3.6 s) within each sector. The size of bubbles and their positions (i.e., the center of mass location) were evaluated using ImageJ [29] and its macro function. During this process, we excluded the poor quality of the processed images of bubbles by using a certain criterion of bubble shape (e.g., circularity≥0.65), which was to keep the reliability of present bubble size analysis. Bubble size was defined as the equivalent diameter which was calculated based on the 2-D projection of bubble images processed via image processing (see Figure IV-6).

As discussed in section C.1, the bubbles observed during this study often bounced and subsequently detached from the heater surface after rapid growth at the nucleation site. Since the bubbles started condensing due to the subcooled liquid as they detached from the heater surface, bubble size naturally decreased after the initial growth because of the bouncing motions. Then, it subsequently increased again once the bubbles reattached to the heater surface. In Figures IV-8~IV-10, the noticeable fluctuations of bubble size observed at the local region $L/L_0 \approx 0.41–0.415$ resulted from such bouncing motions of bubbles near the nucleation site.

In Figure IV-8, the bubble growth behaviors along the flow path affected by the changes in inlet subcooling ($\Delta T_{sub,in}$) are presented. To observe the parametric effect of $\Delta T_{sub,in}$, the bubble growth behaviors were compared for the two different inlet subcooling degrees $\Delta T_{sub,in}=4.5$ and 13.5 °C at constant liquid mass flux (G) and wall heat flux (q_w). Comparisons were made for the three different constant conditions of G and q_w as shown in Figure IV-8. On the top left of Figure IV-8, the fluctuation of bubble size is observed at $0.41<L/L_0<0.415$ for the two test cases shown, which resulted from the bouncing motions of bubbles as discussed before. After the fluctuation, bubble size increases until reaching $L/L_0 \approx 0.44$ for the test case of $\Delta T_{sub,in}=4.5$ °C. In contrast, the bubble size for the test case of $\Delta T_{sub,in}=13.5$ °C decreases after $L/L_0 \approx 0.43$. This is because the bubbles at the higher subcooling condition condensed rather than evaporated after reaching a certain size as the bubble growth process was restricted by the cold bulk liquid around the bubbles. For the other comparisons shown in Figure IV-8 (i.e., top right and bottom), the bubbles grew faster in the direction of flow at lower inlet subcooling conditions ($\Delta T_{sub,in}=4.5$ °C), which is a consequence of the fact that the lower inlet subcooling caused higher heater surface temperature at constant liquid mass flux and wall heat flux conditions. Additionally, we can easily expect that the bubble growth is less restricted by the subcooled bulk liquid around the bubbles at lower subcooling conditions.

However, the above-mentioned variation in bubble size caused by the different inlet subcooling conditions became smaller or even reversed locally for the experimental cases shown in the bottom of Figure IV-8. This is due to the fact that the bouncing motion of bubbles resulting in their condensation was enhanced as the bubbles left the nucleation site by decreasing the subcooling degree. Specifically, we observed that in the case of lower inlet subcooling ($\Delta T_{sub,in}$=4.5 °C) shown in the bottom of Figure IV-8, the bouncing bubbles near the nucleation site tended to move farther after detaching from the heater surface and were less likely to reattach. As a consequence, the bubbles at this test condition often condensed considerably or collapsed as they passed the region $0.41<L/L_0<0.42$, which resulted in the larger portion of smaller bubbles and the fluctuation of average bubble size through this region instead of the consistent increase as shown in the bottom of Figure IV-8.

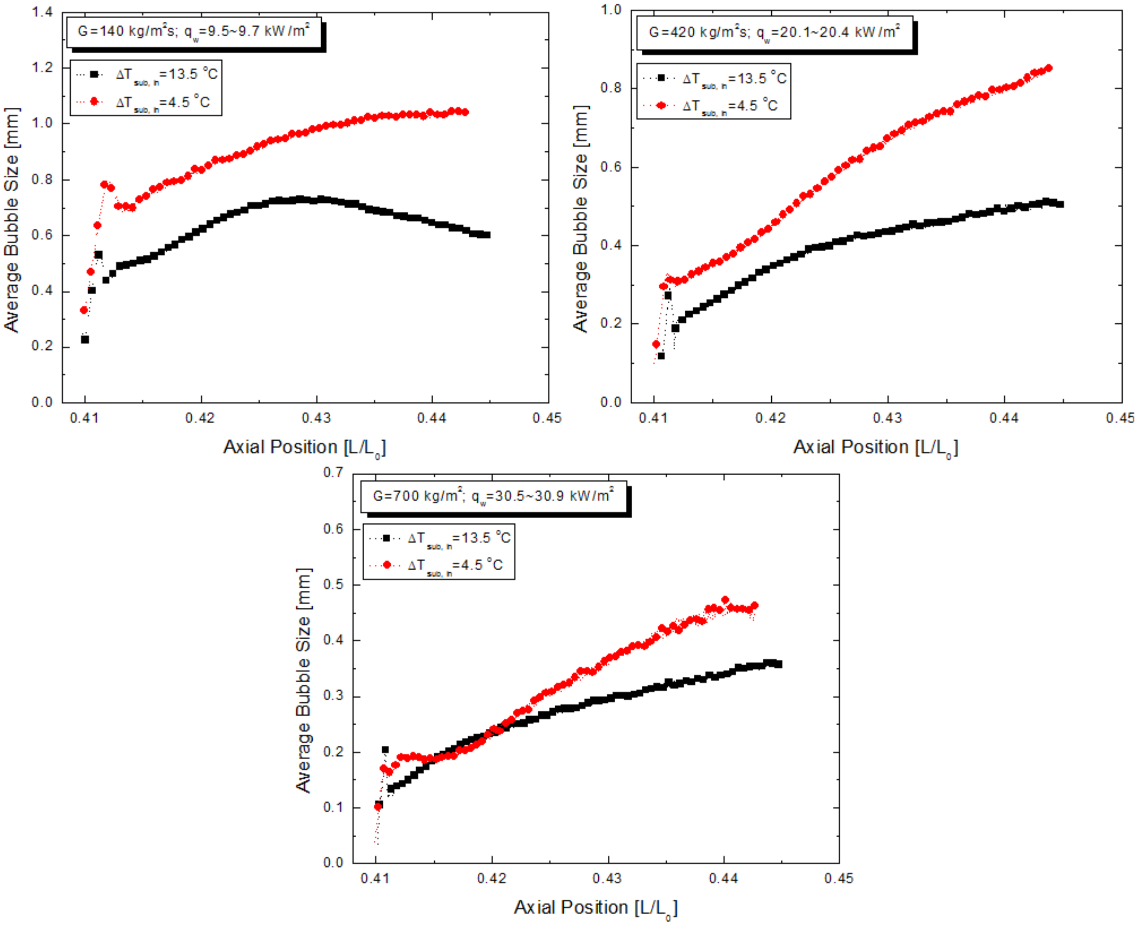

Figure IV-8. Effects of inlet subcooling ($\Delta T_{sub,in}$) on bubble growth behavior along the flow path

Figure IV-9 shows the effects of varying the liquid mass flux (G) on bubble growth behavior in the upward flow direction: Bubble size became noticeably smaller as G increased. This resulted from the fact that the liquid thermal boundary layer beneath the bubbles became thinner while the condensation of the bubbles due to the subcooled liquid was enhanced as G increased. On the left side of Figure IV-9, we can see that the size of bubbles at G=420 kg/m^{2}s kept growing until reaching the axial location $L/L_0 \approx 0.45$; whereas, bubble size was found to decrease after $L/L_0 \approx 0.43$ at G=140 and

280 kg/m^{2}s. As previously discussed, this is because the bubbles grew faster while sliding at a lower G, which caused more condensation of the bubbles as their exposure to the subcooled liquid increased. A similar behavior was also observed for the parametric study of wall heat flux (q_w), shown on the left side of Figure IV-10 when G was low (i.e., G=140 kg/m^{2}s). However, such behavior (i.e., increase and subsequent decrease of bubble size while sliding) was not found in the results shown on the right side of Figure IV-10 which employed a higher G (i.e., G=700 kg/m^{2}s). Figure IV-10 also shows that the bubble size within the region $0.41<L/L_0<0.45$ tended to increase as q_w increased while holding G and $\Delta T_{sub,in}$ constant. As expected, this is because the heater surface temperature became higher by increasing q_w.

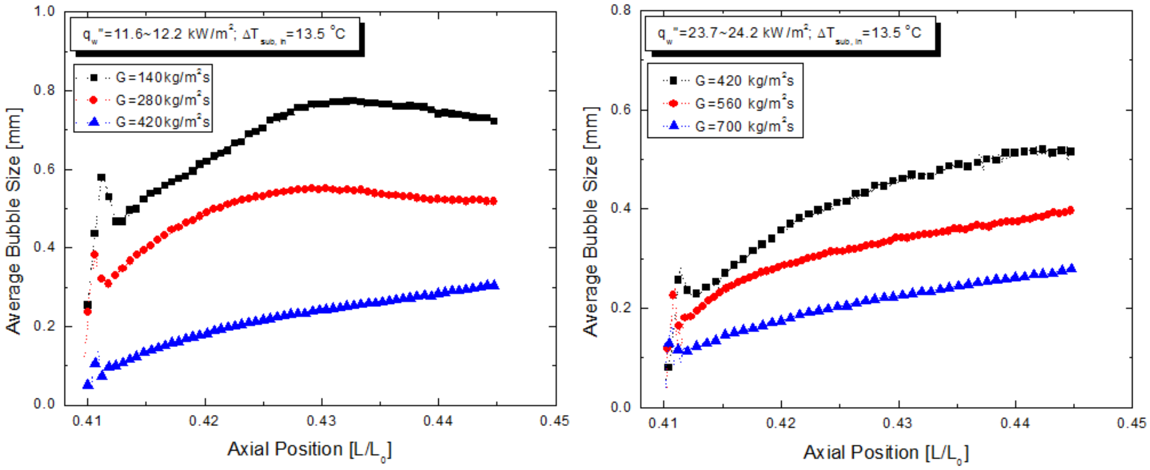

Figure IV-9. Effects of liquid mass flux (G) on bubble growth behavior along the flow path

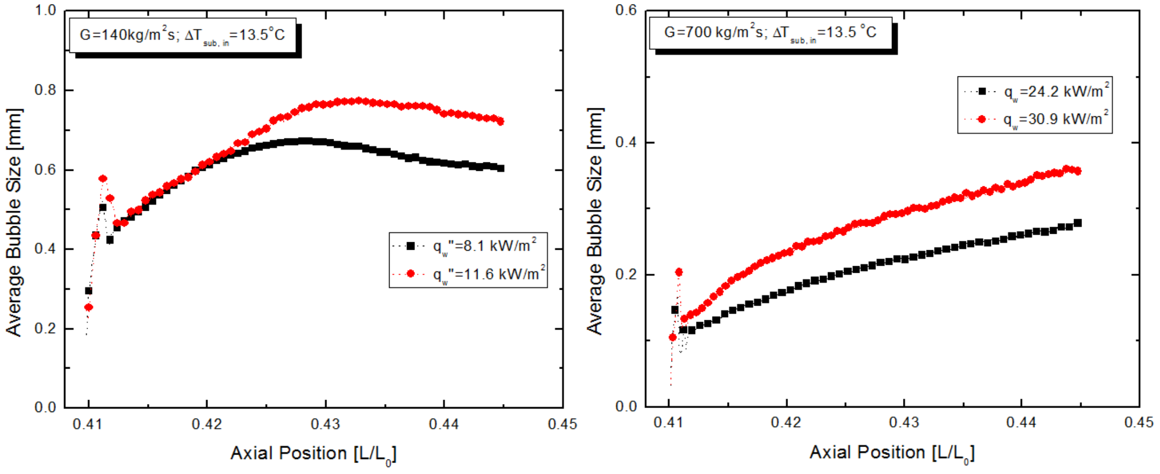

Figure IV-10. Effects of wall heat flux (q_w) on bubble growth behavior along the flow path

3. Axial bubble velocity

The axial bubble velocity near the nucleation site depending on $\Delta T_{sub,in}$, G, and q_w is examined in this section. To evaluate the axial bubble velocity, the displacement of bubbles between the consecutive image pairs was analyzed using the ImageJ plugin software MTrack2 [66] after converting the original images taken by HSV 1 to binary ones for the automatic analysis of numerous images (see Figure IV-6). For this analysis, the total axial flow path viewed from HSV 1 was partitioned into 200 sectors, and the axial velocities of bubbles within each sector were analyzed and subsequently collected over the measurement period (3.6 sec) to estimate the average bubble velocities in the 200 sectors of different axial locations.

Figure IV-11 presents the effect of $\Delta T_{sub,\,in}$ on the axial bubble velocity in the direction of vertical upward flow. Specifically, the variation of axial bubble velocity due to changes in $\Delta T_{sub,\,in}$ is examined for the three different constant conditions of G and q_w.

In Figure IV-11, the axial bubble velocities are seen to increase according to the decreasing $\Delta T_{sub, in}$. This is because the size of vapor bubbles increased as $\Delta T_{sub, in}$ decreased, as discussed in section C.2 (see Figure IV-8), which resulted in a larger buoyancy force, aiding the bubbles' motion in the upward flow direction. In the top left section of Figure IV-11 ($G=140$ kg/m^{2}s; $q_w=9.5\sim9.7$ kw/m^2), however, the axial bubble velocity at the region near the nucleation site $0.41<L/L_0<0.415$ is shown to be slightly less for the case of lower inlet subcooling ($\Delta T_{sub,in}=4.5$ °C), which appears inconsistent with the other observations in Figure IV-11. This is because bubble growth time as well as bubble size at the nucleation site became significantly larger when $\Delta T_{sub,in}$ was decreased at this G and q_w. In other words, the bubbles at the lower inlet subcooling condition stayed longer at the nucleation site while growing before departing from the nucleation site. As a result, the axial bubble velocity was observed to be slightly lower at the region $L/L_0<0.415$.

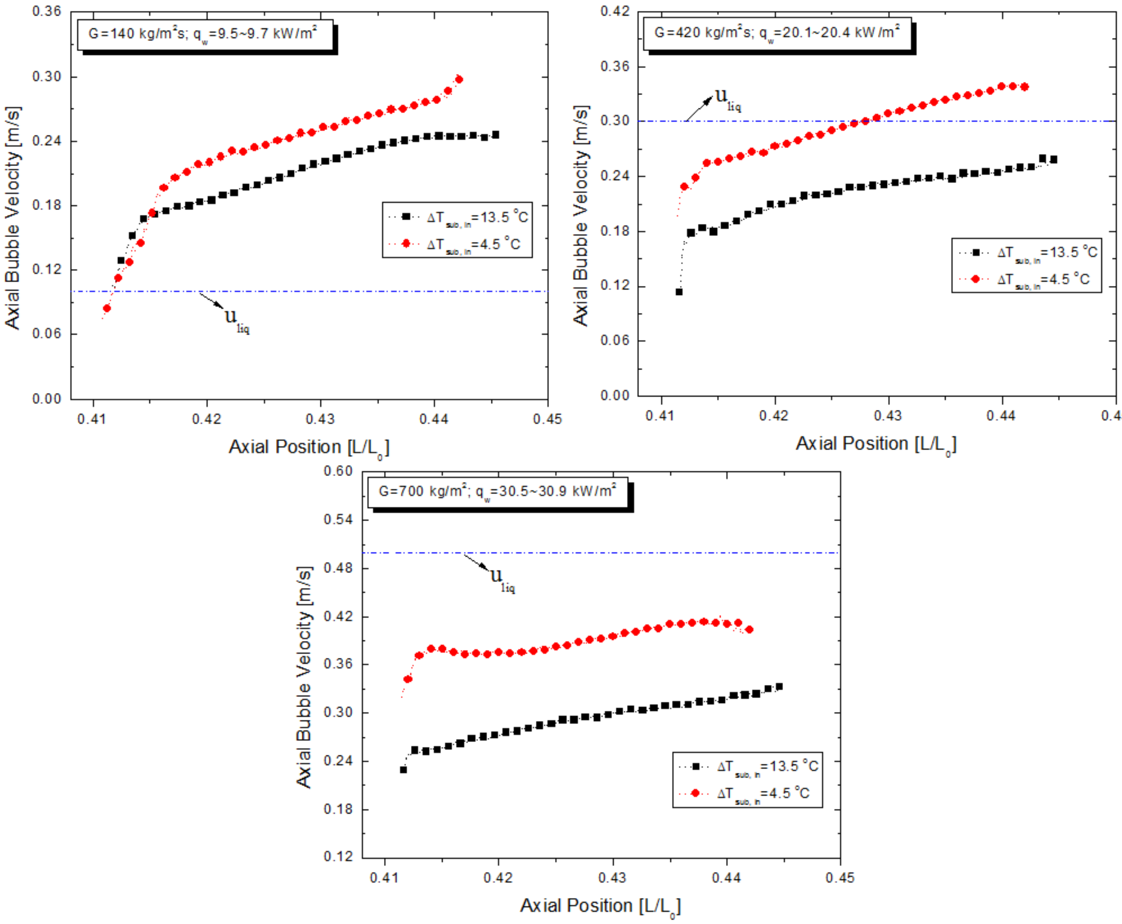

Figure IV-11. Effects of inlet subcooling ($\Delta T_{sub,in}$) on axial bubble velocity

In Figure IV-11, the bulk liquid velocity u_{liq} is also presented (blue dash-dot line) along with the axial bubble velocities. The axial bubble velocities shown on the top left of Figure IV-11 were almost always larger than the u_{liq}, and the difference increased as the axial bubble velocity increased along the flow path. On the other hand, the opposite trend is shown on the bottom of Figure IV-11. That is, the axial bubble velocities were significantly lower near the nucleation site while the difference in velocity between the bubble and the u_{liq} gradually decreased as the bubbles moved downstream.

In Figure IV-12, the parametric effect of G on the axial bubble velocity is presented. It is seen that the axial bubble velocity decreased as G increased at constant q_w and $\Delta T_{sub,in}$. That is, the bubbles generated at the nucleation site traveled more slowly despite the fact that G increased in the direction of flow through the test channel. For this, such variation of axial bubble velocity is considered closely related to the bubble size variation caused by varying G. Bubble growth behaviors for the experimental cases shown in Figure IV-12 are presented in Figure IV-9. As demonstrated in Figure IV-9, the increasing G consistently restricted bubble growth (i.e., caused smaller bubble size) within the region $0.41<L/L_0<0.45$. This means that the buoyancy force driving the bubbles upward along the flow path was also reduced by increasing G. The results shown in Figure IV-12 imply that such effect of buoyancy force dominated the interfacial drag induced by increasing G, which resulted in the trend of decreasing axial bubble velocity as G increased. Figure IV-13 shows that the axial bubble velocity increased as q_w increased. Similarly, this is because the buoyancy force acting on the bubbles was augmented as the bubble size increased due to an increasing q_w as illustrated in Figure IV-10.

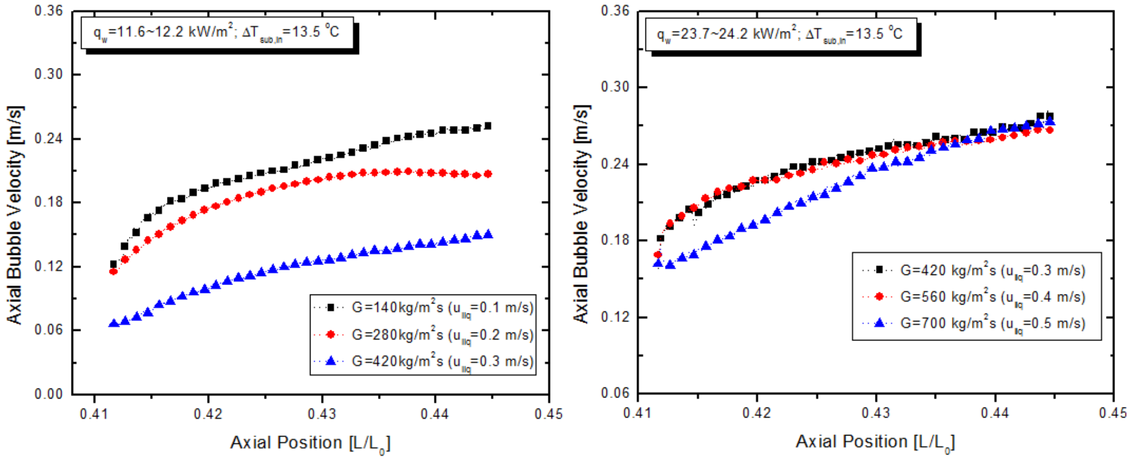

Figure IV-12. Effects of liquid mass flux (G) on axial bubble velocity

Both Figure IV-12 and IV-13 indicate that the relative magnitudes of axial bubble velocity against the u_{liq} were larger at low G conditions while the trend reversed as G increased. These observations further support the assertion that the axial bubble velocity near the nucleation site is dominated more by the buoyancy force than the interfacial drag caused by the flowing liquid.

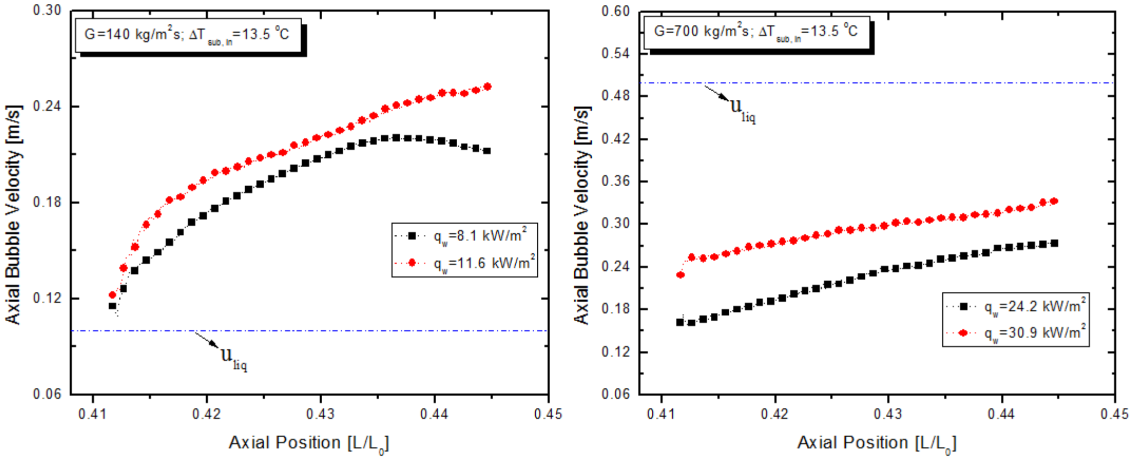

Figure IV-13. Effects of wall heat flux (q_w) on axial bubble velocity

4. Bubble release frequency

The frequency of bubble departure from the nucleation site is also known to be an important parameter to characterize the boiling heat transfer in subcooled boiling flow. In the present study, however, the bubbles produced at the nucleation site were generally in the non-isolated bubble regime, which means that the bubbles frequently interfered with each other before departure from the nucleation site. Despite the high resolutions applied to HSV 1 (10 kHz, 9.09 μm), the departure frequency of isolated bubbles is hard to define visually in this boiling regime. Thus, instead of measuring the bubble departure frequency, we investigated the frequency of bubbles released from the nucleation site a little downstream of the nucleation site $0.41<L/L_0<0.42$, and we define this as the bubble release frequency. To obtain the average bubble release frequency for each test condition, more than 500 samples were typically used. In this section, the dependence of average bubble release frequency on $\Delta T_{sub,in}$, G, and q_w is explored.

Figure IV-14 shows the effect of varying $\Delta T_{sub,in}$ on the average bubble release frequency; the dotted lines connecting the two data points indicate the variation of $\Delta T_{sub,in}$ at a constant G and q_w. The bubble release frequency varied insignificantly (or increases slightly) when $\Delta T_{sub,in}$ increases at low G and q_w (i.e., G=140 kg/m^{2}s, q_w=9.5~9.7 kW/m^2). However, for the other cases, the bubble release frequency significantly decreased as $\Delta T_{sub,in}$ increased. This inverse proportion of the bubble release frequency to $\Delta T_{sub,in}$ implies that the wall heat transfer mode affected by the subcooled liquid outside the thermal boundary layer close to the wall (i.e., heater surface) was enhanced by increasing $\Delta T_{sub,in}$. Specifically, whenever bubbles departed from the nucleation site, the low temperature of subcooled liquid around the bubbles was drawn onto the wall, and this usually induces a large drop in the wall temperature during an ebullition cycle. This sub-process of boiling heat transfer is called quenching, a concept originally proposed by Forster and Greir [67]. According to the mechanistic models proposed in the literature [55, 68], the quenching heat transfer mode depends on several parameters such as bulk liquid temperature, heater surface (or wall) temperature, bubble size, and bubble frequency. Of these, the decrease in bulk liquid temperature (i.e., increasing the subcooling degree) is expected to enhance the cooling performance of quenching heat transfer mode if we assume that the other parameters do not change substantially. This is due to the fact that at higher subcooling conditions, the amount of wall temperature drop during an ebullition cycle will increase because the lower temperature of liquid repeatedly touches the wall as the bubbles leave space while departing. Also, note that in the cases shown in Figure IV-14, the average wall temperature was reduced by increasing $\Delta T_{sub,in}$ at a constant G and q_w. Thus, we can expect that the recovery of wall superheat after the wall temperature drop caused by quenching will progress more slowly at a higher $\Delta T_{sub,in}$. Therefore, it is concluded that mainly both (i) the larger wall temperature drop caused by the quenching process and (ii) the reduced wall superheat at a higher $\Delta T_{sub,in}$ led to an increase in the time intervals between the successive boiling events, which is why the decreasing trend of bubble release frequency was observed in this study as $\Delta T_{sub,in}$ increased, as shown in Figure IV-14.

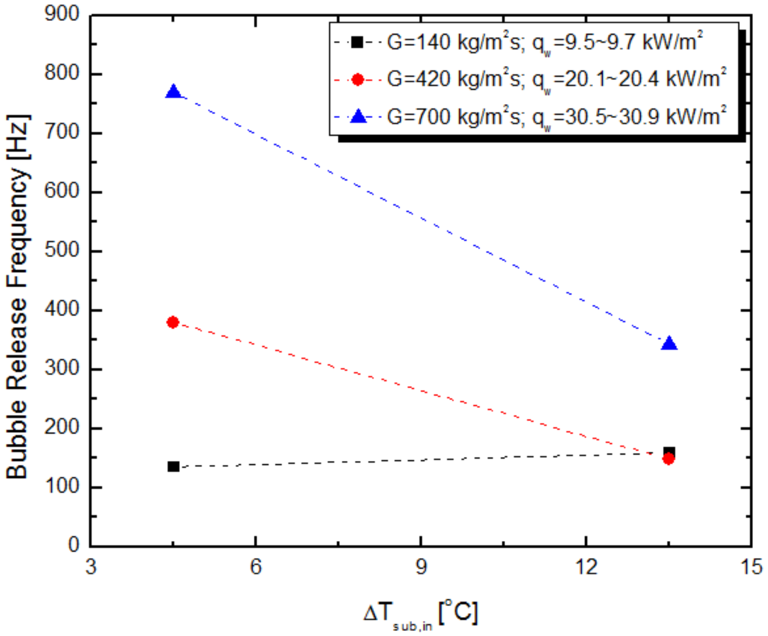

Figure IV-14. Effects of inlet subcooling ($\Delta T_{sub,in}$) on bubble release frequency

In Figure IV-15 and IV-16, the variation of bubble release frequency due to the changes in G at different subcooling conditions is presented. Specifically, Figure IV-15 shows the dependence of the bubble release frequency on G at $\Delta T_{sub,in}$=4.5 °C, while Figure IV-16 presents such dependency at $\Delta T_{sub,in}$=13.5 °C. Comparing the experimental results shown in Figures IV-15 and IV-16, we can see that the bubble release frequency varied according to G in a quite different manner at the two inlet subcooling conditions. That is, when $\Delta T_{sub,in}$ =4.6 °C (Figure IV-15), the bubble release frequency was observed to be in proportion to G. However, such a consistent tendency was not found when increasing G at $\Delta T_{sub,in}$ =13.5 °C, as shown in Figure IV-16. To discuss this, we need to first recall the observation of how bubble size is affected by G, as discussed in section C.2, because the bubble release frequency and the bubble size at departure from the nucleation site can be closely related. We observed that the average bubble size near the nucleation site consistently decreased as G increased, which means that the heat transfer due to evaporation was reduced at a higher G. The efficiency of heat removal by the quenching process may also decrease as G increases due to the relatively small size of the bubbles. That is, the relative magnitude of the drop in the wall temperature caused by the quenching process might be less at a higher G because the small size of departing bubbles may draw only limited amount of surrounding liquid. As a result, the time to reach the required wall superheat needed for subsequent nucleation after the wall temperature drops due to evaporation or quenching could become shorter (i.e., decreasing bubble waiting time). Therefore, we can deduce that the deteriorated evaporation and quenching heat transfer modes by increasing G resulted in a proportional relation of bubble release frequency to G as shown in Figure IV-15.

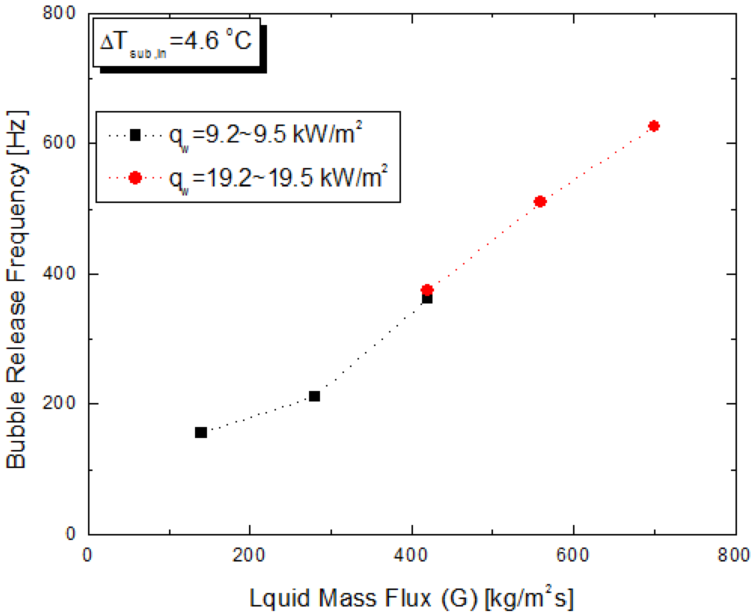

Figure IV-15. Dependence of bubble release frequency on liquid mass flux (G) at $\Delta T_{sub,in}$=4.6 °C

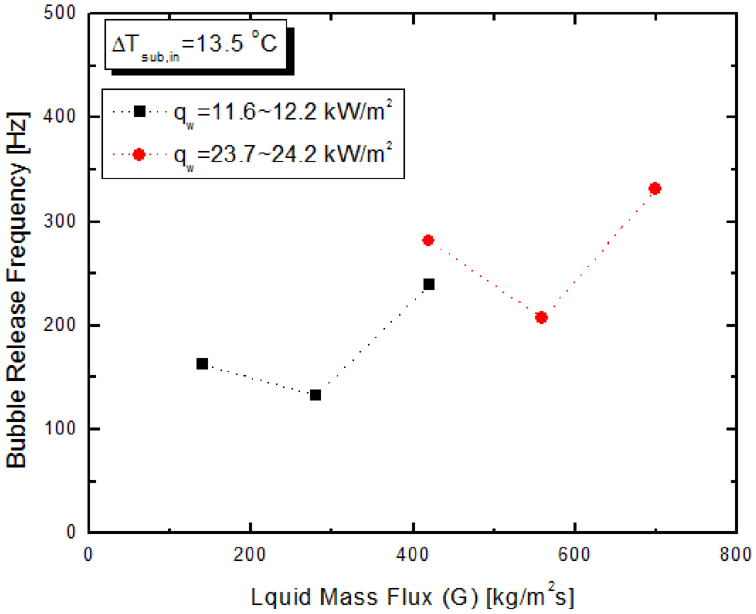

Figure IV-16. Dependence of bubble release frequency on liquid mass flux (G) at $\Delta T_{sub,in}$=13.5 °C

In Figure IV-16, however, it is seen that at $\Delta T_{sub,in}$=13.5 °C, the bubble release frequency did not vary with G in such a consistent manner any longer. Figure IV-16 shows that the bubble release frequency decreased initially as G increased, but the frequency increased again as G increased more. Such a trend was commonly observed for the test cases at different values of q_w and G as shown in Figure IV-16. Regarding this, we argue that the variation of relative significance between the single-phase convection and the bubble-induced heat transfer modes (i.e., evaporation and quenching) while increasing G affected the trend of bubble release frequency. Obviously, the cooling performance due to the single-phase convection is enhanced as G increases. In contrast, since the bubble size decreased as G increased, the relative significance of heat transfer modes due to evaporation and quenching deteriorates as previously discussed (This will be discussed further in section C.5.). The enhanced single-phase convection by increasing G causes the lower wall superheat, extending the time necessary to recover the wall superheat needed for successive nucleation after the wall temperature drop due to evaporation and quenching, which leads to a decrease in bubble release frequency. On the other hand, the diminishing role of bubble-induced heat transfer modes by increasing G reduces the magnitude of the wall temperature drop during an ebullition cycle as well as bubble growth time. This reduces the time required to recover the wall superheat needed for successive nucleation after the wall temperature drop caused by evaporation and quenching, leading to an increase in bubble release frequency. Consequently, it can be said that the variation of bubble release frequency as G increases will depend on whether the wall temperature variation during an ebullition cycle is dominated by the enhancing single phase convection or by deteriorating bubble-induced heat transfer modes. In this context, we suggest that the bubble release frequency in Figure IV-16 initially decreased at each q_w condition as G increased because of the enhanced single-phase convection. The opposite trend was found by increasing G more as the deterioration of bubble-induced heat transfer modes became more significant than the enhancement of single-phase convection. This competing process between the two heat transfer modes (i.e., enhanced single phase convection vs. deteriorated bubble-induced heat transfer) while G increases was confirmed by investigating the variation of bubble size shown in Figure IV-9. All the experimental cases shown in Figure IV-9 correspond to those shown in Figure IV-16. On the left of Figure IV-9, we can see that the bubble size near the nucleation site $L/L_0<0.42$ varies much less as G changed from G=140 to 280 kg/m^{2}s compared to when G changed from G=280 to 420 kg/m^{2}s. This implies that the bubble-induced heat transfer modes were less affected by the increase in G for the former case than for the latter. That is, for the former change of G (from G=140 to 280 kg/m^{2}s), the enhanced single-phase convection affected the bubble release frequency more than the deteriorated bubble-induced heat transfer affected it; and thus, the decrease in bubble release frequency was observed in Figure IV-16 (when q_w=11.6~12.2 kW/m^2) as G increased. On the contrary, for the latter change of G (from G=280 to 420 kg/m^{2}s), the significant deterioration of bubble-induced heat transfer modes is expected due to the decreasing bubble size as shown in Figure IV-9 (left); and for this reason, the increasing trend of bubble release frequency was observed in Figure IV-16 (when q_w=11.6-12.2 kW/m^2) as G increased. The same reasoning can be applied to the other observations shown in Figure IV-9 (right) and Figure IV-16 (when q_w=23.7~24.2 kW/m^2).

Figure IV-17 presents the variation of bubble release frequency according to the wall superheat represented by Ja number at the elevation of the single nucleation site $L/L_0\approx0.41$. The dependence of bubble release frequency on the Ja number at $\Delta T_{sub,in}$=4.5 °C is shown on the left, while such dependence at $\Delta T_{sub,in}$=13.5 °C is shown on the right. In Figure IV-17 (left and right), we can see that the variation of bubble release frequency depending on the Ja number was insignificant when G=140 kg/m^{2}s. Meanwhile, the bubble release frequency tended to increase as the Ja number increased for approximately Ja>25 at higher G values (i.e., G=420 and 700 kg/m^{2}s). This increasing trend of the bubble release frequency while increasing the Ja number is due to the fact that a drop in the wall temperature during an ebullition cycle can be recovered faster at the higher wall superheat condition. However, for lower Ja numbers (i.e., Ja<25), the inverse proportion of bubble release frequency to the Ja number was observed, as shown in Figure IV-17. We consider that this is related to the significant changes of bubble-induced heat transfer modes (i.e., evaporation and quenching) caused by the increase in Ja number. During this study, it was observed that the average bubble size near the nucleation site tended to increase quite noticeably as q_w increased, which increased the Ja number, whenever such a reciprocal relationship existed between the bubble release frequency and the Ja number. Similar to the previous discussion in this section, this indicates that the significant increase of bubble size near the nucleation site resulted in a larger wall temperature drop during an ebullition cycle due to the enhancement of evaporation and quenching heat transfer, which subsequently elongated the time interval between consecutive nucleation events (i.e., increasing bubble waiting time). Also, the bubble growth time increases as the wall superheat increases. Thus, we can argue that the increase in bubble waiting and bubble growth times due to the increasing wall superheat caused the reduction of bubble release frequency for the test cases of Ja<25 in Figure IV-17.

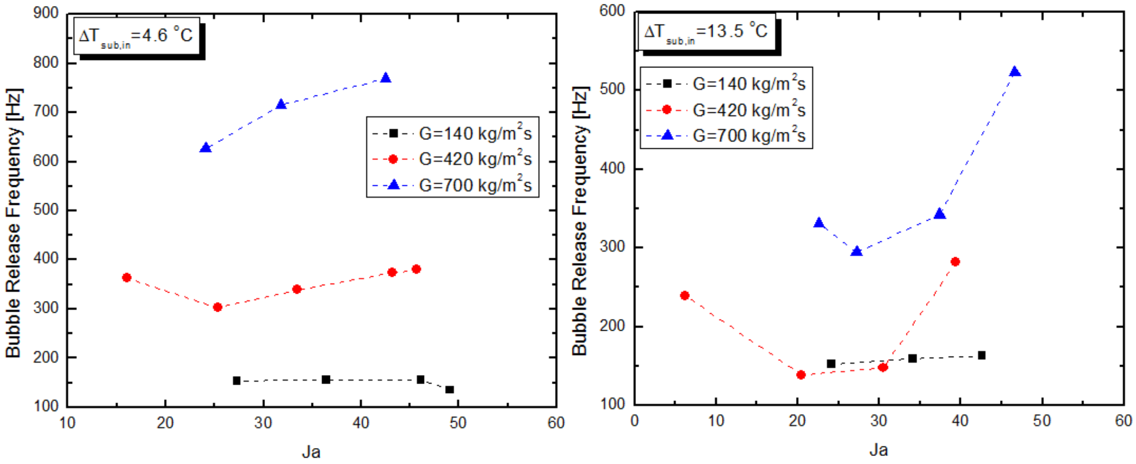

Figure IV-17. Dependence of bubble release frequency on the Ja number

5. Local bubble number variation and evaporative heat flux

The vapor bubbles within the subcooled flow boiling system generally experience processes such as condensation, breakup, and coalescence. Thus, the bubble size as well as the number of bubbles within the system is necessarily affected by those processes. For instance, while the bubbles move through the flow channel after departing from the nucleation site, two different mechanisms can be involved in the bubbles' growing process, i.e., evaporation and coalescence. In many commercial CFD codes employing the wall heat flux partitioning approach [68], the evaporative heat flux (q_e) is calculated by the following relation:

$$q_e = N_a f_b \rho_g h_{fg} \frac{\pi}{6} D_b^3 \qquad \text{(IV-2)}$$

where N_a is the active nucleation site density, f_b is the bubble departure or lift-off frequency, D_b is the bubble departure or lift-off diameter, ρ_g is the vapor density, and h_{fg} is the latent heat of vaporization.

Eq. (IV-2) implies that bubble size, bubble frequency, and the active nucleation site density are the major parameters that must be known in order to evaluate the evaporative heat flux (q_e). The estimation of q_e using Eq. (IV-2) is relatively simple when bubbles are immediately lifted off from the wall when departing from the nucleation site. However, when the bubbles are in the sliding mode after departure as in this study, we should pay more attention to such estimation of q_e because the bubbles can still grow substantially while sliding and often coalescence each other. Specifically, the bubble size and bubble frequency used in Eq. (IV-2) need to be determined by considering the bubble growth while sliding and the growing mechanisms such as evaporation and coalescence within the region of interest. In other words, more specific information about the sliding bubble behaviors under subcooled flow boiling conditions must be taken into consideration in order to evaluate q_e correctly. In this context, we investigated the bubbles' coalescence behavior by observing the variation of local bubble number and bubble frequency through the test channel. The observation was made near the nucleation site $0.41 \leq L/L_0 \leq 0.44$ based on the measurement by HSV 1. Then, q_e was estimated by considering such behavior of sliding bubbles within the region.

To observe the variation of local bubble number, the number of bubbles passing through the axial location close to the nucleation site $L/L_0 \approx 0.41$ and downstream $L/L_0 \approx 0.44$ were counted using the consecutive images of bubbles recorded by HSV 1. In order to track the individual bubbles and the locations of their centers of mass over time, the ImageJ plugin software MTrack2 [66] was utilized, and the output was analyzed based on the in-house post-processing algorithm. For each test condition, about 36,000 consecutive images were analyzed. In most of the test conditions in this study, the number of bubbles hardly varied due to condensation or breakup of bubbles within the region of interest, i.e., $0.41 \leq L/L_0 \leq 0.44$. Noticeable changes in the bubble number due to condensation were found only for Exp. No. 16 in Table IV-1, and no breakup of bubbles was observed in any of present experiments. This means that the number of bubbles varied exclusively due to the coalescence of sliding bubbles. Since there was no breakup of bubbles or other nucleation sites in the heated area, the number of bubbles generated at the single nucleation site decreased monotonically in the upward flow direction because the bubbles merged with each other as they moved through the test channel.

Defining the number of bubbles N as a function of axial location y, the reduction of bubble numbers within the region $0.41 \leq L/L_0 \leq 0.44$ can be represented by the reduction factor R, which can be written as

$$R(y) = 1 - \frac{N(y)}{N_0} \tag{IV-3}$$

where R denotes the reduction factor, *y* is the axial location, N_0 is the number of bubbles released from the nucleation site (i.e., when $y = L/L_0 \approx 0.41$), N(y) is the number of bubbles passing through the axial location y.

The reduction factors obtained under various subcooled flow boiling conditions are presented and compared in Figures IV-18 and IV-19. On the left of Figure IV-18, it is seen that the effect of G on the reduction factor R is obviously inconsistent. However, we found that the varying trend shown in Figure IV-18 (left) is quite similar to that shown in Figure IV-16 presenting the dependence of bubble release frequency on G. Both Figure IV-18 (left) and Figure IV-16 address the same experimental cases. This implies that the reduction factor representing the bubble coalescence behavior within the region $0.41 \le L/L_0 \le 0.44$ is closely related to the bubble release frequency. Specifically, the reduction factor or the bubble coalescence was observed to increase for the cases involving higher bubble release frequency. The right of Figure IV-18 shows that the reduction factor consistently increased as q_w increased. In Figure IV-19, the dependence of the reduction factor on $\Delta T_{sub,in}$ is presented, which shows that the reduction factor tended to decrease as $\Delta T_{sub,in}$ increased. However, the variation of the reduction factor according to $\Delta T_{sub,in}$ shows a slightly different tendency at low G and q_w conditions (i.e., $G=140$ kg/m^{2}s, $q_w=9.5\sim9.7$ kW/m^2). These observations commonly indicate that the effect of q_w and $\Delta T_{sub,in}$ on the bubble reduction factor showed the same trend as their effects on the bubble release frequency (see Figure IV-14 and Table IV-1). That is, the reduction factor representing the bubbles' coalescence behavior near the nucleation site was observed to be enhanced for the test conditions causing higher bubble release frequency. This implies that in such test conditions the bubbles can grow substantially due to the coalescence as well as the evaporation as they slide. Therefore, we can say that the bubble size and bubble frequency measured at the nucleation site are insufficient to correctly evaluate the q_e using Eq. (IV-2). For the proper estimation of q_e, both the varying bubble size and the varying bubble frequency along the flow path should be taken into account as discussed below.

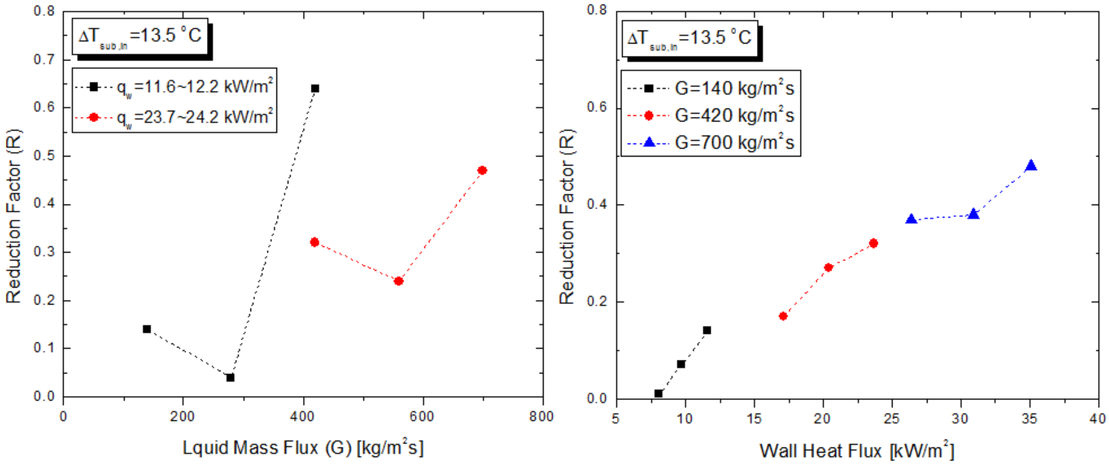

Figure IV-18. Bubble number reduction through the region L/L_0=0.41~0.44 depending on liquid mass flux (G, left) and wall heat flux (q_w, right)

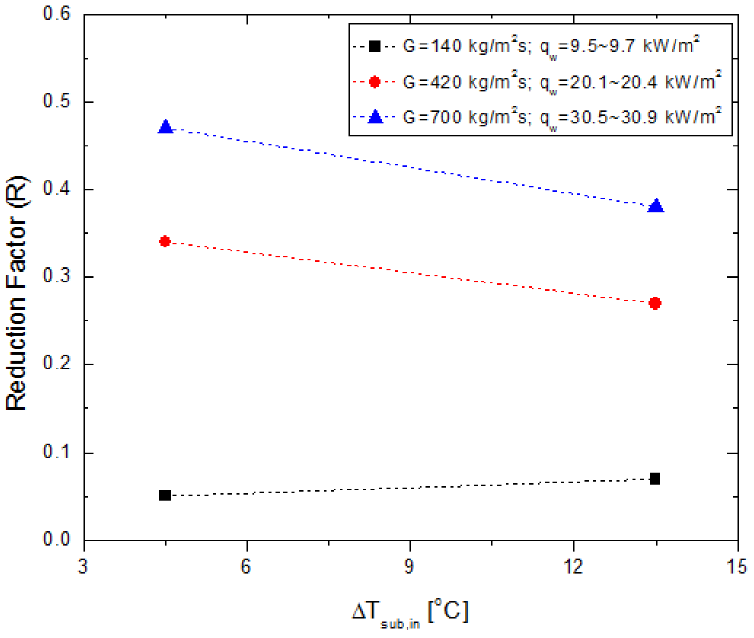

Figure IV-19. Bubble number reduction through the region L/L_0=0.41~0.44 depending on inlet subcooling ($\Delta T_{sub,in}$)

Provided the bubble frequency is defined as the number of bubbles passing through a certain axial location y over the total elapsed time, the bubble frequency can be written as a function of axial location y as follows:

$$f_b(y) = f_{b,0}\frac{N(y)}{N_0} = f_{b,0}[1 - R(y)] \qquad \text{(IV-4)}$$

where $f_{b,0}$ is the bubble release frequency measured close to the nucleation site ($y=L/L_0\approx 0.41$) and $f_b(y)$ is the bubble frequency measured at the axial location y.

Then, the q_e within the region $0.41\leq L/L_0\leq 0.44$ can be estimated by the following relation:

$$q_e = f_b(y_{max})\rho_g h_{fg}\frac{\pi D_{max}^3}{6}\frac{1}{A_h} \qquad \text{(IV-5)}$$

where y_{max} is the axial location where the bubble size reaches its maximum (D_{max}) between $0.41\leq L/L_0\leq 0.44$; D_{max} is the bubble size at maximum within the region of interest; f_b is the bubble frequency; and A_h is the local heated area of interest.

Using both Eq. (IV-5) and the local bubble parameters measured, we estimated the evaporative heat flux occurring within the local region of interest, and the relative portion of evaporative heat flux q_e against the total wall heat flux q_w was evaluated at various subcooled flow boiling conditions. The results are shown in Figures IV-20 and IV-21. As shown on the left of Figure IV-20, the relative portion of evaporative heat flux (q_e/q_w) decreased as G increased at constant q_w and $\Delta T_{sub,in}$. This implies that the bubble growth due to evaporation was suppressed by the subcooled liquid as G became higher. The right side of Figure IV-20 shows that q_e/q_w increased as q_w increased at constant G and $\Delta T_{sub,in}$ conditions. Such increasing trends of q_e/q_w while increasing q_w are shown to be more noticeable at lower G conditions. We also found that even when the bubbles were generated at the nucleation site more frequently at higher G conditions, the relative significance of evaporation stayed low compared to that at lower G conditions. In Figure IV-21, the effect of $\Delta T_{sub,in}$ on q_e/q_w is also presented; q_e/q_w increased as $\Delta T_{sub,in}$ decreased because bubble growth was less restricted by condensation at those conditions due to the higher temperature of bulk liquid in contact with the bubbles. We can see in Figure IV-21 that the effect of varying $\Delta T_{sub,in}$ on q_e/q_w became less distinct at higher G and q_w conditions. Figure IV-21 also shows that q_e/q_w varied more significantly due to the changes in G and q_w at lower inlet subcooling condition, i.e., $\Delta T_{sub,in}$=4.5 °C.

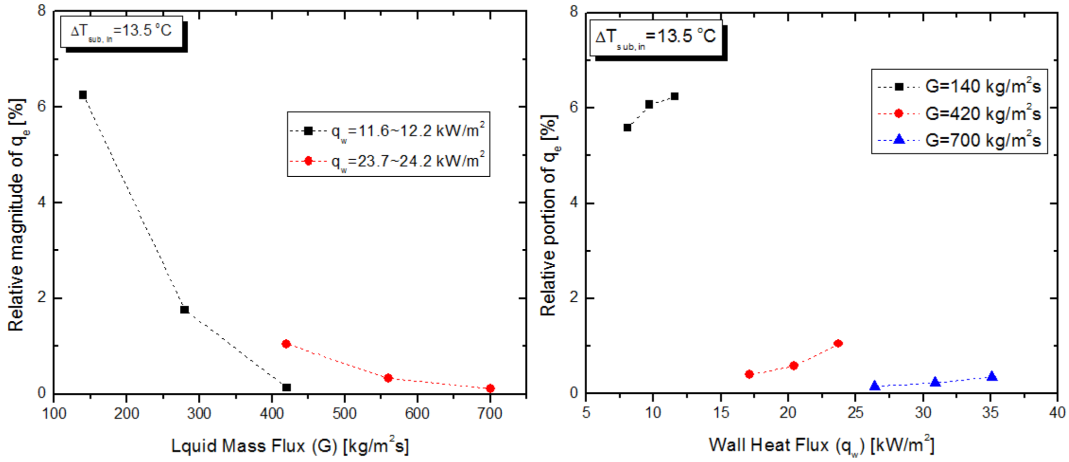

Figure IV-20. Relative portion of local evaporative heat flux (q_e/q_w) depending on liquid mass flux (G, left) and wall heat flux (q_w, right)

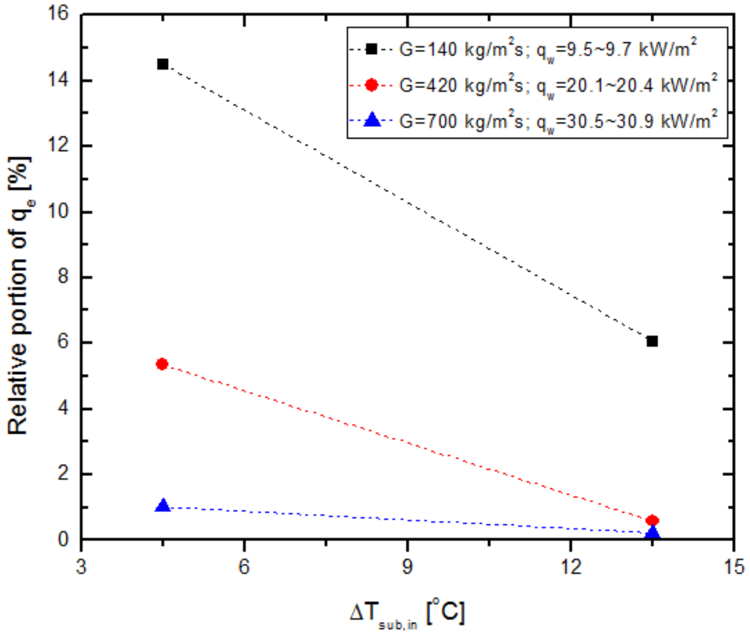

Figure IV-21. Relative portion of local evaporative heat flux (q_e/q_w) depending on inlet subcooling ($\Delta T_{sub,in}$)

D. Summary and conclusions

An experimental investigation of subcooled boiling flow was conducted in a square vertical upward flow channel with a one-sided heater surface using the refrigerant Novec^{TM} 7000. The test section was designed to achieve both enhanced two-phase flow visualization and accurate heater surface temperature measurement. Three high-speed cameras and one IR camera were utilized to observe the bubble behaviors using both micro- and macroscopic views while measuring the heater surface temperature. To avoid the phenomenological complexity resulting from the presence of random nucleation sites as well as the difficulty of visual observation, a single preferential nucleation site was created. This allowed us to clearly observe the boiling behaviors as well as the corresponding wall heat transfer due to changes in (i) inlet subcooling, (ii) liquid mass flux, and (iii) wall heat flux. Another strong feature is that the current experimental results were presented and discussed based on reliable statistics by analyzing the numerous images obtained for each test condition.

This chapter, the first part in a series describing our work shown in Chapters IV and V, focused mainly on discussing the bubble behaviors within the region near the nucleation site $0.41<L/L_0<0.45$. The major findings and conclusions from this study are summarized as follows.

Nucleating and departure behavior

The bouncing motions of bubbles near the nucleation site became more noticeable for the test conditions causing higher wall superheat (i.e., by decreasing inlet subcooling/liquid mass flux or by increasing wall heat flux). Such bubble motions caused the bubble size to fluctuate along the flow path as the bubbles departed from the nucleation site due to condensation by the subcooled bulk liquid until they reattached to the heater surface.

Bubble growth behavior along the flow path

Bubble size increased as the liquid subcooling/liquid mass flux decreased or the wall heat flux increased. However, for a few cases involving significant bubble bouncing motions and/or lift-offs near the nucleation site, this trend was reversed locally. At low liquid mass flux conditions, bubbles grew and subsequently shrank as they slid along the heater surface away from the nucleation site. This was because the condensation effect increased as the bubbles became more exposed to the subcooled bulk liquid while sliding. At high liquid mass flux conditions, however, the bubbles grew almost consistently along the flow path.

Axial bubble velocity along the flow path

Axial bubble velocity became higher as the inlet subcooling or the liquid mass flux decreased or the wall heat flux increased. That is, the test conditions causing larger bubbles led to higher axial bubble velocity within the region observed by HSV 1. From this, we concluded that buoyancy is the dominant factor in determining axial bubble velocity near the nucleation site. Comparing the axial bubble velocity to the bulk liquid velocity (u_{liq}), the axial bubble velocity tended to be higher than u_{liq} at low liquid mass flux conditions, while the opposite trend was found at high liquid mass flux conditions.

Bubble release frequency

Unlike bubble size and axial bubble velocity, the bubble release frequency often varied inconsistently relative to changes in inlet liquid subcooling, liquid mass flux, and wall heat flux. Based on the present experimental evidence, we contend that the competing process between single-phase convection and bubble-induced heat transfer modes (i.e., evaporation and quenching) was the major reason for such observations.

Local bubble number variation

The number of bubbles produced at the single nucleation site monotonically decreased along the flow path, and the main mechanism for this pattern was found to be the coalescence of sliding bubbles. The decrease in bubble number near the nucleation site became more noticeable for the test conditions causing higher bubble release frequencies.

Evaporative heat flux

By considering the bubble growth and coalescence behavior within the region $0.41 \leq L/L_0 \leq 0.44$, the evaporative heat flux (q_e) was calculated for each test condition and the relative magnitude q_e/q_w was compared. The proportion q_e/q_w was found to decrease as the inlet subcooling or liquid mass flux increased or the wall heat flux decreased. However, for the test cases involving high liquid mass flux, q_e/q_w varied less relative to the changes in wall heat flux (q_w) or inlet subcooling ($\Delta T_{sub,in}$).

Overall, the axial velocity of bubbles after departing from the nucleation site was proportional to the bubble size near the nucleation site. Besides, the bubble release frequency was observed to be the critical factor affecting the bubbles' coalescence at this region. Another finding was that the variation of bubble release frequency due to changes in inlet subcooling or wall heat flux was less noticeable at lower liquid mass flux conditions, whereas more variations of q_e/q_w occurred in such parametric studies.

CHAPTER V

EXPERIMENTAL OBSERVATION ON BUBBLE DYNAMICS AND WALL HEAT TRANSFER ARISING FROM A SINGLE NUCLEATION SITE AT SUBCOOLED FLOW BOILING CONDITIONS – PART 2: MACROSCOPIC OBSERVATION OF BUBBLE BEHAVIORS AND WALL HEAT TRANSFER

A. Introduction

The enhancement in wall heat transfer caused by boiling and its underlying mechanism has been a topic of great interest within the heat transfer community over the last half century. In particular, forced convective boiling, the focus of this study, is frequently encountered in various industrial applications such as cooling channels and evaporators of engineered systems. However, the boiling heat transfer mechanism is yet to be fully understood, and achieving accurate prediction of the process mechanistically is still a challenge due to the lack of knowledge about the basic principles.

In previous boiling studies, as an efficient way to analyze and predict the boiling heat transfer, the total heat transfer has been often formulated as the sum of subcomponents. In empirical approaches, one of the earliest models to describe the total boiling heat flux with the combined effects of single-phase convection ($q_{1\O}$) and bubble motions (q_B) was proposed by Rohsenow [69]; a similar approach was taken by Bowring [70]. This superposition method was originally suggested in an effort to provide a smooth predictive boiling curve over a wide range of forced convective boiling regimes, from single-phase forced convection to fully developed boiling. Later, this modelling concept was employed by many researchers to develop empirical correlations that can be used to predict the total wall heat flux in various flow boiling circumstances [71-75].

The partitioning of total wall heat flux has been also attempted in empirical correlations which mainly aimed to predict the bulk void fraction in different regimes of forced convective boiling [70, 76-78]. In particular, Bowring [70] firstly devised a model considering four sub-processes of boiling heat transfer, including the effect of (i) single-phase convection, (ii) evaporation, (iii) bubble agitation (or quenching), and (iv) condensation (this is normally neglected). In this model, the (ii) and (iii) were originally defined as a function of fundamental bubble parameters such as bubble release frequency, active nucleation site density, and bubble departure diameter. However, due to the difficulties of measuring such parameters at that time, Bowring [70] proposed a way to estimate the wall heat flux components rather macroscopically by introducing an empirical parameter characterizing the ratio between (ii) and (iii).

Recently, advances in computing power and high-speed visualization technique have made it possible to investigate more detailed features of two-phase flow during the boiling process. As a consequence, recent experimental efforts have been made to observe fundamental features of boiling which could hardly be captured before. This has opened up the possibility of utilizing mechanistic models which are expected to have more generality in application than the previous empirical correlations. Among others, the mechanistic model developed by Kurul and Podowski [68] has been one of the most widely used until recently. This model basically employed the wall heat flux partitioning concept of Bowring [70], in which three subcomponents are included to represent the total wall heat flux (q_w): single-phase convection ($q_{1Ø}$), transient conduction (or quenching, q_Q), and evaporation (q_e). Kurul and Podowski [68] used q_Q as defined in Delvalle and Kenning [79] while q_e is calculated by the relation given by Bowring (1962). In order for this mechanistic model to possess high confidence in predictive ability, the fundamental bubble parameters used to calculate each subcomponent should be well-defined, and this is where experimental insight plays a critical role. In general, the bubble departure/lift-off diameter [3, 8, 11], bubble release frequency [9, 10], and active nucleation site density [80] are the parameters commonly used to determine the heat flux components q_e and q_Q. As discussed in Chapter II (or [57]), these fundamental bubble parameters (or wall nucleation parameters) should be measured with care to avoid misleading experimental results and consequently misleading conclusions.

Compared to the boiling behaviors at the nucleation site (e.g., nucleation, bubble growth and departure), bubble dynamics after departure from the nucleation site such as bubble sliding have been relatively less explored in experimental studies of forced convective boiling to date. However, several authors have reported that such bubble motions can substantially influence the wall heat transfer characteristics in a flow boiling system. Cornwell [81] measured the wall heat transfer of the forced convective boiling of R-113 in a tube bundle. He supposed that the total heat transfer is determined by three mechanisms: liquid forced convection, nucleation, and sliding bubbles. The relative significance of each mechanism was found to depend on heat flux conditions as well as locations within the tube. Cornwell [81] argues that, in the presence of bubbly flow, the sliding bubbles downstream in the tube contributed significantly to the wall heat transfer enhancement. Thorncroft et al. [6] observed a significant difference in bubble dynamics between the boiling experiments of vertical upward and downward flows. In upward flows, the bubbles departing from the nucleation site typically slid along the heater surface without lift-off; whereas, in downward flows, the bubbles lifted off directly from the nucleation site or lifted off after sliding.

From the observation of larger heat transfer coefficients for upward flow compared to those for downward flow under identical experimental conditions except for flow direction, Thorncroft et al. [6] deduced that such increases in wall heat transfer for the upward flow result from the bubble sliding behavior. Regarding this, further experimental evidence was provided by Thorncroft and Klausner [82], in which the turbulence enhancement of the bulk liquid was considered the main mechanism for the increasing wall heat transfer caused by sliding bubbles. A similar observation was also made by Houston and Cornwell [83]; they argued that the effect of increasing turbulence caused by sliding bubbles is more significant within a narrow channel than in an ordinary sized channel.

The above mentioned studies revealed the significance of sliding bubble motions on wall heat transfer in a forced convective boiling system and have subsequently inspired further research employing high-speed visualization techniques. Okawa et al. [84] observed the rise characteristics of bubbles after departure from a nucleation site in a vertical upward subcooled flow boiling tube. Three different bubble rise characteristics were observed, which included (i) bubbles sliding for a long distance, (ii) bubbles lifting-off from the heater surface after sliding a few millimeters, and (iii) bubbles lifting off but subsequently reattaching to the heater surface. Okawa et al. [84] proposed that the bubble lift-off is mainly attributable to the bubble shape deformation. Yuan et al. [85] studied the effects of pressure on bubble dynamics during a subcooled flow boiling experiment in a vertical rectangular narrow channel. The bubble behavior captured by a high-speed camera showed that pressure had a significant effect on bubble growth, lift-off, and sliding. Under lower pressure, bubbles growing at the nucleation site lifted off directly from the heater wall and collapsed without sliding. In contrast, bubbles under higher pressure kept growing while sliding along the heater wall even after the bubbles left (or departed from) the nucleation site. They also found that sliding bubble velocity as well as sliding distance was significantly affected by the bubble growth rate while sliding. Xu et al. [86] observed sliding bubble dynamics in the vertical upward flow of a narrow channel. Several sliding bubble parameters such as bubble shape, bubble growth, and bubble velocity after departing from the nucleation site, were investigated. They found that the contact angles of the bubbles hardly changed during the sliding motion, and the sliding bubble velocity showed a proportional relation to the bubble diameter and liquid flow rate. Similarly, Li et al. [59] investigated the bubble sliding behaviors in subcooled boiling flow in a vertical narrow channel. The parameters of main interest were the bubble number, bubble size, and sliding bubble velocity. In particular, they studied both the mean and the statistical distribution of such parameters under different experimental conditions. According to them, the bubble size distribution depended significantly on the inlet subcooling and was less affected by the wall heat flux. They also found that the distribution of sliding bubble velocity followed the normal distribution and the mean velocity increased when the inlet subcooling decreased.

However, despite the efforts by previous investigators, experimental insight about bubble dynamics after departure from nucleation site is still lacking, and the mechanism of enhancing wall heat transfer due to the bubble motions like sliding is not understood well enough. In this context, we investigated various aspects of bubble dynamics after departure from a nucleation site in vertical upward subcooled flow boiling channel. The observation of bubbles was made with a relatively low-resolution camera HSV 3 used in the present subcooled flow boiling experiments described in Chapter IV to capture the bubble motions over a large area of flow path; this is distinguished from the observation of detailed bubble motions near the nucleation site with a high-resolution camera HSV 1. Also, special effort was made to better characterize the bubble behaviors as well as wall heat transfer along the flow path by analyzing numerous images. As discussed in Chapter IV, this will reduce the uncertainty of statistical averages obtained from the current experiments and thus improve the reliability of results.

This chapter is the second part study with the subcooled flow boiling experiment, following the first part study described in Chapter IV. The overall description of the experimental facility, the test conditions, and the visualization and data analysis strategies have been described in detail in Chapter IV. In the following sections, after describing the specific interests of this chapter based on the measurements by a HSV 3 and infrared (IR) thermometry (section B), the reliability of the measurements (section

C), the experimental uncertainties (section D), and the experimental results (section E) are discussed.

B. Main interests of present study

The discussion in this chapter is based on the observation of bubbles by HSV 3 which captured the bubble behaviors from the top of bubbles (i.e., top view, with the heater wall defined as the bottom) over a large area of flow path. The cameras arrangement, including HSV 3, in the present subcooled flow boiling experiment is described in Chapter IV. Figure V-1 shows the representative bubble images captured by HSV 3, the axial location of single nucleation site ($L/L_0 \approx 0.41$) within the view (L_0 is the total heated length, L_0=224 mm; L is the axial location within the heated length, $0 \leq L \leq L_0$), and the image analysis procedure.

The spatial and temporal resolutions used in HSV 1 (9.09 μm, 10 kHz), the experimental results of which are discussed in Chapter IV, were higher than those of HSV 3 (78.7 μm, 0.5 kHz). This posed a significant challenge to HSV in capturing the local and fast boiling characteristics close to the nucleation site. For instance, the fluctuating bubble size caused by the bouncing motions of bubbles near the nucleation site (i.e., $0.41 < L/L_0 < 0.42$) was hardly captured by HSV (section E.1) while such behaviors were captured in detail by HSV 1 as discussed in Chapter IV. In addition, the measurement perspective of HSV 3 (i.e., top view) may limit observation of the bubble departure process at the nucleation site as discussed in Chapter II or [57]. Nevertheless, except for such local and fast motions of bubbles near the nucleation site, HSV 3 can provide useful information about bubble behaviors over a larger area of flow path while the observation view of HSV 1 was limited to a smaller area. Specifically, as shown in Figure V-1, the measurement view of HSV 3 covered the test channel region $0.39<L/L_0<0.75$ (≈81 mm), which is approximately 9 times larger than that of HSV 1, $0.41<L/L_0<0.45$ (≈9 mm). This implies that by utilizing this macroscopic view of HSV 3, bubble behaviors downstream in the test channel such as sliding bubble motions after departure from a nucleation site can be observed; and we discuss the experimental results in this chapter. In particular, we investigated the axial development of the bubble behaviors (i.e., bubble growth while sliding, axial bubble velocity, bubble number variation, bubble size distribution) within the view captured by HSV 3 based on the reliable statistics obtained from the data (i.e., image) acquisition and analysis strategy shown in Figure V-1.

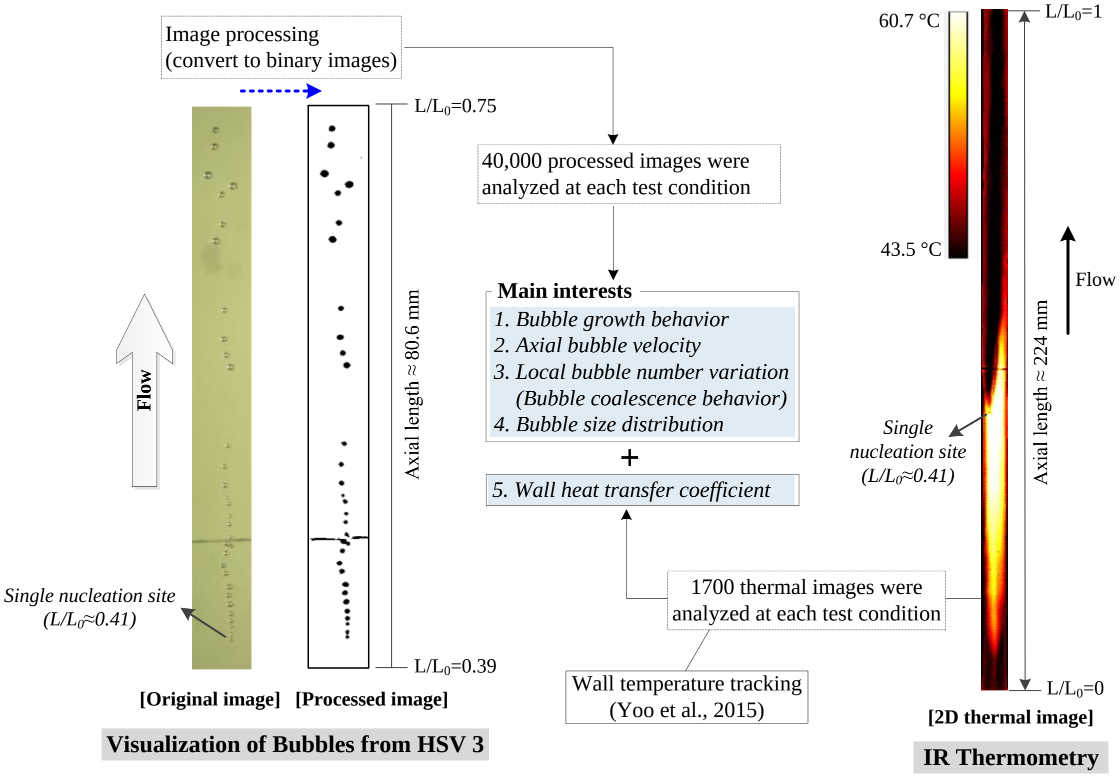

Figure V-1. Measured parameters of interest and the image analysis procedures

In addition, in the present experiment, the heater surface temperature was measured over the entire heated area (7.5×224 mm^2) using IR thermometry while capturing the bubble behaviors by high-speed video cameras. Since the bubble behaviors through the test channel affect the wall heat transfer along the heater surface significantly, understanding the relationship between such bubble dynamics and the corresponding wall heat transfer in subcooled boiling flow is obviously important. Therefore, we also discuss such relationship in this chapter based on the measurements of the bubble behaviors and the heat transfer parameters (i.e., heater surface temperature and local heat flux). Particularly, the axial variation of local heat transfer coefficients depending on various boiling characteristics at a single nucleation site was investigated. In Figure V-1 (right), the representative 2-D thermal image obtained by IR thermometry and the post-processing procedure are briefly described. Also, all the parameters of interests explored in this chapter are summarized in Figure V-1.

C. Repeatability test

To evaluate the reliability of statistics for the measured parameters obtained by taking the data acquisition strategy shown in Figure V-1, a repeatability test was conducted for one of the subcooled flow boiling test conditions within the present set of experiments described in Chapter IV. In particular, we focus here on the four parameters measured by HSC 3 and IR thermometry: bubble growth behavior along the flow path, axial bubble velocity, the distribution of bubble size, and the time-averaged heater surface (wall) temperature profile. Considering the inherently stochastic nature of boiling, the statistical averages of such parameters measured in the current facility are expected to have some uncertainty depending on the sample size and the statistical variation. Of course, if the sample size is large enough compared to the statistical variation, such uncertainty will be reduced, which will necessarily lead to improved repeatability of statistics obtained from the separate measurements.

Figure V-2 shows the results of repeatability tests 1 and 2, performed separately under identical test conditions. All the measured parameters of interest show quite good agreement between the repeatability tests 1 and 2. This implies that the characteristics of bubble behaviors as well as of the wall heat transfer through the test channel can be well-represented at the given test condition while employing the current data acquisition strategy, and that the uncertainty introduced by the randomness (or stochastic feature) of the measured data is negligibly small. In other words, the sample size used is large enough to ensure reliable statistics.

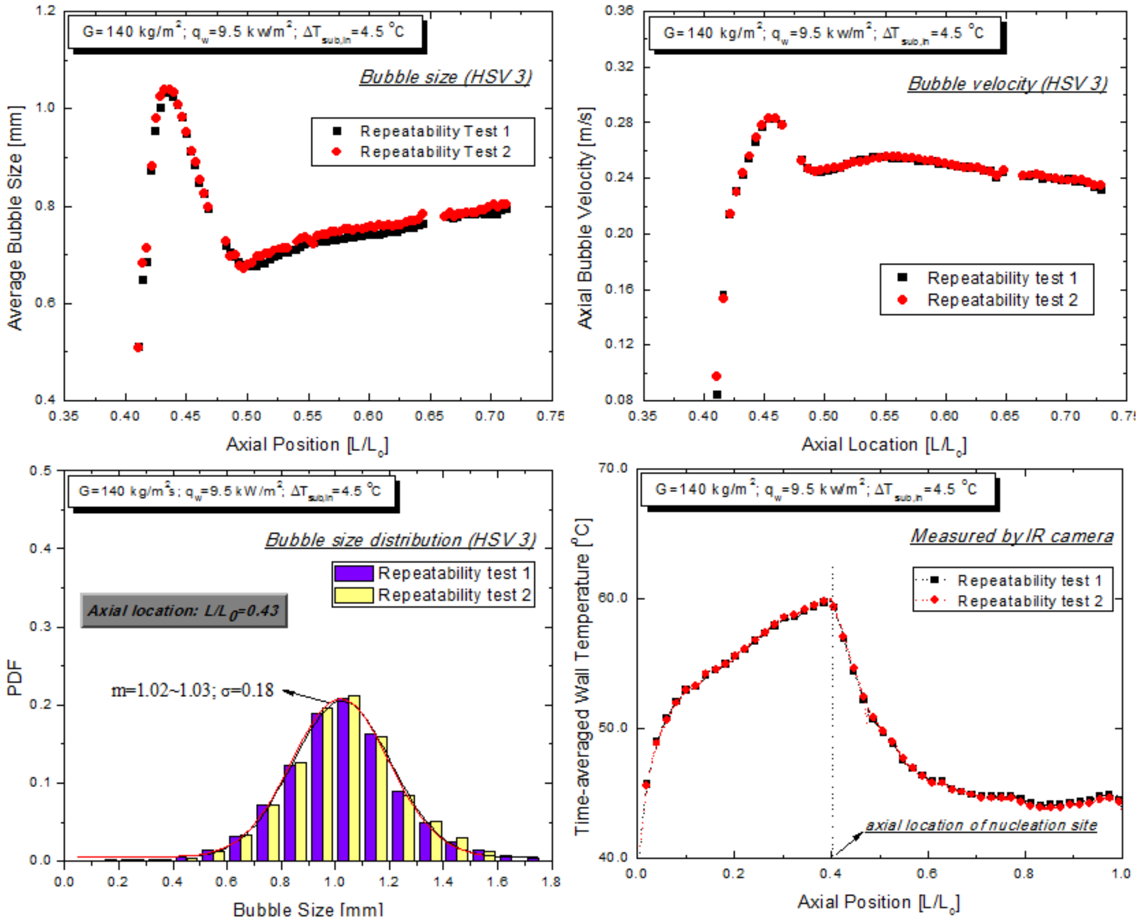

Figure V-2. Repeatability tests on the parameters measured in present study

D. Measurement uncertainty (for HSV 3 and IR thermometry)

We discussed in Chapter IV that the limited sample size (i.e., number of bubbles) is one of the major sources of uncertainty for the bubble size measurement by HSV 1. However, as discussed in Section C, this is not the case for the bubble size measurement by HSV 3, and the main reason is that the number of samples (i.e., bubbles) taken by HSV 3 was much larger due to the longer period of measurement time (80 sec) than that of HSV 1 (3.6 sec). Instead, the relative significance of spatial resolution used in HSV 3 (78.7 μm) and the random errors introduced by the user-dependent image processing algorithm become more important to the final determination of uncertainty. Thus, by combining such sources of uncertainty [25], the uncertainty of bubble size measurements based on HSV 3 was determined to be 153.9 μm.

In a similar context, the random error associated with the statistical variation of the axial bubble velocity was ignored for the uncertainty estimation of axial bubble velocity measured by HSV 3. Instead, the uncertainty was calculated by considering the spatial and temporal resolution of HSV 3 according to the uncertainty propagation method [25]. Consequently, the uncertainty of axial bubble velocity was estimated as 5.6×10^{-2} m/s.

The uncertainty analysis for the temperature measurement of the heating surface (i.e., the ITO film) through the multi-layer heater wall was performed and described in Chapter III or [64]. However, during the present work an additional polyimide tape was attached to the ITO film as described in Chapter IV. Thus, the uncertainty associated with the thermal properties of the elements composing the polyimide tape was additionally considered, i.e., ±0.01 W/m-K was used as the uncertainty for the thermal conductivity of the polyimide film and the silicone adhesive. Consequently, the uncertainty for the heater surface temperature measurement was determined to be 0.77 °C. The experimental uncertainty for the heat flux measurement was estimated as 0.6 kW/m^2.

E. Experimental results and discussion

1. Bubble growth behavior

This section discusses bubble growth behaviors along the upward flow path depending on the changes in inlet subcooling ($\Delta T_{sub,in}$), wall heat flux (q_w), and liquid mass flux (G) based on the measurements by HSV 3. The bubbles were observed from the nucleation site at $L/L_0 \approx 0.41$ downstream to $L/L_0 \approx 0.75$; the bubbles were largely observed to be in sliding mode in this section of the test channel during this study. To analyze the numerous images of bubbles taken by HSV 3, the observed flow path shown in Figure V-1 (left) was first partitioned into 100 sectors. Then, the size of the bubbles captured within each sector at each frame was analyzed over the whole measurement period (40,000 images in 80 s). From this, the average bubble size in each of the 100 sectors at different axial locations was obtained for each test condition. For this analysis, the macro function of ImageJ [29] was utilized to identify both the bubbles' center of mass location and their size. To avoid errors caused by poor image quality after image processing, only bubbles satisfying the shape criterion of circularity>0.6~0.65 were taken into account for the analysis. Typically, $10^3 \sim 10^4$ order of bubble images were used to estimate the average bubble size within each sector. Bubble size was defined as the equivalent diameter based on the 2D projection of bubble images captured by HSV 3. As discussed in section B, the local and rapid fluctuation of bubble size due to the bouncing motions of bubbles near the nucleation site, $0.41<L/L_0<0.42$, observed by HSV 1, was barely observed by HSV 3 due to the resolution used.

In Figure V-3, the effect of $\Delta T_{sub,in}$ on bubble growth behaviors in the direction of flow is presented. Specifically, the bubble growth behaviors at the two different inlet subcooling conditions (i.e., $\Delta T_{sub,in}$=4.5 and 13.5 °C) were compared while G and q_w were kept constant; such comparison was made for the three different G and q_w as shown in Figure V-3. On the top left side of Figure V-3, the bubble growth behaviors for the two $\Delta T_{sub,in}$ are compared at low G and q_w (i.e., G=140 kg/m^{2}s; q_w=9.5~9.7 kW/m^2). Bubbles in the both cases grew fast near the nucleation site, and after reaching a maximum size at about $L/L_0\approx0.43$, the bubbles began to shrink significantly. Subsequently, at about $L/L_0\approx0.45$ for $\Delta T_{sub,in}$=13.5 °C and $L/L_0\approx0.5$ for $\Delta T_{sub,in}$=4.5 °C, the bubbles started growing again as they moved downstream. We found that the bubbles in the lower inlet subcooling condition (i.e., $\Delta T_{sub,in}$=4.5 °C) grew much faster near the nucleation site ($L/L_0<0.43$) compared to those in the higher inlet subcooling condition (i.e., $\Delta T_{sub,in}$=13.5 °C). This difference is attributed to the fact that both the heater surface temperature and the bulk liquid temperature around the bubbles increased as the liquid subcooling was reduced. The top left graph in Figure V-3 shows that the size of bubbles at $\Delta T_{sub,in}$=4.5 °C decreased for a longer distance in the direction of flow after the bubble size reached the maximum about $L/L_0\approx0.43$. This decreasing bubble size implies that, while the bubbles passed through this region, the condensation effect increased relative to evaporation; such augmentation of condensation resulted from the fact that the bubbles became more exposed to the subcooled bulk liquid while growing. That is, the relative magnitude between evaporation and condensation changed during the bubbles' growth after departure from the nucleation site, which plays an important role in determining the bubble growth behavior shown in the top left graph in Figure V-3. As expected, the decrease in $\Delta T_{sub,in}$ at constant G and q_w caused the higher temperature of the heater surface. This leads to higher rate of bubble growth because stronger evaporation occurs within the superheated liquid layer beneath the bubbles. As a result, the bubbles at $\Delta T_{sub,in}$=4.5 °C grew faster until $L/L_0 \approx 0.43$. But once the condensation effect became dominant and began to control the bubble size at $L/L_0 > 0.43$, the bubbles shrank over a longer distance at $\Delta T_{sub,in}$=4.5 °C, as shown in the top left graph of Figure V-3. This is because the bubbles moved faster in the upward flow direction at the lower subcooling condition (see section E.2). In Figure V-3, we can see that such a large increase and subsequent decrease (i.e., fluctuation) of bubble size along the flow path occurred only for the cases of low G and q_w (i.e., G=140 kg/m^{2}s; q_w=9.5~9.7 kW/m^2) shown on the top left of Figure V-3. This suggests that under these conditions the bubbles readily reached a point where significant changes took place between evaporation and condensation, resulting from the rapid bubble growth after departure from the nucleation site.

In both experimental cases shown in the top left of Figure V-3, it is seen that the bubbles grew slowly downstream following the significant fluctuation of bubble size and that the bubble size between the two cases became comparable at $L/L_0>0.65$. Regarding this observation, we found that both the coalescence and the lift-offs of sliding bubbles depending on inlet subcooling conditions affected such bubble growth behavior downstream in the test channel. Specifically, the bubbles observed were more likely to coalesce at $\Delta T_{sub,in}=13.5$ °C, which enhanced bubble growth while sliding along the flow path (see top left of Figure V-9). Meanwhile, the bubbles at $\Delta T_{sub,in}=4.5$ °C lifted off from the heater surface more often after sliding a distance, which caused the bubble shrinkage downstream in the test channel (at about $L/L_0>0.6$). As a consequence, the average bubble size measured at the two different subcooling conditions became comparable at $L/L_0>0.65$, despite the significant differences upstream. The details about the bubbles' coalescence behavior are discussed in section E.3.

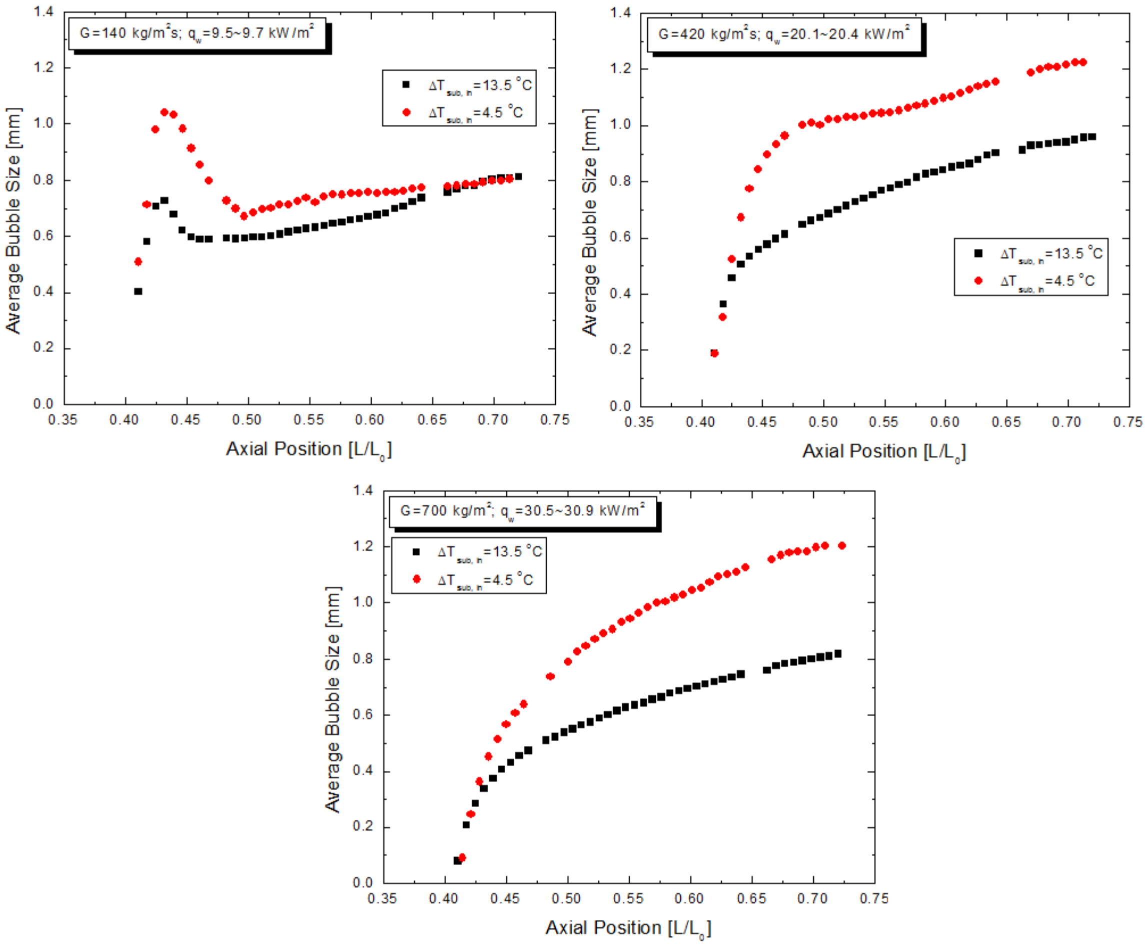

Figure V-3. Effects of inlet subcooling ($\Delta T_{sub,in}$) on bubble growth along the flow path

On the top right of Figure V-3, a similar comparison was made for the two different $\Delta T_{sub,in}$ at higher G and q_w (i.e., G=420 kg/m^{2}s; q_w=20.1~20.4 kW/m^2). As expected, bubbles at $\Delta T_{sub,in}$=4.5 °C grew faster due to the higher heater surface temperature as well as the higher bulk liquid temperature. However, such a large fluctuation of bubble size shown in the top left of Figure V-3 was not found. Instead, we can see a noticeable slope change at about $L/L_0 \approx 0.43$ for $\Delta T_{sub,in}$=4.5 °C and $L/L_0 \approx 0.48$ for $\Delta T_{sub,in}$=13.5 °C. On the bottom of Figure V-3, the bubble growth behaviors for the two different $\Delta T_{sub,in}$ were compared at the highest G and q_w conditions tested (i.e., G=700 kg/m^2s; q_w=30.5~30.9 kW/m^2). Bubbles for the both cases grew smoothly through the entire flow path observed. We can see here that the difference in bubble size between the two cases gradually increased along the flow path, which is different from the other comparisons shown in Figure V-3.

In Figure V-4, bubble growth behaviors along the flow path depending on changes in G while q_w and $\Delta T_{sub,in}$ were kept constant are shown. The left side of Figure V-4 shows that varying G caused the bubbles to experience different growth processes along the flow path. Specifically, for the lowest G (140 kg/m^2s), bubble size sharply increased and subsequently decreased at the upstream region near the nucleation site $L/L_0<0.5$, after which the bubbles grew steadily through the rest of the test channel. However, such fluctuation in bubble size near the nucleation site was significantly reduced by increasing the G to 280 kg/m^2s, and when the G increased to 420 kg/m^2s, the bubbles grew steadily along the flow path. Note that increasing G causes a decrease in heater surface temperature while condensation heat transfer between bubbles and subcooled bulk liquid is enhanced. Thus, we can expect that the bubble's growth process will be restricted more as G increases. Consequently, we can see in Figure V-4 that as G increased, the bubbles grew more slowly after departing from the nucleation site. Interestingly, however, the left side of Figure V-4 shows that as the bubbles passed $L/L_0\approx0.48$, the bubble size measured at G=280 kg/m^2s became larger than that measured at G=140 kg/m^2s. This is because, after the fluctuation of bubble size upstream, the bubbles measured at G=280 kg/m^2s recovered the increasing trend of bubble size along the flow path earlier than those measured at G=140 kg/m^{2}s. That is, the different bubble growth behavior upstream in the test channel near the nucleation site significantly affected the bubble size downstream.

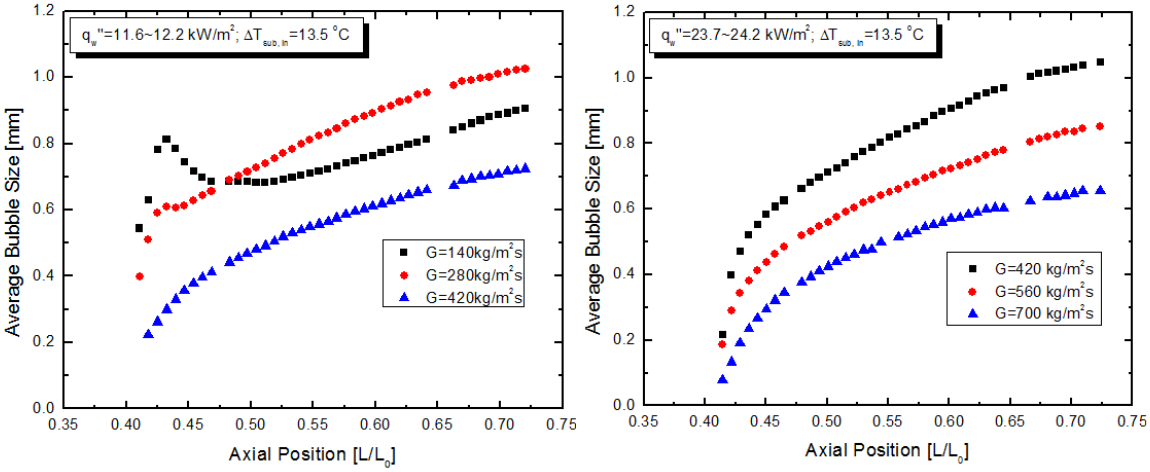

Figure V-4. Effects of liquid mass flux (G) on bubble growth along the flow path

Figure V-5 shows bubble growth behaviors along the flow path depending on changes in q_w. As expected, the increase in q_w at constant G and $\Delta T_{sub,in}$ caused higher heater surface temperature beneath the bubbles. Thus, the sliding bubbles at higher q_w were observed to be larger within the entire flow path observed, as shown in both left and right of Figure V-5. However, it is noted that, in the left of Figure V-5, the difference in bubble size between the two cases of different q_w was reduced downstream compared to the difference upstream near the nucleation site. As discussed before, this resulted from the fluctuations in bubble size. Specifically, for the higher q_w (11.6 kW/m^2), we can see that bubble size decreased over a longer distance after the maximum size was reached at about $L/L_0 \approx 0.43$. However, bubbles at q_w=8.1 kW/m^2 recovered the increasing growth trend along the flow path earlier, which resulted in reduced differences in downstream bubble size between the two cases shown in the left of Figure V-5.

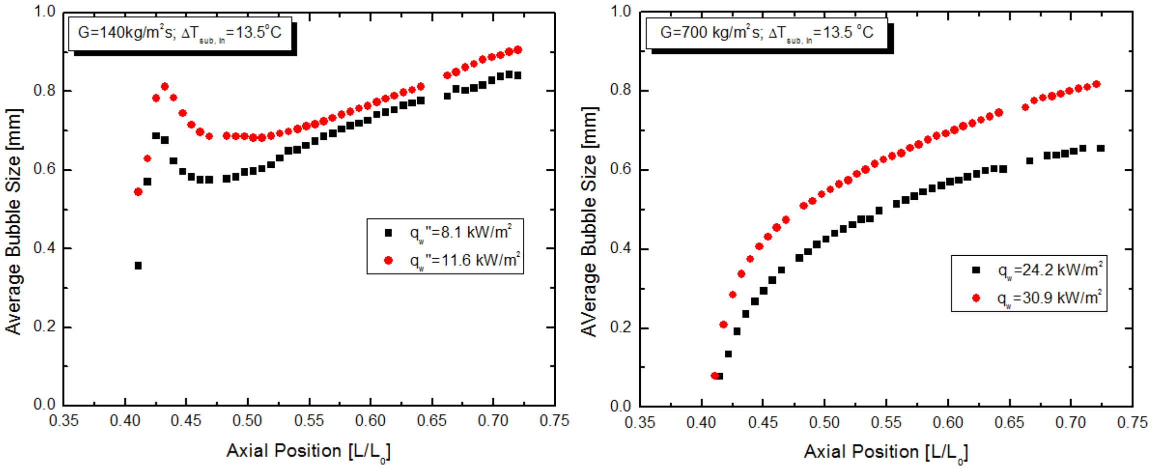

Figure V-5. Effects of wall heat flux (q_w) on bubble growth along the flow path

2. Axial bubble velocity

This section discusses the variation of axial bubble velocity, which depends on $\Delta T_{sub,in}$, q_w, and G, for the same experimental cases discussed in Section E.1. For the analysis, the axial flow path viewed from HSV 3 was partitioned into 200 sectors. Then, each bubble moving along the flow path within the view was analyzed over the whole measurement period (80 sec); from this analysis, the average axial bubble velocity at each sector was obtained for each test condition. It is noted the bubble velocity presented in this section based on the measurements by HSV 3 may have substantial error near the nucleation site (i.e., $L/L_0 \leq 0.42$) due to the limited resolution of HSV 3 (500 Hz, 78.7

μm). More precise results for the axial bubble velocity at this region should be obtained by applying a higher resolution of camera HSV 1, as discussed in Chapter IV.

In Figure V-6, the effect of $\Delta T_{sub,in}$ on axial bubble velocity along the flow path is presented. All the cases included in Figure V-6 correspond to those shown in Figure V-3 describing the bubble growth behavior along the flow path.

On the top left of Figure V-6, it is seen that axial bubble velocity at $\Delta T_{sub,in}$=4.5 °C increased faster initially in the direction of flow after departure from the nucleation site compared to axial bubble velocity at the higher liquid subcooling condition, $\Delta T_{sub,in}$=13.5 °C. Also, we can find that, in both cases, the axial bubble velocity decreased after reaching the maximum at $L/L_0 \approx 0.44 \sim 0.46$; this looks similar to the fluctuating bubble size (i.e., increase and subsequent decrease in bubble size while sliding) shown in Figure V-3 (top left). Subsequent to the fluctuation, the axial bubble velocity at $\Delta T_{sub,in}$=4.5 °C continued to slowly increase; whereas, the bubble velocity at $\Delta T_{sub,in}$=13.5 °C decreased slightly after $L/L_0 \approx 0.55$. This variation of axial bubble velocity along the flow path looks similar to the bubble growth behavior shown in Figure V-3 (top left). This indicates that the buoyancy force aiding the bubbles' upward motion in the direction of flow affected the axial bubble velocity. Specifically, it is expected that the buoyancy force significantly increase during the rapid bubble growth within the region close to the nucleation site, which leads to a sharp increase in axial bubble velocity at that region. Also, for this reason, the bubbles at the lower inlet subcooling condition ($\Delta T_{sub,in}$=4.5 °C) were accelerated more after departure from the nucleation site than those at the higher inlet subcooling condition ($\Delta T_{sub,in}$ =13.5 °C) because the bubbles at the lower subcooling condition grew faster, as shown in Figure V-3 (top left). Similarly, the fluctuation of axial bubble velocity within the region $L/L_0 \approx 0.43 \sim 0.50$, shown in Figure V-6 (top left), can be considered the result of the fluctuating bubble size while sliding shown in Figure V-3 (top left).

The top left of Figure V-6 also shows that the axial bubble velocity at $\Delta T_{sub,in}=4.5$ °C tended to decrease slightly at $L/L_0>0.55$ instead of increasing, which is considered to be related to the decrease in bubble size around that region as shown in Figure V-3 (top left). In the top left of Figure V-6, bulk liquid velocity (u_{liq}) is also presented as blue dash-dot line, from which we can see that the axial bubble velocity at the two different $\Delta T_{sub,in}$ were almost always higher than the u_{liq} within the flow path observed by HSV 3.

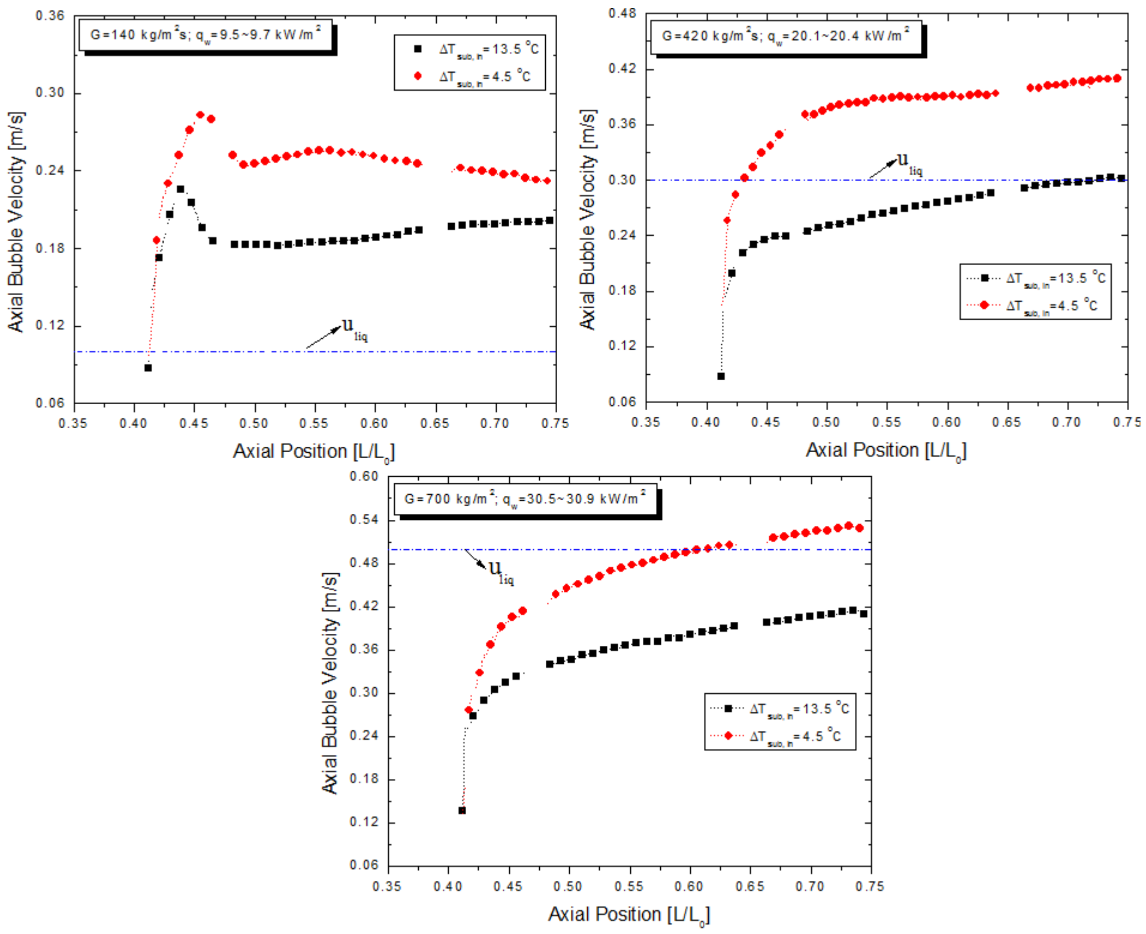

Figure V-6. Effects of inlet subcooling ($\Delta T_{sub,in}$) on axial bubble velocity

On the top right of Figure V-6, axial bubble velocity at the two different $\Delta T_{sub,in}$ is also compared; this comparison was made at higher G and q_w than those shown on the top left of Figure V-6. The experimental cases used on the top right of Figure V-6 are the same as the ones used on the top right of Figure V-3 presenting the bubble growth behavior. The top right of Figure V-6 shows that the axial bubble velocity at $\Delta T_{sub,in}$=4.5 °C was higher than that measured at $\Delta T_{sub,in}$=13.5 °C. As discussed before, this occurs because the larger bubbles at the lower liquid subcooling condition caused the bubbles to move faster in the upward flow direction due to the enhanced buoyancy force (see top right of Figure V-3). Comparing the axial bubble velocity with u_{liq} shows that the axial bubble velocity at $\Delta T_{sub,in}$=4.5 °C was lower than u_{liq} near the nucleation site ($L/L_0<0.43$), but it subsequently exceeded u_{liq} as the bubbles moved downstream. However, the axial bubble velocity at $\Delta T_{sub,in}$=13.5 °C was almost always lower than the u_{liq} within the flow path observed, but the difference between the axial bubble velocity and u_{liq} became smaller and finally became negligible at $L/L_0>0.70$.

The other parametric study for $\Delta T_{sub,in}$ is shown on the bottom of Figure V-6, in which even higher values of G and q_w were used. Higher axial bubble velocity was observed at lower inlet subcooling condition (i.e., $\Delta T_{sub,in}$=4.5 °C), which is similar to the other observations in Figure V-6 and is due to the higher buoyancy force of bigger bubbles (see Figure V-3, bottom). The bottom of Figure V-6 also shows that the axial bubble velocity at $\Delta T_{sub,in}$=4.5 °C exceeded u_{liq} at $L/L_0\approx0.60$ while the axial bubble velocity at $\Delta T_{sub,in}$=13.5 °C was always significantly lower than u_{liq}.

In Figure V-7, axial bubble velocities affected by changes in G are compared. All the experimental cases shown in Figure V-7 correspond to those shown in Figure V-4. On the left of Figure V-7, the axial bubble velocity decreased as G increased at $L/L_0<0.53$. Meanwhile, in Figure V-4 (left), we can see that the bubbles' growth while sliding at similar region $L/L_0<0.48$ was more restricted as G increased. These observations imply that the varying trend of axial bubble velocity according to G was significantly affected by variation in the buoyancy force (or bubble size) at those regions. That is, in Figure V-7 (left), the axial bubble velocity at the lowest value of G (140 kg/m^2s) became the highest at the region $L/L_0<0.53$ because the bubble size around that region was the biggest as shown in Figure V-4 (left). However, further downstream in the test channel, i.e., $L/L_0>0.53$, Figure V-7 (left) shows that the axial bubble velocity at G=280 kg/m^{2}s became larger than that at G=140 kg/m^{2}s; a similar trend can also be found in the bubble growth behavior shown in Figure V-4 (left). This also suggests a close relationship between bubble size and axial bubble velocity.

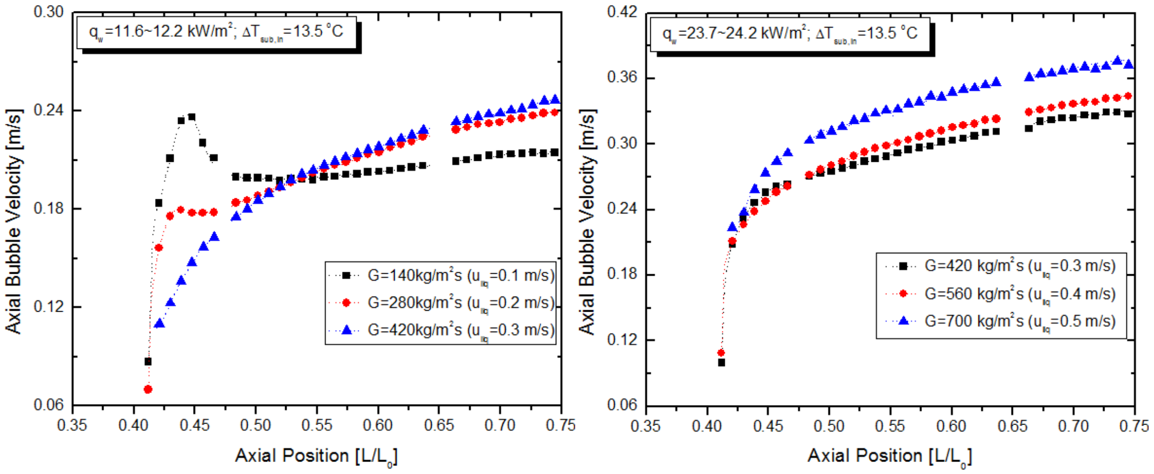

Figure V-7. Effects of liquid mass flux (G) on the axial bubble velocity

However, in Figure V-7 (left), the axial bubble velocity at G=420 kg/m^{2}s became the highest as the bubbles moved downstream $L/L_0>0.53$ despite the smallest bubble size over the total flow path observed by HSV 3 as shown in Figure V-4 (left). From this, we can infer that a certain force other than buoyancy became more important in determining the axial bubble velocity at this downstream region ($L/L_0>0.53$), which is considered interfacial drag. Regarding this, on the right of Figure V-7, we can also see that the variation of axial bubble velocity depending on G shows quite different tendencies compared to those shown on the left side of Figure V-7. Specifically, the right of Figure

V-7 shows that the difference in axial bubble velocity depending on G was insignificant at $L/L_0<0.45$, while at the downstream region $L/L_0>0.50$, it is clearly seen that the axial bubble velocity became higher as G increased. Note that, in Figure V-4 (right) the bubble size consistently became smaller as G increased for the same experimental cases shown in Figure V-7 (right). This clearly indicates that the interfacial drag induced by the flowing liquid played a more critical role than the buoyancy force in determining the axial bubble velocities at $L/L_0>0.50$.

In addition, comparing the axial bubble velocities with the values of u_{liq} shown in Figure V-7 (left) led to the observation that at the lowest G, the relative magnitude of axial bubble velocity was higher than u_{liq} while the trend was reversed at the highest G (420 kg/m^2s); a similar trend is found on the right of Figure V-7. The other experimental cases shown in Figure V-7 (left and right) indicates that the axial bubble velocity was initially lower than u_{liq} after departure from the nucleation site but later exceeded u_{liq} as the bubbles moved downstream.

Figure V-8 shows the effect of q_w on axial bubble velocity along the flow path. The experimental cases shown in Figure V-8 (left and right) are the same ones used in Figure V-5 to discuss the bubble growth behavior depending on q_w. In Figure V-8, it is seen that a higher q_w led to a higher axial bubble velocity along the flow path for the two comparisons shown in Figure V-8. We can expect that this trend of axial bubble velocity increasing according to q_w is attributable to the increasing buoyancy force (i.e., increasing bubble size) with q_w as shown in Figure V-5. Meanwhile, it is also seen that the axial bubble velocities shown on the left of Figure V-8 were mostly higher than u_{liq}

(blue dash-dot line) through the flow path observed; whereas, the axial bubble velocities on the right of Figure V-8 were always lower than u_{liq}. Based on our previous observations, this difference appears to be related to the significant difference in the G applied in the cases on the left (G=140 kg/m^2s) versus in those on the right (G=700 kg/m^2s) in Figure V-8. That is, the magnitude of axial bubble velocity was mostly higher than u_{liq} under the lower G (Figure V-8, left) while this became reversed with the higher G (Figure V-8, right).

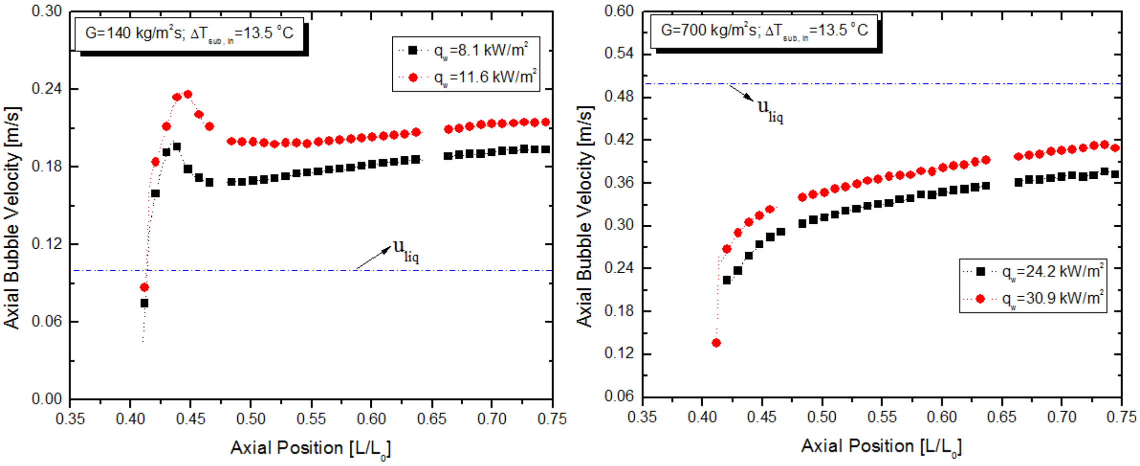

Figure V-8. Effects of wall heat flux (q_w) on axial bubble velocity

3. Local bubble number variation

The variation of the bubble number due to bubble coalescence, breakup, and the condensation processes is a common phenomenon that can be observed in any forced convective boiling system. Within the present set of experiments, the bubble number within the test channel was observed to vary primarily due to the coalescence of bubbles rather than the other processes. This section discusses the variation of the bubble number along the flow path based on the observations by HSV 3. However, since HSV 3 has considerable limitations in capturing the detailed bubble departure process as well as the nucleating behavior at the nucleation site due to the limited resolution and measurement view (see Chapter II or [57]), we used the experimental results obtained from HSV 1 as well to compensate for the limitations. It is noted that the HSV 1 was simultaneously employed with HSV 3 to capture the detailed bubble behaviors near the nucleation site as described in Chapter IV.

The specific procedures to analyze the bubble number variation along the flow path are as follows: The total number of bubbles produced at the nucleation site (N_0) during the measurement time of HSV 3 (80 sec) was first estimated based on the average bubble release frequency measured by HSV 1. That is, N_0 was obtained by multiplying the average bubble release frequency by the total measurement time of HSV 3. The number of bubbles passing through the axial location $L/L_0<0.45$, after departure from the nucleation site, was estimated in a similar way. Meanwhile, the number of bubbles passing through the axial locations at $L/L_0>0.45$ was directly counted by analyzing the trajectory of the sliding bubbles observed by HSV 3. Then, the variation in the bubble number along the flow path was presented by N/N_0 for each test condition; N denotes the number of bubbles passing through a specific axial location (L/L_0) of the test channel during the measurement period of HSV 3. Note that N/N_0 is always 1 at the axial location of the single nucleation site, here defined as $L/L_0 \approx 0.41$. The bubbles' trajectory during the measurement period of HSV 3 was analyzed using the ImageJ plugin software MTrack2 [66]. The discussion in this section is based on the same experimental cases used to discuss the parametric effects of $\Delta T_{sub,in}$, G, and q_w on bubble growth behavior and axial bubble velocity in the sections E.1 and E.2.

In Figure V-9, the variation of the bubble number along the flow direction (N/N_0) was compared using the cases of different $\Delta T_{sub,in}$ while G and q_w were held constant. On the top left side of Figure V-9, it is seen that N/N_0 decreased more sharply along the flow path for the higher inlet subcooling ($\Delta T_{sub,in}$=13.5 °C). Considering that the bubble number was observed not to vary due to condensation of bubbles during these tests, the top left of Figure V-9 indicates that bubbles coalesced more at the higher inlet subcooling condition ($\Delta T_{sub,in}$=13.5 °C). It is inferred that the bubbles' trajectory depending on $\Delta T_{sub,in}$ could be one of the causes of such differences in coalescing behavior shown in Figure V-9 (top left). Specifically, we observed that, due to the decreasing $\Delta T_{sub,in}$, the bubbles released from the nucleation site were distributed in lateral directions more widely as they moved downstream. This implies that the bubbles had less chance to collide each other at the condition $\Delta T_{sub,in}$=4.5 °C because the bubbles were located over the larger area while travelling at this condition.

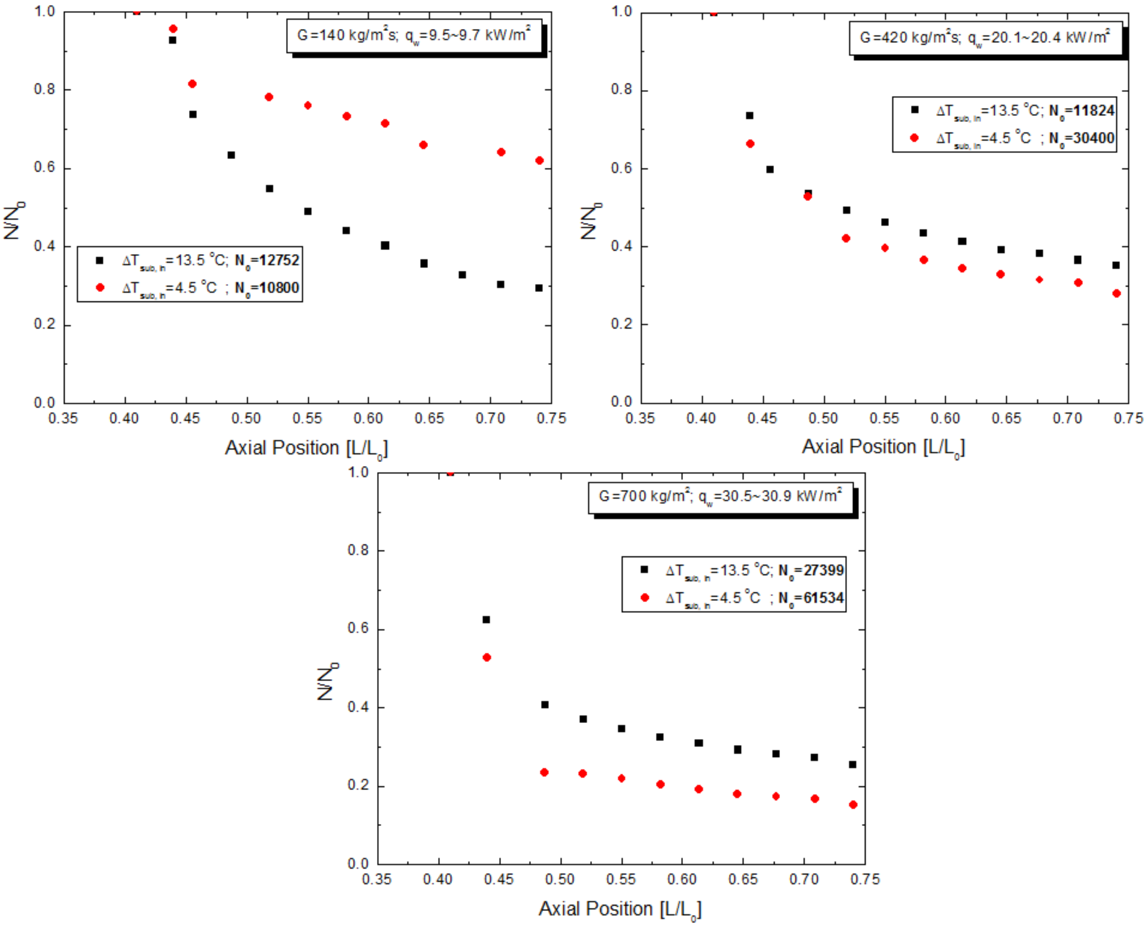

Figure V-9. Effects of inlet subcooling ($\Delta T_{sub,in}$) on local bubble number variation along the flow path

However, similar comparisons made at the higher G and q_w shown in Figure V-9 (i.e., top right and bottom) show the opposite trend. That is, on the top right of Figure V-9, the decreasing trend of N/N_0 along the flow path became sharper in the case with lower $\Delta T_{sub,in}$ (=4.5 °C). A similar trend can also be seen on the bottom of Figure V-9. Such a decreasing trend of N/N_0 depending on $\Delta T_{sub,in}$ is closely related to the bubble release frequency; note that N_0 is proportional to the bubble release frequency. Specifically, in both 'top right' and 'bottom' graphs of Figure V-9, we can commonly see that N/N_0 decreased more along the flow path for the cases of higher N_0 which means a higher bubble release frequency. This implies that in such test conditions the bubbles were more likely to merge with each other.

Figure V-10 shows the bubble number variation along the flow path depending on G with constant q_w and $\Delta T_{sub,in}$ conditions. On the left of Figure V-10, we can see that N/N_0 for G=420 kg/m^{2}s decreased quite sharply near the nucleation site compared to the other cases of lower G (i.e., 140 and 280 kg/m^{2}s). Also, at the test condition G=420 kg/m^{2}s, the number of bubbles far from the nucleation site (L/L_0>0.55) barely changed; whereas, for the other cases (G=140 and 280 kg/m^{2}s), N/N_0 kept decreasing as the bubbles moved downstream. In this study, we found that N/N_0 tended to decrease more sharply along the flow path near the nucleation site (L/L_0<0.45) as the bubble release frequency (or N_0) increased. However, the decreasing trend along the flow path significantly slowed down downstream in the test channel when such sharp decrease in N/N_0 existed upstream near the nucleation site. A similar trend can also be found on the right of Figure V-10.

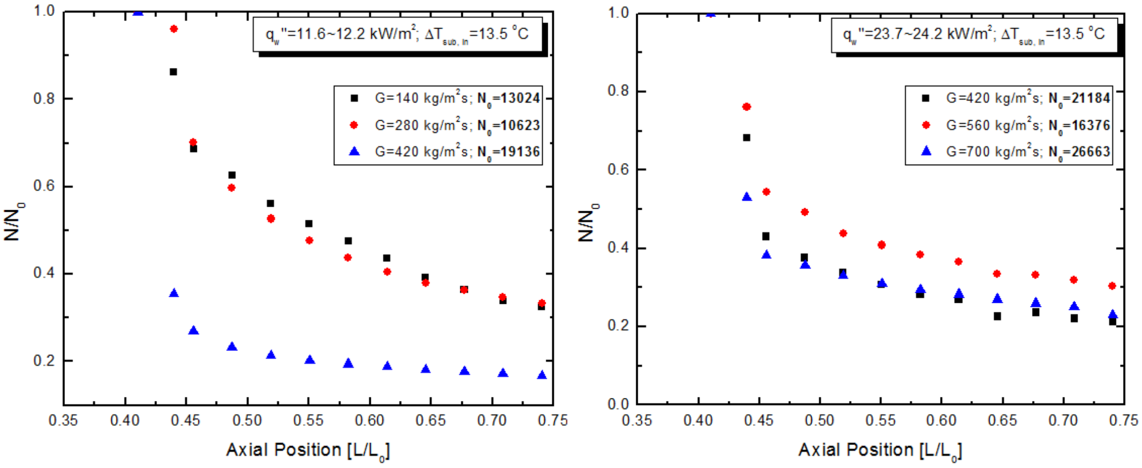

Figure V-10. Effects of liquid mass flux (G) on local bubble number variation along the flow path

In Figure V-11, the axial variation of the bubble number N/N_0 along the flow path is compared in cases of different q_w at constant G and $\Delta T_{sub,in}$ conditions. On the left of Figure V-11, we can see that N/N_0 decreased more sharply near the nucleation site $L/L_0<0.45$ at higher q_w (=11.6 kW/m^2) compared to lower q_w (=8.1 kW/m^2). However, the decreasing trend at $L/L_0>0.45$ was observed to be alleviated more at the higher q_w than at the lower q_w. This observation of the varying trend of N/N_0 is similar to the above mentioned discussion with Figure V-10. On the right of Figure V-11, the difference in the decreasing trend of N/N_0 along the flow path depending on q_w seems insignificant.

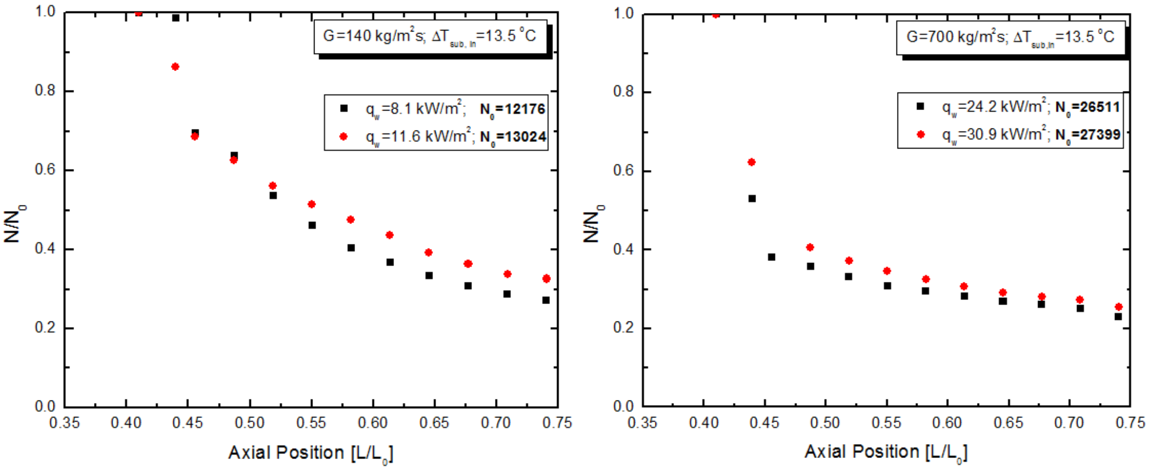

Figure V-11. Effects of wall heat flux (q_w) on local bubble number variation along the flow path

4. Local bubble size distribution

The stochastic nature of boiling parameters such as bubble departure and lift-off diameter in forced convective boiling has been reported in the literature [3, 6], and the importance of addressing this boiling characteristics has been increasingly emphasized in recent publications both for the improved modeling and the reliable measurement [57, 87]. In order to characterize the stochastic behavior properly through the experiments, the sample size must be large enough to ensure the reliability of statistics. In this section, based on the analyses of the numerous experimental data ensuring the reliability of statistics, we discuss the characteristics of bubble size distribution. In particular, the axial development of the bubble size distribution along the flow path under various subcooled flow boiling conditions is of our interest.

To gain insight into the stochastic nature of bubble size, probability density functions (PDFs) were established at two different axial locations in the test channel for each test condition: One was obtained relatively close to the nucleation site at $L/L_0 \approx 0.43$, and the other was obtained farther from the nucleation site at $L/L_0 \approx 0.71$. During this study, more than 13,000 and 5,000 data samples were used to construct the PDFs for the bubble size at these axial locations, i.e., upstream ($L/L_0 \approx 0.43$) and downstream ($L/L_0 \approx 0.71$) in the test channel, respectively, for each test condition. The PDFs created in this way are shown in Figures V-12~V-14, in which the bubble size distribution at the axial locations $L/L_0 \approx 0.43$ and 0.71 were presented by bar graphs in different colors. In addition, since we found that within the present set of experiments, the PDFs for bubble size were mostly well-fitted to the Gaussian distribution; the fitted curves were also shown in Figures V-12~V-14 along with the bar graphs. The mean (m) and standard deviation (σ) of the bubble size shown within these figures were obtained from the fitted Gaussian curves.

In Figure V-12, the PDFs for bubble size at both upstream ($L/L_0 \approx 0.43$) and downstream ($L/L_0 \approx 0.43$) locations in the test channel are shown. Here we can investigate the effects of $\Delta T_{sub,in}$ on the statistical distribution of bubble size by comparing the sub-figures embedded in the left and the right columns of Figure V-12. The experimental cases at higher inlet subcooling ($\Delta T_{sub,in}$=13.5 °C) shown in the left column of Figure V-12 indicate that the mean bubble size increased as the bubbles moved downstream from $L/L_0 \approx 0.43$ to 0.71 while the σ of the bubble size barely changed. On the other hand, for the cases at lower inlet subcooling ($\Delta T_{sub,in}$=4.5 °C) shown in the right column of Figure V-12, we can see a trend of the σ decreasing as the bubbles moved downstream. Comparing the sub-figures in the left and right columns of

Figure V-12, we can see that the σ of bubble size became slightly larger both upstream ($L/L_0 \approx 0.43$) and downstream ($L/L_0 \approx 0.71$) in the test channel by decreasing the $\Delta T_{sub,in}$. Additionally, the PDFs for bubble size shown in Figure V-12 mostly followed the Gaussian distribution quite well, except for the case shown on the top right of Figure V-12 at $L/L_0 \approx 0.71$. Regarding this, it is noted that the sliding bubbles downstream in the test channel were more likely to detach from the heater surface in this experimental case, which resulted in the frequent occurrence of small bubbles significantly deviating from the mean bubble size at $L/L_0 \approx 0.71$.

Figure V-13 shows the effects of varying G on the PDFs for bubble size within the test channel. That is, by comparing the left and right columns of Figure V-13, the effect of G on the PDFs for bubble size can be discussed. The σ of bubble size changed only insignificantly along the direction of flow compared to the mean value of the bubble size; such trends were commonly found regardless of the G applied. Meanwhile, it can be seen that, by increasing G, the σ of bubble size tended to decrease slightly at the both axial locations $L/L_0 \approx 0.43$ and $L/L_0 \approx 0.71$.

In Figure V-14, the effects of q_w on the PDFs for bubble size are presented. The experimental cases at lower q_w conditions are in the left column, while the cases of higher q_w are placed in the right column, which allows us to investigate the impact of q_w on the statistical distribution of bubble size within the test channel. The σ of bubble size changed much less along the flow path compared to the mean value of bubble size for all of the cases shown. However, it is seen that the σ of bubble size slightly increased at both the upstream ($L/L_0 \approx 0.43$) and downstream ($L/L_0 \approx 0.71$) locations in the test channel by increasing the q_w.

The observations mentioned above commonly indicate that the test conditions involving the higher heater surface temperature (so, higher wall superheat) tended to increase the σ of bubble size both upstream ($L/L_0 \approx 0.43$) and downstream ($L/L_0 \approx 0.71$) in the test channel. However, the variation in σ in the direction of upward flow was always much smaller than that in mean bubble size.

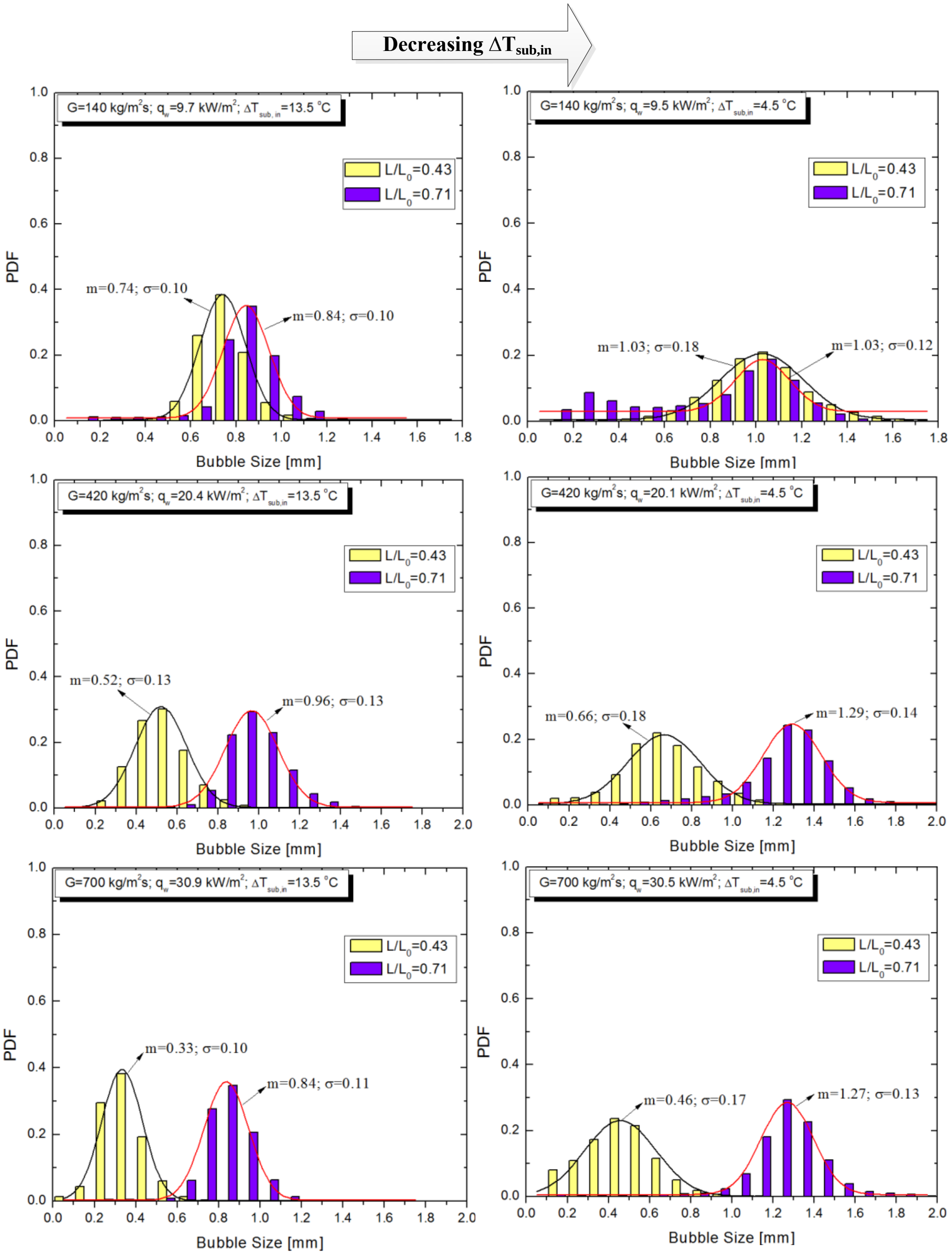

Figure V-12. Effects of inlet subcooling ($\Delta T_{sub,in}$) on probability density function (PDF) for bubble size and its development in the upward flow direction

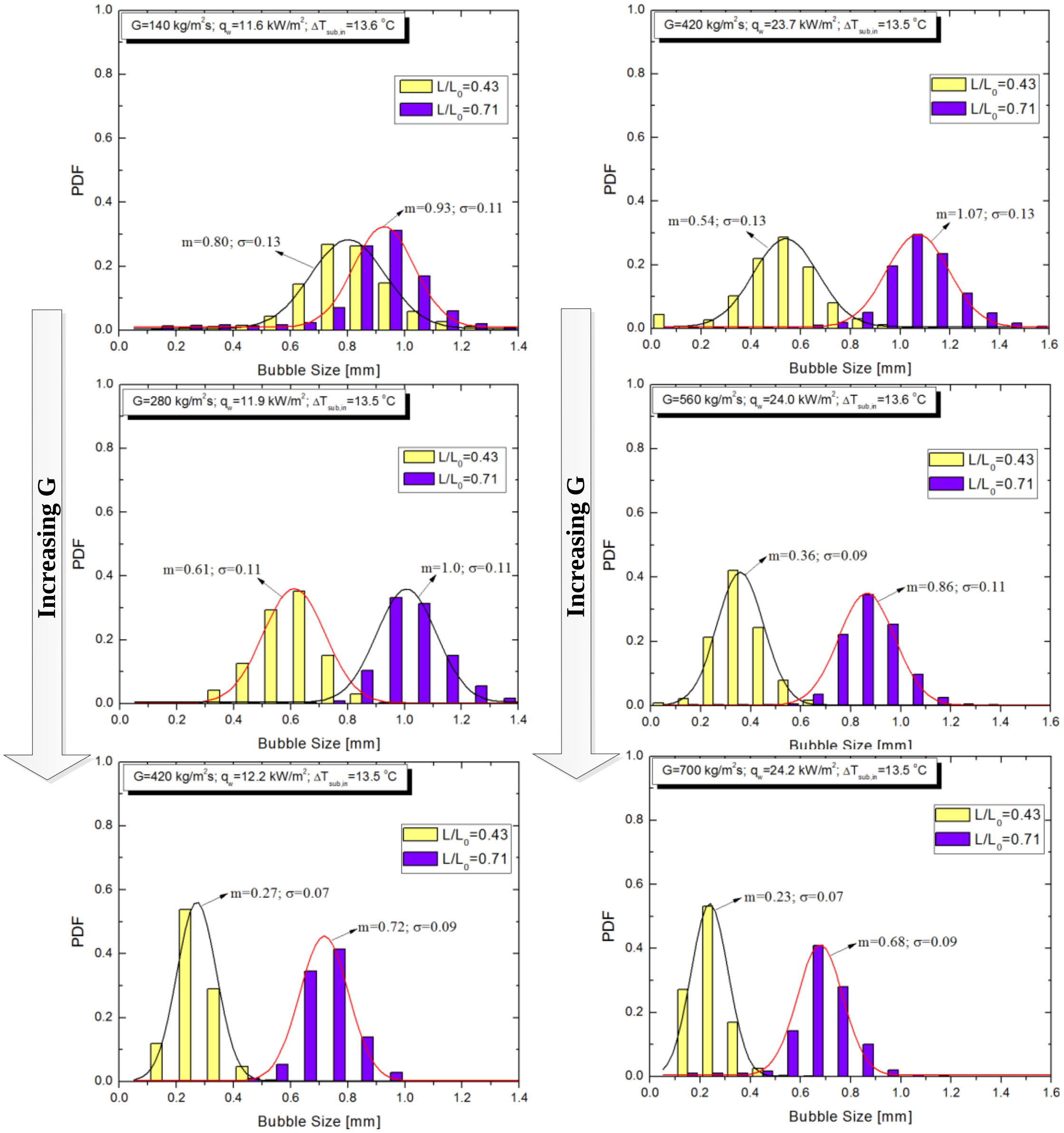

Figure V-13. Effects of liquid mass flux (G) on probability density function (PDF) for bubble size and its development in the upward flow direction

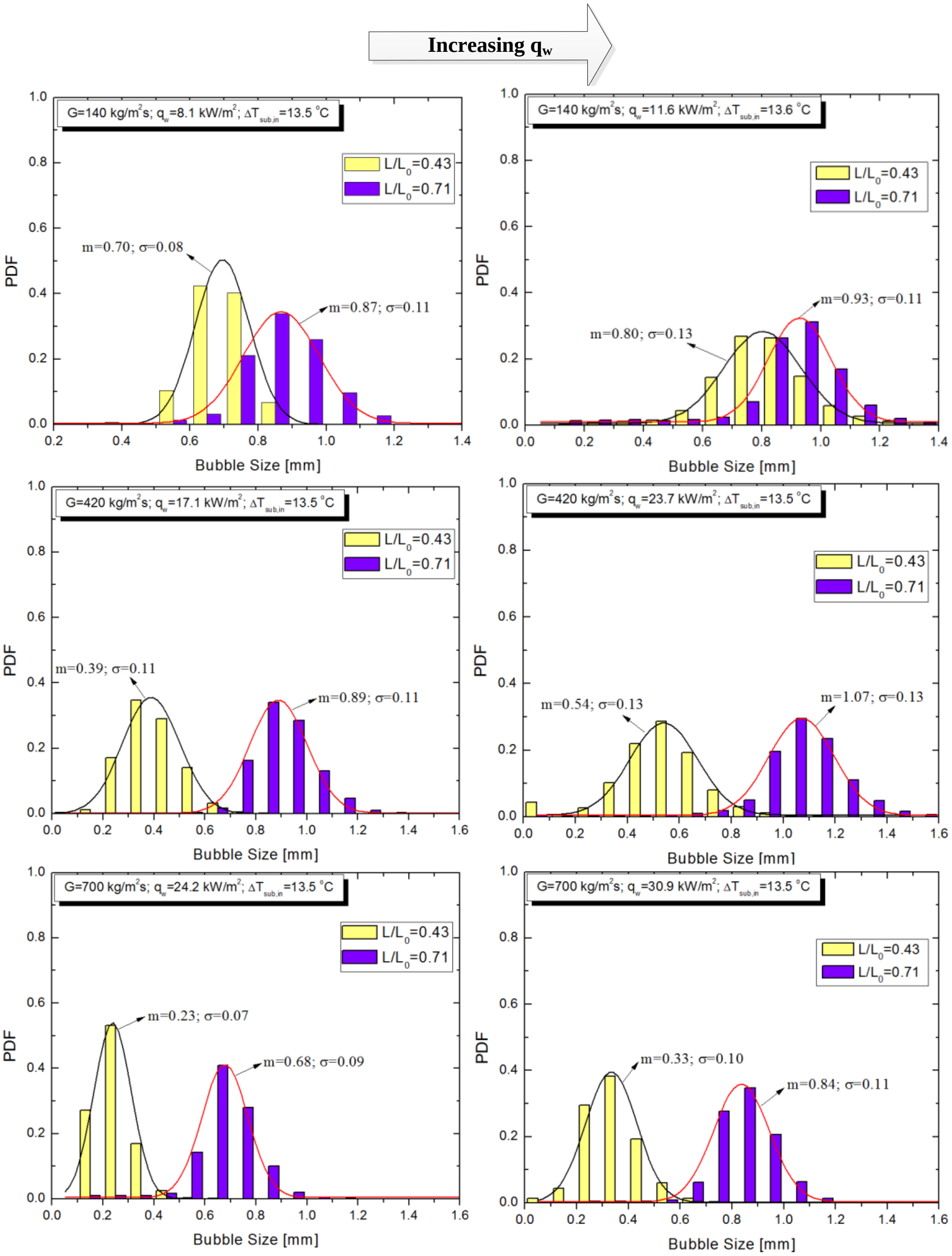

Figure V-14. Effects of wall heat flux (q_w) on probability density function (PDF) for bubble size and its development in the upward flow direction

5. Time-averaged local wall heat transfer coefficient

In the previous sections, the characteristic behaviors of bubbles within the subcooled flow boiling channel were investigated in various aspects, during which numerous experimental data were collected and analyzed to achieve reliable statistics. In this section, boiling heat transfer associated with the bubble characteristics observed is discussed based on the heater surface (wall) temperature measurement using IR thermometry. The specific interest is the wall heat transfer enhancement caused by the vapor bubbles originating from the single nucleation site. For this study, the time-averaged wall heat transfer coefficients within the test channel were estimated by the following relation:

$$q_w = H[T_w(y) - T_l(y)] \tag{V-1}$$

where H is the time-averaged wall heat transfer coefficient; $T_w(y)$ and $T_l(y)$ are the average wall temperature and the bulk liquid temperature, both at the axial location y, respectively; and q_w is the wall heat flux entering the fluid. T_w was obtained based on the IR thermometry (see Chapter IV) while the T_l was estimated by assuming that the total heat entering the fluid was eventually used to raise the bulk liquid temperature.

For the present discussion, we defined the heated section upstream of the single nucleation site (i.e., $0 \le L/L_0 \le 0.41$) as a single-phase (1Ø) heat transfer region while downstream (i.e., $0.41 < L/L_0 \le 1$) was defined as a subcooled boiling or two-phase (2Ø) heat transfer region. Then, the transition from the single-phase heat transfer to the subcooled boiling heat transfer can be clearly identified by the abrupt increase of wall heat transfer coefficient along the flow path as shown in Figures V-15~V-17. A typical wall temperature profile induced by the existence of a single nucleation site in a similarly designed flow boiling test channel can be seen in Chapter III or [64].

The flow boiling loop was configured to ensure that the flow was fully developed hydrodynamically before entering the test channel. However, in most cases, the flow was still thermally developing within the test channel until it reached the axial location of the nucleation site $L/L_0 \approx 0.41$. For this reason, we could still find a decreasing trend in the single-phase heat transfer coefficient in the direction of flow, rather than a constant value upstream of the nucleation site. Figures V-15~V-17 show the axial distribution of time-averaged wall heat transfer coefficient between $L/L_0=0.30\sim0.90$, which covers both the single-phase and the subcooled boiling heat transfer regions in the test channel. In Figures V-15~V-17, we can commonly see that the wall heat transfer coefficient sharply increased once the boiling was initiated at $L/L_0 \approx 0.41$, but the amount of increase varied substantially depending on the specific test conditions. Also, the flow became thermally fully developed quite fast once boiling was initiated. In order to quantitatively express the relative magnitude of wall heat transfer enhancement caused by boiling for various experimental cases, we introduce the ratio $H_{2Ø}/ H_{1Ø}$, in which $H_{1Ø}$ denotes the single-phase heat transfer coefficient measured upstream of the nucleation site, i.e., at $L/L_0 \approx 0.4$ and $H_{2Ø}$ is the subcooled boiling heat transfer coefficient measured downstream in the test channel at $L/L_0 \approx 0.90$.

In Figure V-15, time-averaged wall heat transfer coefficients through the test channel are compared for the two inlet subcooling conditions ($\Delta T_{sub,in}$=4.5 and 13.5 °C) at constant G and q_w, and comparisons were made for the three different pairs of G and

q_w. The three comparisons shown in Figure V-15 commonly show that the magnitude of wall heat transfer enhancement relative to single-phase convection, i.e., $H_{2Ø}/H_{1Ø}$ increased as $\Delta T_{sub,in}$ decreased. This indicates that the wall heat transfer modes associated with boiling, e.g., evaporation, quenching, and liquid mixing due to sliding bubbles, were enhanced as $\Delta T_{sub,in}$ decreased. About this, an important discussion is that the bubble size and the axial bubble velocity increased as $\Delta T_{sub,in}$ decreased as well, as shown in Figures V-3 and V-6; all experimental cases presented in Figures V-3 and V-6 correspond to those in Figure V-15. In addition, as we discussed in Chapter IV, the decrease in $\Delta T_{sub,in}$ tends to cause an increase in bubble release frequency at the nucleation site. Taken together, these observations regarding the dependence of bubble behaviors on $\Delta T_{sub,in}$ explain why the lower inlet subcooling ($\Delta T_{sub,in}$=4.5°C) caused the higher value of $H_{2Ø}/ H_{1Ø}$ as shown in Figure V-15.

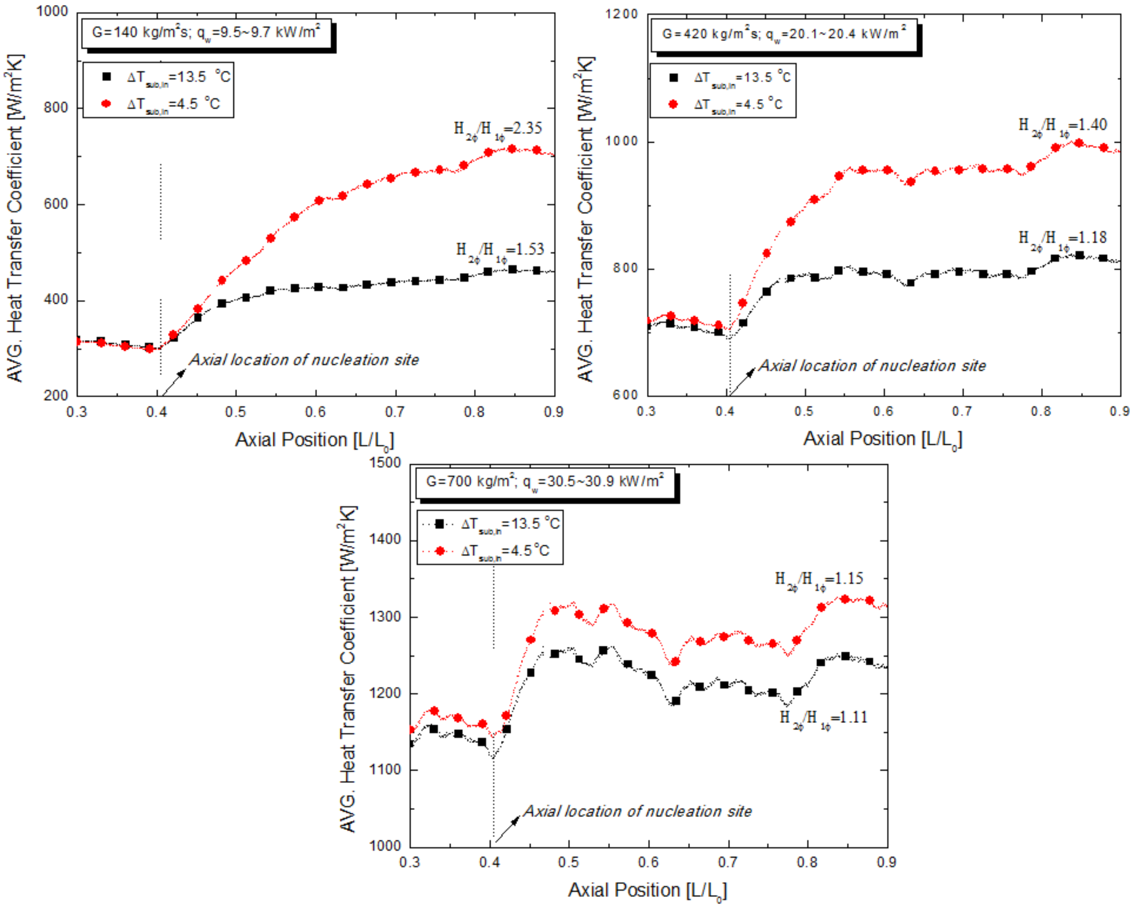

Figure V-15. Effects of inlet subcooling ($\Delta T_{sub,in}$) on time-averaged wall heat transfer coefficient

Figure V-16 shows how the time-averaged wall heat transfer coefficient depends on G within the test channel. As expected, the wall heat transfer coefficients both in single-phase region ($L/L_0<0.41$) and in subcooled boiling region ($L/L_0>0.41$) became larger as G increased. However, comparing the ratio $H_{2Ø}/ H_{1Ø}$ for each case using different values of G indicates that the magnitude of wall heat transfer improvement caused by boiling relative to single-phase convection decreased as G increased. Regarding this, we saw in section E.1 that bubble growth tended to be more restricted when G increased, especially near the nucleation site, thus causing the sliding bubbles to become smaller as G increased as shown in Figure V-4 (the experimental cases presented in Figures V-4 and V-7 correspond to those in Figure V-16). In section E.2, it was also discussed that the axial bubble velocity at the regions relatively near the nucleation site decreased as G increased, and this trend was clearer when the values of G were relatively low, as shown on the left of Figure V-7. These observations imply that the decrease in bubble size and axial bubble velocity near the nucleation site led to the decreasing $H_{2Ø}/ H_{1Ø}$ as G increased. A similar discussion is also in Chapter IV; we argued that the increasing G caused the boiling heat transfer modes associated with evaporation and quenching to deteriorate, and this explained the variations in bubble release frequency according to G observed in the present study as well. Using all these observations and arguments, we can explain why the $H_{2Ø}/H_{1Ø}$ was reduced by increasing G, shown in Figure V-16. Figure V-16 also shows that the value of $H_{2Ø}/H_{1Ø}$ was relatively low for cases with higher G when compared to those with lower G, even when the bubble release frequency at the nucleation site increased significantly as G increased (see Chapter IV). In addition, it is noted that the abrupt increase in wall heat transfer always occurred within the region relatively near the nucleation site while the variation downstream was relatively insignificant. It is also important to say that even for cases in which the varying trends of bubble size and axial bubble velocity depending on G were reversed downstream in the test channel as shown in Figures V-4 and V-7, such effects did not critically affect the trend of wall heat transfer downstream. This implies that the bubble behaviors observed near the nucleation site played a dominant role in determining the ultimate level of wall heat transfer improvement due to boiling within the test channel.

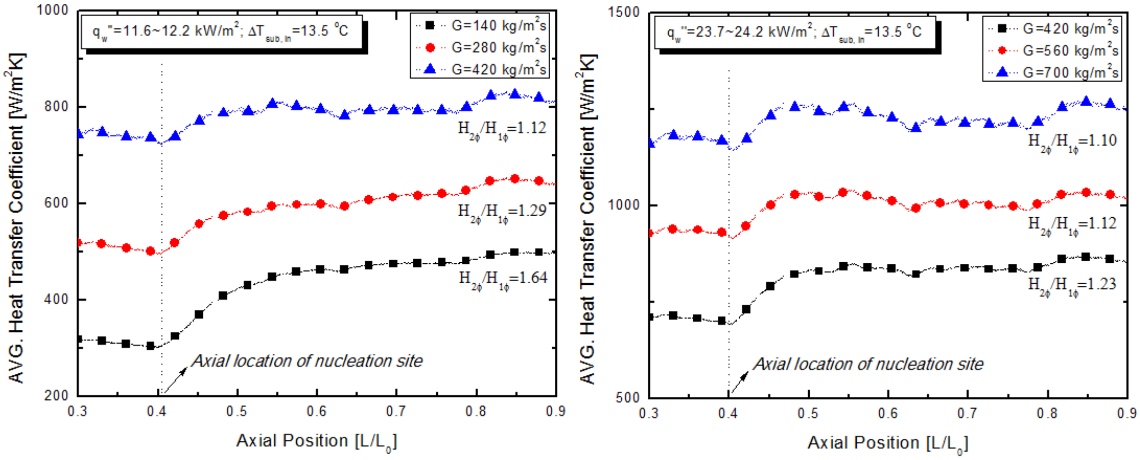

Figure V-16. Effects of liquid mass flux (G) on time-averaged wall heat transfer coefficient

In Figure V-17, the axial distribution of the time-averaged wall heat transfer coefficient affected by variation in q_w is presented. On the left of Figure V-17, we can see that $H_{2Ø}/H_{1Ø}$ increased slightly as q_w increased while holding G and $\Delta T_{sub,in}$ constant. As discussed before in this section, this is related to the fact that the bubbles became larger and moved faster while sliding near the nucleation site as q_w increased, as shown in Figures V-5 and V-8 (the experimental cases shown in Figure V-17 correspond to those in Figures V-5 and V-8). That is, the variation of bubble behaviors induced by increasing q_w improved the heat transfer modes associated with boiling, e.g., evaporation, quenching, and liquid mixing due to sliding bubbles. However, for the similar comparison performed at higher G (=700 kg/m^{2}s) shown on the right side of

Figure V-17, noticeable change in $H_{2\emptyset}/H_{1\emptyset}$ cannot be found between the two cases with different q_w, although the variation in q_w was larger than that shown on the left of Figure V-17. This indicates that the impact of variation in q_w on $H_{2\emptyset}/H_{1\emptyset}$ is relatively low at these higher G conditions. Additionally, it can be seen that both the magnitudes of $H_{2\emptyset}/H_{1\emptyset}$ shown on the right of Figure V-17 are much smaller than those shown on the left. This implies that the significance of boiling phenomenon to enhance the wall heat transfer relative to single-phase convection was reduced for the cases with higher value of G.

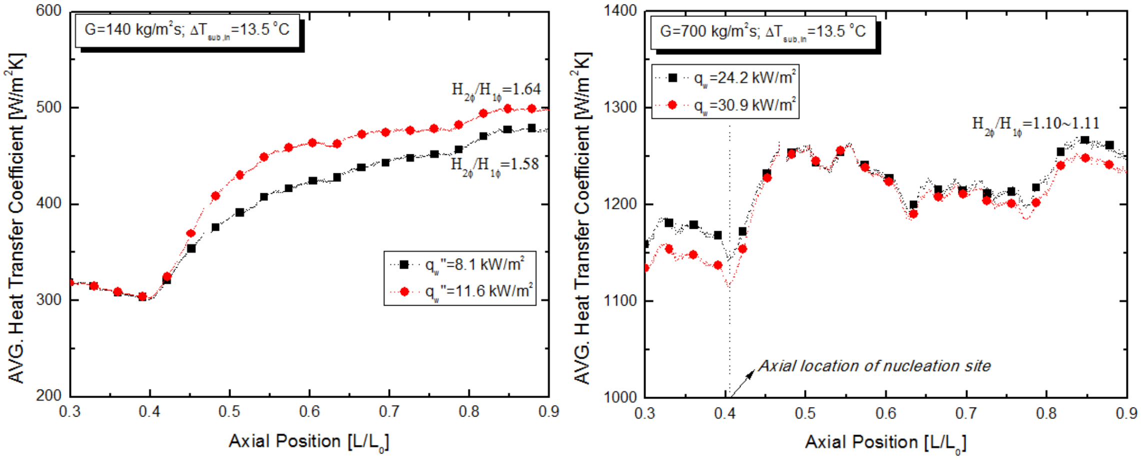

Figure V-17. Effects of wall heat flux (q_w) on time-averaged wall heat transfer coefficient

F. Summary and conclusions

Subsequent to Chapter IV discussing detailed bubble behaviors near a single nucleation site under subcooled flow boiling conditions, this chapter investigates the behaviors of bubbles over a larger area of flow path defined as $0.41<L/L_0<0.75$ after departure from the nucleation site. For the most part, the bubbles were in sliding mode within the view observed by HSV 3, with the exception of two cases among the present set of experiments. The wall heat transfer enhancement associated with the sliding bubble behaviors is also discussed based on measurements using IR thermometry. The major findings and conclusions are summarized as follows.

Bubble growth behavior

For the cases with low G, bubble size increased and subsequently decreased significantly as the bubbles slid along the flow path. After such fluctuation, the sliding bubbles began to grow again rather slowly downstream along the flow path. The fluctuation of bubble size upstream significantly affected subsequent bubble growth behavior downstream. For this reason, when such significant fluctuation occurred, the effect of inlet subcooling, liquid mass flux, and wall heat flux on bubble size observed near the nucleation site often became reduced or even reversed as the bubbles moved downstream.

Axial bubble velocity

Unlike the dominant influence of buoyancy force on the axial bubble velocity near the nucleation site, the significance of interfacial drag increased as the bubbles moved downstream while sliding. Thus, the trend of decreasing axial bubble velocity as liquid mass flux increased, which was observed near the nucleation site, was reversed downstream in the test channel. This reverse trend between upstream and downstream locations was especially noticeable for the cases with low G (i.e., Figure V-7, left).

Local bubble number variation

The test conditions causing the higher bubble release frequency enhanced coalescence efficiency (i.e., more decrease in bubble number) near the nucleation site. However, for the cases involving a sharp decrease in the bubble number near the nucleation site, the decreasing trend along the flow path significantly slowed down downstream, which suggests that the bubbles coalescing was relatively limited in that region.

Local bubble size distribution

In most experimental cases, the PDFs for bubble size followed the Gaussian distribution quite well both upstream and downstream in the test channel. For the cases at high inlet subcooling ($\Delta T_{sub,in} \approx 13.5$ °C), the standard deviation of bubble size varied little through the test channel while the cases at lower inlet subcooling ($\Delta T_{sub,in} \approx 4.5$°C) showed more changes. However, such changes in standard deviation through the test channel were observed to be much less compared to the changes in mean bubble size. Also, the standard deviation of bubble size tended to increase for the cases involving a higher wall superheat by decreasing the inlet subcooling/liquid mass flux or increasing the wall heat flux.

Time-averaged wall heat transfer coefficient

The magnitude of wall heat transfer enhancement relative to single-phase convection ($H_{2Ø}/H_{1Ø}$) increased in the test conditions causing a higher wall superheat. That is, the ratio $H_{2Ø}/H_{1Ø}$ increased as the inlet subcooling/liquid mass flux decreased or the wall heat flux increased.

The abrupt increase in wall heat transfer due to boiling occurred within the region relatively near the nucleation site. Also, the increase in wall heat transfer caused by boiling was closely related to bubble size and axial bubble velocity near the nucleation site rather than the values measured downstream in the test channel. In other words, the bubble behaviors near the single nucleation site played a dominant role in determining the ultimate level of wall heat transfer enhancement within the test channel.

CHAPTER VI

SUMMARY AND CONCLUSIONS

A series of experimental work has been performed, including (i) the identification of optical measurement issues for fundamental bubble parameters, (ii) the establishment of experimental methodology to apply both IR thermometry and high-speed photography with high fidelity, and (iii) the simultaneous measurement of bubble dynamics as well as wall heat transfer in the subcooled flow boiling experiment with a square, vertical, upward flow channel. The main contributions of this research can be summarized as follows:

- With respect to the measurement of fundamental bubble parameters through visualization, we revealed that in previous experimental works there are still several unidentified issues which have never been explicitly addressed despite their critical impacts on experimental results. Through a series of systematic experimental investigations, the visual measurement of bubble departure diameter as well as bubble departure frequency was found to be significantly affected by (i) measurement views, (ii) recording speeds of images, and (iii) the number of experimental observations (sample size). Also, based on our experimental findings, recommendations were made for a proper observation and characterization of the fundamental bubble parameters. One of the important recommendations is to collect the number of experimental observations until ensuring the convergence of the statistical average at a given test condition as illustrated in Chapter II.

● An image analysis method was developed to analyze the numerous images of boiling bubbles so that the quantitative information for the wall nucleation process can be extracted efficiently and accurately.

● An experimental strategy was established to achieve both enhanced two-phase flow visualization and accurate wall temperature/heat flux measurement in a convective boiling system involving a large heated area. During this work, the details on the test section design, IR thermal imaging issues, visualization strategy, wall temperature tracking method, and experimental validations were extensively addressed. Also, the feasibility of the current experimental strategy was demonstrated through a subcooled flow boiling experiment in a square, vertical, upward flow channel.

● Based on the experimental strategy established, an experimental investigation of subcooled boiling flow was conducted. Intentionally, a single nucleation site was activated at a predefined location to study the fundamentals of the subcooled flow boiling process. To gain better insight into relationships among various thermal-hydraulic sub-processes, both intensive and extensive observations of bubble parameters as well as wall heat transfer were made at various subcooled flow boiling conditions. The measured parameters of interest included bubble growth behavior, axial bubble velocity, bubble release frequency, bubble size distribution, local bubble number variation, and local heat transfer coefficient, etc. During this study, the axial development of these parameters along the flow path was observed by employing both micro- and macroscopic views of high-speed cameras simultaneously (i.e., multi-scale observation). In particular, the impacts of inlet subcooling, liquid mass flux, and wall heat flux on such bubble behaviors and wall heat transfer were intensively discussed, and the underlying mechanisms of the observed behaviors were also studied.

● One of the important experimental findings was that buoyancy was the dominant factor in determining the magnitude of axial bubble velocity near the nucleation site, while the effect of interfacial drag on the axial bubble velocity increased as the bubbles moved downstream.

● Bubble release frequency was observed to be closely related to the bubbles' coalescence behavior along the flow path, especially near the nucleation site.

● PDFs for bubble size mostly followed the Gaussian distribution both upstream and downstream in the test channel, except for the case in which the significant number of bubbles lifted off from the heater surface after sliding for a distance. Also, it was found that the standard deviation of bubble size varied much less compared to the changes in average bubble size while the bubbles slid through the test channel.

● The ultimate level of wall heat transfer enhancement due to boiling within the test channel was mainly determined by bubble characteristics close to the single nucleation site rather than by those downstream in the test channel.

It is expected that the current experimental findings can be used to develop, validate, and improve the mechanistic models of subcooled boiling flow by reflecting a proper physics discussed in this study. Such effort will be particularly useful when bubbles are in sliding mode after departing from nucleation sites. The next step of this research is to extend our understanding by acquiring experimental data under more complex boiling conditions such as multiple nucleation sites.

REFERENCES

1. N. Kurul and M.Z. Podowski. On the modeling of multidimensional effects in boiling channels. in *Proceedings of the 27th National Heat Transfer Conference*. 1991. Minneapolis, MN.
2. M. Ishii and T. Hibiki, Thermo-fluid dynamics of two-phase flow. 2nd ed. 2011: Springer, New York.
3. J.F. Klausner, R. Mei, D.M. Bernhard, and L.Z. Zeng, Vapor bubble departure in forced-convection boiling. *International Journal of Heat and Mass Transfer,* 1993. **36**(3): p. 651-662.
4. L.Z. Zeng, J.F. Klausner, D.M. Bernhard, and R. Mei, A unified model for the prediction of bubble detachment diameters in boiling systems: 2. Flow boiling. *International Journal of Heat and Mass Transfer*, 1993. **36**(9): p. 2271-2279.
5. L.Z. Zeng and J.F. Klausner, Nucleation site density in forced-convection boiling. *Journal of Heat Transfer-Transactions of the Asme*, 1993. **115**(1): p. 215-221.
6. G.E. Thorncroft, J.F. Klausner, and R. Mei, An experimental investigation of bubble growth and detachment in vertical upflow and downflow boiling. *International Journal of Heat and Mass Transfer*, 1998. **41**(23): p. 3857-3871.
7. V. Prodanovic, D. Fraser, and M. Salcudean, Bubble behavior in subcooled flow boiling of water at low pressures and low flow rates. *International Journal of Multiphase Flow,* 2002. **28**(1): p. 1-19.

8. R. Situ, T. Hibiki, M. Ishii, and M. Mori, Bubble lift-off size in forced convective subcooled boiling flow. *International Journal of Heat and Mass Transfer*, 2005. **48**(25-26): p. 5536-5548.

9. R. Situ, M. Ishii, T. Hibiki, J.Y. Tu, G.H. Yeoh, and M. Mori, Bubble departure frequency in forced convective subcooled boiling flow. *International Journal of Heat and Mass Transfer*, 2008. **51**(25-26): p. 6268-6282.

10. D. Euh, B. Ozar, T. Hibiki, M. Ishii, and C.H. Song, Characteristics of bubble departure frequency in a low-pressure subcooled boiling flow. *Journal of Nuclear Science and Technology*, 2010. **47**(7): p. 608-617.

11. I.C. Chu, H.C. No, and C.H. Song, Bubble lift-off diameter and nucleation frequency in vertical subcooled boiling flow. *Journal of Nuclear Science and Technology*, 2011. **48**(6): p. 936-949.

12. C.S. Brooks, B. Ozar, T. Hibiki, and M. Ishii, Interfacial area transport of subcooled boiling flow in a vertical annulus. *Nuclear Engineering and Design*, 2014. **268**: p. 152-163.

13. J.F. Klausner, R. Mei, and L.Z. Zeng, Predicting stochastic features of vapor bubble detachment in flow boiling. *International Journal of Heat and Mass Transfer*, 1997. **40**(15): p. 3547-3552.

14. P.H. Strenge, A. Orell, and J.W. Westwater, Microscopic study of bubble growth during nucleate boiling. *Aiche Journal*, 1961. **7**(4): p. 578-583.

15. V.I. Tolubinsky and J.N. Ostrovsky, On the mechanism of boiling heat transfer (vapour bubbles growth rate in process of boiling of liquids solutions and binary

mixtures). *International Journal of Heat and Mass Transfer*, 1966. **9**(12): p. 1463-1470.

16. K. Birch, Estimating uncertainties in testing - an intermediate guide to estimating and reporting uncertainty of measurement in testing, 2001, British Measurement and Testing Association.
17. B. Ozar, Interfacial area transport of steam-water two-phase flow in a vertical annulus at elevated pressures, PhD Dissertation, 2009, Purdue University: West Lafayette, Indiana.
18. N. Basu, G.R. Warrier, and V.K. Dhir, Wall heat flux partitioning during subcooled flow boiling: Part 1 - Model development. *Journal of Heat Transfer-Transactions of the Asme*, 2005. **127**(2): p. 131-140.
19. N. Basu, Modeling and experiments for wall heat flux partitioning during subcooled flow boiling of water at low pressures, 2003, University of California, Los Angeles.
20. D. Fraser, V. Prodanovic, and M. Salcudean. Experimental study of bubble behavior in subcooled flow boiling of water at low pressures. in *NHTC'00 34th National Heat Transfer Conference*. 2000. Pittsburgh, Pennsylvania.
21. T. Okawa, H. Kubota, and T. Ishida, Simultaneous measurement of void fraction and fundamental bubble parameters in subcooled flow boiling. *Nuclear Engineering and Design*, 2007. **237**(10): p. 1016-1024.

22. R. Maurus, V. Ilchenko, and T. Sattelmayer, Automated high-speed video analysis of the bubble dynamics in subcooled flow boiling. *International Journal of Heat and Fluid Flow*, 2004. **25**(2): p. 149-158.

23. R. Maurus, V. Ilchenko, and T. Sattelmayer, Study of the bubble characteristics and the local void fraction in subcooled flow boiling using digital imaging and analysing techniques. *Experimental Thermal and Fluid Science*, 2002. **26**(2-4): p. 147-155.

24. R.J. Moffat, Contributions to the theory of single-sample uncertainty analysis. *J. Fluid Eng. Trans. ASME,* 1982. **104 (2)**: p. 250-260.

25. S.J. Kline and F.A. McClintock, Describing uncertainties in single-sample experiments. *Mechanical Engineering*, 1953. **75**: p. 3-8.

26. N. Basu, G.R. Warrier, and V.K. Dhir, Onset of nucleate boiling and active nucleation site density during subcooled flow boiling. *Journal of Heat Transfer-Transactions of the Asme*, 2002. **124**(4): p. 717-728.

27. D. Chen, L. Pan, D. Yuan, and X. Wang. An experimental investigation of bubble growth in water subcooled flow boiling in a vertical narrow rectangular channel. in *Fourth Korea-China Workshop on Nuclear Reactor Thermal Hydraulics (WORTH-4)*. 2009. jeju, Korea.

28. T. Okawa, T. Ishida, I. Kataoka, and M. Mori, Bubble rise characteristics after the departure from a nucleation site in vertical upflow boiling of subcooled water. *Nuclear Engineering and Design,* 2005. **235**(10-12): p. 1149-1161.

29. W.S. Rasband, ImageJ, 1997-2014, http://imagej.nih.gov/ij/: U.S National Institutes of Health, Bethesda, Maryland, USA.

30. S.R. Sternberg, Biomedical image processing. *IEEE Computer*, 1983. **16**(01): p. 22-34.

31. C.E. Estrada-Perez and Y.A. Hassan, PTV experiments of subcooled boiling flow through a vertical rectangular channel. *International Journal of Multiphase Flow*, 2010. **36**(9): p. 691-706.

32. D.B.R. Kenning, T. Kono, and M. Wienecke, Investigation of boiling heat transfer by liquid crystal thermography. *Experimental Thermal and Fluid Science*, 2001. **25**(5): p. 219-229.

33. B.B. Bayazit, D.K. Hollingsworth, and L.C. Witte, Heat transfer enhancement caused by sliding bubbles. *Journal of Heat Transfer-Transactions of the Asme*, 2003. **125**(3): p. 503-509.

34. R. Muwanga and I. Hassan, Local heat transfer measurements in microchannels using liquid crystal thermography: Methodology development and validation. *Journal of Heat Transfer-Transactions of the Asme*, 2006. **128**(7): p. 617-626.

35. I. Hapke, H. Boye, and J. Schmidt, Onset of nucleate boiling in minichannels. *International Journal of Thermal Sciences*, 2000. **39**(4): p. 505-513.

36. T.G. Theofanous, J.P. Tu, A.T. Dinh, and T.N. Dinh, The boiling crisis phenomenon - Part I: nucleation and nucleate boiling heat transfer. *Experimental Thermal and Fluid Science*, 2002. **26**(6-7): p. 775-792.

37. T.G. Theofanous, T.N. Dinh, J.P. Tu, and A.T. Dinh, The boiling crisis phenomenon - Part II: dryout dynamics and burnout. *Experimental Thermal and Fluid Science*, 2002. **26**(6-7): p. 793-810.

38. M.C. Diaz, H. Boye, I. Hapke, J. Schmidt, Y. Staate, and Z. Zhekov, Investigation of flow boiling in narrow channels by thermographic measurement of local wall temperatures. *Microfluidics and Nanofluidics*, 2006. **2**(1): p. 1-11.

39. J. Jung, S.J. Kim, and J. Kim, Observations of the critical heat flux process during pool boiling of FC-72. *Journal of Heat Transfer-Transactions of the Asme*, 2014. **136**(4).

40. I. Golobic, J. Petkovsek, M. Baselj, A. Papez, and D. Kenning, Experimental determination of transient wall temperature distributions close to growing vapor bubbles. *Heat and Mass Transfer*, 2009. **45**(7): p. 857-866.

41. C. Gerardi, J. Buongiorno, L.W. Hu, and T. McKrell, Study of bubble growth in water pool boiling through synchronized, infrared thermometry and high-speed video. *International Journal of Heat and Mass Transfer*, 2010. **53**(19-20): p. 4185-4192.

42. C. Kunkelmann, K. Ibrahem, N. Schweizer, S. Herbert, P. Stephan, and T. Gambaryan-Roisman, The effect of three-phase contact line speed on local evaporative heat transfer: Experimental and numerical investigations. *International Journal of Heat and Mass Transfer*, 2012. **55**(7-8): p. 1896-1904.

43. J. Barber, K. Sefiane, D. Brutin, and L. Tadrist, Hydrodynamics and heat transfer during flow boiling instabilities in a single microchannel. *Applied Thermal Engineering*, 2009. **29**(7): p. 1299-1308.

44. H. Boye, Y. Staate, and J. Schmidt, Experimental investigation and modelling of heat transfer during convective boiling in a minichannel. *International Journal of Heat and Mass Transfer*, 2007. **50**(1-2): p. 208-215.

45. N. Schweizer and P. Stephan, Experimental study of bubble behavior and local heat flux in pool boiling under variable gravitational conditions. *Multiphase Science and Technology*, 2009. **21**(4): p. 329-350.

46. S. Fischer, S. Herbert, A. Sielaff, E.M. Slomski, P. Stephan, and M. Oechsner, Experimental investigation of nucleate boiling on a thermal capacitive heater under variable gravity conditions. *Microgravity Science and Technology*, 2012. **24**(3): p. 139-146.

47. T.H. Kim, E. Kommer, S. Dessiatoun, and J. Kim, Measurement of two-phase flow and heat transfer parameters using infrared thermometry. *International Journal of Multiphase Flow*, 2012. **40**: p. 56-67.

48. M.F. Trujillo, J. Alvarado, E. Gehring, and G.S. Soriano, Numerical simulations and experimental characterization of heat transfer from a periodic impingement of droplets. *Journal of Heat Transfer-Transactions of the Asme*, 2011. **133**(12).

49. N. Horny, FPA camera standardisation. *Infrared Physics & Technology*, 2003. **44**(2): p. 109-119.

50. M. Vollmer and K.-P. Mollmann, Infrared thermal imaging: Fundamentals, research and applications. 2011: John Wiley & Sons.

51. F.P. Incropera and D.P. Dewitt, Introduction to heat transfer. 2002: John Wiley & Sons, Inc.

52. M.Z. Podowski and R.M. Podowski, Mechanistic multidimensional modeling of forced convection boiling heat transfer. *Science and Technology of Nuclear Installations*, 2009.

53. B.U. Bae, B.J. Yun, H.Y. Yoon, C.H. Song, and G.C. Park, Analysis of subcooled boiling flow with one-group interfacial area transport equation and bubble lift-off model. *Nuclear Engineering and Design*, 2010. **240**(9): p. 2281-2294.

54. E. Krepper and R. Rzehak, CFD for subcooled flow boiling: Simulation of DEBORA experiments. *Nuclear Engineering and Design*, 2011. **241**(9): p. 3851-3866.

55. G.H. Yeoh, S.C.P. Cheung, J.Y. Tu, and M.K.M. Ho, Fundamental consideration of wall heat partition of vertical subcooled boiling flows. *International Journal of Heat and Mass Transfer*, 2008. **51**(15-16): p. 3840-3853.

56. H. Anglart, O. Nylund, N. Kurul, and M.Z. Podowski, CFD prediction of flow and phase distribution in fuel assemblies with spacers. *Nuclear Engineering and Design*, 1997. **177**(1-3): p. 215-228.

57. J. Yoo, C.E. Estrada-Perez, and Y.A. Hassan, A proper observation and characterization of wall nucleation phenomena in a forced convective boiling system. *International Journal of Heat and Mass Transfer*, 2014. **76**: p. 568-584.

58. H.C. Unal, Maximum bubble diameter, maximum bubble growth time and bubble growth rate during subcooled nucleate flow boiling of water up to 17.7 MN/M2. *International Journal of Heat and Mass Transfer*, 1976. **19**(6): p. 643-649.

59. S.D. Li, S.C. Tan, C. Xu, P.Z. Gao, and L.C. Sun, An experimental study of bubble sliding characteristics in narrow channel. *International Journal of Heat and Mass Transfer*, 2013. **57**(1): p. 89-99.

60. T. Okawa, T. Ishida, I. Kataoka, and M. Mori, On the rise paths of single vapor bubbles after the departure from nucleation sites in subcooled upflow boiling. *International Journal of Heat and Mass Transfer*, 2005. **48**(21-22): p. 4446-4459.

61. A.H. Abdelmessih, S. Nangia, and F.C. Hooper, Flow effects on bubble growth and collapse in surface boiling. *International Journal of Heat and Mass Transfer*, 1972. **15**(1): p. 115-118.

62. G. Kocamustafaogullari and M. Ishii, Interfacial area and nucleation site density in boiling systems. *International Journal of Heat and Mass Transfer*, 1983. **26**(9): p. 1377-1387.

63. H.J. Ivey, Relationships between bubble frequency departure diameter and rise velocity in nucleate boiling. *International Journal of Heat and Mass Transfer*, 1967. **10**(8): p. 1023-1040.

64. J. Yoo, C.E. Estrada-Perez, and Y.A. Hassan, An accurate wall temperature measurement using infrared thermometry with enhanced two-phase flow visualization in a convective boiling system. *Int J Therm Sci*, 2015. **90**: p. 248-266.

65. R. Maurus and T. Sattelmayer, Bubble and boundary layer behaviour in subcooled flow boiling. *International Journal of Thermal Sciences*, 2006. **45**(3): p. 257-268.

66. N. Stuurman, MTrack2, 2003, http://valelab.ucsf.edu/~nstuurman/ijplugins/MTrack2.html.

67. H.K. Forster and R. Greif, Heat transfer to a boiling liquid - mechanisms and correlations. *Journal of Heat Transfer-Transactions of the Asme*, 1959. **81**: p. 43-53.

68. N. Kurul and M.Z. Podowski, Multidimensional effects in forced convection subcooled boiling, in *Proceedings of the 9th International Heat Transfer Conference*1990, Hemisphere Publishing Corporation: Jerusalem, Israel. p. 21-26.

69. W.M. Rohsenow, Heat transfer with evaporation. 1953, Chapter in Heat Transfer, University of Michigan Press.

70. R.W. Bowring, Physical model based on bubble detachment and calculation of steam voidage in the subcooled region of a heated channel, 1962, OECD Halden Reactor Project Report HPR-10.

71. A.E. Bergles and W.M. Rohsenow, The determination of forced convection, surface boiling heat transfer. *Journal of Heat Transfer-Transactions of the Asme*, 1964. **86**: p. 365-372.

72. R.W. Bjorge, G.R. Hall, and W.M. Rohsenow, Correlation of forced-convection boiling heat-transfer data. *International Journal of Heat and Mass Transfer,* 1982. **25**(6): p. 753-757.

73. S.G. Kandlikar, A general correlation for saturated 2-phase flow boiling heat-transfer inside horizontal and vertical tubes. *Journal of Heat Transfer-Transactions of the Asme*, 1990. **112**(1): p. 219-228.

74. S.G. Kandlikar, A model for correlating flow boiling heat-transfer in augmented tubes and compact evaporators. *Journal of Heat Transfer-Transactions of the Asme*, 1991. **113**(4): p. 966-972.

75. M.M. Shah, Chart correlation for saturated boiling heat transfer: Equations and further study, in *ASHRAE Trans.*1982. p. 185-196.

76. P. Griffith, J.A. Clark, and W.M. Rohsenow, Void volumes in subcooled boiling, in *National Heat Transfer Conference* 1958: Chicago, U.S.

77. R.T. Lahey. A mechanistic subcooled boiling model. in *Proceedings of the 6th International Heat Transfer Conference*. 1978. Toronto, Canada: Hemisphere Publishing Corporation, Washington.

78. O. Zeitoun, Subcooled flow boiling and condensation, PhD Dissertation, 1994, McMaster University: Ontario, Canada.

79. V.H. Delvalle and D.B.R. Kenning, Subcooled flow boiling at high heat-flux. *International Journal of Heat and Mass Transfer*, 1985. **28**(10): p. 1907-1920.

80. T. Hibiki and M. Ishii, Active nucleation site density in boiling systems. *International Journal of Heat and Mass Transfer*, 2003. **46**(14): p. 2587-2601.

81. K. Cornwell, The influence of bubbly flow on boiling from a tube in a bundle. *International Journal of Heat and Mass Transfer*, 1990. **33**(12): p. 2579-2584.

82. G.E. Thorncroft and J.F. Klausner, The influence of vapor bubble sliding on forced convection boiling heat transfer. *Journal of Heat Transfer-Transactions of the Asme*, 1999. **121**(1): p. 73-79.

83. S.D. Houston and K. Cornwell, Heat transfer to sliding bubbles on a tube under evaporating and non-evaporating conditions. *International Journal of Heat and Mass Transfer*, 1996. **39**(1): p. 211-214.

84. T. Okawa, T. Ishida, I. Kataoka, and M. Mori, An experimental study on bubble rise path after the departure from a nucleation site in vertical upflow boiling. *Experimental Thermal and Fluid Science*, 2005. **29**(3): p. 287-294.

85. D.W. Yuan, L.M. Pan, D.Q. Chen, H. Zhang, J.H. Wei, and Y.P. Huang, Bubble behavior of high subcooling flow boiling at different system pressure in vertical narrow channel. *Applied Thermal Engineering*, 2011. **31**(16): p. 3512-3520.

86. J.J. Xu, B.D. Chen, Y.P. Huang, X. Yan, and D.W. Yuan, Experimental visualization of sliding bubble dynamics in a vertical narrow rectangular channel. *Nuclear Engineering and Design*, 2013. **261**: p. 156-164.

87. R. Martinez-Cuenca, C.S. Brooks, J.E. Julia, T. Hibiki, and M. Ishii, Stochastic nature of wall nucleation and its impact on the time average boundary condition. *Journal of Heat Transfer-Transactions of the Asme*, 2015. **137**: p. 021504.

APPENDIX A.

A.1. Derivation of apparent reflectivity and apparent transmissivity

In Figure A-1, the semi-transparent medium ‘m’ is located in the middle of the medium ‘∞’. Consider that the incoming radiation E_{inc} hits the left side of ‘m-∞’ interface. Then, part of E_{inc} is reflected at this interface; the reflected amount is $\rho_{m\text{-}\infty}E_{inc}$ while the remainder $(1\text{-}\rho_{m\text{-}\infty})E_{inc}$ passes through the interface and subsequently reaches the other side of the ‘m-∞’ interface. The energy reaching this ‘m-∞’ interface on the right side is attenuated by the transmissivity of the medium $(1\text{-}\rho_{m\text{-}\infty})\tau_m E_{inc}$. Part of this energy is reflected again at this interface (‘m-∞’), the amount of which is $\rho_{m\text{-}\infty}(1\text{-}\rho_{m\text{-}\infty})\tau_m E_{inc}$ while the remainder $(1\text{-}\rho_{m\text{-}\infty})^2\tau_m E_{inc}$ passes through this interface. The total amount of reflection and transmission by the semi-transparent medium can be estimated by considering these infinite number of reflections and transmissions within the medium, from which apparent reflectivity ($\rho_{app,m\text{-}\infty}$) and apparent transmissivity ($\tau_{app,m\text{-}\infty}$) can be obtained. As illustrated in Figure A-1, $\rho_{app,m\text{-}\infty}$ and $\tau_{app,m\text{-}\infty}$ can be calculated using the analytical form of the infinite series as follows:

- *Total energy reflected by the semi-transparent medium ‘m’*

$$
\begin{aligned}
&[\rho_{m-\infty} + (1-\rho_{m-\infty})^2\rho_{m-\infty}\tau_m^2 + (1-\rho_{m-\infty})^2\rho_{m-\infty}^3\tau_m^4 + (1-\rho_{m-\infty})^2\rho_{m-\infty}^5\tau_m^6 \cdots]E_{inc} \\
&= [\rho_{m-\infty} + \frac{(1-\rho_{m-\infty})^2\rho_{m-\infty}\tau_m^2}{1-\rho_{m-\infty}^2\tau_m^2}]E_{inc} \qquad \text{(A-1)} \\
&= \rho_{app,m-\infty}E_{inc}
\end{aligned}
$$

- *Total energy transmitted through the semi-transparent medium 'm'*

$$\begin{aligned}
&[(1-\rho_{m-\infty})^2\tau_m + (1-\rho_{m-\infty})^2\rho^2_{m-\infty}\tau^3_m + (1-\rho_{m-\infty})^2\rho^4_{m-\infty}\tau^5_m + \cdots]E_{inc} \\
&= [\frac{(1-\rho_{m-\infty})^2\tau_m}{1-\rho^2_{m-\infty}\tau^2_m}]E_{inc} \\
&= \tau_{app,m-\infty}E_{inc}
\end{aligned} \tag{A-2}$$

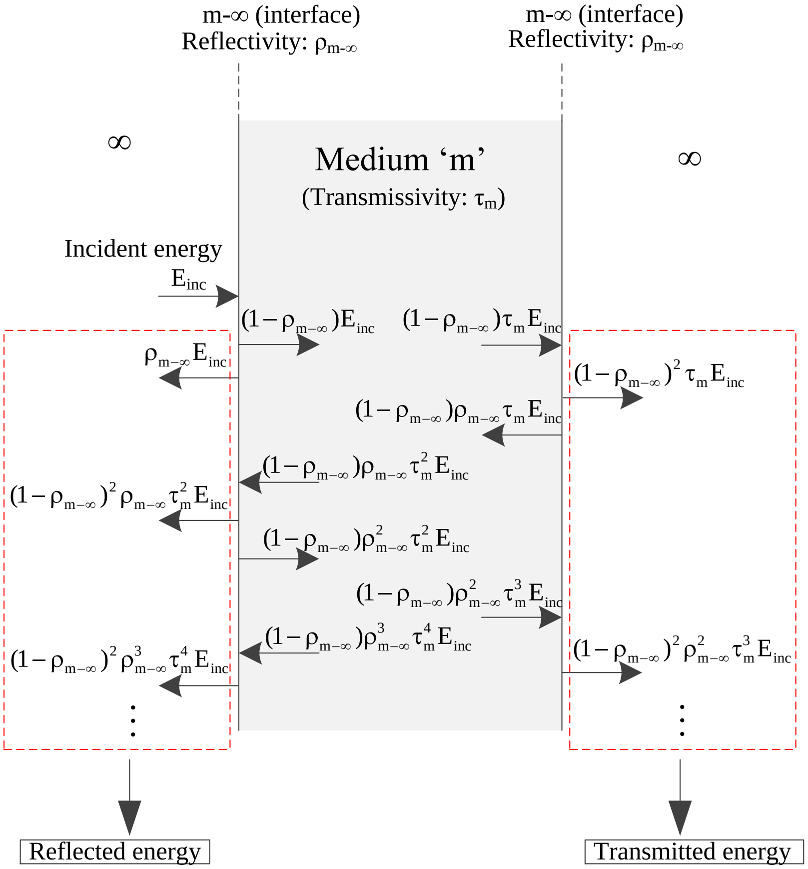

Figure A-1. Energy reflection and transmission throughout the semi-transparent medium

A.2. Radiation balance equation and coefficients required for validation tests in Section D.2 in Chapter III

Figure A-2 shows the experimental setup used in the validation test with a single layer of semi-transparent medium. The blackbody source temperature is observed through the semi-transparent medium ‘m’ (i.e., soda-lime glass, sapphire) using the IR camera. Note that the apparent reflectivity at interface 1, $\rho_{app,m\text{-}\infty,1}$ as shown in Figure A-2 is considered to be the same as normal reflectivity $\rho_{m\text{-}\infty}$ because the reflection from the blackbody source is negligible due to the special coating applied to its surface.

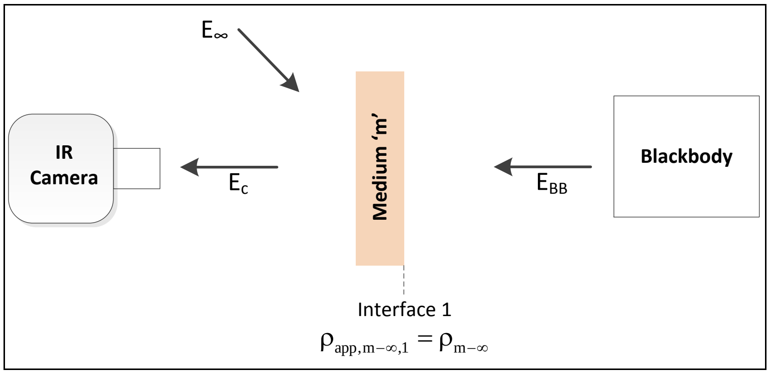

Figure A-2. Experimental setup for validation test with a single layer of medium

The governing equation as well as the derivation of coefficients used to track the blackbody source temperature through the medium is described in Figure A-3. In it, E_c represents the total amount of energy reaching the IR camera. The first term on the right-hand side of the balance equation is the energy due to the background radiation reflected by the target objects. The second term is the energy due to the emission from the medium, and the third term is the energy contribution from the blackbody source through the medium. In Figures A-4 and A-5, the experimental set up, governing equation, and the coefficients for the double-layer validation test are also shown. The governing equation and coefficients are obtained using the same principle and assumption mentioned in the single-layer validation test. The apparent reflectivities at different interfaces are obtained as shown in Figure A-4, which are required to simplify the derivation process of the coefficients shown in Figure A-5.

Energy Balance Equation: $\boxed{E_c = \rho^*_{app,m-\infty} E_\infty + \varepsilon^*_{app,m-\infty} E_m + \tau^*_{app,m-\infty} E_{BB}}$ where $E_{BB} = \varepsilon_{BB} \sigma F_{3-5\mu m}(T) T^4_{BB}$, $E_\infty = \sigma F_{3-5\mu m}(T) T^4_\infty$

$$E_m = \int_0^{L_m} e_m \sigma F_{3-5\mu m}(T) T^4_m(x) \exp(-a_m x) dx$$

Estimation of Coefficients

$$\begin{aligned}
\rho^*_{app,m-\infty} &= \rho_{m-\infty} + (1-\rho_{m-\infty})^2 \tau^2_m \rho_{app,m-\infty,1} + (1-\rho_{m-\infty})^2 \rho_{m-\infty} \tau^4_m \rho^2_{app,m-\infty,1} + \dots \\
&= \rho_{m-\infty} + \frac{(1-\rho_{m-\infty})^2 \tau^2_m \rho_{app,m-\infty,1}}{1-\rho_{m-\infty}\rho_{app,m-\infty,1}\tau^2_m} \\
\varepsilon^*_{app,m-\infty} &= [\rho_{app,m-\infty,1}\tau_m(1-\rho_{m-\infty}) + \rho^2_{app,m-\infty,1}\tau^3_m \rho_{m-\infty}(1-\rho_{m-\infty}) + \dots] \\
&\quad + [(1-\rho_{m-\infty}) + \rho_{m-\infty}\rho_{app,m-\infty,1}\tau^2_m(1-\rho_{m-\infty}) + \rho^2_{m-\infty}\rho^2_{app,m-\infty,1}\tau^4_m(1-\rho_{m-\infty}) + \dots] \\
&= \frac{\rho_{app,m-\infty,1}\tau_m(1-\rho_{m-\infty})}{1-\rho_{app,m-\infty,1}\rho_{m-\infty}\tau^2_m} + \frac{(1-\rho_{m-\infty})}{1-\rho_{app,m-\infty,1}\rho_{m-\infty}\tau^2_m} \\
&= \frac{(1-\rho_{m-\infty})(1+\rho_{app,m-\infty,1}\tau_m)}{1-\rho_{m-\infty}\rho_{app,m-\infty,1}\tau^2_m} \\
\tau^*_{app,m-\infty} &= (1-\rho_{m-\infty})^2 \tau_m + (1-\rho_{m-\infty})^2 \rho_{m-\infty}\tau^3_m \rho_{app,m-\infty,1} + (1-\rho_{m-\infty})^2 \rho^2_{m-\infty}\tau^5_m \rho^2_{app,m-\infty,1} + \dots \\
&= \frac{(1-\rho_{m-\infty})^2 \tau_m}{1-\rho_{m-\infty}\rho_{app,m-\infty,1}\tau^2_m}
\end{aligned}$$

Figure A-3. Radiation balance equation and coefficients used for the single-layer validation test

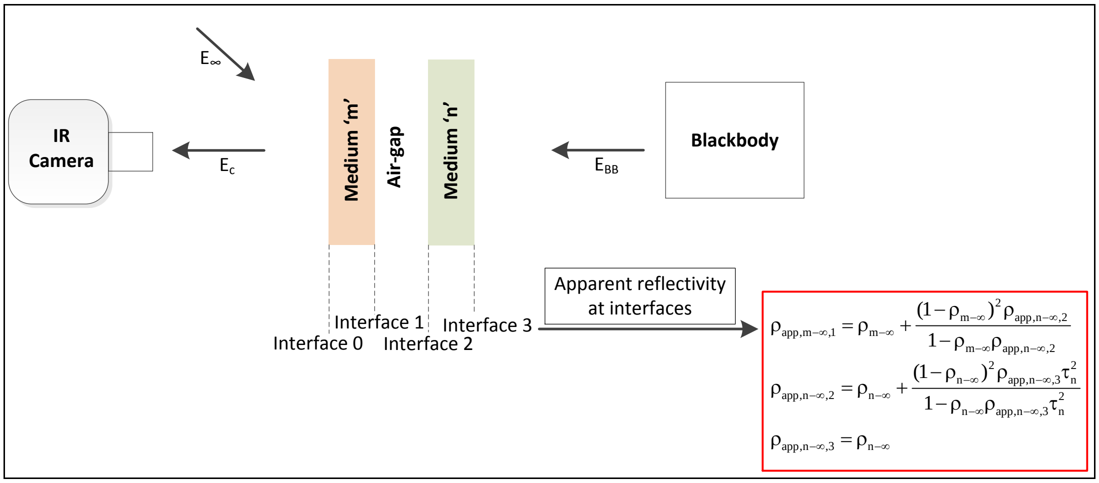

$$\rho_{app,m-\infty,1} = \rho_{m-\infty} + \frac{(1-\rho_{m-\infty})^2 \rho_{app,n-\infty,2}}{1-\rho_{m-\infty}\rho_{app,n-\infty,2}}$$

$$\rho_{app,n-\infty,2} = \rho_{n-\infty} + \frac{(1-\rho_{n-\infty})^2 \rho_{app,n-\infty,3}\tau_n^2}{1-\rho_{n-\infty}\rho_{app,n-\infty,3}\tau_n^2}$$

$$\rho_{app,n-\infty,3} = \rho_{n-\infty}$$

Figure A-4. Validation test with double layers of medium

Energy Balance Equation: $\boxed{E_c = \rho_{\infty-c,m}E_\infty + \varepsilon_{m-c}E_m + \varepsilon_{n-c}E_n + \tau_{BB-c}E_{BB}}$ where $E_{BB} = \varepsilon_{BB}\sigma F_{3-5\mu m}(T)T_{BB}^4,\ E_\infty = \sigma F_{3-5\mu m}(T)T_\infty^4$

$$E_m = \int_0^{L_m} e_m \sigma F_{3-5\mu m}(T)T_m^4(x)\exp(-a_m x)dx$$

Estimation of Coefficients

$$\rho_{\infty-c,m} = \rho_{m-\infty} + (1-\rho_{m-\infty})^2\tau_m^2\rho_{app,m-\infty,1} + (1-\rho_{m-\infty})^2\rho_{m-\infty}\tau_m^4\rho_{app,m-\infty,1}^2 + \ldots$$

$$= \rho_{m-\infty} + \frac{(1-\rho_{m-\infty})^2\tau_m^2\rho_{app,m-\infty,1}}{1-\rho_{m-\infty}\rho_{app,m-\infty,1}\tau_m^2}$$

$$\varepsilon_{m-c} = [(1-\rho_{m-\infty}) + \rho_{m-\infty}(1-\rho_{m-\infty})\tau_m^2\rho_{app,m-\infty,1} + (1-\rho_{m-\infty})\rho_{m-\infty}^2\tau_m^4\rho_{app,m-\infty,1}^2 + \ldots]$$

$$+[(1-\rho_{m-\infty})\rho_{app,m-\infty,1}\tau_m + (1-\rho_{m-\infty})\rho_{m-\infty}\rho_{app,m-\infty,1}^2\tau_m^3 + (1-\rho_{m-\infty})\rho_{m-\infty}^2\rho_{app,m-\infty,1}^3\tau_m^5 + \ldots]$$

$$= \frac{(1-\rho_{m-\infty})}{1-\rho_{m-\infty}\rho_{app,m-\infty,1}\tau_m^2} + \frac{(1-\rho_{m-\infty})\rho_{app,m-\infty,1}\tau_m}{1-\rho_{m-\infty}\rho_{app,m-\infty,1}\tau_m^2}$$

$$= \frac{(1-\rho_{m-\infty})(1+\rho_{app,m-\infty,1}\tau_m)}{1-\rho_{m-\infty}\rho_{app,m-\infty,1}\tau_m^2}$$

$$\varepsilon_{n-c} = [(1-\rho_{n-\infty}) + \rho_{n-\infty}(1-\rho_{n-\infty})\tau_n^2\rho_{app,n-\infty,3} + (1-\rho_{n-\infty})\rho_{n-\infty}^2\tau_n^4\rho_{app,n-\infty,3}^2 + \ldots$$

$$+(1-\rho_{n-\infty})\rho_{app,m-\infty,3}\tau_n + (1-\rho_{n-\infty})\rho_{n-\infty}\rho_{app,m-\infty,3}^2\tau_n^3 + (1-\rho_{n-\infty})\rho_{n-\infty}^2\rho_{app,n-\infty,3}^3\tau_n^5 + \ldots]\cdot[\frac{1-\rho_{m-\infty}}{1-\rho_{m-\infty}\rho_{app,n-\infty,2}}]\cdot[\frac{(1-\rho_{m-\infty})\tau_m}{1-\rho_{m-\infty}\rho_{app,m-\infty,1}\tau_m^2}]$$

$$= [\frac{(1-\rho_{n-\infty})}{1-\rho_{n-\infty}\rho_{app,n-\infty,3}\tau_n^2} + \frac{(1-\rho_{n-\infty})\rho_{app,n-\infty,3}\tau_n}{1-\rho_{n-\infty}\rho_{app,n-\infty,3}\tau_n^2}]\cdot[\frac{1-\rho_{m-\infty}}{1-\rho_{m-\infty}\rho_{app,n-\infty,2}}]\cdot[\frac{(1-\rho_{m-\infty})\tau_m}{1-\rho_{m-\infty}\rho_{app,m-\infty,1}\tau_m^2}]$$

$$= [\frac{(1-\rho_{n-\infty})(1+\rho_{app,n-\infty,3}\tau_n)}{1-\rho_{n-\infty}\rho_{app,n-\infty,3}\tau_n^2}]\cdot[\frac{1-\rho_{m-\infty}}{1-\rho_{m-\infty}\rho_{app,n-\infty,2}}]\cdot[\frac{(1-\rho_{m-\infty})\tau_m}{1-\rho_{m-\infty}\rho_{app,m-\infty,1}\tau_m^2}]$$

$$\tau_{BB-c} = [\frac{(1-\rho_{n-\infty})\tau_n}{1-\rho_{n-\infty}\rho_{app,n-\infty,3}\tau_n^2}]\cdot[\frac{1-\rho_{n-\infty}}{1-\rho_{m-\infty}\rho_{app,n-\infty,2}}]\cdot[\frac{(1-\rho_{m-\infty})^2\tau_m}{1-\rho_{m-\infty}\rho_{app,m-\infty,1}\tau_m^2}]$$

Figure A-5. Radiation balance equation and coefficients used for the double-layer validation test

A.3. Heater wall temperature tracking through the multilayer

The wall temperature tracking through the multilayer shown in Figure III-2 is performed using the two-way coupled algorithm between the radiation balance equation and 1D heat conduction equation (Section C in Chapter III). In Figure A-6, the coupling algorithm and the governing equations employed are presented. It is noted that we defined the apparent reflectivities at interface 1 and interface 2 shown in Figure A-6 to make the derivation of coefficients used in Eq. (III-1) more convenient. Using the definitions, the infinite number of transmissions/reflections between interface 1 and interface 3, between interface 2 and interface 3 can be treated implicitly during the derivation as shown in Figure A-7 which describes the derivation process of the coefficients for Eq. (1) with their physical meanings.

Also, to solve the Eq. (1), the amount of radiation emitted by each layer is estimated as follows:

First, for the semi-transparent layer to mid-wave IR radiation (i.e., sapphire, soda-lime glass), the volumetric effect of radiation must be considered to calculate the amount of energy emitted. In other words, E_{sap} or E_g is calculated by integrating the local emission and attenuation within the volume of each medium. Let us consider the radiation flux (W/m^2) emitted by a differential layer of thickness dx in the x-direction with an emission coefficient of e_m (m^{-1}). Then, the radiation flux from the small thickness is given by $e_m \sigma F_{3\text{-}5\mu m}(T) T_m^4(x) dx$. Considering the attenuation across the medium of thickness Lm, the total emission (E_m) by a medium is obtained by

$$E_m = \int_0^{L_m} e_m \sigma F_{3-5\mu m}(T) T_m^4(x) \exp(-a_m x) dx \qquad \text{(A-3)}$$

where m refers to the medium (i.e., sap or g), e is the emission coefficient, a is the absorption coefficient, L_m is the thickness of the medium, and T_m is the temperature of the medium.

Applying Kirchhoff's law, which assumes a relationship of equality between the emission and absorption coefficient (i.e., e=a), Eq. (2) can be rewritten as

$$E_m = \int_0^{L_m} a_m \sigma F_{3-5\mu m}(T) T_m^4(x) \exp(-a_m x) dx \qquad \text{(A-4).}$$

The radiation generated by the ITO film, which is opaque to IR radiation, is estimated as

$$E_{ITO} = \varepsilon_{ITO} \sigma F_{3-5\mu m}(T) T_{ITO}^4 \qquad \text{(A-5)}$$

where ε_{ITO} is the emissivity of ITO and T_{ITO} is the temperature of the ITO film.

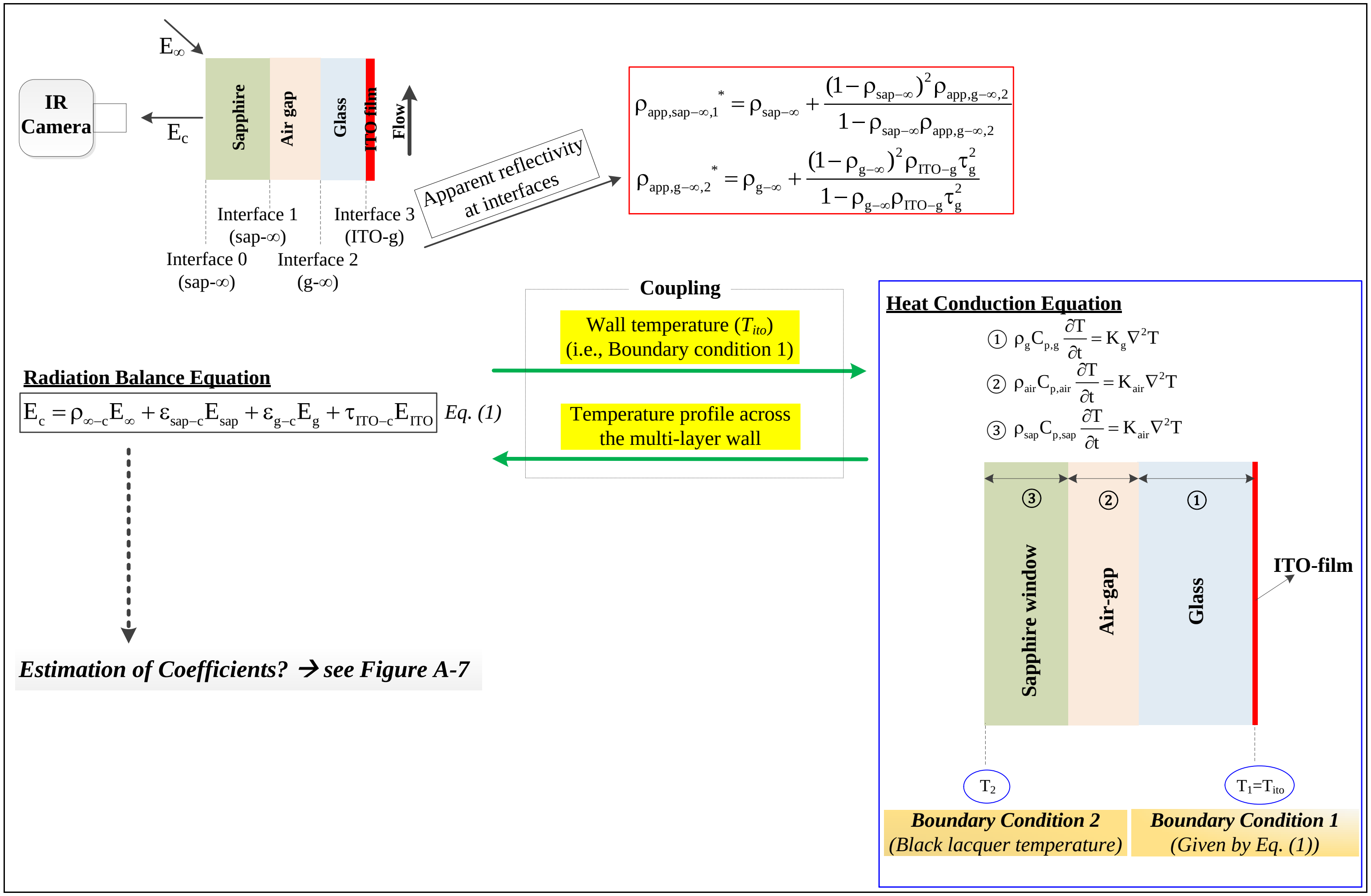

Figure A-6. Schematic of wall temperature tracking algorithm

Estimation of Coefficients

$$1.\ \rho_{\infty-c}=\rho_{sap-\infty}+(1-\rho_{sap-\infty})^2\tau_{sap}^2\rho_{app,sap-\infty,1}^{*}+(1-\rho_{sap-\infty})^2\rho_{sap-\infty}\tau_{sap}^4\rho_{app,sap-\infty,1}^{2\,*}+\ldots$$

$$=\boxed{\rho_{sap-\infty}+\frac{(1-\rho_{sap-\infty})^2\tau_{sap}^2\rho_{app,sap-\infty,1}^{*}}{1-\rho_{sap-\infty}\rho_{app,sap-\infty,1}^{*}\tau_{sap}^2}}\longrightarrow$$

Portion of background radiation reaching IR camera after being reflected by target objects

$$2.\ \varepsilon_{sap-c}=(1-\rho_{sap-\infty})+\rho_{sap-\infty}(1-\rho_{sap-\infty})\tau_{sap}^2\rho_{app,sap-\infty,1}^{*}+(1-\rho_{sap-\infty})\rho_{sap-\infty}^2\tau_{sap}^4\rho_{app,sap-\infty,1}^{2\,*}+\ldots$$

$$+(1-\rho_{sap-\infty})\rho_{app,sap-\infty,1}^{*}\tau_{sap}+(1-\rho_{sap-\infty})\rho_{sap-\infty}\rho_{app,sap-\infty,1}^{2\,*}\tau_{sap}^3+(1-\rho_{sap-\infty})\rho_{sap-\infty}^2\rho_{app,sap-\infty,1}^{3\,*}\tau_{sap}^5+\ldots$$

$$=\frac{(1-\rho_{sap-\infty})}{1-\rho_{sap-\infty}\rho_{app,sap-\infty,1}^{*}\tau_{sap}^2}+\frac{(1-\rho_{sap-\infty})\rho_{app,sap-\infty,1}^{*}\tau_{sap}}{1-\rho_{sap-\infty}\rho_{app,sap-\infty,1}^{*}\tau_{sap}^2}$$

$$=\boxed{\frac{(1-\rho_{sap-\infty})(1+\rho_{app,sap-\infty,1}^{*}\tau_{sap})}{1-\rho_{sap-\infty}\rho_{app,sap-\infty,1}^{*}\tau_{sap}^2}}\longrightarrow$$

Portion of sapphire emission reaching the IR camera

$$3.\ \varepsilon_{g-c}=[(1-\rho_{g-\infty})+\rho_{g-\infty}(1-\rho_{g-\infty})\tau_g^2\rho_{ITO-g}+(1-\rho_{g-\infty})\rho_{g-\infty}^2\tau_g^4\rho_{ITO-g}^2+\ldots$$

$$+(1-\rho_{g-\infty})\rho_{ITO-g}\tau_g+(1-\rho_{g-\infty})\rho_{g-\infty}\rho_{ITO-g}^2\tau_g^3+(1-\rho_{g-\infty})\rho_{g-\infty}^2\rho_{ITO-g}^3\tau_g^5+\ldots]\cdot[\frac{1-\rho_{sap-\infty}}{1-\rho_{sap-\infty}\rho_{app,g-\infty,2}^{*}}]\cdot[\frac{(1-\rho_{sap-\infty})\tau_{sap}}{1-\rho_{sap-\infty}\rho_{app,sap-\infty,1}^{*}\tau_{sap}^2}]$$

$$=[\frac{(1-\rho_{g-\infty})}{1-\rho_{g-\infty}\rho_{ITO-g}\tau_g^2}+\frac{(1-\rho_{g-\infty})\rho_{ITO-g}\tau_g}{1-\rho_{g-\infty}\rho_{ITO-g}\tau_g^2}]\cdot[\frac{1-\rho_{sap-\infty}}{1-\rho_{sap-\infty}\rho_{app,g-\infty,2}}]\cdot[\frac{(1-\rho_{sap-\infty})\tau_{sap}}{1-\rho_{sap-\infty}\rho_{app,sap-\infty,1}^{*}\tau_{sap}^2}]$$

$$=\overset{(a)}{\boxed{[\frac{(1-\rho_{g-\infty})(1+\rho_{ITO-g}\tau_g)}{1-\rho_{g-\infty}\rho_{ITO-g}\tau_g^2}]}}\cdot\overset{(b)}{\boxed{[\frac{1-\rho_{sap-\infty}}{1-\rho_{sap-\infty}\rho_{app,g-\infty,2}^{*}}]}}\cdot\overset{(c)}{\boxed{[\frac{(1-\rho_{sap-\infty})\tau_{sap}}{1-\rho_{sap-\infty}\rho_{app,sap-\infty,1}^{*}\tau_{sap}^2}]}}\longrightarrow$$

***(a)** Portion of glass emission passing through interface 2*
***(b)** Portion passing through interface 1 from (a)*
***(c)** Portion reaching the IR camera from (b)*

$$4.\ \tau_{ITO-c}=\overset{(d)}{\boxed{[\frac{\tau_g}{1-\rho_{g-\infty}\rho_{ITO-g}\tau_g^2}]}}\cdot\overset{(e)}{\boxed{[\frac{1-\rho_{g-\infty}}{1-\rho_{sap-\infty}\rho_{app,g-\infty,2}^{*}}]}}\cdot\overset{(f)}{\boxed{[\frac{(1-\rho_{sap-\infty})^2\tau_{sap}}{1-\rho_{sap-\infty}\rho_{app,sap-\infty,1}^{*}\tau_{sap}^2}]}}\longrightarrow$$

***(d)** Portion of ITO emission reaching interface 2*
***(e)** Portion reaching interface 1 from (d)*
***(f)** Portion reaching the IR camera from (e)*

Figure A-7. Derivation of coefficients used in Eq. (III-1)